UNIVERSITY
OF TRENTO - Italy
Department of Materials Engineering
and Industrial Technologies

Doctoral School in Materials Engineering – XXIII cycle

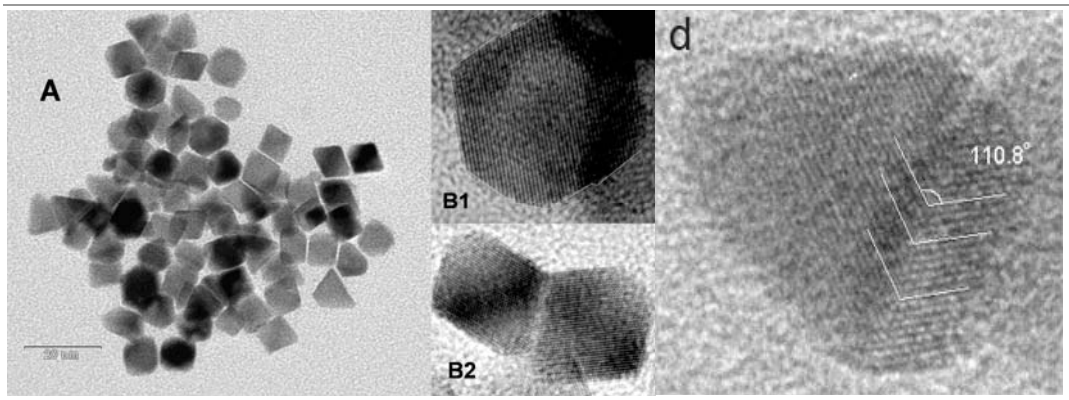

Simulation and Modeling of the Powder Diffraction Pattern from Nanoparticles:

Studying the Effects of Faulting in Small Crystallites

Kenneth Roy Beyerlein

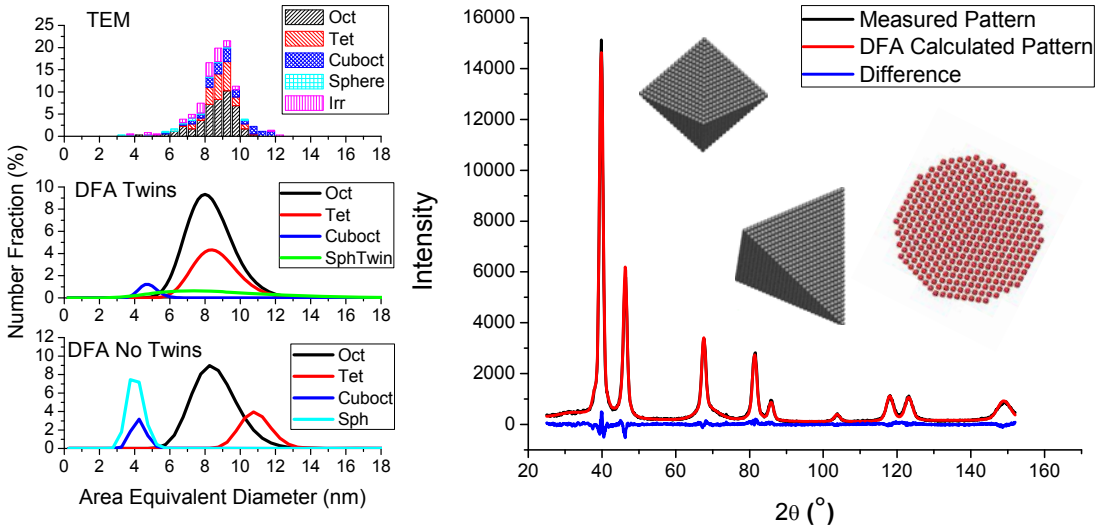

June 2011

SIMULATION AND MODELING OF THE POWDER DIFFRACTION PATTERN FROM NANOPARTICLES: STUDYING THE EFFECTS OF FAULTING IN SMALL CRYSTALLITES

Approved by:

Professor Paolo Scardi, Advisor
School of Materials Engineering and Industrial Technologies
University of Trento, Italy

Professor Angus Wilkinson
School of Chemistry
Georgia Institute of Technology

Professor Matteo Leoni
School of Materials Engineering and Industrial Technologies
University of Trento, Italy

Professor Zhong L. Wang
School of Materials Science and Engineering
Georgia Institute of Technology

Professor Robert L. Snyder
School of Materials Science and Engineering
Georgia Institute of Technology

Professor Mo Li
School of Materials Science and Engineering
Georgia Institute of Technology

Date Approved: 13 June 2011

To my parents, for all of their support and encouragement.

PREFACE

Another thesis has also been submitted to the Georgia Institute of Technology in Atlanta, Georgia, USA, for fulfillment of the requirements of the dual-degree program. The interested reader is then referred to that manuscript entitled "Simulation and Modeling of the Powder Diffraction Pattern from Nanoparticles: Studying the Influence of Surface Strain," where they will find a chapter discussing the effect of surface strain gradients on the powder diffraction peak profiles.

ACKNOWLEDGEMENTS

I have had the fortune of been given the opportunity to be the first to participate in dual-degree program between the Georgia Institute of Technology and the University of Trento, Italy. Uncertain to what lay ahead, I set out on my first trip to Italy with little more than a rudimentary understanding of Spanish, a few words of Italian, and two huge suitcases — all of which immediately became formidable obstacles during my first night in Venice. While the distance from home, and frustrations which accompany living in any foreign country, were hard at times, the countless ways in which this period has enriched my life, and the way I do science, does not make me want to change a thing about it. So, for their guidance, trust, patience, and never ending support I am very grateful to my advisers, Professor Bob Snyder and Professor Paolo Scardi.

Throughout the course of my PhD I was also influenced by the exchange of ideas, imagination and the push for more fundamental insight which was encouraged from working with my co-adviser, Professor Mo Li. Finally, I have to thank a fourth mentor, Professor Matteo Leoni, who has helped deepen my understanding of diffraction through hours of discussions, and has spent a lot of time developing the PM2K analysis software, which has added another dimension to much of the studies which are presented in this work. I would also like to thank Professor

Angus Wilkinson and Professor Z.L. Wang for serving on my committee and their many helpful suggestions throughout my thesis.

I am certainly deeply appreciative and thankful for the many lasting international friends and colleagues that I have come to know along the course of my PhD. In particular I would like to thank Professor Emmanuel Garnier and Professor Jose Sulla-Gullon for their hard work in the synthesis, TEM and electrochemical characterization of the platinum nanoparticles which were studied. Also, I have to thank the group in Trento for taking me in, and teaching me all the necessary Italian, both good and bad. Thank you Cristy, Hector, David, Luca, Matteo, Melanie, Alberto, Mahmoud, Mirco, Sergio, and finally Giovanna! Also the group that works with Professor Li has been very helpful and inquisitive throughout my PhD. Thank you Tao, Hao, Xueqian, Jie and Yuzheng!

Finally, I am endlessly thankful and indebted to my family, especially my parents, Lyle and Carol Beyerlein who have always been so supportive and encouraging throughout my education. Saving the best for last, I have to thank the woman who has always stuck by me with love and encouragement, my lovely, Rachel Anscher. Her constant support was a driving force throughout my thesis.

TABLE OF CONTENTS

LIST OF TABLES

LIST OF FIGURES

SUMMARY

Nanostructured materials are currently at the forefront of nearly every emerging industry, as they offer promising solutions to problems ranging from those facing energy technologies, to those concerning the structural integrity of materials. With all of these future applications, it is crucial that methods are developed which can offer accurate, and statistically reliable characterization of these materials in a reasonable amount of time. X-ray diffraction is one such method which is already widely available, and can offer further insight into the atomic structure, as well as, microstructure of nanomaterials.

This thesis work is then focused on investigating how different structural features of nanoparticles influence the line profiles of the x-ray powder diffraction pattern. Due to their extremely small size, the contribution from crystallite size broadening becomes the dominating feature in an observed diffraction peak. Therefore, the theory of size broadening was critically reviewed concerning the considerations necessary when the crystallite size approaches a few nanometers. Furthermore, the analysis of synthesized shape controlled platinum nanoparticles was carried out using a developed line profile analysis routine, based on the Debye function analysis (DFA) approach, to determine the distribution of particle size and shape in the sample.

The Debye function simulates the powder diffraction pattern from atomistic models. This allows for the coupling of this technique with atomistic simulations, like molecular dynamics (MD), to gain further understanding of the diffraction pattern from nanoparticles. Techniques were developed to study how lattice dynamics, and the resulting thermal diffuse scattering, are affected by the small crystallite domains. The different results from Al and Cu particles were discussed. Also, the use of atomic models allowed for an in depth study of how the presence of twin and deformation faults affects the diffraction pattern from small crystallites. This study then improves the understanding of diffraction from small crystallites, and showcases the level of insight which is achievable through the coupling of simulation and diffraction pattern analysis.

CHAPTER I

INTRODUCTION

1.1 General Motivation

It is fair to say that in present day, the phrase "nanotechnology" has a Jules Verne quality about it. Stories touting the latest discoveries of scientists, which just yesterday were science fiction, commonly fill the pages of popular science magazines, and captivate all who read about what life will be like in the nano-future. While some projections of when these discoveries will precipitate into a real product are somewhat ambitious, exciting proposals include the use of nanotechnology in the fields of electronics, photonics, energy, and composites with unique mechanical properties. However, the interest in nanotechnology goes far beyond these applications, as almost all properties of a material have been found to have some degree of size dependence. Trying to understand the physical origins of this size dependence, not to mention the development of the fabrication processes necessary to make these small materials, is forcing scientists to really understand the behavior of materials at the atomistic level. The ultimate goal is then enough understanding that the fabrication of materials might begin with the consideration of their atomistic assembly, and continue with structuring over larger length scales. Then,

from a list of desired properties, like strength or electrical conductivity, one would be able to make the appropriate material in a lab — much like constructing a building to desired specifications.

The further understanding of any material's behavior is contingent upon observations, which means the further development of characterization techniques is crucial. These measurements serve to ensure that the fabricated material actually exhibits the desired characteristics, as well as, helps to understand the influence of different aspects of the fabrication process. The small size of nanostructured materials can pose a problem for many characterization techniques. In order to study the structure of these small materials, special techniques in microscopy are commonly employed, which include transmission electron microscopy (TEM), scanning electron microscopy (SEM) and atomic force microscopy (AFM). While these techniques allow for invaluable images, and can even resolve the atomic structure of materials, they are somewhat limited in that only a small volume of the synthesized material can be studied in a reasonable amount of time. Nanomaterials which are produced industrially require a yield on the level of kilograms, orders of magnitude larger than the milligrams which are produced in the laboratory. A complete characterization of such a large batch of material by microscopy can be costly and time consuming.

X-ray powder diffraction (XRD) offers a complementary structural characterization technique, where information from a large statistical

sampling of a material can be extracted from the diffraction pattern. The diffraction pattern contains information over many length scales, from the atomic structure to the microstructure of a material. However, obtaining the detailed information on the microstructure of a material can be complicated. It involves modeling subtle changes in the shape of the observed diffraction peaks, and has been largely developed considering materials with somewhat large crystalline domains. So, before XRD can be effectively used in the characterization of nanomaterials, it is necessary to extend, and test, the existing models which describe diffraction from small crystalline domains.

1.2 Focus of Thesis

The current thesis work will then exhibit the progress made in developing better diffraction pattern analysis techniques for small crystalline domains, focusing on the case of metal nanoparticles. Research on nanoparticles has progressed rapidly in recent years, as they have found application in the fields of catalysis, medicine, electronics, and photonics [112]. Synthesis techniques have been developed to control not only size, but also the shape of nanoparticles [42]. The high yield production of shape specific nanoparticles opens a new door in materials engineering by allowing for desirable properties to be achieved by tuning the particle shape.

One of the most promising applications of these shape controlled nanoparticles is their use as a highly efficient, reaction selective, heterogeneous catalysts. Heterogeneous catalysts are an important part

of the chemical manufacturing industry as they reduce the amount of energy necessary to carry out a chemical reaction by promoting the reaction to take place on their surface. Nanoparticles are expected to make an impact in this field because their small size results in more surface area per gram of catalyst which improves the catalytic efficiency. The reduction of the amount of catalyst is important since many catalysts are made of precious metals like platinum and ruthenium. The ability of tailoring the shape can result in preferential exposure of the highly catalytically active surfaces. Furthermore, the exact chemical reaction which is promoted can be controlled by engineering the nanoparticles to preferentially expose specific faces. Therefore, the use of shape controlled nanoparticles can result in a further improvement in efficiency by promoting the chemical reaction which requires less energy. As these nanoparticles begin to be increasingly used in the industry, an improved analysis of the structure from the diffraction pattern can be important in characterizing shape of the synthesized nanoparticles, as well as, any structural modifications which might occur throughout their lifetime of use.

The initial goal of the present research is then to develop a powder diffraction pattern analysis technique which can determine the different particle shapes which make up a sample. As it will be shown in the following work, the shape of a spot in reciprocal space, and also the shape of the powder diffraction peak, is a direct consequence of the shape of

the crystallite. However, the crystallite size and shape are not the only characteristics which influence the diffraction peak profiles. Crystalline defects of all kinds are known to change the peak shapes, each in a different and specific way. Not to mention there can also be contributions from a general strain gradient, and thermal motion of the atoms. Therefore, in order to achieve a reliable characterization of a nanoparticle shape, the influence of these other effects must be considered. However, many models which have been developed to describe the influences of these crystal defects assume the case of large crystallites. Therefore, the current research will also be focused on testing and extending the models for the influence of crystal defects on the diffraction pattern considering the case of small crystallites.

In order to achieve these goals the current research will employ a developing powder diffraction pattern analysis technique which relies on atomistic descriptions of the crystallites. The powder diffraction pattern can be directly obtained from any arrangement of atoms in a volume through the Debye function [37]. The analysis of the diffraction pattern by this approach has not been extensively developed in the past due to the computational burden which is demanded. However, this problem becomes tractable as computers become cheaper and faster. The Debye function then opens the door to a deeper understanding of the features observed in the diffraction pattern. Atomistic models can be constructed

with desired characteristics, the diffraction pattern simulated by the Debye function, and the influence of each characteristic on the diffraction pattern can be directly observed. This approach can systematically test, and improve upon, the models which exist in the diffraction literature regarding the influences of crystallite size, crystal defects and strains on the diffraction pattern.

Interesting avenues of research also begin to emerge when it is realized that atomistic simulations like molecular dynamics (MD) can be integrated into this approach. Atomic models which are the result of MD simulations can be used to simulate the diffraction pattern and study features which are the result of an energetically more favorable model. The long term goal might be to one day incorporate MD simulations directly into the analysis of diffraction patterns. This would allow diffraction pattern analysis to evolve beyond arguments based on symmetries of the crystal lattice, and incorporate the energetics and dynamics of the system. Also, in the reverse sense, the merging of diffraction and MD simulations allows for a further method of testing the atomic structure and microstructure predicted by atomistic simulations with that found experimentally. This kind of feedback can give unique insight over multiple length scales, which allows for the improvement of MD methods, and development of better interatomic potentials.

CHAPTER II

POWDER DIFFRACTION BACKGROUND

2.1 Physical Basis of X-ray Diffraction

By definition, the word "diffraction" is a characteristic of waves which describes their ability to spread out and fill space. This phenomenon is common in everyday life, and explains why light from a street lamp can bend around a corner, or why you to can hear someone without seeing them. In the field of optics, the word diffraction takes on a slightly different meaning, and is used to describe the combination of two phenomena: scattering and interference (i.e. a diffraction grating). In this sense, diffraction is the study of the interference pattern resulting from the light which scatters from an object. Historically, the presence of such an interference pattern actually proved that light is a wave and diffracts, as opposed to traveling ballistically. Therefore, any experiments studying such an interference pattern have come to be called diffraction experiments.

X-rays are a bandwidth of light with a wavelength, λ, much shorter than the visible spectrum — in the range from 0.5Å to 2.5Å. When x-rays encounter matter they scatter from the electrons in the atoms. X-ray diffraction is then the use of x-rays to produce an interference pattern

to measure the arrangement of atoms in a material. Knowledge of the atomic structure is important for explaining physical properties like the strength, or electrical conductivity, of a material. It is by no means the only scattering method useful in materials characterization, and many of the same principles of diffraction which will be presented here also apply to techniques like neutron and electron diffraction. The fundamental difference in these techniques being the physical mechanism of how the incident radiation (i.e. x-rays, neutrons or electrons) is scattered by the atoms.

An x-ray can scatter from an atom following two primary mechanisms. In the first case, when an x-ray encounters an atom, it can seem to instantaneously "bounce off" of the electron density around an atom. The mechanism of this scattering event begins by considering that light can be described as an oscillating electromagnetic field. When such an oscillating field approaches an atom, it causes the electron density of the atom to oscillate also. This oscillating electron density produces an oscillating dipole made of the negative electron cloud, and the positive atomic nucleus. Classical electrodynamics tells us that an oscillating dipole radiates an electromagnetic field, or light. When this oscillating dipole produces x-rays of the same wavelength as the incident x-ray, energy is conserved — a process which is called *elastic* scattering, or Thompson scattering. In the second scattering mechanism, the atom absorbs some energy from the incident x-ray, and the scattered radiation

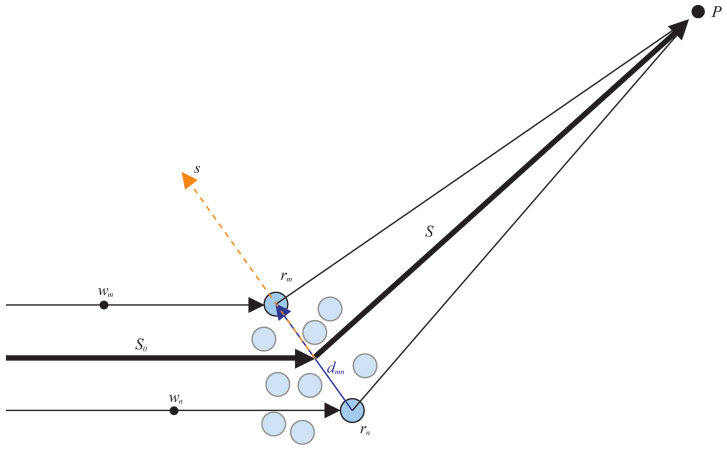

Figure 1: Cartoon of x-rays scattered by a collection of scatterers

is emitted with a lower energy. This mechanism is thus an example of *inelastic* scattering, and is more commonly called Compton scattering. The scattered radiation from both the elastic and inelastic scattering events, which occur at different atoms in a material, interfere to form the observed diffraction pattern. The effect of the elastic scattering gives rise to the prominent Bragg reflections, due to the interference of light with the same wavelength. Meanwhile, the effect of Compton scattering is largely featureless, due to the destructive interference of x-rays with multiple wavelengths. This scattered radiation contributes to the background signal, and becomes more important to consider when discussing the contributions of diffuse scattering.

2.1.1 Interference from multiple scattering centers

In the following discussion the intensity of scattered radiation at a point $\mathbf{p}$ in space from a collection of scatterers at positions $\mathbf{r_1}$, $\mathbf{r_2}$, ..., $\mathbf{r_n}$(depicted

in Figure 1), will be discussed considering the interference of monochromatic waves. As this is a rather general treatment of diffraction, the reader is assumed to already have an introduction to wave mechanics, and is referred to the text by Cullity [32] for more basic information. The incoming waves are assumed to be parallel, traveling in the direction $\mathbf{S_0}$, and allowed to be incoherent. As such, the phase of the incident radiation when it scatters is allowed to differ from one incident wave to the next. The phase of each incident wave is considered through the points $\mathbf{w_1}$, $\mathbf{w_2}$, ..., $\mathbf{w}_n$, which represent points along the path of the incident wave where its amplitude is at a maximum. While this happens repeatedly along the wave path, only one such point is depicted for each incident wave in Figure 1.

Once scattered, the path taken by each wave to reach the observation point $\mathbf{p}$ is described by the direction $\mathbf{S_n}$, which we will approximate by a constant vector, $\mathbf{S}$, by assuming that the observation point, $\mathbf{p}$, is far away from the scatterers. The amplitudes of the scattered waves observed at point $\mathbf{p}$ can be expressed in general as

$$\epsilon_n = E_n \exp\left[2\pi i \left(\nu t - l_n/\lambda\right)\right], \tag{1}$$

where E_n signifies the electric field amplitude, and l_n the distance traveled by wave n from $\mathbf{w}_n$ to $\mathbf{p}$. The variables t, ν and λ signify the propagation time, wave frequency, and wavelength respectively. Since the speed of x-rays is generally independent of the propagation medium, the waves are traveling at approximately the speed of light. Then given that the

scatterers are sufficiently clustered together, it is safe to assume that the propagation times are equal. Therefore, the phase difference between the x-rays is determined by the distance traveled, l_n. Studying the geometry of Figure 1, one finds that this distance can be expressed as

$$l_n = |\mathbf{r}_n - \mathbf{w}_n| + |\mathbf{p} - \mathbf{r}_n|, \tag{2}$$

and l_n/λ becomes

$$l_n/\lambda = \mathbf{S}_0 \cdot (\mathbf{r}_n - \mathbf{w}_n) + \mathbf{S} \cdot (\mathbf{p} - \mathbf{r}_n). \tag{3}$$

The amplitudes of waves are additive, while the intensity is the square modulus of the amplitude, implying that the intensity of the scattered radiation at point $\mathbf{p}$ is given by the relationship

$$I = AA^* = \sum_m \epsilon_m \sum_n \epsilon_n^*. \tag{4}$$

Substituting this into Equation (1) leads to the expression

$$I = \sum_n |E_n|^2 + \sum_m \sum_{n \neq m} E_m E_n^* \exp\left[-2\pi i \left(l_m - l_n\right)/\lambda\right]. \tag{5}$$

From Equation (3), the argument of the exponential is found to be expressible in terms of the scattering wave vectors as

$$\begin{aligned} \left(l_m - l_n\right)/\lambda &= (\mathbf{w_m} - \mathbf{w_n}) \cdot \mathbf{S_0} - (\mathbf{r_m} - \mathbf{r_n}) \cdot \mathbf{S_0} + (\mathbf{r_m} - \mathbf{r_n}) \cdot \mathbf{S} \\ &= (\mathbf{r_m} - \mathbf{r_n}) \cdot (\mathbf{S} - \mathbf{S_0}) + (\mathbf{w_m} - \mathbf{w_n}) \cdot \mathbf{S_0}. \end{aligned} \tag{6}$$

We then define the scattering vector, $\mathbf{s}$, as

$$\mathbf{s} = \mathbf{S} - \mathbf{S}_0, \tag{7}$$

where the magnitude of $\mathbf{s}$ is defined as $|\mathbf{s}| = s = 2\sin\theta/\lambda$, and 2θ is the scattering angle between the vectors $\mathbf{S}$ and $\mathbf{S_0}$. Also defining the distance vector between scatterers as $\mathbf{d_{mn}} = \mathbf{r_m} - \mathbf{r_n}$, and the extra phase factor $\phi_{mn} = (\mathbf{w_m} - \mathbf{w_n}) \cdot \mathbf{S_0}$, the expression for the intensity at $\mathbf{p}$ becomes

$$I = \sum_n |E_n|^2 + \sum_m \sum_{n \neq m} E_m E_n^* \exp\left[-2\pi i(\mathbf{d_{mn}} \cdot \mathbf{s} + \phi_{mn})\right]. \tag{8}$$

From this description of the intensity we find that for a perfectly coherent source, where $\phi_{mn} = 0$, the intensity is given by the familiar relation

$$I = \sum_n |E_n|^2 + \sum_m \sum_{n \neq m} E_m E_n^* \exp\left[-2\pi i(\mathbf{d_{mn}} \cdot \mathbf{s})\right]. \tag{9}$$

Then, in the case that the scattering vector is parallel to the distance vector, (as depicted in Figure 1) and that their scalar product equals an integer, n, we obtain the well known Bragg Law from the scalar product relation,

$$\begin{aligned} \mathbf{d_{mn}} \cdot \mathbf{s} &= n, \\ 2d_{mn}\sin\theta &= n\lambda. \end{aligned} \tag{10}$$

However, real instruments only exhibit a certain degree of spatial, as well as temporal, coherency. The measured intensity is then the result of an average over the possible phase factors, ϕ_{mn}, from the many waves which are interfering at the point $\mathbf{p}$. The form of this phase factor distribution is characteristic of the source, optics and measurement geometry. In powder diffraction this is one of many factors which are incorporated into what is called the instrumental profile. The existence of these kind

of instrumental effects is one reason why the inverse Fourier transform of the measured intensity cannot be directly used to yield information on the electron density and microstructure. To properly account for incident beam coherency, and other instrumental effects, the intensity found assuming an ideal instrument (perfect coherency) must be convolved with the instrumental profile. While proper consideration of the instrument is of the utmost importance, the work presented here is focused on describing the features of the diffraction pattern resulting from the scattering of a crystallite, and as such makes the above assumptions leading up to Equation (9). In reciprocal space methods the instrumental effect is then considered by convolving the intensity determined assuming perfect coherence, with the profile function attributed to the instrument. This treatment is in contrast to that taken in direct space methods (i.e. total scattering and Debye function analysis), which attempt to remove the instrumental effect by deconvolving it from the measured intensity.

The diffraction theory which is treated in this work only considers the possibility of one scattering event for a given incident wave. Known as the *kinematical* approximation, this assumption is well suited to describe x-ray scattering from imperfect, sub-micron crystallites. However, in general, any scattered wave can again scatter before exiting the crystallite, resulting in significant changes in the observed intensity. For this case the theory of dynamical scattering [77] has been developed, and it becomes essential in the interpretation of electron diffraction patterns.

2.1.2 Scattering from an atom

Now, we want to calculate the intensity observed at point $\mathbf{p}$ considering the scatterers are actually electrons in a single atom. Quantum mechanics tells us that electrons are also described as waves, and are not localized at a point in space. In order to calculate the observed intensity we must assume that each volume of space, $\mathrm{d}v_r$, at position $\mathbf{r}$ contains a charge $e\rho\left(\mathbf{r}\right)\mathrm{d}v_r$ and scatters with a power proportional to that charge. In this relationship e is the charge of an electron, and $\rho\left(\mathbf{r}\right)$ is the normalized charge density at point $\mathbf{r}$. It can be shown that the scattered amplitude from a single electron, j, is given as

$$f_j(s) = \frac{e^2}{m_e c^2}\frac{Pol'}{R}\int \rho_j(\mathbf{r}) \exp\left(-2\pi i \mathbf{r}\cdot\mathbf{s}\right)\mathrm{d}v_r, \tag{11}$$

where the integral is done over all space for the total scattering power of an electron. Here the mass of an electron, and the speed of light, are denoted as m_e and c respectively. The factor Pol' denotes the effect which polarization has on diminishing the amplitude for different scattering angles, and will be discussed later in terms of its effect on the intensity. The variable R then denotes the distance from the scattering event to the observation point. Assuming that the scattering amplitudes from each electron in an atom simply add, we find the intensity as

$$I = \frac{e^4}{m_e^2 c^4}\frac{Pol}{R^2}\left[\sum_j \left|f_j\right|^2 + \sum_j\sum_{k\neq j}\int\int \rho_j(\mathbf{r}_j)\rho_k(\mathbf{r}_k)\exp\left(-2\pi i \mathbf{d_{jk}}\cdot\mathbf{s}\right)\mathrm{d}v_j\mathrm{d}v_k\right]. \tag{12}$$

Instead of using the atomic scattering factor determined by Equation (12), it is common to use a more numerically amenable atomic scattering factor which is given by a series of exponentials of the form

$$f_n(s) = \sum_j a_j \exp(-b_j s^2/4) + c. \tag{13}$$

The coefficients of this form of the atomic scattering factor are found by either fitting to measurements, or from numerical calculations of the intensity given by Equation (12). It should be noted that this treatment is only valid when the wavelength of radiation is not near an absorption edge. When this criterion is no longer true it is necessary to include a dispersion term in the atomic scattering factor, and the anomalous scattering factor must be used [77].

2.1.3 X-ray polarization effect

As in the case of any reflection, when an x-ray is scattered by the electron in an atom it becomes polarized. Without getting into the details, polarization implies that observation of the scattered beam is the strongest in a direction normal to the polarization direction, and falls off as a function of the scattering angle [155]. If unpolarized incident radiation is assumed, then the polarization factor in Equation (12) becomes

$$Pol = \frac{1 + \cos^2 2\theta}{2}. \tag{14}$$

However, if a monochromator is used, or the scattering experiment is done at a synchrotron, then the incident beam is already polarized, and

the general polarization expression becomes

$$Pol = \frac{(1+Q) + (1-Q)\cos^2 2\theta_{mono}\cos^2 2\theta}{1+\cos^2 2\theta_{mono}}. \tag{15}$$

In this expression $2\theta_{mono}$ is the scattering angle of the monochromator, and Q is a variable denoting the degree of polarization. For unpolarized x-rays, $Q = 0$, and Equation (15) reduces to Equation (14), while in the case of radiation from a synchrotron source $Q = 1$.

2.1.4 Generalization of the scatterer

The additive property of wave amplitudes allows the definition of a scatterer to become a more general concept over larger length scales. This allows us to also determine the intensity which is observed at the point $\mathbf{p}$ from a cluster of atoms. This cluster can be the basis atoms of a unit cell, or the atoms in a small particle. As before, the amplitude of the scattered wave is the sum of the scattered waves from each atom, $F_n = \sum_n f_n$, where the atomic scattering factor is described by Equation (13). This expression is commonly called the *structure factor* when calculating the scattering from a unit cell basis, or the *form factor* when calculating the scattering from an entire crystallite. The intensity assuming coherent radiation is then given by

$$I = I_e \frac{Pol}{R^2}\left[\sum_n |f_n|^2 + \sum_m \sum_{n\neq m} f_m f_n^* \exp\left(-2\pi i \mathbf{d_{mn}}\cdot\mathbf{s}\right)\right], \tag{16}$$

where the notation $I_e = e^4/m_e^2c^4$ denotes the total scatting power of an electron. The double summation in Equation (16) is carried out assuming each atom is represented by its effective atomic scattering factor f_n.

In most cases the atomic scattering factor is assumed to be independent of the local environment of an atom, and changes only with its oxidation state. This representation then effectively assumes that two atoms scatter independently, and that their electron densities do not overlap a significant amount, as the overlap integral in Equation (12) is not carried out. The relationship in Equation (16) is the starting point of most scattering theory, and the basic relationship necessary to calculate the structure factor for a lattice.

In some cases, it is also useful to treat an entire crystallite as a single scatterer positioned at its center of mass. The larger length scale commonly associated with these systems results in the diffraction pattern features falling in the small-angle regime. Following the same considerations concerning the scattered amplitude, $A = \sum_n F_n$, we arrive at an analogous expression for the scattered intensity

$$I = I_e \frac{Pol}{R^2} \left[\sum_n |F_n|^2 + \sum_m \sum_{n \neq m} F_m F_n^* \exp\left(-2\pi i \mathbf{d_{mn}} \cdot \mathbf{s}\right) \right]. \qquad (17)$$

However, it becomes more important to carefully consider the independent scatterer assumption in this case. In small-angle scattering, if the crystallites are infinitely dilute, the scattered intensity is given only considering the self-scattering term, or the first summation of Equation (17), where F_n is commonly called the crystallite *form factor*. However, this is an ideal limit, and most materials must be reasonably concentrated to observe a signal. In which case, the inter-crystallite scattering, or the double summation in Equation (17), must be considered. When dealing

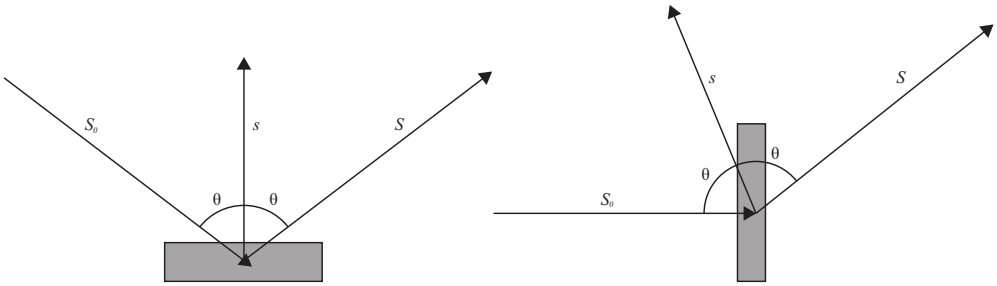

Figure 2: Illustrations of reflection and transmission measurement geometries are shown.

with identical scatters, the term $|F_n|^2$ can be factored out of the double summation in Equation (17), and the remaining summation is called the *structure factor* in small-angle scattering literature. While not generally considered, the inter-crystallite scattering can have an influence on the wide-angle pattern as well. It will be shown in Chapter 6 that it only becomes important to consider when the crystallites become aligned, and regularly spaced into some super-structure. In this case, it is no longer valid to consider each crystallite as scattering independently, and the full expression of Equation (17) must be evaluated.

2.1.5 Absorption Corrections

As an incident beam passes through a material, its intensity is diminished due to the described scattering events, as well as, other photon-electron interactions. This effect is called absorption, and is a determining factor in the absolute value of the observed intensity. The intensity reduction is dependent on the scattering angle, and its exact functional form is determined by the experiment geometry. Only the final forms of the

absorption corrections important to the work carried out in this thesis are described below, and the reader is referred to the *International Tables of Crystallography, Vol. C* [108] for more information.

When the diffraction experiment is carried out in a reflection geometry of a thin sample, which is illustrated in Figure 2, the absorption correction takes on the form

$$Abs = 1 - \exp\left(-\frac{2\mu_l t\rho}{\sin\theta}\right). \tag{18}$$

In absorption correction factors like Equation (18), the variable μ_l denotes the linear mass absorption coefficient, t the sample thickness, and ρ the mass density of the material. The value of μ_l is determined by the material's chemical composition, and the wavelength of incident radiation. In this study the values of this quantity measured, and provided by the National Institute of Standards and Technology (NIST) [69] were used.

When the scattering measurement is done using a capillary, the measurement is described as a transmission geometry, which is illustrated in Figure 2. Assuming that the sample is larger than the incident beam diameter, the absorption correction becomes

$$Abs = {}^{\exp\left(\mu_l t\rho\left(1-\frac{1}{\cos\theta}\right)\right)}\!/_{\cos\theta}, \tag{19}$$

while when the sample is smaller than the beam, this factor reduces to

$$Abs = \exp\left(\mu_l t\rho\left(1 - \frac{1}{\cos\theta}\right)\right). \tag{20}$$

2.2 General Powder Diffraction Theory

Relations like Equations (9) and (16) only describe the diffracted intensity from a single crystallite fixed in space. Another class of materials which is common to exist is composed of many crystallites. In diffraction the term "powder" is often used to describe this polycrystalline form. In order to be properly classified as an ideal powder, the microstructure of a material must:

i) have a crystallite size which is small enough to provide good counting statistics, and

ii) have no preferential orientation of the crystallites in the material.

While a granular material, like sand, is automatically associated with a powder, it must be confirmed that the internal crystallite size is small enough before it can be classified as a powder in terms of diffraction. Dense polycrystalline materials, like processed metals, can also be described as a powder. However, it is common that the procedures used in processing result in a preferential alignment, or texture, of the crystallite orientations within the material. This texture will cause the diffraction pattern to deviate from what is expected from a powder. The following section will then focus on describing the diffraction pattern from a powder, showing how it is related to the single crystal intensity.

Assuming each crystallite scatters independently, the powder intensity is then the summation of the intensities from each crystallite in the sample. For the moment, we will assume a material microstructure with a uniform crystallite size. Then the intensities from two crystallites in the material which are oriented differently with respect to the scattering vector will appear as a two single crystal intensities, one correspondingly rotated with respect to the other in reciprocal space (RS). Figure 3 shows an example of this concept for the case of a cubic crystallite composed of a cubic atomic lattice. If both crystallites are present in the beam path, a superposition of the two patterns, like that depicted in the reciprocal space portion of Figure 3, will be observed as the diffraction pattern. A powder can have millions of crystallites in the beam, oriented at all possible directions. In order to conceptualize the diffraction pattern from such a system, it can be useful to consider the superposition of the intensity in reciprocal space from each crystallite. In such a case the distinct Bragg spots will no longer be well defined, and the intensity at a given distance from the origin of reciprocal space will be blurred together, forming concentric shells about the origin. We will call one of these spherical shells a powder diffraction sphere (PDS), whose radius corresponds to $s_{hkl} = 1/d_{hkl}$, where d_{hkl} is the distance between the hkl planes in the atomic lattice. A two-dimensional slice through such a series of concentric spheres would then look something like the rings depicted in Figure 4.

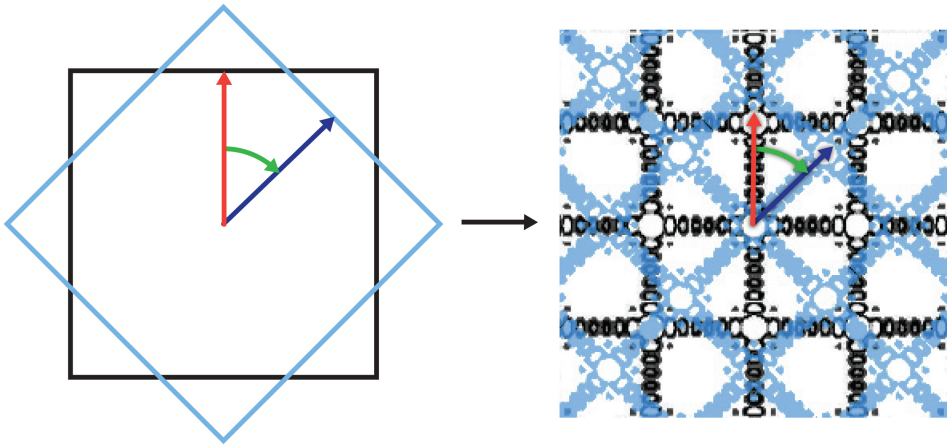

Figure 3: The relationship between the crystallite orientation and the diffraction pattern observed in reciprocal space is exhibited assuming cubic crystallites composed of a cubic lattice. It is assumed that the incident beam is directed into the page, normal to one of the faces of the cube. A two-dimensional cross-section of the diffraction patterns in the xy-plane is depicted.

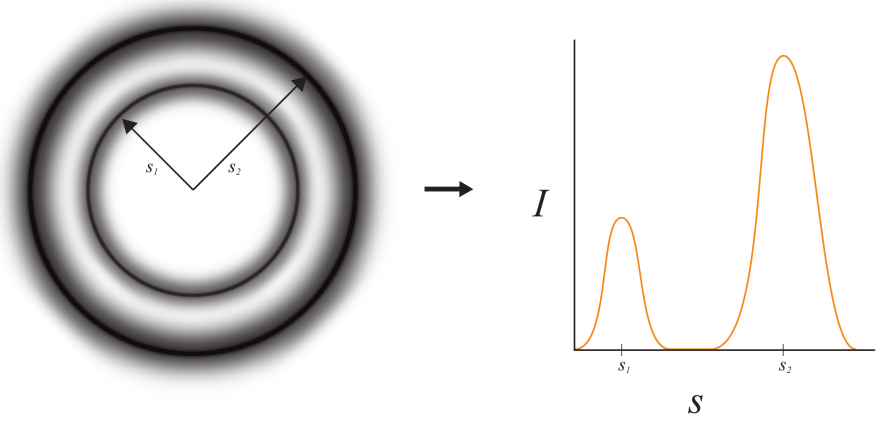

Figure 4: The relationship between the distribution of a powder pattern in reciprocal space and the intensity measured with a point detector is depicted.

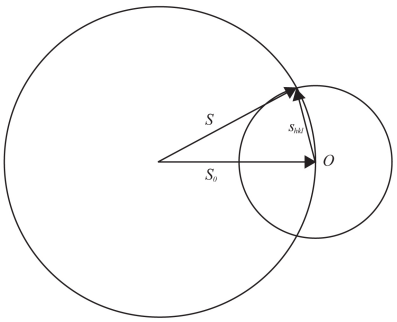

Figure 5: The geometry of how an Ewald sphere intersects a "powder sphere" in reciprocal space is depicted.

The portion of reciprocal space observable by an x-ray measurement can be described by the Ewald sphere. The Ewald sphere is then a sphere of radius $1/\lambda$, which intersects the origin of reciprocal space at a point on its surface, and whose center is determined by the orientation of the incident radiation with respect to the crystallite lattice, $\mathbf{S}_0$. A two-dimensional depiction of the Ewald sphere, relative to the scattered intensity from powder associated with a given hkl, is found in Figure 5. In three dimensions, the intersection of the Ewald sphere with the powder intensity produces rings, known as the Debye-Scherrer rings, named after the scientists who first attributed these diffuse halos, or rings, to the powder microstructure of a material [38].

The powder intensity measured at a successively larger scattering angles, 2θ, traces a path on the surface of the Ewald sphere. Instead of measuring the entire powder ring, point detectors measure the intensity accurately at a point in reciprocal space. By considering the Ewald

sphere, it is found that scanning this kind of a detector over an angle corresponds to a measurement of the intensity in reciprocal space along the radial direction relative to the origin. Figure 4 then depicts the relationship between the observed peaks, and the full powder intensity distribution in reciprocal space. As will be shown throughout the current work, the shape of these peaks contains information on the microstructure, and crystal defects present in the material.

The powder diffraction intensity measured at some scattering vector, s, in the curve depicted in Figure 4 will then have contributions from all regions of the single crystal intensity which are equidistant from the RS origin. This region of reciprocal space then corresponds to a PDS of radius s. The powder diffraction intensity is then found by averaging the intensity from a single crystallite on the PDS, and then scaling by the number of crystallites in the sample. We will refer to this averaging as the powder integral, and it involves integrating the single crystal intensity on the surface of the PDS. The powder intensity, I_P, is then found by the powder integral defined as

$$I_P(s) = \frac{\int I(\mathbf{s}) \mathrm{d}\Omega}{4\pi s^2}, \tag{21}$$

where Ω represents the spherical solid angle in reciprocal space, and the Jacobian of Equation (21) is expressible as $\mathrm{d}\Omega = s^2 \sin\theta d\theta d\phi$.

2.2.1 Lorentz factor for reciprocal space powder intensity

In general there are two approaches to arriving at the powder pattern which differ in the whether the powder integral, or the interference calculation, like that in Equation (16), is carried out first. The more traditional approach to arriving at the powder intensity is done by first determining the diffracted single crystal intensity in reciprocal space, $I(\mathbf{s})$, and then assuming it is uniformly distributed on the PDS, sometimes called the powder average. While this procedure is repeatedly covered in many texts on x-ray diffraction, confusion can arise concerning the correct form of the Lorentz factor, which corrects for the geometrical considerations of taking the powder average. The appropriate correction becomes increasingly important for very small crystallites, therefore, it will be briefly reviewed in the following discussion.

Discussions of the Lorentz factor in the classic diffraction texts consists of stringing together a series of seemingly unrelated considerations concerning the percentage of crystallites in the diffracting position at a given angle, and averaging the intensity over the powder ring [77, 156]. It is also common to lump the Lorentz factor with the effect of polarization, creating a Lorentz-Polarization factor which includes all angular dependence of the intensity due to the measurement geometry [32]. Instead of clarifying the Lorentz factor, it is the opinion of the author that these descriptions tend to just confuse, and hide, its origins.

The Lorentz factor comes from the fact that we are considering the

powder intensity, and arriving to a suitable model requires we take the powder integral. In fact, one commonly found traditional form of the Lorentz factor is already present in the definition of the powder integral, Equation (21). Using the definition $s = 2\sin\theta/\lambda$, the Lorentz factor is found from the term in the denominator to be proportional to $1/\sin^2\theta$. This Lorentz factor is found in the original derivations of the method of approximating the powder integral, called the tangent plane approximation (TPA) [151, 137], as a factor of

$$L_{TPA}(\theta) = \frac{1}{2\pi\sin^2\theta}. \tag{22}$$

A few examples of these tangent planes relative to the PDS are also depicted in Figure 9. As will be discussed in Chapter 3, the TPA only becomes valid for large crystallites, and is only exact for spheres. Furthermore, it will be demonstrated that this expression of the Lorentz factor is really a consequence of the assumption of the TPA, and is not the true Lorentz factor given by the powder integral in Equation (21). Features which suggest the approximate nature of Equation (22) are that: (i) it results in the intensity diverging at $2\theta = 0$, and (ii) one may also notice that the factor of $1/s^2$ in Equation (21) can be canceled by the factor of s^2 coming from $\mathrm{d}\Omega$. Therefore, the correct form of the Lorentz factor is only found by evaluating the powder integral on the surface of the PDS.

As will be discussed in Section 3.1, the true form of the Lorentz factor

for a crystalline material is found to be

$$L(\theta, \theta_{hkl}) = \frac{1}{2\pi \sin\theta \sin\theta_{hkl}}. \tag{23}$$

Patterson was the first to find this form of the Lorentz factor for the special case of the powder intensity from a spherical crystallite [104], and Warren later repeated the exercise using a slightly different mathematical approach [154]. Later, Ino and Minami showed that this form is true for any crystallite shape, by expanding the powder integral into an asymptotic series [71]. In the limit that the crystallite becomes large, the powder peak becomes narrow, and Lorentz factor found in Equation (23) can be approximated by $1/2\pi \sin^2\theta_{hkl}$, which is consistent with the traditional form of Equation (22).

2.2.2 The Debye Function

The second approach to finding the powder intensity is to bring the orientational average of Equation (21) inside the interference calculation of the intensity. Doing so by way of Equation (16) results in an integral of the form

$$I_P(s) = \frac{I_e Pol\ Abs}{4\pi R^2} \sum_{m,n} f_m f_n^* \int \exp\left(-2\pi i s d_{mn} \cos\theta\right) \sin\theta \mathrm{d}\theta \mathrm{d}\phi,$$

which has closed form solution known as the Debye function

$$I_P(s) = \frac{I_e Pol\ Abs}{R^2} \sum_{m,n} f_n f_m^* \frac{\sin\left(2\pi s d_{mn}\right)}{2\pi s d_{mn}}. \tag{24}$$

The relationship depicted in Equation (24) was first described by Peter Debye in a 1915 paper showing that diffraction phenomena does not rely

on a crystalline state, but also exists for molecules [37]. This early work on diffraction from molecules led to the seminal paper by Zernicke and Prins [166], which is the basis for much of the later work on scattering from liquids and amorphous materials.

The primary assumption when using the Debye function is that the same configuration of scatterers is found at all orientations with respect to the incident beam. This assumption is analogous to our definition of a perfect powder, and in fact, the Debye's understanding of the expected intensity from randomly oriented molecules may have directly led to his work with Scherrer on powder patterns [38]. Since Equation (24) intrinsically considers the orientational average, use of a Lorentz factor with this expression is not necessary.

The summation in Equation (24) is a double sum over all interatomic distances, a computational problem which scales as $O(N^2)$, where N denotes the number of scatterers in a system. Assuming that the number of scatterers is proportional to the volume of our system, the calculation problem is found to scale as $O(R^6)$, where R is the radius of an equivalent volume sphere. With this incredible calculation burden, it is understandable why the Debye function was primarily used to calculating the intensity observed from small molecules until the advent of computers. Still, in 1941 Germer and White applied it to the study of nanocrystalline Cu films, and showed the transition of the diffraction pattern from a few atoms to an appreciable crystallite size [54]. Use of the equation

gained some popularity in the early 1990s, through the studies of Hall who demonstrated that the fast Fourier transform (FFT) can be used to improve the calculation time [64]. Since then, the Debye function has become an important tool to understanding the diffraction pattern from small crystallites, or nanoparticles, and is employed in studies scattered throughout current scientific literature.

2.3 Line Profile Analysis - A Brief Historical Survey

Study of the shape of the powder diffraction peaks to extract microstructural information is commonly called line profile analysis (LPA), and has its roots in some of the first diffraction experiments. The evolution of line profile analysis over the years has been largely guided by the type of information obtainable from a diffraction pattern of the time. The first powder diffraction patterns were recorded using photographic film in a Debye-Scherrer camera, and dark lines in the developed film represented the Bragg powder peaks. It was quickly recognized that the integral breadth, or width, of the line was related to the crystallite size and strain. Assuming that there is little or no strain in a material, the crystallite size can be determined from the integral breadth via the Scherrer equation [129], which is defined as

$$\overline{L} = \frac{K\lambda}{\beta \cos\theta_{hkl}}. \tag{25}$$

In this expression $\overline{L}$ denotes an average domain size, commonly given as the cube root of the crystallite volume. The variable β is the integral

breadth of the Bragg peak, θ_{hkl} is the position of the Bragg peak, and K is called the Scherrer constant which is related to the crystallite shape assumed [79]. A strain in the lattice was later shown by Stokes and Wilson [138] to also result in a broadening of the observed lines following the general relationship

$$\epsilon = \frac{\beta}{2} \cot \theta_{hkl}, \tag{26}$$

where ϵ is defined as the "apparent tensile strain" in a distorted lattice. In order to separate these two effects, and determine contributions of size and strain broadening to the measured diffraction pattern, Williamson and Hall developed a method of plotting $\beta \cos \theta_{hkl}$ vs $\sin \theta_{hkl}$ [161] — which is ideally a linear trend whose slope and intercept are related to the crystallite strain and size respectively.

This model of Williamson-Hall embodies the essence of peak broadening. The crystallite size broadens all peaks uniformly, while the microstrain results in a broadening which is dependent on the specific diffraction spot. However, quantitatively this model only goes so far. As stated by Stokes and Wilson in their original paper [138], since most materials are elastically anisotropic, the actual dependence of the integral breadth due to lattice strain is more complicated than the relationship given in Equation (26). This results in a Williamson-Hall plot which is seemingly scattered, and hardly linear. Recently, so-called modified Williamson-Hall analyses have been proposed in an attempt to relate the scattered trend to the contribution of dislocations [144] and faulting [145]. While

these modified analyses might help to understand the type of strain in the material, they have been shown to be quantitatively less reliable in terms of obtaining defect densities [127].

When scintillator detectors became available in the early 1950s, the intensity could be easily recorded on a relative scale, making the full peak shape, or peak profile, easier to obtain. This improved information of the peak allowed for more complex theories to be tested. Notably, the Warren-Averbach method demonstrated the separation of different size and strain contributions to the line profile through the Fourier transform of the peak [156, 157]. The theory that a diffraction spot was the Fourier transform of the crystallite size, and shape, was known at least 10 years earlier [104, 45], however, Warren and Averbach extended this concept by including a strain contribution, and developing the correct methodology for the powder pattern.

Raw data also has contributions from the background, noise, and other aberrations. So, it became customary to fit the data with an analytical function — like a Gaussian or pseudo-Voigt — to extract the peak shape. Advances in peak fitting were largely driven by the Rietveld method [117, 118], which ironically only fits the peaks to obtain an accurate peak position and integrated intensity. Nonetheless, the statistical treatment of each data point as an independent observation marked a milestone in line profile analysis. The portion of the diffraction community interested in the microstructure information then developed a vast

literature on the relationship between the parameters of the various analytical peak functions used, and the desired microstructure characteristics [134].

Modern line profile analysis is seeing a paradigm shift from fitting to *modeling*, where microstructure models are used to describe the measured diffraction data. This avoids the need to assume an analytical peak shape function, which can bias the results [36]. The reciprocal space approach to peak modeling is based on constructing peak shapes by combining independent models describing the effects of features like size and strain broadening. The different effects are convolved to obtain the resulting peak. As an example, if the assumed contributions to the peak profile are: instrumental, crystallite size and faulting effects, then the simulated peak is constructed following an expression like

$$I_{hkl}(s) = \int T^{IP}(L) A^{S}(L) C^{F}(L) \exp(2\pi i L(s - s_{hkl})) \mathrm{d}L, \qquad (27)$$

where $T^{IP}(L)$, $A^{S}(L)$, and $C^{F}(L)$ represent the Fourier transforms of the contributions from instrumental, crystallite size and faulting respectively. The integration in Equation (27) is the Fourier transform with respect to the real space variable L, and more contributions can be included into the peak shape by multiplying their respective transforms in the integral. For further details on the derivation and form of these transforms, the reader is directed to the later chapters covering each. The pattern modeling then proceeds by refining the parameters of each

model, controlling characteristics like the crystallite size or faulting probability, until the best fit with the measured pattern is obtained. Largely the works of Scardi and Leoni in the development of Whole Powder Pattern Modeling (WPPM), and to some extent the work of Ribárik and Ungár in the development of Convolutional Multiple Whole Profile fitting (CMWP)[115, 116], have pushed this method forward, and made it accessible to the diffraction community.

A complementary real space method to model the diffraction pattern which has gained popularity following the interest of the scientific community with nanomaterials is Debye function analysis (DFA). In this approach atomistic constructions are used to simulate the diffraction pattern via the Debye function, which is then compared with the measured pattern. Parameters controlling the probability of a sample containing a crystallite of a given size, shape or defect concentration are then refined until a best fit is obtained.

Due to the computational burden of calculating the Debye function, many studies employing DFA assume the diffraction pattern from homogeneous, monodisperse samples, and are actually more structural studies as opposed to line profile studies. Some of the best of which were conducted by Torchet *et al.* comparing the structure of molecular dynamics simulations to electron diffraction patterns of Ar [47, 48, 49], CO_2[141], and H_2O [142] crystallites. Later, Landman and Whetten led a combined simulation and experimental effort to study the structure of Au

nanoparticles of sizes larger than those given by "magic numbers" using mass spectrometry and x-ray diffraction [29, 31, 159, 160]. Also notable is the more recent work of the Berkeley Nanogeoscience group led by Banfield, Waychunas, and Gilbert, who have studied the structures of iron oxide and zinc sulfide nanoparticles in multiple solvent environments [55, 56, 158].

Among the first to use a polydisperse DFA modeling routine were Hall *et al.*, who investigated the particle size stability of multiple twinned particles [62, 63, 113], along with Gnutzmann and Vogel, who employed DFA to study Pt catalysis and oxidation [58]. In recent years, Cervellino has worked extensively to make the Debye function less computationally intensive for polydisperse particle systems [24]. This technique continues to mature, and recent works are pushing the limits of the DFA, developing it into a full line profile analysis tool capable of modeling particle shape, size, faulting, and strain [14, 23, 88, 97].

CHAPTER III

STUDY OF PARTICLE SIZE EFFECT

The powder diffraction line profile from nanoparticles is dominated by size broadening due to their extremely small dimensions. Therefore, an accurate description of this effect is crucial to modeling their diffraction patterns. In this chapter the methods of both the reciprocal space modeling approach, and the real space, Debye function approach, will be reviewed and compared.

3.1 Dependence of intensity distribution on crystallite shape

The theory of size broadening in powder diffraction first requires an accurate description of the distribution of intensity in reciprocal space from a single small crystallite. The fundamental concept necessary to arrive to the single crystal intensity was already presented in the form of relations like Equation (12) which show the scattered amplitude proportional to the Fourier transform (FT) of the atomic electron density. This treatment is also true in a general sense, as the amplitude of a scattered x-ray wave is related to the distribution of the electron density in space as

$$A(\mathbf{s}) = \int \rho(\mathbf{r}) \exp(-2\pi i \mathbf{s} \cdot \mathbf{r}) \mathrm{d}v_{\mathbf{r}}, \tag{28}$$

with $\rho(\mathbf{r})$ now representing the total electron density at point $\mathbf{r}$. This relation holds for any state of matter, and does not depend on the material being in a crystalline state.

3.1.1 Crystallite Electron Density Description

The electron density from any collection of atoms is expressible in terms of the summation of the contributions from each atom, defined as $\rho(\mathbf{r}) = \sum_j \rho_j(\mathbf{r} - \mathbf{r}_j)$, where $\rho_j(\mathbf{r})$ is the electron density from the j-th atom, positioned at $\mathbf{r}_j$. If the scattering medium happens to be crystalline, then the atomic positions can be described in terms of the regular atomic positions within a unit cell.This leads to an electron density of the form

$$\rho(\mathbf{r}) = \sum_{\mathbf{m}} \sum_{a} \rho_a(\mathbf{r} - \mathbf{m} - \mathbf{r}_a), \tag{29}$$

where $\mathbf{m}$ is the position vector of the unit cell, and $\mathbf{r}_a$ is the position of the a-th atom in the unit cell.

By definition, a crystallite is composed of an atomic lattice which fills a finite volume of space. This volume can be defined in general terms using a *shape function* such as

$$\sigma(\mathbf{r}) \quad = \quad \begin{cases} 1 & \mathbf{r} \in V_c \\ \\ 0 & \mathbf{r} \notin V_c \end{cases}, \tag{30}$$

where $\mathbf{r}$ is a vector in real space and V_c is the volume of the crystallite. The shape function of this form allows the formalism of a lattice, which is by definition infinite, to be employed to describe a crystallite. In the

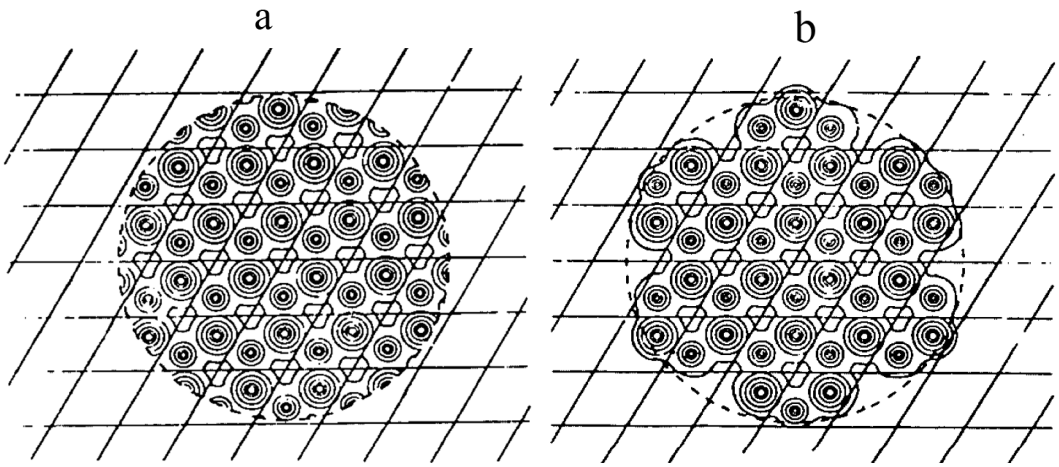

Figure 6: The resulting descriptions of the electron density in a small crystallite are depicted for the cases of (a) the carved infinite e-density, and (b) the Ino-Minami e-density. (Figure from Ino-Minami [70])

original treatment of the shape function by Patterson and Ewald [45, 104], the electron density in a crystallite is defined as

$$\rho_e(\mathbf{r}) = \rho_\infty(\mathbf{r})\sigma(\mathbf{r}), \tag{31}$$

where $\rho_\infty(\mathbf{r})$ denotes the electron density of an infinite lattice. From Equation (29), the electron density for an infinite lattice can be shown to take an equivalent form [70]

$$\rho_\infty(\mathbf{r}) = \sum_a \rho_a(\mathbf{r}) * z(\mathbf{r} - \mathbf{r}_a), \tag{32}$$

where the symbol '$*$' denotes a convolution, the sum is over all a atoms in a unit cell. The function $z(\mathbf{r})$ denotes the positions of the unit cell's a-th atom in the crystallite through a series of delta functions defined as

$$z(\mathbf{r} - \mathbf{r}_a) = \sum_{\mathbf{m}} \delta(\mathbf{r} - \mathbf{m} - \mathbf{r}_a). \tag{33}$$

Then, the convolution in Equation (32) does nothing more than position atoms in space. Combining Equations (31) and (32), the electron density in a crystallite is found to be

$$\rho_e(\mathbf{r}) = \sum_a \left[\rho_a(\mathbf{r}) * z(\mathbf{r} - \mathbf{r}_a)\right] \sigma(\mathbf{r}). \tag{34}$$

This definition of the electron density can be imagined as the equivalent of taking a cookie cutter, and carving out the electron density from the larger lattice. The resulting form of the electron density and description of the crystallite is presented in Figure 6a. However, this representation of the crystallite is somewhat unphysical, as the electron density from atoms which are positioned just outside its surface is still considered to contribute to the crystallite. Nonetheless, this expression of the electron density is reasonable for large crystallites, since the fraction of the volume which is near the surface is low compared to the total volume of the particle.

Assuming that the primary building block of the crystallite is an atom, Ino and Minami (I-M) have proposed an alternative description of the electron density which is more appropriate for small crystallites. The I-M description only considers the electron density from atoms whose centers lie within the shape function. From this consideration, the electron density in a crystallite is expressed as

$$\rho_{IM}(\mathbf{r}) = \sum_a \rho_a(\mathbf{r}) * \left[z(\mathbf{r} - \mathbf{r}_a)\sigma(\mathbf{r})\right]. \tag{35}$$

While switching the order of the convolution and product in Equation

(35), compared to Equation (31), might first seem to be a slight difference, it has important implications on the description of the crystallite. In Equation (35) the shape function now acts as a mask on the lattice function, $z(\mathbf{r})$, only allowing the atoms whose centers are within the crystallite volume to be considered in the crystallite. An example of the resulting description of the electron density in a crystallite is depicted in Figure 6b. When compared to the traditional description, it is evident that the electron density near the surface is more realistically represented by Equation (35).

3.1.2 Scattered Intensity

Following Equation (28), the scattered amplitude is found from the FT of Equations (31) and (35). This action can be carried out considering the FT of the necessary functions. The FT of the electron density of an atom is the atomic scattering factor defined as

$$f_a(\mathbf{s}) = \int \rho_a(\mathbf{r}) \exp(-2\pi i \mathbf{s} \cdot \mathbf{r}). \tag{36}$$

Also, the FT of the lattice function $z(\mathbf{r})$ is given as

$$\begin{aligned} Z(\mathbf{s}, \mathbf{s}_{hkl}) &= \int z(\mathbf{r} - \mathbf{r}_a) \exp(-2\pi i \mathbf{s} \cdot \mathbf{r}) \mathrm{d}v_{\mathbf{r}}, \\ &= \frac{1}{V_{uc}} \exp(-2\pi i \mathbf{s} \cdot \mathbf{r_a}) \sum_{hkl} \delta(\mathbf{s} - \mathbf{s}_{hkl}), \end{aligned} \tag{37}$$

with $\mathbf{s}_{hkl}$ denoting the position of the hkl Bragg spot and V_{uc} representing the volume of the unit cell. Finally, the transform of the shape function

is defined simply as

$$S(\mathbf{s}) = \int \sigma(\mathbf{r}) \exp(-2\pi i \mathbf{s} \cdot \mathbf{r}). \tag{38}$$

Using these definitions, as well as the identities for the FT of convolutions and products, the scattered intensity is then found to take the general form

$$A(\mathbf{s}) = \frac{1}{V_{uc}} \sum_{hkl} F(s, \mathbf{s}_{hkl}) S(\mathbf{s} - \mathbf{s}_{hkl}), \tag{39}$$

where the structure factor, $F(\mathbf{s}, \mathbf{s}_{hkl})$ is dependent on the model chosen to represent the electron density of the crystallite. For the traditional case the structure factor is given by [70]

$$F_e(\mathbf{s}_{hkl}) = \sum_a f_a(s_{hkl}) \exp(2\pi i \mathbf{s}_{hkl} \mathbf{r}_a), \tag{40}$$

while for the I-M description this function takes the form

$$F_{IM}(s, \mathbf{s}_{hkl}) = \sum_a f_a(s) \exp(2\pi i \mathbf{s}_{hkl} \mathbf{r}_a). \tag{41}$$

In these expressions the atomic scatting factor is assumed to by spherically symmetric. The small difference between Equations (40) and (41) means that for the traditional case the intensity at a Bragg spot is only scaled by the value of the atomic scattering factor at the Bragg position, however, for the I-M case the atomic scattering factor modulates the intensity everywhere in space.

As in section 2.1, the observed intensity is given by the square modulus of the scattered amplitude, and is found from Equation (39) to be

$$I(\mathbf{s}) = \frac{k(s)}{V_{uc}^2}\left(\sum_{hkl}|F(\mathbf{s},\mathbf{s}_{hkl})S(\mathbf{s}-\mathbf{s}_{hkl})|^2 + \sum_{hkl}\sum_{h'k'l'}F(\mathbf{s},\mathbf{s}_{hkl})S(\mathbf{s}-\mathbf{s}_{hkl})F^*(\mathbf{s},\mathbf{s}_{h'k'l'})S^*(\mathbf{s}-\mathbf{s}_{h'k'l'})\right), \quad (42)$$

with the indices $h'k'l'$ representing Bragg points different than hkl, and the function $k(s)$ incorporating the effects of polarization, absorption and temperature discussed in Chapter 2. The second set of summations in Equation (42) is commonly neglected by assuming that the crystallite is large enough that the overlap of intensity between between Bragg spots is negligible [77]. However, this assumption becomes less accurate as the crystallite becomes smaller, or as the number of Bragg points become more dense in reciprocal space — which can be due to a lattice with a larger unit cell, or less symmetry.

3.1.3 Random Shift Treatment

In the description of the particle shape just given, it was intrinsically assumed that the shape function and the lattice have the same center. This is not generally true, and shifting the position of the shape function with respect to the underlying lattice can result in a different description of the particle, thus a different diffraction pattern. Mathematically the

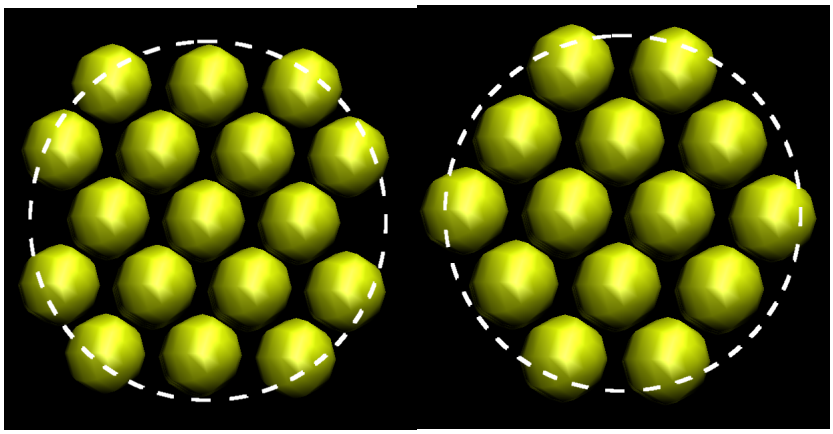

Figure 7: The results of carving a sphere from an FCC lattice for different relative positions of the shape function are depicted.

shape function can be generally expressed relative to its center as

$$\sigma(\mathbf{r}-\mathbf{t}) \;=\; \begin{cases} 1 & \mathbf{r}-\mathbf{t} \in V_c \\ 0 & \mathbf{r}-\mathbf{t} \notin V_c \end{cases}, \tag{43}$$

where $\mathbf{t}$ is formally defined as the vector connecting the lattice origin O, and the shape function center O'. Figure 7 depicts two such particles which are the result of assuming the same shape function, but different displacements of the shape function relative to the lattice. It is evident that the resulting particles describe very different versions of the spherical particle.

The Fourier transformation of the shape function then has a phase shift, due to the introduction of the displacement $\mathbf{t}$, and is given from Equation (38) as

$$S(\mathbf{b},\mathbf{t}) = \exp(-2\pi i \mathbf{b}\cdot\mathbf{t}) \int \sigma(\mathbf{r}') \exp(-2\pi i \mathbf{b}\cdot\mathbf{r}') dv_{\mathbf{r}'} = \exp(-2\pi i \mathbf{b}\cdot\mathbf{t}) S(\mathbf{b}), \tag{44}$$

following a change of variables defined by $\mathbf{r}' = \mathbf{r} - \mathbf{t}$. The intensity obtained by substituting this expression into Equation (42) is then

$$I(\mathbf{s}) = \frac{k(s)}{V_{uc}^2}\left(\sum_{hkl}|F(\mathbf{s},\mathbf{s}_{hkl})S(\mathbf{s}-\mathbf{s}_{hkl})|^2 + \sum_{hkl}\sum_{h'k'l'}\exp(-2\pi i(\mathbf{s}_{hkl}-\mathbf{s}_{h'k'l'})\cdot\mathbf{t})F(\mathbf{s},\mathbf{s}_{hkl})S(\mathbf{s}-\mathbf{s}_{hkl})F^*(\mathbf{s},\mathbf{s}_{h'k'l'})S^*(\mathbf{s}-\mathbf{s}_{h'k'l'})\right), \tag{45}$$

When considering the scattering from a material composed of many crystallites, or a powder, the average intensity is what is observed. Assuming that each crystallite represents a different translation of the shape function, the average intensity is then given as an average over all translations, defined as $\overline{I(\mathbf{s})} = \int I(\mathbf{s},\mathbf{t})d\mathbf{t}$. Since $\int \exp(-2\pi i\mathbf{b}\cdot\mathbf{t})d\mathbf{t} = 0$, the average intensity from Equation (45) is given by

$$\overline{I(\mathbf{s})} = \frac{k(s)}{V_{uc}^2}\sum_{hkl}|F(\mathbf{s},\mathbf{s}_{hkl})S(\mathbf{s}-\mathbf{s}_{hkl})|^2. \tag{46}$$

Therefore, neglecting the second summation in Equation (42) is justified for any particle size, but only if the many crystallites in a material represent a *uniform* distribution of all possible translations of the shape function. This average has been described as the "random shift treatment" [70], or the "ξ- average" [68], and is an important consideration when trying to compare the intensities predicted by reciprocal space descriptions to that calculated by the Debye function.

3.1.4 Common Volume Function

Considering that the intensity from a single crystallite is given by (46), the intensity from a Bragg spot is found to be proportional to

$$I_{hkl}(\mathbf{s}) = |F(s, \mathbf{s}_{hkl})|^2 S(\mathbf{s} - \mathbf{s}_{hkl}) S^*(\mathbf{s} - \mathbf{s}_{hkl}). \tag{47}$$

The product of the shape function Fourier transforms, S and S^*, is equivalent to the Fourier transform of the shape common volume function expressed as

$$S(\mathbf{s} - \mathbf{s}_{hkl}) S^*(\mathbf{s} - \mathbf{s}_{hkl}) = \int v(\mathbf{r}) \exp(-2\pi i(\mathbf{s} - \mathbf{s}_{hkl}) \cdot \mathbf{r}) \mathrm{d}v_{\mathbf{r}}, \tag{48}$$

where the common volume function[1] , $v(\mathbf{r})$, is the integral defined in general as

$$v(\mathbf{r}) = \int \sigma(\mathbf{x}) \sigma(\mathbf{x} - \mathbf{r}) \mathrm{d}v_{\mathbf{x}}. \tag{49}$$

The function $v(\mathbf{r})$ can be envisioned, and calculated, as the common volume between two identical shapes, one displaced relative to the other by the vector $\mathbf{r}$. These two shapes are commonly referred to as the crystal and its "ghost" following the treatment of Stokes and Wilson [137]. A schematic depicting this fundamental concept is shown in Figure 8

The form of $v(\mathbf{r})$ is well known for a few particle shapes. For a rectangular box with edge lengths L_x, L_y, and L_z it is straightforward to show

$$v(\mathbf{r}) = L_x L_y L_z (1 - \frac{x}{L_x})(1 - \frac{y}{L_y})(1 - \frac{z}{L_z}), \tag{50}$$

[1]Hosemann has also described the common volume function as the "convolution square" of the shape function [68].

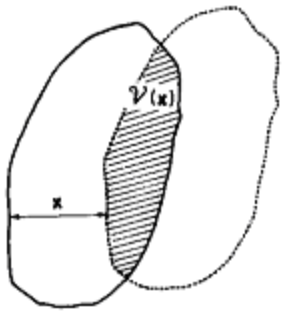

Figure 8: Illustration of the common volume between an arbitrary shape and its "ghost". The region $V(\mathbf{x})$ is equivalent to $v(\mathbf{r})$ defined in Equation (49). (Figure from Guinier p. 39 [59])

with $\mathbf{r} = x\hat{x} + y\hat{y} + z\hat{z}$. While for a sphere of diameter D, the common volume function becomes

$$v(\mathbf{r}) = \frac{\pi}{6}D^3(1 - \frac{3r}{2D} + \frac{r^3}{2D^3}). \tag{51}$$

A cylindrical crystallite becomes slightly more complex, since it can exist with the axis of rotation normal to any crystal plane. For a cylinder of height H, and diameter D, whose rotation axis is defined as the vector $\mathbf{z}$, the common volume function found from the work of Langford and Louër [78] is

$$v(\mathbf{r}) = \frac{1}{2}D^2(H - r\cos\phi)\left[\arccos\alpha - \alpha(1-\alpha^2)^{1/2}\right], \tag{52}$$

where $\mathbf{z}\cdot\mathbf{r} = zr\cos\phi$, and $\alpha = r\sin\phi/D$.

3.1.5 Summary of Derivation

In summary, when applying the reciprocal space description of the particle shape to small crystallites, one must be mindful of the three considerations which have just been discussed:

1. Proper description of the surface electron density,

2. Changes from displacement of the shape function with respect to the lattice,

3. Approximation of neglecting cross terms in Equation (45).

The effects of all three approximations on the diffraction pattern are size dependent, having a larger influence as the particle size decreases.

In addition to the three considerations just outlined, the powder peak profile can be determined using the tangent plane approximation. The validity of this technique is a fourth consideration, which is also dependent on both the crystallite size and shape. As discussed in Section 2.2, the powder intensity is obtained from the single crystal intensity by a powder average. However, in many cases the averaging of the shape function, and integration of the intensity on the powder sphere, does not have an analytical solution, and is approximated by integration along a tangent plane to the powder sphere, known as the tangent plane approximation (TPA). This approximation will introduce a further error, which is more evident for smaller particles due to their larger reciprocal lattice

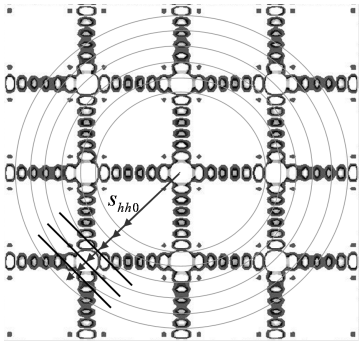

Figure 9: Depicted is a 2D cross section of the scattered intensity from a cubic particle, centered at the origin of reciprocal space. The concentric rings represent the intersection of the powder sphere with the xy-plane, and the appropriate tangent planes are depicted for the *hh0* reflection as straight lines. For this reflection the powder integration will then integrate along path of the ring, while the tangent plane approximation will integrate along the tangent lines.

spots. However, this is a direct consequence of the tangent plane approximation, and not the assumptions made with regard to the representation of the crystallite. A study of the inaccuracy of this approximation for small crystallites is the topic of the next section.

3.2 Powder profile dependence on crystallite shape

The powder diffraction peak is given by integrating the intensity, in Equation (46), over the full surface of the powder diffraction sphere (PDS). This PDS integration is schematically demonstrated in Figure 9 as an integration of the intensity from the single crystallite on a full circle. From Equations (47) and (48), the peak profile is given as

$$I_{hkl}(s) = \frac{|F(s, \mathbf{s}_{hkl})|^2}{4\pi s^2} \int\int v(\mathbf{r}) \exp(-2\pi i(\mathbf{s} - \mathbf{s}_{hkl}) \cdot \mathbf{r}) \mathrm{d}v_{\mathbf{r}} \mathrm{d}\Omega, \qquad (53)$$

where the integration is done over the entire range of the reciprocal space solid angle, $d\Omega$, which is expressed as $s^2 \sin\theta d\theta d\phi$. Changing the order of integration, the orientational average only applies to the exponential, $\exp(-2\pi i \mathbf{s}\cdot\mathbf{r})$, which has the known solution, $\sin(2\pi sr)/2\pi sr$. Therefore, the intensity becomes

$$I_{hkl}(s) = |F(s, \mathbf{s}_{hkl})|^2 \int v(\mathbf{r}) \exp(2\pi i \mathbf{s}_{hkl} \cdot \mathbf{r}) \frac{\sin(2\pi sr)}{2\pi sr} \mathrm{d}v_{\mathbf{r}}, \tag{54}$$

where $r = |\mathbf{r}|$. Since both $v(\mathbf{r})$ and $\sin(x)/x$ are even functions, and the integral is over all space, the imaginary part of the intensity from the exponential is zero, and the integral becomes

$$I_{hkl}(s) = |F(s, \mathbf{s}_{hkl})|^2 \int v(\mathbf{r}) \cos(2\pi \mathbf{s}_{hkl} \mathbf{r}) \frac{\sin(2\pi sr)}{2\pi sr} \mathrm{d}v_{\mathbf{r}}. \tag{55}$$

The integral in Equation (55) is only analytically solvable in special cases when spherical symmetry exists in the shape self-convolution. For instance, in the case of a sphere of diameter D, the common volume function is given by Equation (51), and the powder profile from Equation (55) is found to be

$$I_{hkl}(s) = \frac{V_c |F(s, \mathbf{s}_{hkl})|^2}{2\pi s s_{hkl}} \frac{3D}{8} \left[Z\left(\pi D(s - s_{hkl})\right) - Z(\pi D(s + s_{hkl})] \right, \tag{56}$$

where the function $Z(x)$ is now defined as

$$Z(x) = \frac{1}{x^2} \left[1 + \left(\frac{\sin x}{x} \right)^2 - 2 \frac{\sin 2x}{2x} \right], \tag{57}$$

and V_c denotes the volume of the crystallite [154, 104]. It should be noted that through this powder average the correct Lorentz factor of $1/(s s_{hkl})$ is again found in the expression for the intensity.

3.2.1 Tangent Plane Approximation

For other shapes, instead of evaluating the integral in Equation (55), the peak profile is commonly approximated by the intensity integrated on the tangent plane to the PDS. The TPA is shown in Figure 9 for the case of a $\bar{1}\bar{1}0$ Bragg spot as an integration of the intensity along the lines tangent to the circles representing the powder sphere. From the figure, it becomes clear why the TPA becomes invalid for small crystallites which have diffuse Bragg spots.

The TPA was originally formulated in terms of the common volume function by Stokes and Wilson (S-W TPA) as

$$I_{hkl}^{SW}(s) = \frac{|F(s, \mathbf{s}_{hkl})|^2}{2\pi s^2} \int_0^{L_{max}} v(L\hat{\mathbf{s}}_{hkl}) \cos(2\pi(s - s_{hkl})L) \mathrm{d}L, \tag{58}$$

where $s = \mathbf{s} \cdot \hat{\mathbf{s}}_{hkl}$, L is related to the real space vector $\mathbf{r}$ in Equation (55) by $L = \mathbf{r} \cdot \hat{\mathbf{s}}_{hkl}$, and L_{max} is the maximum displacement in the direction $\hat{\mathbf{s}}_{hkl}$, such that $v(L\hat{\mathbf{s}}_{hkl}) \neq 0$ [137]. This form of the TPA was later shown to be inaccurate for small crystallites by Ino and Minami who have derived appropriate corrections to the TPA intensity through an asymptotic expansion of the integral in Equation (55) [71]. Taking the first order correction, the Ino-Minami tangent plane approximation (I-M TPA) intensity is given by

$$I_{hkl}^{IM}(s) = \frac{|F(s, \mathbf{s}_{hkl})|^2}{2\pi s s_{hkl}} \int_0^{L_{max}} v(L\hat{\mathbf{s}}_{hkl}) \left[\cos(2\pi(s - s_{hkl})L) - \cos(2\pi(s + s_{hkl})L)\right] \mathrm{d}L. \tag{59}$$

Comparing the two forms of the TPA in Equations (58) and (59), one finds important differences between the I-M and S-W TPA expressions. First, the I-M TPA is proportional to $1/ss_{hkl}$, while the S-W TPA is related to $1/s^2$. Furthermore, an additional factor of $\cos(2\pi(s+s_{hkl})L)$ is present in the I-M TPA expression. This additional factor prevents the divergence of the intensity at the origin of reciprocal space from the $1/s$ dependence of the intensity. Comparison of the I-M TPA intensity expression finds striking similarity with the analytical solution to the powder intensity from spherical crystallites expressed in Equation (56).

3.2.2 Numerical Evaluation of the Powder Integral

In the present study, we would like to demonstrate the effectiveness of a different approach which obtains the powder diffraction pattern for small crystallites of any shape by solving the integral in Equation (55) numerically. The intensity from Equation (55) is then approximated by the sum

$$I_{hkl}(s) \simeq |F(s,\mathbf{s}_{hkl})|^2 \sum_m \sum_n \sum_o v(\mathbf{r}) \cos(2\pi \mathbf{s}_{hkl}\mathbf{r}) \frac{\sin(2\pi sr)}{2\pi sr} \Delta V, \qquad (60)$$

where $\mathbf{r} = x\hat{\mathbf{a_1}} + y\hat{\mathbf{a_2}} + z\hat{\mathbf{a_3}}$, with $x = m\Delta x$, $y = n\Delta y$, $z = o\Delta z$; $m, n, o \in \mathbb{Z}$ and $\Delta V = \Delta x \Delta y \Delta z \hat{\mathbf{a_1}} \times \hat{\mathbf{a_2}} \cdot \hat{\mathbf{a_3}}$. Here the vectors, $\hat{\mathbf{a}}_i$, are unit lattice vectors. The volume integration is defined in terms of the atomic lattice, so that the Miller indices of the peak can be directly used in the cosine term, resulting in

$$\cos(2\pi \mathbf{s}_{hkl}\mathbf{r}) = \cos(2\pi(hx + ky + lz)). \qquad (61)$$

The precision of the integration is then controlled by the size of the differential volume, or more explicitly the size of Δx, Δy, and Δz. This form of the intensity has also been described by Ino and Minami [71] to test the validity of their asymptotic expansion of the peak profile.

The speed of calculating the intensity in the form of Equation (60) is limited by having to calculate the volume integral for each scattering vector length, s. This can be dramatically improved by first taking the orientational integral of the shape function and cosine product described as

$$p(r) = \int v(\mathbf{r}) \cos(2\pi \mathbf{s}_{hkl}\mathbf{r}) \mathrm{d}\Omega, \tag{62}$$

where $d\Omega$ now represents a real space solid angle. In practice this orientational integral can be taken by first discretizing space, as described in the discussion surrounding Equation (60), and then summing the contributions from those ΔV's which are equidistant from the origin. The necessary calculations can be further reduced considering that since both $v(\mathbf{r})$ and $\cos(2\pi \mathbf{s}_{hkl} \cdot \mathbf{r})$ are even with respect to the vector $\mathbf{r}$, therefore, the integration only needs to be calculated for half of the angular range and then doubled. Also, the symmetry of $v(\mathbf{r})$ for a given shape can be exploited in calculating $p(r)$. The function $p(r)$ only needs to be tabulated once for a given hkl, and then can be used in the summation of Equation (63). The powder intensity is then reduced to the one dimensional summation

$$I_{hkl}(s) \simeq |F(s, \mathbf{s}_{hkl})|^2 \sum_{t=0}^{t_{max}} p(r) \frac{\sin(2\pi sr)}{2\pi sr} \Delta r, \tag{63}$$

where $r = t\Delta r$. The value of t_{max} is related to the maximum distance between points in a crystallite, r_{max}, and therefore depends on its size and shape. The quantity r_{max} is different than L_{max} in Equation (58) in that L_{max} is the maximum distance in a crystallite in the direction $\hat{\mathbf{s}}_{hkl}$. As will be demonstrated in the following section, the powder integration procedure also allows for the calculation of the 000 peak, or the small-angle signal, for any shape for which the common volume function can be defined.

The final powder pattern is found by summing the contributions from each Bragg spot. In terms of the peak family multiplicity, m_{hkl}, the powder intensity from a single crystallite becomes

$$I(s) = \frac{k(s)}{V_{uc}^2} \sum_{hkl} m_{hkl} I_{hkl}(s), \tag{64}$$

where $I_{hkl}(s)$ is given by relations like Equation (59) or (63).

3.2.3 Comparison of Powder Peak Profiles

The cases of spherical, cubic, and cylindrical particles represent different extremes in terms of the shape function, and resulting powder peak profiles. As previously mentioned, a sphere is a smooth shape with an analytical shape function. However, a cube has sharp edges and corners which makes it difficult to represent in Fourier space. While a long, thin cylinder leads to a nearly planar Bragg spots in RS. These shapes then offer good tests to gauge the performance of the TPA for small sized

particles allowing for it to be compared to that found by the powder integration (PI). In the following examples particles consisting of an FCC gold lattice ($a = 0.40809$nm) were assumed, and the effects of temperature, polarization and absorption have been ignored (i.e. $k(s) = 1$) to highlight the features in the powder pattern profiles. The intensity was simulated over a range in s which is observable with Cu Kα_1 radiation. In calculating the intensity from Equation (63) the differential volume was diminished until the intensity converged to a precision of 10^{-4} over the entire simulated range. The small-angle peak is not possible to calculate by the TPA, and it was found to be necessary to add the PI small-angle peak to the TPA pattern to allow for a proper comparison with the Debye calculated intensity.

Powder patterns were also calculated from atomistic descriptions, consisting of a perfect Au FCC lattice cut into the desired shape, by means of the Debye function, defined as

$$I(s) = f^2(s) \sum_i \sum_j \frac{\sin(2\pi s d_{ij})}{2\pi s d_{ij}}, \tag{65}$$

with $f^2(s)$ representing the square of the atomic scattering factor, and d_{ij} representing the distance between atom i and atom j. The similar form of the Debye function to that of the PI Equations (60) and (63) becomes immediately apparent. When using the Debye function the fundamental concern becomes, "What is the appropriate atomistic description to use when calculating the Debye intensity?" This consideration is accounted for in the previously described RS methods through the random

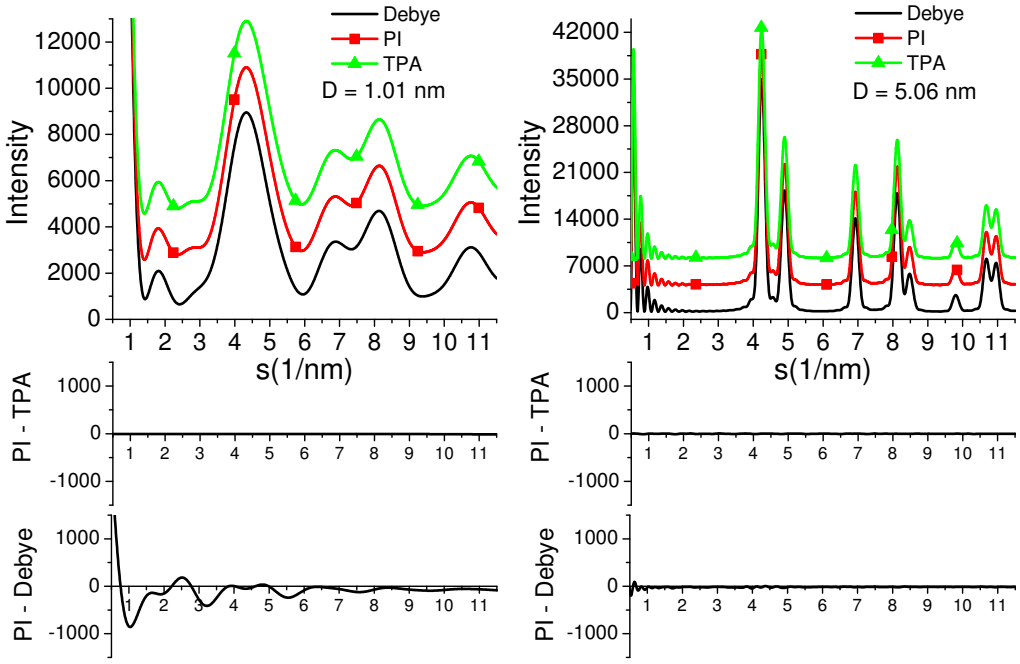

Figure 10: The powder patterns generated by the I-M tangent plane approximation (TPA), powder integration (PI), and Debye function are compared for Au spheres having diameters of 1.01 nm and 5.06 nm. The difference between the intensity obtained by the powder integration, and the other respective methods is displayed below the powder patterns.

shift treatment. However, the intensity calculated by the Debye function does not take into account this consideration, and the calculated Debye diffraction pattern is specific to the atomic description which was used. An exact match between the two methods is then not expected unless the Debye intensity from different atomic descriptions is averaged over all possibilities, or a representative atomic description can be found — the latter will be shown to be possible for some cubic crystallites.

First, the patterns from spherical gold particles with the diameters of

1.01nm and 5.06nm were simulated using Equation (64), assuming the I-M TPA and PI described by Equation (59) and (63) respectively. The comparison of the patterns depicted in Figure 10 shows a remarkable agreement between the two methods. This is somewhat unexpected considering the small size of the crystallites, even for the case of spheres. This result then both affirms the PI method of calculating the diffraction pattern by Equation (63), and suggests that the I-M TPA is more than sufficient to simulate the powder pattern from a spherical crystallite. Also depicted in Figure 10 are the corresponding Debye patterns from single atomistic descriptions of the spherical particles. A difference between the Debye and PI patterns is only apparent in case of the extremely small sphere, showing the slightly different peak profiles resulting from the specific Debye atomic description versus the random shift treatment. It is interesting to note that for the sphere with a diameter of only 5.06 nm ($D \sim 12.4a$) the difference in the patterns from the two methods becomes negligible. This implies that the differences due to the specific and averaged crystallite descriptions can only be discerned for extremely small crystallites, which are composed of a few unit cells. This result is in agreement with a similar study conducted by Cervellino et al. who found that a crystallite with a size of $D \sim 10a$ was sufficient for good agreement between the Debye and RS patterns from Au spheres [25]. The authors would only like to emphasize, that while Cervellino et al. called the difference in the patterns an "error" on the part of using the RS

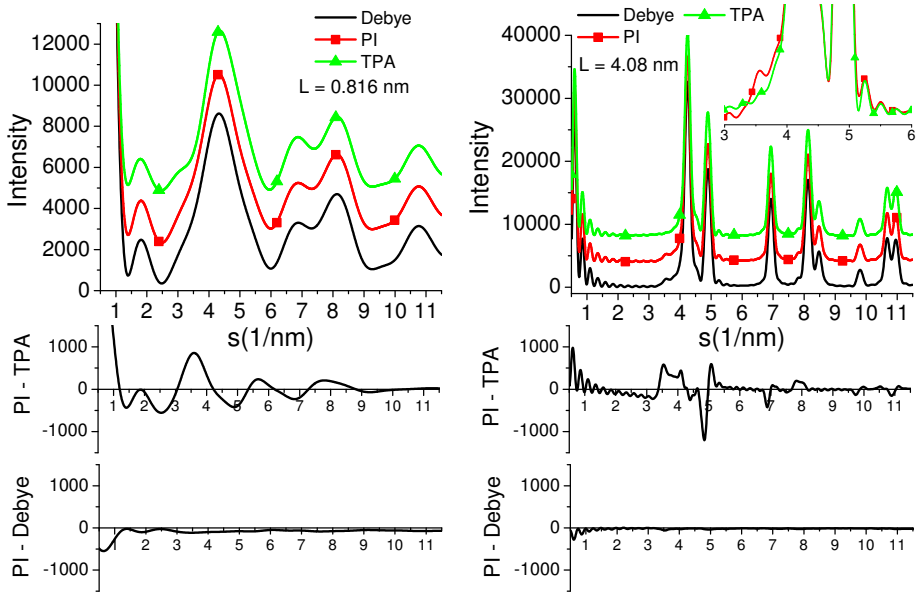

Figure 11: The powder patterns generated by the I-M tangent plane approximation (TPA), powder integration (PI), and Debye function are compared for Au cubes having edge lengths of 0.816 nm and 4.08 nm. The difference between the intensity obtained by the powder integration, and the other respective methods is displayed below the powder patterns.

random shift treatment, it is really an understandable and expected difference from the crystallite descriptions assumed in the two techniques. In the past the authors have also shown the agreement between the Debye and I-M TPA patterns to be extremely good when considering a size distribution of spherical crystallites, as the subtle differences in the peak shapes from the two methods begin to be averaged out by considering different sized crystallites [12].

The representation of the powder intensity from cubic crystallites poses a slightly tougher test for the TPA. Figure 11 shows the patterns for cubes with edge lengths of 0.816 nm and 4.08nm again calculated

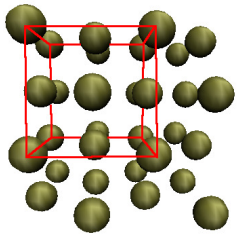

Figure 12: Atomic description used in calculating the Debye function intensity from a cube having a side length of 0.816nm ($2a$) viewed normal to one of the cube faces. The outline of an f.c.c. unit cell is also drawn to help guide the eye.

from the I-M TPA, PI and Debye methods. The sizes of these cubes were chosen such as to have an equal volume as the previously studied spheres. Careful comparison of the profiles from the I-M TPA and PI for the $L = 0.816$nm case finds that the TPA is unable to match the exact profile shapes, or the relative intensities, of the low angle peaks. For the larger $L = 4.08$nm case, the agreement becomes better for the higher angle peaks, however, the I-M TPA is still unable to properly represent the 111 and 200 peaks. For instance, the I-M TPA pattern shows an offset of the 111 and 200 peak positions relative to the patterns from the PI method and Debye function. While this effect is not huge it is still visible for the small crystallites considered.

The patterns for the $L = 4.08$nm case is plotted on a log scale to

demonstrate that the 111 peak from a cube contains an abnormal shoulder to low angle, best described as a sharp ledge. The I-M TPA is found to be unable to recreate this peak shape, and results in a smooth asymmetric tail. In fact, as one might expect, the 111 peak is not the only *hkl* which exhibits this strange peak shape for a cube, but other members of the family, like 222, have similar features which is not immediately apparent in the figure due to the superposition with other peaks. The presence of this feature is also found in the diffraction pattern simulated by the Debye function, and a nearly exact match of the Debye intensity with the PI pattern is found for both cubes considered. The unique shape of the 111 peak is one example of a defining characteristic of a powder peak profile from a cubic crystallite which is lost when considering the TPA.

The kind of agreement observed between the Debye and PI intensity for the cubes studied here is more of the exception than the rule. When the cube side length becomes a multiple of the unit cell parameter (i.e. $L = 0.816\text{nm} = 2a$ and $L = 4.08\text{nm} = 10a$), a special case exists where a single representative atomic description of the cube can be found which is equivalent to the random shift treatment. Such a construction is depicted in Figure 12, and comes from the consideration of periodic boundary conditions, where atoms on the faces cannot exist on both sides of a cube. For other cube sizes, and atomic constructions, a slight difference between the PI and Debye patterns — similar to that observed for the

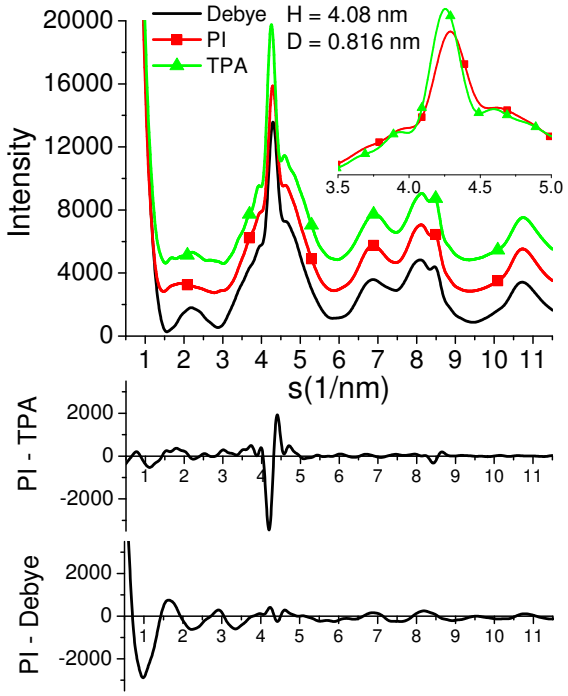

Figure 13: The powder patterns generated by the I-M tangent plane approximation (TPA), powder integration (PI), and Debye function are compared for an Au cylinder having a diameter 0.816 nm, height of 4.08 nm and its rotation axis normal to the 111 planes of the lattice. The difference between the intensity obtained by the powder integration, and the other respective methods is displayed below the powder patterns.

case of the spheres — was found when considering crystallites smaller than 5 nm. Still, the agreement which has been demonstrated shows the ability of the PI method to correctly simulate the powder intensity for cubic crystallites.

Finally, the case of a small cylindrical rod having a height, H, of 4.08nm and a diameter, D, of 0.816nm ($H/D = 5$) was considered to compare the three methods. The resulting patterns are depicted in Figure

13. The rod was assumed to have its rotation axis normal to the 111 planes of the internal lattice. Comparison of the TPA and PI intensities finds a generally good agreement except when it comes to the 111 peak, which is the sharpest peak in the patterns. The TPA intensity is shown to poorly represent the position and symmetry of the 111 peak. These kind of inaccuracies can lead to not only a poor determination of the crystallite size, but the position offset can also lead to a wrong lattice parameter. Reasonable agreement is again seen between the PI and Debye intensities in Figure 13 considering the small size of the rod, and the fact that a representative atomic description does not exist for the case of a cylinder, as was the case for some cubes.

The presented cases of cubic and cylindrical crystallites are prime examples of why it is extremely important to have an accurate description of the peak profile when modeling the pattern from nanocrystallites. Skepticism of the accuracy of RS LPA methods at determining such microstructural quantities for small crystallites has been the topic of some recent studies in the diffraction literature [99, 100]. In the work of Palosz and co-workers, the patterns from Debye calculated diffraction patterns were fitted with smooth analytical functions, like pseudo-Voigts, and the fits were analyzed to determine information on the crystallite size and unit cell parameter. It was concluded that the small size of the crystallites prohibited the accurate determination of these quantities, and trends of the apparent lattice parameters (ALPs) have been studied. Given the

careful study on the sensitivity of the powder peak description which has been presented here, it becomes clear that a series of pseudo-Voigts, or any other analytical function, cannot properly model the powder pattern from a nanocrystallite. It is then possible that their observed size dependent, ALPs are nothing more than an exemplification of this fact. The level of agreement of the developed powder integration procedure with the Debye patterns exhibited in the present study is evidence that accurate microstructural information of nanocrystallites can be obtained following the proper considerations.

To ensure that any mismatch of the intensity from the I-M TPA and PI methods is not caused by an improper representation of the scale parameter, or the I-M TPA Lorentz factor $1/ss_{hkl}$, a study of the integrated intensity from the TPA peaks and the PI peaks was conducted. The same integrated intensity was found for a given hkl peak simulated by the two methods for a given crystallite shape and size. Furthermore, it was found that the $\cos(2\pi(s - s_{hkl})L)$ term in Equation (59) was important for an exact match of the integrated intensity. This affirms that both methods of simulating the pattern preserve the scattering power of the single crystallite, and reinforces the claim that the observable differences between the I-M TPA and PI methods originate from the tangent plane approximation to the powder integral.

3.3 Diffraction pattern from a size distribution

The discussion until now has been concerned with the diffraction pattern from a powder of particles having the same size and shape — something which is somewhat experimentally unrealistic. In nature, a powder is actually composed of particles of various sizes and shapes, with their distribution determined by the kinetics and thermodynamics of the crystal growth mechanism. As it will be shown, the existence of a size distribution requires further averaging of the powder diffraction pattern, which can reduce some of the influences of the three approximations outlined in Section 3.1.

In order to test this, a study was conducted where the diffraction pattern was simulated for a size distribution using the Debye function, and was then modeled using the reciprocal space line profile analysis method of Whole Powder Pattern Modelling (WPPM), attempting to determine the full size distribution from just the peak profiles. This study also serves as a direct comparison of accuracy of the two methods when applied to small crystallites. It is then a benchmark to verify the methods used to simulate a size distribution with the Debye function, as well as, probe the range of validity of the reciprocal space methods for very small particles. A brief description of each method to simulate the diffraction pattern from a powder containing a size distribution will be given to understand the differences in both approaches.

3.3.1 Simulating a size distribution by the Debye function

The methods used to simulate the diffraction pattern from a powder having a distribution of sizes by the Debye function is fairly intuitive. Given enough computational resources, the powder intensity for a crystallite of any size and shape can be obtained by direct use of Equation (24). For a given shape, the average pattern from a distribution of sizes is then given by a weighted average of the respective patterns such as

$$\overline{I_P(s)} = \sum_D w(D) I_P(s, D), \tag{66}$$

here D represents some size determining parameter of a shape, which would be the diameter for a sphere. Since the intensity calculated by the Debye function is intrinsically scaled by the number of scatterers in the particle, the weights, $w(D)$ in Equation (66), are then related to the *number fraction* of each size, and follow the normalization condition, $\sum_D w(D) = 1$. It is common to assume a continuous functional form of the size distribution with respect to the size parameter, D. The weights of Equation (66) can then be given by

$$w(D) = \frac{g(D)\Delta_D}{\sum_D g(D)\Delta_D},$$

where $g(D)$ is the size distribution function assumed and Δ_D is the sampling interval of the size distribution.

It now should be apparent that the average pattern from Equation (66) is really an approximation for a continuous size distribution, the

accuracy of which is determined by the sampling interval. Since a finite number of particles must be considered, and the direct average is necessary, the sampling interval cannot go to zero. However, a reasonable sampling interval can be determined when considering particle made of a crystal lattice. For example, for a particle composed of a polygon shape which is defined by limiting planes, this sampling interval can be defined as the interplanar distance of the lattice — since any interval smaller than this would not change the atoms included in the shape. Other arguments can be made to conserve the stoichiometry, or the atomic volume, in a particle. So, this parameter varies depending on the lattice and circumstance. However, until this study the accuracy of this approximation to represent the influence of a size distribution on the diffraction pattern had not been assessed.

3.3.2 Simulating a size distribution by reciprocal space methods

The basic approach to simulating the effect of a size distribution by reciprocal space methods follows that described for the Debye function. The intensity for each peak is found from the average of different crystallite sizes, weighted by the size distribution. However, in the reciprocal space approach the average is incorporated into the Fourier transform of the peak profile, instead of taken over the resulting pattern as in the case of the Debye function.

Adopting the tangent plane approximation, the average profile can

be expressed as

$$\overline{I_P(s)_{hkl}} = k(s)\frac{|F(s,s_{hkl})|^2}{\int g(D)V_c(D)dD}\int\int v(L\hat{\mathbf{s}}_{hkl},D)g(D)V_c(D)\exp(2\pi i(s-s_{hkl})L)\mathrm{d}D\mathrm{d}L, \tag{67}$$

which is just a re-expression of Equation (66) in the limit where $\Delta_D \to 0$, and using the intensity given by Equation (58), where the self-convolution function is now explicitly described as a function of the particle size parameter D. The term $k(s)$ in front of Equation (67) represents the contributions to the pattern which are dependent on the geometry of the measurement, such as the terms outside of the integral in Equation (16). In Equation (67) the number size distribution, $g(D)$, is now weighted by the crystallite volume, $V_c(D)$, giving the *volumetric* size distribution, to account for the fact that a larger crystallite has more scattering power than a smaller one, and will then have more influence on the diffraction pattern.

Assuming a system of crystallites composed of the same shape but different sizes, the average over D in Equation (67) can be taken resulting in the intensity of the form

$$\overline{I_P(s)_{hkl}} = k(s)|F(s,s_{hkl})|^2\int A^S_{hkl}(L)\exp(2\pi i(s-s_{hkl})L)\mathrm{d}L,$$

where the Fourier coefficients of the peak shape due to the crystallite size and shape are found to be

$$A^S_{hkl}(L) = \frac{1}{\int g(D)V_c(D)dD}\int v(L\hat{\mathbf{s}}_{hkl},D)g(D)V_c(D)\mathrm{d}D. \tag{68}$$

These coefficients are then useful in modeling the diffraction pattern using an approach such as that described by Equation (27). If the size distribution is described by an analytical function then the integral of Equation (68) can be solved in terms of its parameters. For example, assuming a log normal distribution which is defined in terms of the two parameters M and S as

$$g(D) = \frac{1}{DS(2\pi)^{1/2}} \exp\left[-\left(\ln D - M\right)^2 / 2S^2\right], \tag{69}$$

the Fourier coefficients become

$$A^S_{hkl}(L, M, S) = \sum_{n=0}^{3} H^c_{n,hkl} \mathrm{erfc}\left[\frac{\ln(LK^c_{hkl}) - M - (3-n)S^2}{S2^{1/2}}\right] \frac{\mu_{l,3-n}}{2\mu_{l,3}} L^n, \tag{70}$$

where $H^c_{n,hkl}$ and K^c_{hkl} are coefficients corresponding to the crystallite shape — examples are given in [127] — and $\mu_{l,i}$ is the i-th moment of the log normal distribution. More forms of the Fourier coefficients corresponding to crystallite sizes following Gamma or York distributions are found in [124].

3.3.3 Comparison of direct space and reciprocal space methods

It is important to explore differences between the Debye (real space) approach, and the traditional (reciprocal space) approach to LPA. This is particularly interesting to assess the compatibility of the results obtained for nanocrystalline systems with domains in the order of 3 to 10 nm, where both approaches are possible to use. To this purpose, diffraction

patterns simulated using a Debye algorithm have been modeled using the whole powder pattern modelling (WPPM) approach [124]. Results show a good compatibility between the methods, and point out the key role of noise (i.e., data quality) in limiting our possibility to unveil the finest details of the nanostructure.

In this study, simulations are focused on spherical gold crystals with a lattice parameter of 4.081 Å. Spheres were chosen because the shape function has an analytical expression that can be treated more strictly by WPPM. The Debye approach utilized four unique log normal size distributions in simulating the patterns. These distributions were chosen to create sets of patterns defined by a common Scherrer size. This allowed for the study of any differences in the peak profiles calculated by the two approaches due to the effect of the distribution shape, while preserving the integral peak breadth. Two sets of diffraction patterns were simulated to have Scherrer sizes, $< D >_V$, of 2.7 nm and 4.0 nm, respectively; while the log normal standard deviations, σ, used were 0.15 nm and 0.40 nm resulting in a narrow and wide distribution for each set. (See Equation (116) and (117) for definitions of $< D >_V$ and σ respectively.)

The Debye simulated pattern was calculated following the approach outlined in Section 3.3.1. In this study two rules were assumed to govern the sampling interval: i) that Δ_D is constant, ii) that the volume increment between consecutive clusters is an integer multiple of the Wigner-Seitz unit cell volume. Using these two assumptions it can be shown

that

$$\Delta_D = a(3/2\pi)^{1/3} \sim 0.78a, \tag{71}$$

where a is the FCC lattice parameter. The sampled distance sets for each particle were used to calculate diffraction patterns via a suitably adapted Debye formula, which is amenable to a fast transform. More details on the fast Debye simulation algorithms can be found elsewhere [25, 24].

Three levels of Poisson noise were then added to the simulated intensity to obtain patterns with signal-to-noise ratios, $SNR = \sqrt{I_{max}}$, of 316.2, 100, and 31.6 (max noise added). Then simulated patterns were modeled with the WPPM approach [124, 86], refining the parameters of the FCC lattice, size distribution, small angle scattering contribution and a Chebyshev polynomial background. A range of trial size distribution forms was assumed including: continuous and discrete log normal distributions, and a continuous gamma distribution. The results of these analyses for each distribution are given in the following discussion.

3.3.3.1 Continuous log normal distribution

The patterns calculated by the Debye approach were first modeled assuming a continuous log normal distribution of spheres in the WPPM framework. The obtained size distributions matched exactly the expected Debye distribution for all studied patterns. Even at the small particle size range of 1-10 nm, the WPPM method was able to accurately distinguish the different log normal parameters of two size distributions resulting in patterns with the same integral breadth. The exact match between the

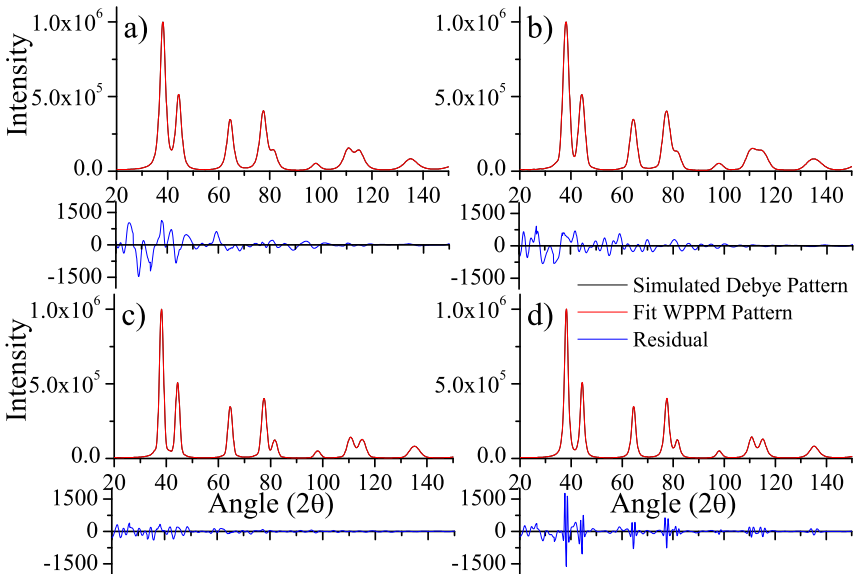

Figure 14: Results of modeling the Debye patterns assuming a continuous log normal distribution: (a) $< D >_V$= 2.7nm σ =0.1491nm wss= 3072.61, (b) $< D >_V$=2.7nm σ =0.3975nm wss= 4088.86, (c) $< D >_V$=4.0nm σ = 0.1494nm wss= 766.35, and (d) $< D >_V$= 4.0nm σ =0.3946nm wss= 990.89.

discrete distribution used in the Debye simulations and the continuous curve employed in WPPM was beyond expectations (see figure 15).

The lower residual and weighted sum of squares, defined as

$$wss \equiv \sum [(I_{Debye} - I_{WPPM})/I_{Debye}]^2,$$

for the distributions with a larger Scherrer size of 4.0nm was somewhat expected (see figure 14) . As the size increases the differences between the discrete Debye crystal, and the spatially averaged reciprocal space method, become less influential. Furthermore, as discussed in section 3.2.3, at larger sizes the shape of the particle created in the Debye approach is increasingly well represented by a sphere. The agreement of the

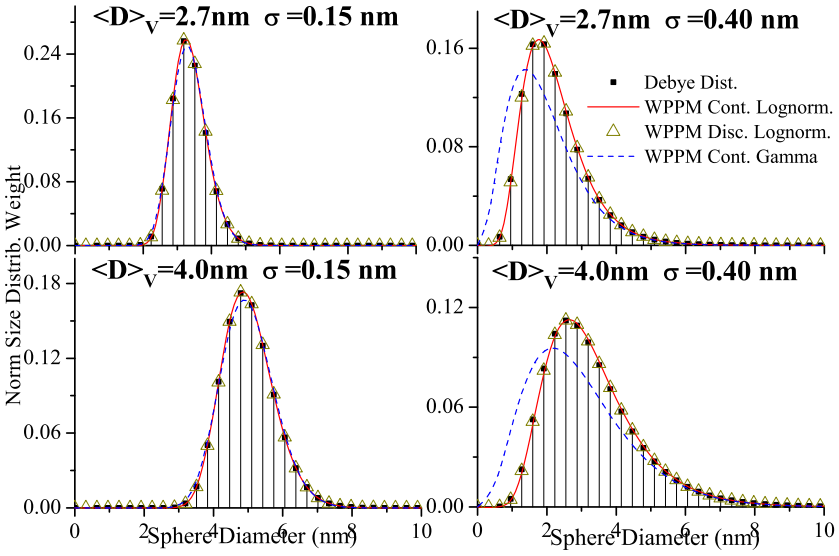

Figure 15: The distributions obtained from the modeling of patterns before the addition of noise are compared.

obtained WPPM distribution with that used in the Debye simulations remained excellent as the SNR was decreased in the patterns. There was only a very slight deviation from the expected distribution at the highest investigated noise level. In particular, the obtained distribution tended to broaden and shift to sizes smaller than expected.

3.3.3.2 Discrete log normal distribution

A discretely sampled log normal size distribution was also employed in WPPM to mimic the form of the size distribution used in the Debye approach. This distribution consisted of a set of weighted delta functions at the same regular steps as that used in the Debye simulation, given by Equation (71). The weight of each delta function was governed by the

value of a log normal distribution, and the parameters of this governing function were then refined in the WPPM framework, keeping the number of free parameters the same as in the continuous case. This form of the distribution was chosen in order to make the WPPM method more consistent with the discreteness of the Debye approach, and give a reference point to the continuous distribution assumption.

The discrete log normal size distribution parameters found had the same agreement with the expected values as those found for the continuous case (see Figure 15). The weighted sum of squares, and residual intensity, did not show any significant improvement from the continuous case. Furthermore, the background obtained when utilizing this distribution was found to be very similar to that obtained when assuming the continuous log normal distribution. Therefore, it is not accounting for unseen effects on the pattern due to the discreteness of the size distribution. It is then our conclusion that the discrete size distribution utilized in the described Debye approach does not result in noticeable effects in the simulated pattern. As noise was added to the data the agreement of the discrete distribution followed the same general trend as the continuous log normal distribution.

3.3.3.3 Continuous gamma distribution

To investigate the sensitivity of these methods to the functional form of the size distribution, the simulated patterns were also modeled assuming a gamma distribution in WPPM. The total number of parameters which

was concurrently refined did not change as the gamma distribution is described by two parameters, just like the case of the log normal. The inaccurate assumption of a gamma distribution was only noticeable in the modeling of the patterns from the broader and skewed size distributions (see Figure 15). In these cases the character of the distribution used in modeling becomes evident, and the gamma distribution was in better agreement at larger volumes due to the larger influence of this size range on the diffraction pattern. The ability of WPPM to recover a good representation of the expected distribution in the small size range became worse as the SNR was decreased. However, modeling of the patterns with increased noise obtained Scherrer sizes that were still in good agreement with the expected values. Therefore, even when the assumed distribution is not representative of the actual particle sizes, such as in the case of the broader size distributions, the correct Scherrer size was found by the modeling.

Differences in the quality of the fit assuming either the log normal, or gamma, distributions were observed only in the noise-free patterns, where the weighted sum of squares was 5-10 times lower when assuming the log normal distribution. With the addition of noise, the weighted sum of squares became nearly equivalent, masking the ability to discern which size distribution form was a better model (see Figure 16). Therefore, while the Scherrer size was always matched, reliable details of the size distribution form could not be obtained from the noisy data. This

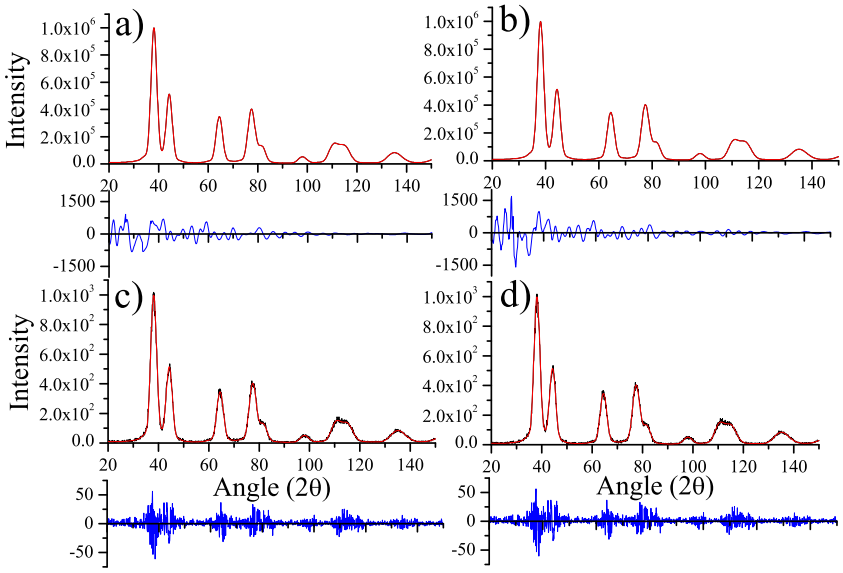

Figure 16: Best fit models of the $< D >_V$= 2.7nm σ =0.15nm pattern assuming (a) continuous log normal dist. no noise, (b) continuous gamma dist., no noise, (c) continuous log normal dist. with SNR = 31.6, (d) continuous gamma dist., SNR = 31.6.

conclusion is important to modeling noisy experimental data, as it seems hopeless to distinguish the two distributions from diffraction alone. In this case, the growth conditions and other observations must be taken into consideration.

3.4 Conclusions of Size Effect Study

The important conclusion of this study is that the correct description of the particle, or shape function, is increasingly significant as the size reduces. In reciprocal space methods the shape function describes a continuous body and commonly assumed to be an average over many specific

description. In the case of the Debye method this attribute is strictly dependent on all assumptions made when constructing the crystallite and simulating the diffraction pattern. Thus, when deciding between methods to model a diffraction pattern it is most important to consider if the underlying averaging of the reciprocal space approaches, or the specificity of the Debye method, is more appropriate to describe the studied system.

Another theme which runs throughout this chapter is that when employing reciprocal space methods to study crystallites with a size on the order to 10nm, it can be necessary to reconsider the common assumptions made for large crystallites. For instance, it was shown how use of the shape function description given by Ino and Minami, and avoiding the tangent plane approximation, becomes increasingly important for crystallites of small size and specific shape. These more appropriate descriptions push the validity of reciprocal space methods to smaller crystallite size, and to the limit of what can be called a crystallite.

The agreement seen in the final study considering different crystallite size distributions can only be attributed to the effect of averaging over multiple crystallite sizes. This effect is believed to be similar to the average over random shift treatment described in Section 3.1, as more descriptions of the crystallite shape and surface electron density near the surfaces are considered as the size distribution broadens. This improves the accuracy of traditional reciprocal space methods in this small size range for a realistic sample with a crystallite size distribution.

CHAPTER IV

DEBYE FUNCTION ANALYSIS OF PT 111 NANOPARTICLES

The development of modern synthesis methods which control the shape and size of nanoparticles [20, 87] has further increased interest in their use as chemical catalysts. As many chemical reactions have been established to be surface structure sensitive, control of the particle shape makes possible the engineering of high surface area catalysts which are efficient and reaction selective [18, 85, 119]. Transmission Electron Microscopy (TEM) measurements have been commonly used to characterize the shape controlled nanoparticles and information about the surfaces is then inferred [18, 119]. While this analysis can give some information on the size and shape of the nanoparticles, obtaining these results can be time consuming and consider only a small fraction of particles. Furthermore, TEM is an ex-situ measurement which is done in an environment much different than that in which the catalyst is used. For TEM analysis of a nanoparticles, the sample is often dried onto a sample holder. This sample holder is then placed into a vacuum chamber for measurement in the electron beam. It is then possible that the structure which is found via TEM is not consistent with that found in an electrochemical reaction

environment. In-situ wide-angle diffraction analysis then offers a possible useful tool to characterize a nanoparticle sample.

In the present study it will be demonstrated that wide-angle x-ray diffraction measurements can be used to determine a reliable statistical representation of particle size, as well as shape. This information will be extracted from the experimentally measured pattern via the developing method called Debye Function Analysis (DFA) which simulates the diffraction pattern from atomic models of nanoparticles. This method also allows for the characterization of strains and defects, such as faulting, which might exist in a nanoparticle sample. Observation of faulted nanoparticles is not uncommon in TEM studies of metal nanoparticles. Twinned particles have been found to exist as Lamellar Twinned Particles (LTPs), which contain one or more parallel fault planes, as well as Multiple Twinned Particles (MTPs), which contain intersecting fault planes [91]. The characterization of MTPs by a DFA method has been carried out in the literature for a variety of different metal nanoparticle compositions [23, 31, 63, 150, 149, 165], however, until now LTPs have not been widely considered. The results of the DFA method will be compared to that obtained by Whole Powder Pattern Modelling (WPPM)[124, 126], a reciprocal space based technique of diffraction pattern analysis. WPPM models the diffraction pattern by combining the different effects that microstructure features, such as crystallite size and strain, have on the

diffraction pattern line profiles. The presented study then offers an evaluation of how well two very different diffraction pattern modeling approaches can model the diffraction pattern from nanoparticles.

4.1 Nanoparticle synthesis and TEM characterization

The Pt nanoparticles used in this study were prepared by H_2(g) reduction of an aqueous solution consisting of H_2PtCl_6, and sodium polyacrylate using a methodology similar to that previously reported [2, 1, 105, 135, 148]. In brief, 1 ml of 0.1 M sodium polyacrylate solution was added to 100 ml of an aged 1×10^{-4} M solution containing the Pt precursor, H_2PtCl_6. The pH of the solution was adjusted to 7 with 0.1 M HCl. Finally, the solutions were purged, 5 min of Ar bubbling and 1 min of H_2 bubbling were used. The reaction vessel was then sealed, and the solution was left overnight. After complete reduction (12-14 hours), two NaOH pellets were added to produce the precipitation of the nanoparticles. After complete precipitation, the nanoparticles were washed 3-4 times with ultra-pure water.

Transmission Electron Microscopy (TEM) and High Resolution Transmission Electron Microscopy (HRTEM) have been employed to investigate the size and shape of the synthesized nanoparticles. TEM experiments were performed with a JEOL, JEM-2010 microscope working at 200 kV whereas HRTEM experiments have been carried out on a JEOL 3010 microscope (LaB6, Cs=1.1 mm) operated at 300 kV, providing a

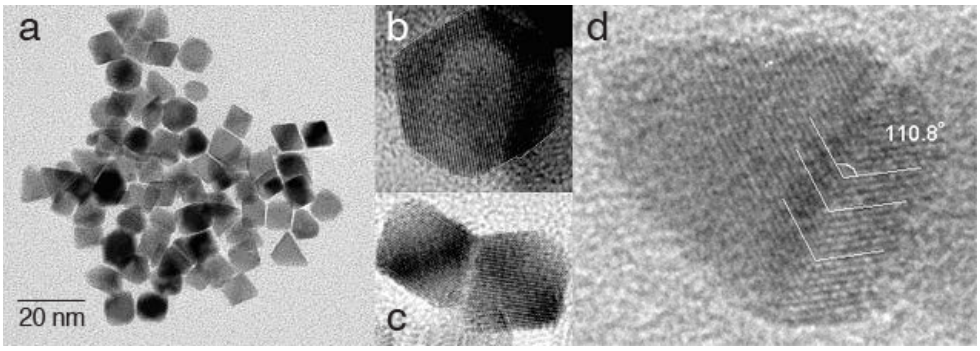

Figure 17: TEM of images of the synthesized Pt nanoparticles are depicted. (a-c) The mixture of particle shapes of different degrees of faceting was produced and (d) the existence of twin faulting was also observed.

point-to-point resolution of 0.19 nm. The nanoparticles observed in Figure 17a have triangular, diamond and hexagonal projections (also shown in Figure 17b), suggesting the existence of tetrahedral, octahedral, and cuboctahedral or possibly cubic nanoparticles respectively. As depicted in Figure 17c, octahedral as well as tetrahedral particles were commonly observed with truncated tips. Some particles, such as that depicted in Figure 17d, were also found to contain a twin fault. In this case a twin fault is present as the average angle between the atomic planes is found to be 110.8° which is very close to the tetrahedral angle between (111) and $(1\bar{1}\bar{1})$ in an FCC lattice: 109.5°. A statistic of shapes was made from 360 particles which were clearly focused giving the results: octahedral: 46%, tetrahedral: 22%, cuboctahedral: 14%, spherical: 4% and irregular shapes: 14%.

The determination of the particle size and shape is not straightforward as each shape has a different characteristic length and projected area which depends on the orientation of the particle relative to the electron beam. The diameter of a circle having an equal projected area to the observed particle was used as a universal measure to characterize the particle size. The particle size histogram obtained by analysis of TEM images is displayed in Figure 22, and reveals a Pt mean particle size of 8.714 nm and a standard deviation of 1.59 nm. A theorem first shown by Cauchy says that the average projected area of a convex shape considering all possible orientations is given as one quarter of the shape's surface area [22]. Since the surface area of the shapes assumed in the XRD modeling is known, relationships can be derived to find the equivalent diameter of the average projected area of each shape. This allows the size distributions determined by TEM to be compared with those obtained by XRD.

4.2 Dependence of the calculated pattern on particle shape

Before the results of modeling the diffraction pattern from the prepared Pt (111) sample can be fully appreciated a brief study of how nanoparticle shape affects the diffraction pattern and a description of the developed DFA algorithm is necessary. The powder diffraction intensity for any arrangement of x-ray scatterers can be calculated directly using the Debye function.

The generality of Equation (24) allows for the Debye function to be employed to simulate the nanoparticle diffraction pattern of particles having any shape. It can be reasoned that a sphere is the most energetically favorable shape of an isolated nanoparticle as it has the lowest surface area for a given volume, thereby, minimizing the surface energy. However, different surfaces of a crystal lattice can have dramatically different energies, which can result in a nanoparticle having a shape resembling a polygon given by the Wulff construction. These surface energies are then altered through the adsorption of organic molecules during particle growth, allowing for the synthesis of different particle shapes. A few commonly observed shapes of metal nanoparticles are displayed in Figure 18a which are the result of the preference to expose different amounts of either the (111) or (100) surfaces. Cubic nanoparticles are the result of the preference to expose only (100) faces, while all surfaces of both the octahedron and tetrahedron are (111). Other truncated shapes, such as the cuboctahedron, are more likely and are a mixture of exposed (111) and (100) surfaces.

The dependence of the diffraction pattern on the particle shape can be understood by considering how the shape affects the pair distribution function (PDF), which is defined in Section 5.3. The major differences in the PDFs of each shape shown in Figure 18a are primarily seen in the trend of the function at longer distances, as well as the maximum interatomic distance present when considering shapes having the same

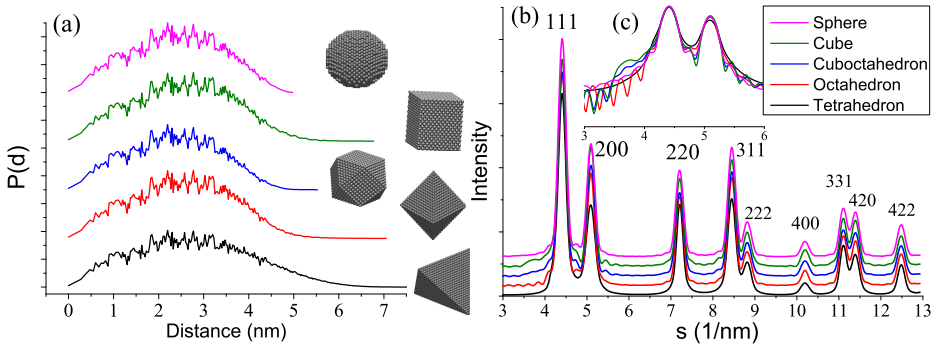

Figure 18: The PDF and resulting powder intensity is depicted for a series of crystallite shapes.

volume. The decay rate of the PDF in this range depicts the relative amount of long range order present in a given shape. Therefore, scattering from this long range order will have more influence on the diffraction pattern of shapes like tetrahedra or cubes. These subtle differences result in the distinguishing features of diffraction pattern peaks in Figure 18b, which are primarily noticed at smaller scattering vectors around the 111 and 200 peaks of platinum, as seen in Figure 18c. A tetrahedron has broader 111 and 200 peaks, which are devoid of any satellite peaks due to the lack of centrosymmetry of the shape. Satellite peaks are seen around the 111 peak of an octahedron due to the symmetry induced by the (111) surfaces. In the case of a cube there are satellite peaks around the 200 peaks due to its (100) faces, but also the 111 peak exhibits a strong asymmetric tail to smaller scattering angles. A blend of features seen in the cube and octahedron diffraction patterns is observed in the

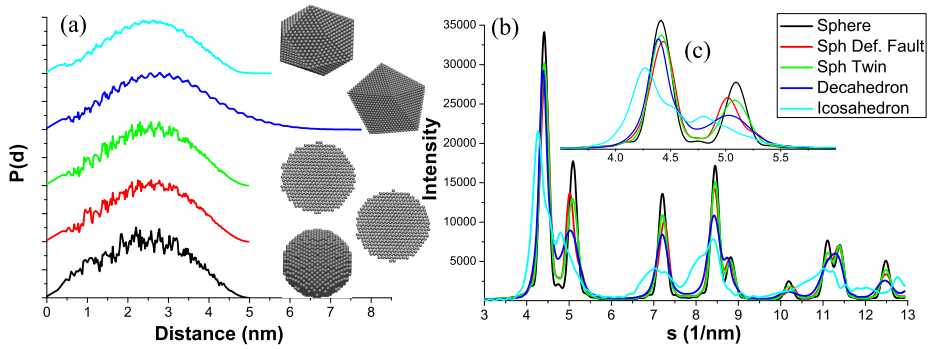

Figure 19: The PDF and powder intensity is depicted for particles containing different kinds of faulting.

pattern of a cuboctahedron, since the shape can be envisioned as a combination of the two. Also, the pattern from a cuboctahedron is very similar to that of a sphere, which is somewhat expected as visually a cuboctahedron is a rough approximation to the sphere. When a distribution of particle sizes is considered, the oscillations observed in Figure 18c around the peaks are smoothed, but the diffraction peak shape and broadening remain dependent on the particle shape and size distribution. [12, 79, 123]

Also considered in this study were particles which contain twin and deformation stacking faults. The character of faulting present in the prepared nanoparticle sample was determined by considering four different particle structures: a sphere containing a deformation fault in the center, a sphere containing a twin fault in the center, an icosahedron, and a decahedron. The icosahedron is an MTP which contains three orthogonal twin planes, while the decahedron is the result of five intersecting

twin planes, and both have all (111) surfaces. The PDFs and diffraction patterns for each faulted particle considered are displayed in Figures 19a, and 19b respectively. The diffraction peaks from a sphere containing a twin exhibit broadening, while those of a sphere containing a fault plane exhibit both broadening and a slight shifting. These findings are consistent with the effects of faulting described by Warren [153], and Paterson [103]. The icosahedron and decahedron exhibit very different patterns as the high degree of faulting present in these particles results in a different effective crystal symmetry. A detailed description of these MTPs has been presented by Cervellino, et al. [23], and elsewhere in the literature.

4.3 Description of DFA Routine

A Debye Function Analysis (DFA) algorithm was developed to determine the relative amounts of the different particle shapes present in a sample by analyzing the measured diffraction pattern. The diffraction pattern from a polydisperse collection of particles having multiple sizes and shapes can be expressed as a weighted average of the pattern from each particle as in

$$I(2\theta) = \sum_{shape} w_{shape} \sum_{D} w(D)_{shape} I_D^{shape}(2\theta) \tag{72}$$

where $I_D^{shape}(2\theta)$ is the diffraction pattern for each particle size and shape calculated from Equation (24). The weight $w(D)_{shape}$ represents the numerical fraction of particles of a given shape of size D, while the weight w_{shape} represents the numerical fraction of particles of a given shape.

As discussed in Section 3.3, the discrete sampling of the size distribution was done in the calculation of the Debye pattern. In this method the particle can be described in terms of an onion-like structure consisting of concentric shells. In the case of the spherical particles, the shell thickness, or size sampling interval, Δ_D, was taken to be the nearest-neighbor distance, or $\Delta_D = a\sqrt{2}/2$, while for other shapes the sampling interval was determined by the distance between complete shells of atoms which retain the shape. For instance, for the case of an FCC cubic particle this distance is $a/2$. A particle of any size can then be described as a union of the necessary shells. This description saves computational time, as well as, memory space, since the weighting of different particle sizes can be re-expressed in terms of weighting the scattering attributed to a given shell as

$$w(shell) = \sum_{D=D_{shell}}^{D_{max}} w(D). \tag{73}$$

This expression follows from considering that the minimum particle size containing a given shell is $D_{shell} = (shell) * \Delta_D$, and all particles up to the maximum size, D_{max}, will contain this shell. Using this expression, the diffraction pattern for a polydisperse sample becomes

$$I(s) = \sum_{shape} w_{shape} \sum_{shell} w(shell)_{shape} I^{shape}_{shell}(s). \tag{74}$$

Here the intensity from a given shell, $I^{shape}_{shell}(s)$, is more than just scattering between atoms within a given shell, but also must include scattering

between the atoms in the shell, and all smaller shells.

It is important to keep in mind that the size and shape distributions used in Equations (72) and (74) are *numerical* distributions. The Debye function automatically conserves the scattering power of a collection of atoms, which is proportional to the volume, or number, of the atoms. So a larger particle with more scattering power will result in a larger intensity than that of a smaller particle. If volumetric, or mass, distributions are used in the weighting of the average pattern, then the signal from the larger particles will be further enhanced, and the resulting diffraction pattern will be wrong.

In fitting the simulated pattern to an experimental pattern, it is always necessary to scale the diffraction pattern since measurements can be collected for different times, and detectors are never one hundred percent efficient. However, as just mentioned, the scattering power in the intensity described by Equation (72) changes with the particle shapes, and size distributions considered in the modeling. This will lead to correlation between the scale parameter and the size distributions obtained. In order to reduce the amount of correlation the unit scattered intensity should be used by normalizing the pattern calculated in Equation (74) by the number of scatterers in the simulated system, N [59]. The intensity then takes the form

$$I_N(s) = \frac{1}{N} \sum_{shape} w_{shape} \sum_{D} w(D)_{shape} I_D^{shape}(s), \tag{75}$$

with the number of atoms in the system determined simply by

$$N = \sum_{shape} w_{shape} \sum_{D} w(D)_{shape} N(D)_{shape}, \tag{76}$$

with $N(D)_{shape}$ being the number of atoms in a particle of a given shape and size, D. It should be noted that as an alternative, the unit scaled pattern from each particle can be used in the average of Equation (75). However, in this case it then becomes necessary to use the volumetric size and shape distributions for the appropriate weighting of the patterns in the average.

The intensities measured in a laboratory x-ray diffraction pattern are influenced by not only the scattering power of the material, but also phenomena and measurement parameters such as: x-ray polarization, x-ray absorption, the measurement geometry, and the thermal motion of atoms. In order to model experimental data with the Debye Function, the known effects of each of these phenomena was multiplied by the intensity calculated in (75), arriving at the simulated intensity through an expression of the form

$$I_{calc}(2\theta) = A(2\theta) \cdot Pol \cdot DW \cdot Abs \cdot I_N(2\theta) + BG(2\theta) \tag{77}$$

where $A(2\theta)$ is a variable scale factor which can be a function of 2θ, Pol is the polarization factor, DW is the Debye-Waller factor, Abs is the x-ray absorption factor, and $BG(2\theta)$ is a function to model the background. Unless otherwise noted the scale factor was assumed to be a constant, independent of scattering angle. However, as will be discussed in the

following section, it can also be expressed as a function of the scattering angle in an attempt to account for aberrations of the measured intensity from non-ideal instrument and measurement conditions. A Chebyshev polynomial background function was added to the calculated pattern to account for features such as scattering by the environment, and the parameters of which were refined along with the other parameters in the model. An independently measured background was not subtracted from the experimental pattern as it can change when the sample is present because of absorption by the sample.

The continuous diffraction pattern generated by the Debye function poses a problem to incorporate effects like instrumental peak broadening into the modeling as the commonly used Caglioti convolution [21] is no longer possible. In this study, the breadth of the measured diffraction peaks (shown in Figures 20 and 23) was observed to a Full-Width-Half-Maximum (FWHM) on the order of 1.0 deg. The instrumental broadening was determined by separately measuring the pattern of a LaB6 standard (SRM 660a), and the FWHM was found to be on the order of 0.01 deg. (2ϑ). Therefore, the observed broadening is dominated by the particle morphology, and the instrumental contribution can be ignored with small relative error.

Relatively few parameters are necessary to fully determine a simulated diffraction pattern. The total number is largely based on the number of shapes considered in the model, and the kind of size distribution assumed.

Other standard parameters control the background and scaling of the diffraction pattern. In total around 20 parameters are necessary for a system of 4 different shapes with each described by a distinct log normal size distribution. The challenge of modeling a diffraction pattern is then to determine the parameters which result in the best agreement with the measured pattern. This agreement was measured considering the value of χ^2 defined as

$$\chi^2 = \left[\frac{1}{n-p} \sum_{2\theta} \left[I_{calc}(2\theta) - I_{exp}(2\theta) \right]^2 / I_{exp}(2\theta) \right]^{1/2}, \tag{78}$$

with $I_{calc}(2\theta)$ and $I_{exp}(2\theta)$ respectively representing the simulated and experimental intensities composed of n points, and p is the number of free parameters considered in the model. To this end a least-squares minimization routine based on the Levenberg-Marquardt (L-M) algorithm [92] was developed. At a given step in the L-M routine the local gradient of the parameter space is considered in order to continually move the model in a direction which is expected to give a better fit. In the present study, since analytical expressions of the intensity are not readily obtainable, the local gradient was evaluated numerically. The component of the gradient corresponding to a free parameter is then found by slightly changing the parameter, evaluating the χ^2 corresponding to the new system, and then taking the ratio

$$\frac{\partial \chi^2}{\partial p} \cong \frac{(\chi^{'2} - \chi_0^2)}{p^{'} - p_0}. \tag{79}$$

While the L-M routine has the advantage of always moving in a direction

which improves the fit, it also has a tendency to get stuck in local minima, and not explore a substantial portion of the parameter space. Therefore, when it is being used, it is always necessary to assume different starting values of the parameters to find the best fit.

4.4 Modeling of the measured diffraction pattern

X-ray powder diffraction patterns of the prepared Pt (111) sample were measured in a laboratory setting using a Rigaku PMG/VH diffractometer fitted with a copper tube and a monochromator, so that only Cu Kα radiation illuminated the sample (Cu Kα_1: $\lambda = 0.154059$ nm and Cu Kα_2: $\lambda = 0.154445$ nm). The nanoparticles were spread onto a Si wafer, and measured in a reflection geometry over the 18–154° range with a step of 0.20°, and a counting time of 60s/step.

Since fine details about the particle shape and structure were sought, input from the complimentary analyses previously presented was used as a starting point in the modeling of the diffraction pattern. For instance, multiple combinations of particle shapes that were observed in the TEM images were attempted in the previously described DFA routine to model the collected pattern. Each shape was assumed to have a log normal size distribution, and the parameters controlling the size and shape distributions were simultaneously refined with factors such as the scale factor, background function and x-ray absorption thickness.

In an effort to efficiently obtain a good fit, it is important to systematically switch free different parameters. The first parameters to refine

are the scale and background. Followed by the parameters governing the lattice to find the right peak positions. This allows the modeling to get a rough idea of the peak heights, and positions, before refining the fine details of the peak profiles. Next the parameters controlling the size distribution, absorption and temperature factor can be set free, followed by the finer details concerning the shape distributions and defect densities. As previously stated, it is important to test different initial configurations of shapes of different relative weights, and size distributions before deciding on the best fit parameters. The remaining discussion will compare the best fit parameters determined by the modeling assuming different combinations of shapes.

When defects and strains were not considered, a model consisting of 56 % octahedral, 17% tetrahedral, 7% cuboctahedral, and 20% spherical particles resulted in a good fit of the measured pattern ($\chi^2 = 2.12$). The fit significantly improved when particles containing twin faults where present in the modeling, with the best fit obtained when twinned spheres were considered ($\chi^2 = 1.73$). In this case particles were found to have a size of 8.4 ± 1.9nm and consisting of 60% octahedra, 27% tetrahedra, 3% cuboctahedra, and 10% twinned spheres. A comparison of this best fit to the measured pattern is depicted in Figure 20. An improvement of the fit from the defect free model was also found when icosahedral particles were included in the modeling ($\chi^2 = 1.95$). While this did not result in the absolute best fit, the possibility of the sample containing some amount

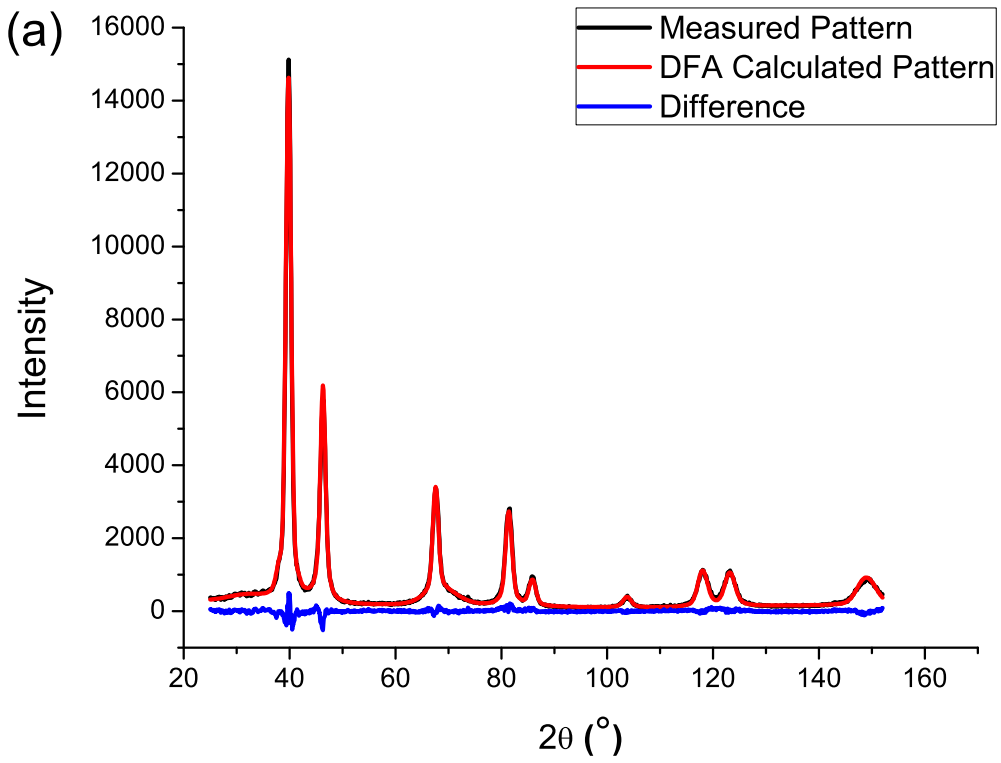

Figure 20: The Debye fit of the pattern measured from the Pt nanoparticle system is depicted.

of these nanoparticles cannot be ruled out. However, the more likely existence of single twinned particles over MTPs, for nanoparticles of the size studied here, has also been found in the case of Au nanoparticles[31, 150]. Furthermore, no particles were observed in the TEM analysis which exhibited the characteristic five fold symmetry of an icosahedron.

Some correlation of the parameters governing particle sizes and shapes is expected, but the results were found to be very stable as the algorithm converged to the same values given small perturbations. The case of dramatically different shape fractions resulted in a poorer fit of the data and a higher value of χ^2. Also, the results of complementary analyses validate the findings of the modeling. Figure 21 shows that the most abundant shapes determined by the DFA routine (octahedra and tetrahedra) matches that observed by TEM for each assumed mixture of particle shapes. These dominant shapes also agree with the Electrochemical characterization of the sample, which determined that the synthesized nanoparticle sample had a dominant (111) surface. The existence of particles containing some twin character is supported by HRTEM analysis of the synthesized nanoparticles, see Figure 17. The size distributions of each shape which resulted in the best fit are shown in Figure 22 to be in very good agreement with that obtained by TEM image analysis. The slightly smaller particle size determined by the DFA algorithm can be attributed to the unaccounted for instrumental broadening. The lattice parameter determined from this best fit was 0.39196 nm, slightly smaller

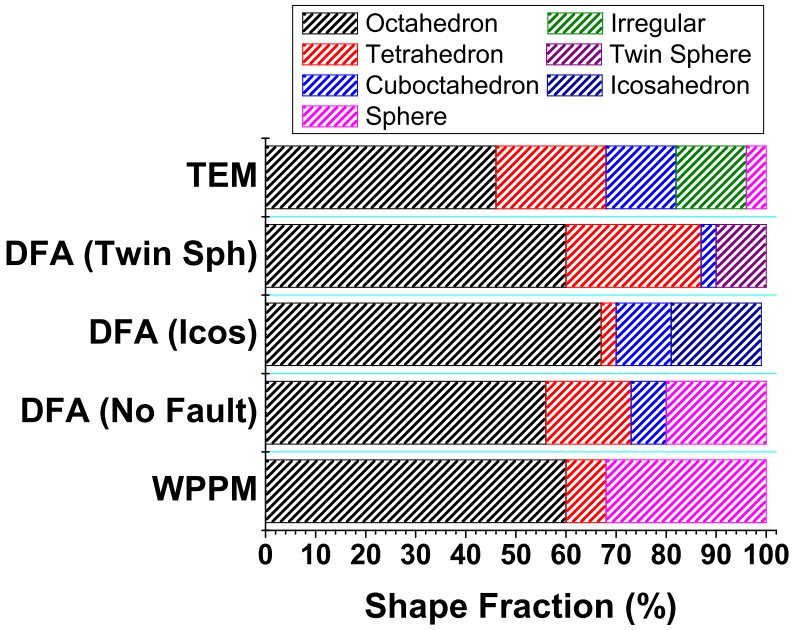

Figure 21: The particle shape distributions obtained from different characterization techniques is compared.

than the accepted bulk value of 0.3924 nm for Platinum. This might be due to a particle size dependent lattice parameter as a value of the same magnitude for Pt clusters has been previously reported [122].

The same diffraction pattern was also analyzed using a program called PM2K [86], the latest software developed based on the WPPM method. The modeling was carried out using the same assumptions regarding the particle size distributions and pattern background as that in the DFA routine. The resulting best fit shown in Figure 23, was obtained from 8.0 ± 3.7nm particles consisting of 60% octahedra, 8% tetrahedra, and 32% spheres. Again, as also shown in Figure 21, the most abundant shapes of octahedra and tetrahedra are identified from this method. The

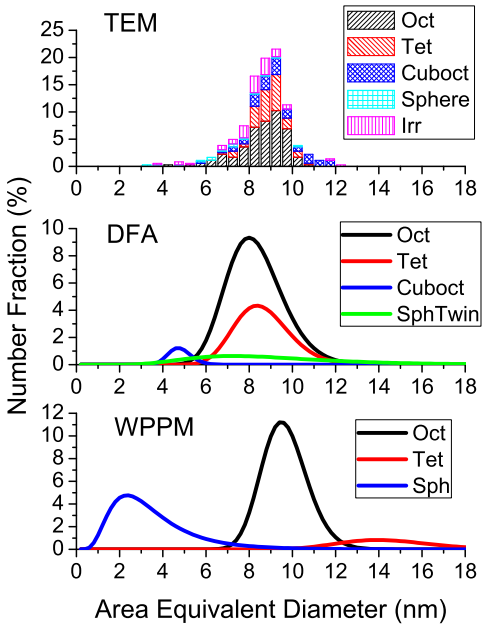

Figure 22: The size distributions obtained by TEM, DFA and WPPM methods are compared.

determined size distributions, depicted in Figure 22, show some deviation from the TEM measurements, which might be explained from the inability of the WPPM approach to consider truncated shapes. In contrast, DFA offers complete flexibility in the particle shapes considered as only a list of atomic coordinates are necessary to simulate the pattern. Along with information on particle size and shape, the WPPM modeling determined a twin fault probability of about 1.3%, which is consistent with the DFA and TEM analyses. Also, a small edge dislocation density of about $2.0 \times 10^{15} \mathrm{m}^{-2}$ was obtained, using contrast factors determined by a new general model [93], and assuming $c_{11} = 347$ GPa, $c_{12} = 251$ GPa, and $c_{44} = 76.5$ GPa [133]. It is possible that the determined dislocation density is actually accounting for other strain fields present in the particles, such as those due to particle agglomeration. A lattice parameter of 0.39190 nm was found in the modeling, which is consistent with that found using DFA.

The fit of the measured pattern determined by WPPM, displayed in Figure 23, exhibits a nearly featureless difference pattern, and finds the best χ^2 of 1.37. The better fit observed by using WPPM is partially due to its ability to refine the integrated intensity of each peak independently. Conversely, the diffraction patterns simulated by DFA are strictly determined by the model assumed, and can involve idealized measurement assumptions. For instance, in the present study the sample was assumed

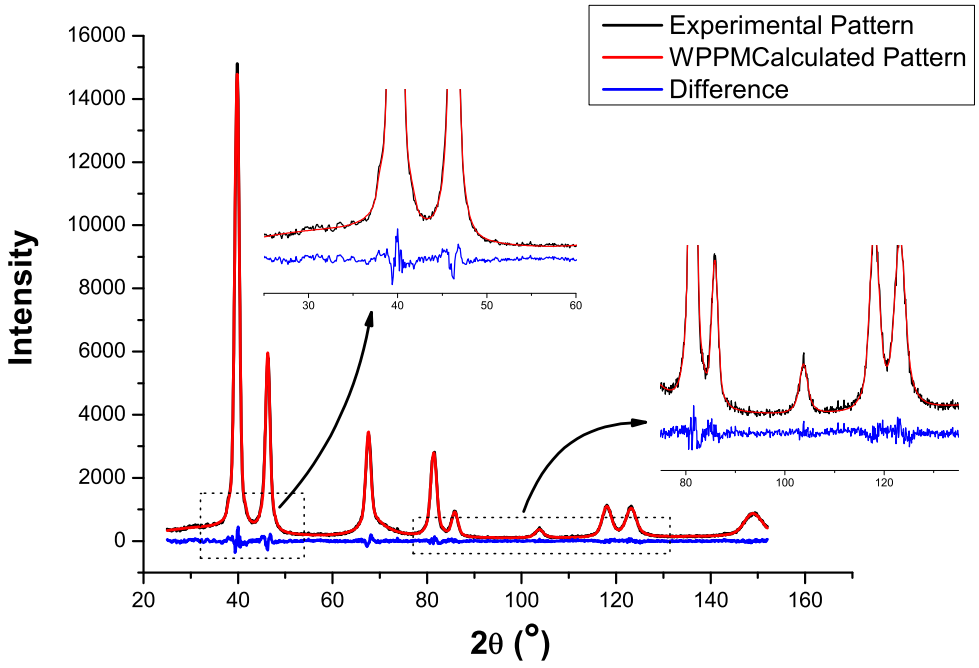

Figure 23: The best fit of the particle pattern obtained by PM2K is shown.

to be homogeneously spread on the silicon wafer with a uniform thickness. The more likely case of a variable sample thickness will induce a change in the observed intensity that is dependent on the scattering angle. In fact, study of the integrated intensity of each peak in the measured pattern found that the consideration of the Lorentz-polarization factor, secondary monochromator, and Debye-Waller factor were not enough to completely account for the trend of integrated intensity as a function of the scattering angle. The existence of an inhomogeneous sample thickness is one possible explanation of this discrepancy. The use of DFA then requires a perfect measurement to obtain a perfect fit of the data. A variable scale parameter, which is a function of the scattering angle, $A(2\theta)$, was used in an attempt to account for these kind of measurement aberrations. A slight improvement from the best DFA fit was found when a scale parameter expressed as a 5th order Chebyshev polynomial was used ($\chi^2 = 1.59$). The parameters of this function were not found to be correlated to those of the background, as the same background was found when the variable scale parameter was used. This can be expected as the two functions model scattering from different sources. The variable scale parameter models the diffracted scattering power from the sample, while the background is largely determined by scattering from the sample holder and surrounding environment. The particle size and shape parameters, which were the result of this improved fit, showed no considerable difference from what was already reported.

4.5 Summary

Pt nanoparticles have been synthesized, by reduction of a Pt salt in a solution containing polyacrylate, to have a preferential (111) surface. Three very different characterization methods of TEM analysis, XRD measurements and cyclic voltammetry showed consistent results, as the preferential (111) surface was found to be due to the presence of octahedral and tetrahedral nanoparticles with a size of about 8.7nm. DFA modeling of the x-ray diffraction pattern found an abundance of octahedra with a size that agreed with TEM observations. The modeling improved when particles containing twinning were considered, and the predominance of particles containing a single twin was found over multiple twinned particles. The different pattern analysis of WPPM found consistent results. A complete, and coherent, statistical determination of the important characteristics of nanoparticles which are intended for catalytic applications was demonstrated here through combined electrochemical and x-ray diffraction measurements.

CHAPTER V

MOLECULAR DYNAMICS BACKGROUND

> "the atomic hypothesis (or the atomic fact, whatever you wish to call it) that all things are made of atoms – little particles that move around in perpetual motion, attracting each other when they are a little distance apart, but repelling upon being squeezed into one another [...] provides an enormous amount of information about the world, if just a little imagination and thinking are applied." -Richard Feynman [50]

5.1 Basic Principles of Molecular Dynamics

Molecular dynamics (MD) is a robust computational method of simulating the structure, and dynamics, of materials on an atomistic level. Since its conception in the 1950s [3, 4], its application has spanned all fields of science, allowing for useful insight into the problems like the structure of proteins, and material deformation mechanisms. In the MD framework atoms are assumed to be the fundamental unit of a material, and are represented in the simulation by little more than its position, velocity, mass and charge. The atoms act on each other through interatomic potentials which in the MD framework are given by empirical functions, ϕ_{ij}. More formally, a potential energy function describes the energy of an atomic

bond between the atom i and atom j in the simulation. A more comprehensive review of some of these potential forms will be given in Section 5.2, for now let us just assume that ϕ_{ij} represents a smooth differential function. Potentials can also be formulated considering some three-body, or many-body interaction, but the two-body interaction is enough for the purposes of the present discussion.

The total kinetic energy of the atoms in the simulation is then given directly by

$$K = \sum_i m_i \mathbf{v}_i^2, \tag{80}$$

while the potential energy is given by

$$U = \sum_i \sum_{j \neq i} \phi_{ij}. \tag{81}$$

Also, following classical Newtonian mechanics, it is evident that the equations of motion of the atoms in the system are governed by the relationship

$$m_i \frac{d^2 \mathbf{r}_i}{dt^2} = -\frac{dU_i}{d\mathbf{r}_i}, \tag{82}$$

where U_i represents contribution to the potential energy by atom i.

An MD simulation is then carried out by assuming an initial configuration of atoms in space, and then letting the system evolve by iteratively solving Newton's equation of motion for all atoms in the system. A time step then consists of one step in time taken by the simulation. The size of this step should be on the scale of the motion of the atoms in a material in order to properly capture this motion. For most crystalline materials,

this is on the order of a femtosecond, or 10^{-15}s, which is a minute fraction of time as we perceive it. Also, an atom is really a tiny representation of a material, as in just one cubic centimeter of a material, there are on the order of 10^{23} atoms. Therefore, MD simulations are suitable for the better understanding of phenomena which occur at small time and length scales. It is not the only simulation technique used to model materials. For problems of an even smaller scale, density functional theory (DFT) simulation techniques offer the ability to study the electronic structure of materials. While for problems of a larger scale, continuum mechanics can be used to model the mechanical stability of materials. A brief overview of the main materials simulation methods, and time and lengths scales which they can cover, is depicted in Figure 24. Molecular dynamics is then a crucial link in understanding how discrete atoms assemble to make a larger material, which is then describable as a continuous body.

5.1.1 Verlet time integration

As previously mentioned, the evolution of the atomic system in an MD simulation is solved in a stepwise fashion by integrating Newton's equations of motion for each atom in the system. Then it can be said that the position, and velocity, of an atom evolves following a deterministic chain such as

$$r_i(t) \rightarrow r_i(t + \Delta t) \rightarrow r_i(t + 2\Delta t). \tag{83}$$

Many algorithms have been developed to integrate Newton's equations of motion over the time step Δt, each having their own costs and

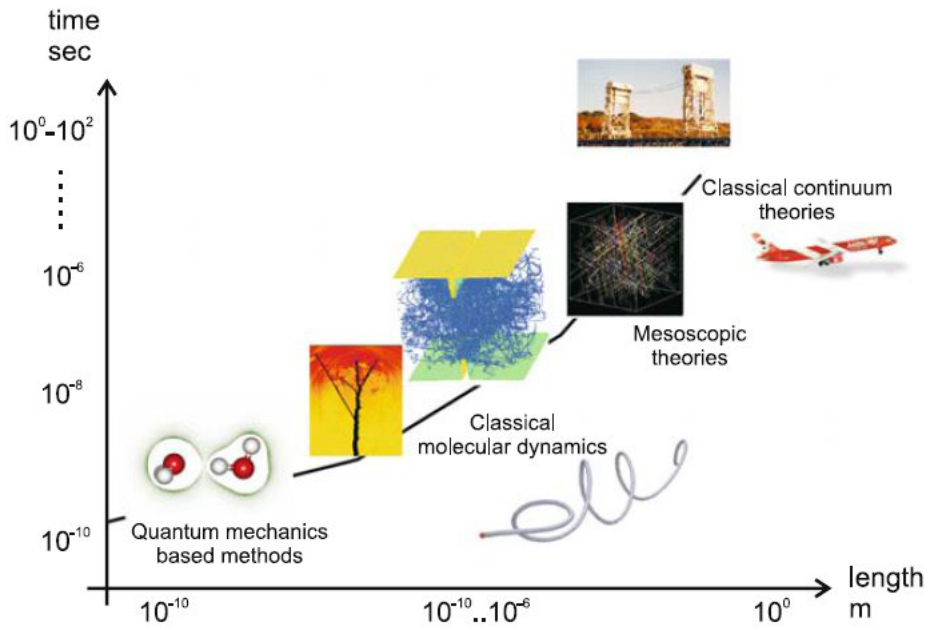

Figure 24: Graph showing the different length scales of computer simulations. (Image from Buehler [19])

benefits [5]. In the present study the Verlet algorithm was employed which is based on an assumption of the reversibility of time. The position of an atom at a future time can be expressed as

$$r_i(t + \Delta t) = r_i(t) + v_i(t)\Delta t + \frac{1}{2}a_i(t)\Delta t^2 + O(\Delta t^3), \tag{84}$$

and similarly the position at a time in the past is given by

$$r_i(t - \Delta t) = r_i(t) - v_i(t)\Delta t + \frac{1}{2}a_i(t)\Delta t^2 - O(\Delta t^3). \tag{85}$$

Summing Equations (84) and (85) yields the relation

$$r_i(t + \Delta t) = 2r_i(t) - r_i(t - \Delta t) + a_i(t)\Delta t^2 + O(\Delta t^4), \tag{86}$$

which is used to solve for the future position of the atoms. A similar expression can also be derived to solve for the velocity of the atom at a future time. The acceleration of the atom, $a_i(t)$, is found from considering Equation (82). Using the Verlet relationship of Equation (86) is also more accurate than solving Equation (84) directly, as the error in the Verlet algorithm expected to be $O(\Delta t^4)$ instead of $O(\Delta t^3)$.

5.1.2 Simulation box and periodic boundary conditions

A molecular dynamics simulation can then be thought of as a virtual experiment which studies how Newton's equations of motion can control a complex interconnected system of atoms. The virtual volume of space within which this experiment is taking place is commonly called the simulation box. The simulation box should be considered more than just

a rigid confinement space for the atoms, but can also have characteristics which makes it an important dynamic aspect of any MD simulation. For instance, the volume of the simulation box can be allowed to change throughout the course of the simulation, controlling the pressure of the system. Also, its boundaries do not have to be rigid walls, which change an atom's trajectory upon impact, but can be periodic so that an atom which passes through the boundary will appear on the other side of the box. The use of periodic boundary conditions (PBCs) also allows atoms near the boundary to have interactions with atoms on the other side of the boundary. This treatment is a generalization of the one-dimensional Born-von Karman periodic boundary condition which was developed to study the atomic vibrations in a linear chain of harmonic resonators [16]. In the Born-von Karman treatment the linear chain is actually described as a closed loop so that all atoms have the same local environment, and no fixed boundary conditions are necessary.

The PBCs in an MD simulation can be envisioned as surrounding the simulation box on all sides with other boxes containing a copy of the atomic system in the original box. Atoms in the central simulation box are allowed to interact with neighbors across the boundary, and all motion of the atoms in the central box is mimicked in the surrounding boxes. Then if an atom moves out of the central box it will appear on the other side as the atom in the neighboring box has then just moved into the central box. A graphical depiction of this concept is shown in Figure

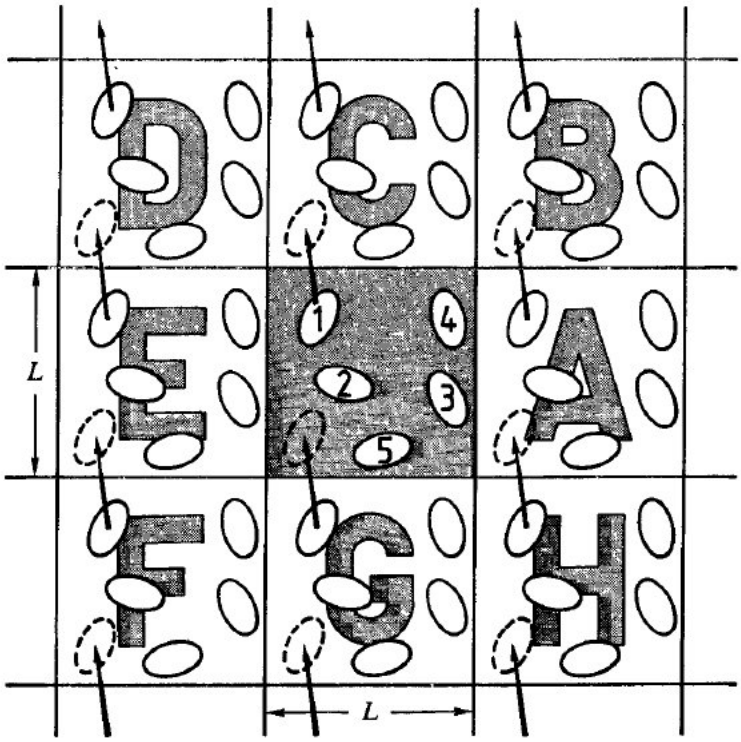

Figure 25: Graphic illustrating periodic boundary conditions (Image from Allen [5])

25. While the use of PBCs is an important tool in the efficient simulation of a material, the long range periodic nature which it implies can lead to artifacts in a calculated diffraction pattern. This aspect will be discussed in Chapter 6 along with a comparison of different approaches to avoid these kind of artifacts.

5.1.3 Thermodynamics and statistical ensembles

While directly solving Newton's equations of motion can yield a lot of information on the atomic structure of a material, it is somewhat limited

in that it is always driven to the end where all forces between atoms are neutralized, and the energy is minimized. This evolution lacks the consideration of the effects which temperature, and pressure, have on the structure of a material. The simulation of temperature and pressure then requires slightly altering Newton's equations of motion.

One method to simulate the effects of temperature in a system follows the classical statistical mechanics method of considering the atoms as being in contact with a thermal reservoir. Energy is then allowed to flow back and forth between the atomic system and the reservoir in an effort to keep the temperature in the system constant. This approach ensures that the energy of the total system (atoms + reservoir) is conserved throughout the simulation time. Following the original description by Nosé [98], the temperature of the atomic system is adjusted by scaling the velocities of the atoms following

$$\mathbf{v} = s\dot{\mathbf{r}}, \tag{87}$$

where s is a scale parameter related to the energy transferred between the atoms and the reservoir, and $\dot{\mathbf{r}}$ is the time derivative of the atomic positions. The potential energy of the thermal reservoir is then given by

$$U_s = (f+1)k_B T \ln s, \tag{88}$$

where f is the number of degrees of freedom in the atomic simulation ($f = 3N - 3$). Similarly, the kinetic energy associated with the reservoir

is

$$K_s = \frac{1}{2} Q_T \dot{s}, \tag{89}$$

where Q_T is a parameter representing the thermal "mass" of the reservoir. The total Lagrangian is then given by the sum of kinetic and potential energies from the atoms and reservoir, and the usual differentiation to find the equations of motion results in

$$\ddot{\mathbf{r}} = \mathbf{F}/ms^2 - 2\dot{s}\dot{\mathbf{r}}/s, \tag{90}$$

and

$$Q_T \ddot{s} = \sum_i m\dot{\mathbf{r}}_i^2 s - (f+1)k_B T/s, \tag{91}$$

which are respectively the adjusted equations of motion for the atoms, and thermal reservoir parameter s. The parameter Q_T is specified at the beginning of the simulation, and governs the rate at which energy is transferred between the reservoir and the atoms. When Q_T is large then the exchange is slow, while when Q_T is small the exchange is fast. Therefore, an appropriate value of Q_T must be determined for a given simulation so that the exchange is not too fast leading to radical temperature fluctuations, while fast enough to allow for a timely convergence of the system to the desired temperature.

Controlling the pressure in the system can be done following similar considerations, where instead of considering flow of energy from a thermal reservoir, one must consider the energy associated with the volume of the simulation box. This is analogous to controlling the pressure in a liquid or

a gas using a piston. Considering the energy associated with the volume of the box, a similar expression to that of Equation (91) can be derived governing the change of the box volume with time [5]. Also, once again the rate of fluctuation of the box volume is governed by a parameter, Q_p, which is analogous to the mass of a piston, and an appropriate value must be specified to ensure the system is not subjected to radical pressure fluctuations.

The basic considerations presented here to control the temperature and pressure of an MD simulation are able to be combined into a framework which simultaneously links the atomic system to multiple virtual thermal reservoirs, and systems controlling the box volume [94, 96]. These are known as a Nosé-Hoover chains, and their inclusion also helps to avoid sporadic fluctuations in the temperature and pressure of the system [95]. Also, the shape of the box can be altered to control more than just the hydrostatic pressure, but also the amount of shear stress in the system with time [101]. For the latest and most complete formulation of the theoretical framework of temperature and pressure control in MD simulations the reader is referred to the work of Shinoda, Shiga and Mikami [132].

Not all parameters of the system can be controlled simultaneously, and one must decide which conjugate variables to control. For example, the pressure and volume of the system cannot be simultaneously constant throughout a simulation, and one or the other must be chosen to be

Table 1: Table of ensemble names in MD and classical thermodynamics

MD Name	Classical Name
NVE	Microcanonical ensemble
NVT	Canonical ensemble
NPT	Isobaric-isothermal ensemble
μPT	Grand canonical ensemble

controlled. This is exactly the concept of thermodynamic ensembles in statistical mechanics. In MD simulations these ensembles are named by three characters signifying which parameters are assumed to be constant. For instance, a constant number of atoms (N), constant volume (V) and constant energy (E) is called NVE. Table 1 refers these names to the more classical names used to refer to these ensembles in statistical mechanics and thermodynamics.

5.2 Interatomic Potentials

As mentioned in the discussion surrounding Equation (81), an MD simulation relies on empirical potential energy functions to describe the interaction between atoms. This interaction does not have to only consider pairs of atoms, but also can be generalized to consider the influence of all neighboring atoms. The former interaction is called a pair potential while the latter interaction is commonly called a many-body potential. A common thread among most potentials, whether pair or many-body, is that they are composed of a repulsive term and an attractive term.

The combination of attractive and repulsive parts to build a potential

is epitomized in the Lennard-Jones (LJ) potential defined as

$$\phi_{ij}(d_{ij}) = 4\epsilon_0 \left[\left(\frac{\sigma}{d_{ij}} \right)^{12} - \left(\frac{\sigma}{d_{ij}} \right)^{6} \right], \tag{92}$$

where σ and ϵ_0 are variable parameters which determine the characteristics of the bond. Since the LJ potential is only dependent on the distance between atoms, d_{ij}, it is in fact a pair potential. The attractive part of the LJ potential is then the portion raised to the sixth power, while the repulsive part is component raised to the twelfth power. An appropriate balance of these two components is then necessary to describe the bonding in a material. While pair potentials are a good pedagogical example, it was found that they are not capable of reproducing the elastic properties of some materials. For instance, a pair potential has been shown to always follow the Cauchy relation, defined as $c_{12} = c_{44}$, where c_{12} and c_{44} are the elastic constants [51]. In fact, most metals are known to violate this relationship, and this was a driving force for developing many-body potentials.

The Embedded-atom method (EAM) potential has been shown to be one of the more robust many-body potential formulations which has been devised to describe the bonding in metals [35, 34, 52, 33]. It also has the benefit of not requiring much more computation than a pair potential. The EAM potential describes the interaction of atom i with its surrounding neighbors as

$$\phi_i = F(\sum_j \rho_j(r_i)) + \sum_{j \neq i} \Phi(d_{ij}),$$

and is composed of a many-body and pair potential part. The many-body part is contained in the embedding function $F(\rho)$, which is dependent the total electron density at the position r_i from the contributions of the surrounding neighbors, $\rho_j(r_i)$. Figure 26 depicts this embedding principle, and how the electron density from a set of neighbors is determined by the arrangement of its neighbors. The relationship then gets its name from this concept, as this portion of the potential can be thought of as the energy necessary to embed the atom i in the electron density of the surrounding atoms. Meanwhile, the pair interaction is embodied in the function Φ_{ij} which consists of an effective coulombic repulsive expression,

$$\Phi_{ij} = Z_i Z_j / d_{ij},$$

where Z_i represents the effective charge of atom i. The embedding function, $F(\rho)$, is then the attractive term of this relationship, and is also the hardest to formulate, since it cannot be directly measured. However, since the forms of the electron density and coulombic repulsion are known, a reasonable form is found assuming an appropriate equation of state for the metal. The EAM potential is then formulated assuming the Rose equation of state, which describes the energy of a metallic bond in terms of its deviation from the ideal lattice parameter by

$$E(a) = -E_{sub}(1 + a^*)e^{-a^*},$$

with E_{sub} representing the sublimation energy [121]. The reduced parameter a^* is expressed as

$$a^* = (a/a_0 - 1)/(E_{sub}/9B\Omega)^{1/2},$$

where a_0 is the equilibrium lattice constant, B is the bulk modulus, and Ω represents the equilibrium atomic volume. The embedding function is then found by fitting the potential to this equation of state, which has the benefit of being determined by only a few characteristic properties of the metal.

Besides the ability to represent the elastic properties of a material, the EAM potential can adjust itself to account for many different scenarios. This ability comes from the flexibility of the many-body term, which is dependent on the local electron density. For example, this electron density can come from atoms of different types allowing the EAM to also represent the interactions of bimetallic alloys [33]. The EAM potential is also able to adjust to change the description of the interactions for atoms near a surface or interface. The lower coordination number and electron density of atoms near a surface results in a softer bond in the EAM formulation. The EAM potential has been used in the study of some low index single crystal surfaces with qualitatively good results [33].

While it is a large step forward in the representation metallic bonding, the EAM potential has a few serious drawbacks. First, in the fitting of the potential only bulk properties are considered. Therefore, if real accurate information is desired about the surface of a material, the EAM

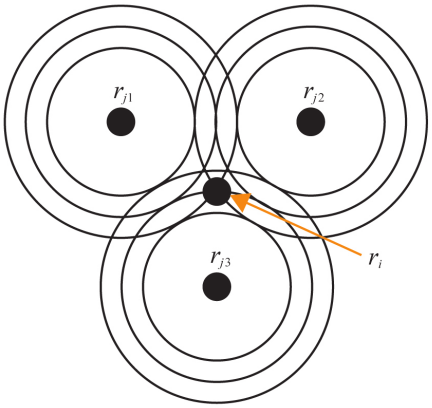

Figure 26: The embedding concept is shown as the energy of an atom is the total local electron density from its neighbors.

potential is not able to do more than mimic the general trend between elements. Secondly, the many-body interaction is formulated with spherically symmetric electron density distributions in mind. Therefore, any directional nature in a bond cannot be represented by the EAM potential.

For the reasons just described, the original formulation of the EAM potential was later adjusted by Baskes into what is known as the modified embedded-atom method (MEAM) [11]. The basis of the modifications were to allow for the possibility of directional bonding in the expressions for the electron density. This begins to allow the EAM framework to properly represent the bonding in materials like silicon. The changes to the original EAM formulation are not dramatic, as the electron density in the MEAM potential are represented by a superposition of ellipsoids. However, the precise formulation of the MEAM potential varies in the

literature, as different expressions have been tried to fix problems of inconsistencies between MEAM predictions and experimental observations [82]. For instance, it was shown that the most stable crystal structure of BCC metals was predicted by the original MEAM potential to be different than what one expects. This was found to be remedied by including a stronger second nearest neighbor interaction in the MEAM (2NN-MEAM) of the BCC metals [82, 83]. This new 2NN-MEAM formulation was also later found to be necessary to correct for problems in describing the structural stability of FCC metals at finite temperature [84]. Such problems included an inaccurate thermal expansion of the lattice and inaccurate surface reconstructions of the low index surfaces. However, it is still unclear to what extent the MEAM potential is able to accurately represent the surface structural, and thermal properties, of materials. This inconclusiveness is more due to the lack of accurate experimental data on the subject than lack of computing resources.

Other formulations of the EAM framework have also been proposed which claim to be more suited for the simulation of surfaces and small collections of atoms. The surface embedded-atom method (SEAM) was one of the first of such to be proposed. The SEAM was developed to take into account the effect of bonding near the surface more correctly as the interaction volume is allowed to change and flatten out as an atom moves toward the surface [60, 61]. While this is suited for planar single crystal surfaces, this formulation has not yet been tested in a more

general sense on high index, or curved surfaces. A more recent take on solving the shortcomings of the EAM potential for clusters of atoms is the extended embedded-atom method (XEAM) [81]. In this approach the local atomic electron density is slightly altered to introduce an element of directionality in the boding, and distinguish between different local orientation of neighboring atoms. While this approach tends to find good agreement with the density functional theory simulations which are used to fit the data, it has yet to be shown to work in a general sense and mimic the behavior of real materials.

5.3 Simulation Characterization

An MD simulation can generate an excessive amount of data, and the correct analysis of this information is as important as the proper construction of a simulation. A brief description of the how this atomic information is related to observable quantities is presented in the following section.

Perhaps the most straightforward property measurable from a simulation is the temperature of the system at a given moment in time. Temperature is related to the amount of kinetic energy of the system through the relation

$$T = \frac{2}{3}\frac{K}{Nk_B}, \tag{93}$$

where the kinetic energy, K, is calculated by Equation (80), N represents the number of atoms in the simulation and k_B is the Boltzmann constant.

The atomic positions can be used to study the correlations in the distances between atoms in the simulation. One such function called the radial distribution function (RDF) measures the relative fluctuations in the atom density of the system. The RDF is calculated by counting the number of atoms contained within a spherical shell of radius d, where the center of the sphere is an atom in the simulation. The result is averaged over the system by considering all atoms as the center of the sphere. and normalized to the number of atoms expected at that distance assuming a uniform atomic density. The RDF can then be expressed as

$$g(d) = \frac{m(d)}{NV_s\rho_0} \tag{94}$$

where $m(d)$ is the total number of atomic pairs at a distance d, V_s is the volume of the spherical shell (expressible as $4\pi d^2\Delta_d$), and ρ_0 is the average atomic density of the system defined as N/V, with V being the volume of the simulation box. Another function commonly defined as a measure of atomic structure is called the pair distribution function (PDF). This function then gives the average number of atomic pairs at a distance d, and is found by the relationship

$$p(d) = \frac{m(d)}{N\Delta_d}. \tag{95}$$

The structural information in these distribution functions is the fundamental property of a system which determines its powder diffraction pattern. In fact, the quantity $m(d)$ can be directly used in the Debye

function to calculate the powder pattern. Then assuming that the system is composed of only one type of atom, the powder pattern intensity is related to the PDF and RDF by the expressions

$$\begin{aligned} I(s) &= k(s)f^2(s)\sum_d m(d)\frac{\sin(2\pi sd)}{2\pi sd}, & (96)\\ &= k(s)f^2(s)N\Delta_d\sum_d p(d)\frac{\sin(2\pi sd)}{2\pi sd}, & (97)\\ &= k(s)f^2(s)N\rho_0\sum_d V_s g(d)\frac{\sin(2\pi sd)}{2\pi sd}, & (98)\\ &= \frac{2f^2(s)\rho_0}{s}\sum_d dg(d)\sin(2\pi sd)\Delta_d, & (99) \end{aligned}$$

which can also be expressed as the sine transform of $dg(d)$ assuming $\Delta_d \to 0$. This expression of the final relation in Equation (96) as an integral is the basis of the analysis of Total Scattering methods in diffraction [41].

If the simulation is conducted at a finite temperature, then the atoms are vibrating around a mean position as a function of time. The structure of these vibrations can also be studied by calculating the velocity auto-correlation function (VAF). This relationship measures the rate at which the velocity of the atoms is changing, and is useful in obtaining information on the phonon structure present in the simulation. The VAF for atom j is defined as

$$c_j(\Delta t) = \langle \mathbf{v}_j(t_0) \cdot \mathbf{v}_j(t_0 + \Delta t) \rangle \quad (100)$$

where the brackets $\langle ... \rangle$ denote an average over all initial times, t_0, in the simulation. This function is related to the vibrational density of states

(VDOS) through the Fourier transform defined as

$$\Gamma(\omega) = \frac{1}{k_B T} \int \sum_j m_j c_j(t) \exp(-i\omega t) \mathrm{d}t, \tag{101}$$

where m_j is the mass of atom j.

The forces between atoms also give information on the stresses in the system. However, the fundamental limitation to defining stress in an MD simulation is that one cannot think in terms of a continuum, which is defined at every point in the volume, but instead considers an atomic system, which is defined at discrete points in space. Therefore, the stress in an MD simulation can be calculated in a few slightly different forms, and it is important to specify the exact definition being used. In the present study the common definition was employed, which gives a component of the 3-dimensional stress tensor of the system for a pair potential as

$$\sigma_{ij} = -\frac{1}{V} \left(\sum_\alpha m_\alpha v_{\alpha,i} v_{\alpha,j} + \frac{1}{2} \sum_\alpha \sum_{\beta \neq \alpha} F_{\alpha\beta,i} d_{\alpha\beta,j} \right), \tag{102}$$

where $v_{\alpha,i}$ represents the i-th component of the velocity vector of atom α, similarly $F_{\alpha\beta,i}$ is the i-th component of the force vector between atom α and β, and $d_{\alpha\beta,j}$ the j-th component of the distance vector between the atoms. The first term in Equation (102) is a kinetic term accounting for the energy of the atoms associated with thermal motion, while the second term is called the virial stress and dominates the value of the stress tensor at low temperatures. When many-body potentials are used then the stress tensor can be expanded accordingly. The pressure of the

system is then related to the trace of the stress tensor, $P = -\mathrm{Tr}(\sigma)/3$, resulting in the expression

$$P = Nk_BT + \frac{1}{3V}\sum_{\alpha}\sum_{\beta\neq\alpha}\mathbf{F}_{\alpha\beta}\cdot\mathbf{d}_{\alpha\beta}, \tag{103}$$

where the kinetic energy term is now expressed in terms of the system temperature.

5.4 Nanoparticle Simulation Review

The small size of nanoparticles makes them an ideal case to study using MD simulations. Early simulations of nanoparticles were focused on atomic clusters consisting of no more than 1000 atoms, and having a size around 1 nm. MD simulations were used to find the atomic configurations which resulted in the minimum energy state of the cluster. At this size the minimum energy state is no longer the atomic lattice, and finding the most stable atomic configuration required inventive genetic algorithms to search the many possibilities of the cluster description [164]. These algorithms were able to solve the atomic configurations of the "magic number" clusters which are more likely to be exist in nature due to their closed-shell electronic structure.

Work on slightly larger nanoparticles (D = 1 - 10 nm) has been largely focused on also determining the stable structure of the isolated nanoparticles. In this size range it was again found that the bulk atomic lattice is not necessarily the most stable structure, and particles were found to exist which contain an intersecting network of twin boundaries [91]. These

types of particles are commonly referred to as multiple twin particles (MTPs), and often contain a characteristic five-fold symmetry axis. The more widely observed examples of MTPs are icosahedral and decahedral particles, which are schematically depicted in Figure 27. These MTPs cannot grow to be very large as the stacking fault energy associated with the multiple twin planes will cause the configuration to be unstable. Then MD simulations have been carried out which try to predict the particle size ranges where MTPs become a more stable configuration than a particle made of the bulk atomic lattice. This is in an effort to create a size-dependent phase diagram for most transition metals which describes the thermodynamically stable structure of nanoparticles of different sizes [10].

A few different approaches have been proposed for studying the size-dependent structure of nanoparticles. The first approach consists of starting from a melted state of the metal and then rapidly cooling the system, or quenching, to a lower temperature [26, 27, 28, 66, 131]. The atomic positions in the resulting particle are then analyzed to characterize the particle structure. While this approach properly considers any relaxation and restructuring of the atoms near the surface, it is somewhat unrealistic as the slowest quench rate which is achievable in an MD simulation is still orders of magnitude faster than what can be achieved in practice. Furthermore, a recent study has found that the resulting structure can be dependent on the quench rate assumed in the MD simulation [27].

Another approach to predict the minimum energy structure is by constructing a series of particles of different size and shape, calculating the corresponding energies, and comparing the energy curves as a function of particle size [7, 8, 28, 30, 29, 31, 66]. These curves are then used to map the expected phase diagram of nanoparticles from the structure resulting in the lowest energy. While this method can give an idea of the most stable structure, it is really only the most stable of the configurations which are envisioned to be correct. The most stable atomic configuration might be something which was not considered at the outset of the study. Furthermore, the study of the minimum energy state is only applicable to the describing the system at a temperature of 0K. The addition of thermal energy can mean that the stable particle configuration may well be another atomic structure, or result in a equal likelihood of many different atomic structures. Finally, while MD simulations begin to offer a suggestion of the stable atomic configuration it should always be kept in mind that this is really only in terms of the interatomic potential is used and the corresponding assumptions of how the bonding in the particle is described [27]. The simplified vision of bonding described by MD simulations may be manifested in a different sense as the particle size decreases to the nanoscale.

Until recently most MD simulations of nanoparticles have been minimum energy structural studies trying to determine whether the atomic lattice, or some MTP description is more stable. A few notable exceptions

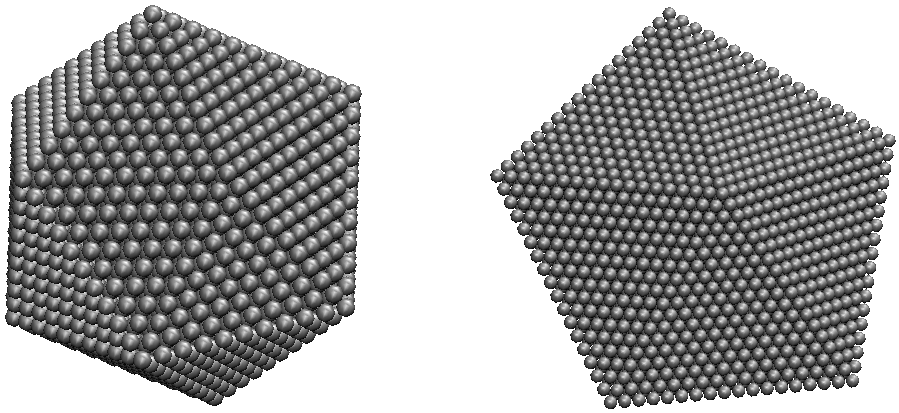

Figure 27: Figure of icosahedral and decahedral particles

include those simulations which have been already mentioned in Section 2.3 regarding their contribution to diffraction studies. Many nanoparticles are synthesized with a surfactant which bonds to the surface of the particle and limits their growth and agglomeration. The studies of Landman were some of the first to consider the influence of this interaction in their MD simulations of Au nanoparticles capped by an alkylthiol surfactant [89]. This chemical then makes an Au-S bond on the surface of a nanoparticle which will change the surface energetics of the nanoparticle. Luedke and Landman conducted a rather thorough investigation of the resulting structure and dynamics of the encapsulated nanoparticle and were able to identify likely bonding sites of the alkylthiol on the surface of the Au nanoparticle. Simulations of this kind can give great insight into the role of surfactants in the nucleation and growth mechanisms of nanoparticles. In this direction the simulations of Gilbert et al. are also significant contributions [55, 57]. Gilbert and co-workers have simulated

the structure and dynamics of nanoparticles which are dispersed in a solvent like water. The important interaction of the particle and the solvent is commonly overlooked, or ignored, in simulation studies. Their simulations have been able to explain the solvent dependent phase stability, and transformations, of TiO_2, and ZnS nanoparticles. These simulations show the importance of properly considering the interactions on the surface of nanoparticles is necessary before comparison with experimental measurements is possible.

CHAPTER VI

POWDER DIFFRACTION FROM SYSTEMS OF CRYSTALLITES

In describing the diffraction pattern from materials we have so far only considered the case where the crystallites in a material can be treated as independent scatterers. This means only considering the interference of x-rays which have scattered within a single crystallite, or the contribution of *intra-crystallite scattering* to the diffraction pattern. This ignores the interference of scattered waves originating from different crystallites in the material, what we will refer to as *inter-crystallite scattering*. When two crystallites in a material are not positioned, or oriented, in a regular fashion, the lack of order, or coherency, results in the inter-crystallite intensity summing to zero in the wide-angle regime. This then allows for the their treatment as independent scatterers. However, it is not entirely clear to what extent crystallites must be misoriented to satisfy this claim, and what observable effects ordering might have on the wide-angle powder pattern. The following chapter will begin to explore these questions by applying the Debye function calculation to systems of multiple crystallites.

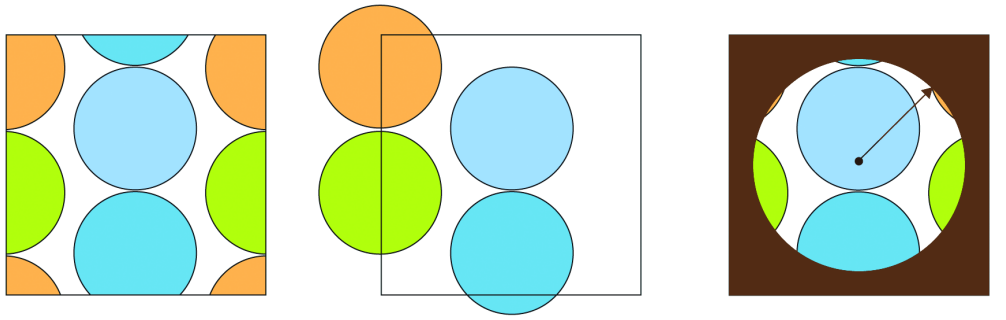

Figure 28: The view of a crystallite system in terms of the different techniques to simulate the diffraction pattern are shown.

In simulating a system of multiple crystallites, a more practical question arises concerning how many crystallites are necessary to obtain a representative diffraction pattern. This consideration is gaining importance as the Debye function is increasingly applied to generate the diffraction pattern from polycrystalline atomic simulations [17, 40]. Therefore, a parallel topic throughout the following chapter will be the study the size of the simulation necessary to achieve a reliable diffraction pattern.

6.1 Calculating the powder diffraction pattern from systems of crystallites

Often in the generation of a system of crystallites, or microstructures, periodic boundary conditions (PBCs) are necessary for more realistic simulations of a computationally reasonable size. However, as already discussed, improperly calculating the diffraction pattern from such a system can result in artifacts, due to the cutting of the domains by the

boundaries, and the new periodic order possible in the system. Then the first challenge when simulating a system of multiple crystallites is how to properly consider the finite size of the simulation space, and avoid any artifacts due to the use of periodic boundary conditions in the simulation box. Two slightly different methods exist for solving this problem, and calculating the diffraction pattern from a system of multiple crystallites.

The first, which we will refer to as the crystallite reconstruction (CR) method, uses the PBCs to reconstruct crystallites which are cut by the boundaries. As shown in the example of Figure 28, in the reconstruction only one copy of a crystallite is allowed, so a decision must be made as to the position of the crystallite relative to the box. In the present study the crystallites were reconstructed on the side of the box corresponding to the crystallite center of mass. The diffraction pattern is then calculated by applying the Debye function of Equation (24), but slightly reformulating it as

$$I_P(s) = k(s)f^2(s)\sum_d m(d)\mathrm{sinc}\left(2\pi sd\right), \tag{104}$$

where all of the distances of the same length have been tabulated into $m(d)$, which is then the multiplicity of the distance d_i, and $k(s)$ is a function representing the constants and factors in front of Equation (24). As shown in Section 5.3, the multiplicity function is related to the PDF, $p(d)$, or the RDF, $g(d)$, by $m(d) = Np(d)\Delta_d$ and $m(d) = 4\pi d^2 N\Delta_d\rho_0 g(d)$ respectively. As will be shown in Section 6.2.2, the finite size of the reconstructed system will result in features in the small-angle regime of

the simulated pattern.

The use of this method to calculate the diffraction pattern allows for the easy separation of the inter-crystallite and intra-crystallite contributions to the total intensity. Following the same reasoning which lead to Equation (17), the powder intensity from a system of crystallites can be expressed as

$$I_P(s) = k(s)f^2(s)\left(\sum_M I_M + \sum_M \sum_{M\neq N} I_{MN}\right), \tag{105}$$

where I_M is the intensity scattered from the M-th crystallite, and I_{MN} is the intensity from the interference of waves which have scattered from the different M-th and N-th crystallites. The first summation is then the intra-crystallite contribution, while the cross summation amounts to the inter-crystallite contribution. In both cases the intensity takes the form of Equation (104), with the difference of course being whether the distance is considered between atoms in the same crystallite or not. Effectiveness of the independent scatterer assumption can then be assessed by studying the inter-crystallite intensity.

The second method of calculating the diffraction pattern from periodic systems of multiple crystallites consists of assuming that at some distance from an atom, any ordered structure of a material is lost. In this case, the long range structure can be considered homogeneous, and the PDF is approximated as

$$p(d) = 4\pi d^2 \rho_0, \tag{106}$$

which is found from integrating the average atomic density, ρ_0, on the surface of a sphere of radius d. A cartoon exhibiting how this treatment relates to the initial PBC microstructure is depicted in Figure 28. Then for each atom in the system, the interatomic distances only need to be calculated to the critical distance, r_c, which defines the transition to the homogeneous regime, and the intensity is given by

$$I_P(s) = k(s)f^2(s)\left(N + \sum_{d>0}^{r_c} m(d)\mathrm{sinc}\left(2\pi s d\right) + N4\pi\rho_0 \sum_{d>r_c}^{\infty} d^2 \mathrm{sinc}\left(2\pi s d\right)\Delta_d\right). \tag{107}$$

The second summation can be expressed as an integral with the following solution

$$N4\pi\rho_0 \int_{r_c}^{\infty} r^2 \mathrm{sinc}\left(2\pi s r\right) \mathrm{d}r = N4\pi\rho_0 \left(\frac{r_c \cos(2\pi s r_c)}{(2\pi s)^2} - \frac{\sin(2\pi s r_c)}{(2\pi s)^3}\right). \tag{108}$$

Therefore, the homogeneous approximation (HA) intensity [40] is given by

$$I_P(s) = k(s)f^2(s)\left[N + \sum_{d>0}^{r_c} m(d)\mathrm{sinc}\left(2\pi s d\right) + N4\pi\rho_0\left(\frac{r_c \cos(2\pi s r_c)}{(2\pi s)^2} - \frac{\sin(2\pi s r_c)}{(2\pi s)^3}\right)\right]. \tag{109}$$

The benefit of the HA method is that it does not require any reconstruction of the atomic positions to evaluate the intensity, as the PBCs are used in the calculation of the interatomic distances. However, it is only valid for systems which can be said to be homogeneous in the long

range limit, and is therefore not applicable to any systems which exhibit long range order. One important step when using Equation (109) is determining the appropriate critical distance, r_c, which separates the structured and homogeneous regimes. In most cases, this can be defined by studying a precalculated PDF, and determining when it can be approximated by Equation (106). However, again the case of periodic boundaries must be carefully considered as r_c must be smaller than the simulation size. Finally, it should not be disregarded that the integration of Equation (108) neglects the influence of absorption as it extends to infinity. The full implications of this approximation on the calculated intensity are still unclear. Nonetheless, the HA intensity has the desirable quality that it masks the finite size of the simulation box. This will be shown to be effective in the simulation of the small-angle pattern from a system of densely packed particles as it results in clear features from the particle configuration.

The HA method can also require less computational power than the CR method. In the CR method the number of computations required always scales as N^2. However, this factor is less for the HA method as the number of distances to calculate is related to the smaller volume defined by r_c. However, as already discussed, the HA method requires some precalculation of the PDF for the proper determination of r_c, and with current understanding of the technique, further trial and error can be necessary to find the best value of r_c which produces a reliable diffraction

pattern. This increases the computational demands calculating the HA intensity, and may result in the HA method costing the same amount of computational resources as the CR method.

6.2 Patterns from Random packing of spheres

In the present study we will use different packing of spherical crystallites to study the influence of inter-crystallite scattering on the powder diffraction pattern. While this is a crude representation of a microstructure, it embodies the features which are of interest to us as the positions and orientations of the crystallites are able to be controlled. The simulated systems also allow for some insight into the effects of inter-crystallite scattering on the small-angle pattern from densely packed systems.

6.2.1 Particle system generation

To represent a system where no ordering existed in the microstructure, a method of packing the spherical crystallites to a specified density was devised. This method follows the considerations of random hard-sphere packing which has been developed for densification studies of granular materials, as well as, to simulate the structure of amorphous glasses [73, 76, 143].

The algorithm begins by creating the population of the particles in a system. Given the number of particles, N, and the size distribution, $g(D)$, the number of particles in the population of a given size, $n(D)$, is

found to be

$$n(D) = Ng(D)\Delta_D, \tag{110}$$

where Δ_D is the sampling interval of the size distribution — analogous to that defined in Section 3.3.1. A volume of free space is then created considering the desired packing density, ρ, which is defined as the ratio of the volume of the particles to the total simulation volume. The simulation space is defined as a cube whose volume is given by

$$V_{box} = \frac{\sum_D n(D)V(D)}{\rho}, \tag{111}$$

where $V(D)$ is the volume of a particle of size D. With the simulation box created, the center of each particle is assigned an initial random position in the box. In this initial configuration it is likely that some particles are too close and have an overlapping volume.

An iterative approach roughly based on Monte-Carlo methods was used for finding the separated particle positions. During this repositioning routine, PBCs were assumed for the simulation box to avoid impingement of particles by the box boundaries. In an iteration, if two spheres are found to be overlapping, then the particles are slightly separated by a random distance which is bounded by a maximum displacement. This maximum displacement is adjusted throughout the course of the separation routine by trying to keep the fraction of particle displacements which result in successful particle separation equal to 0.5 [5]. Once all particles have been separated the routine stops, and the periodic boundary conditions of the box can be removed depending on the pattern simulation

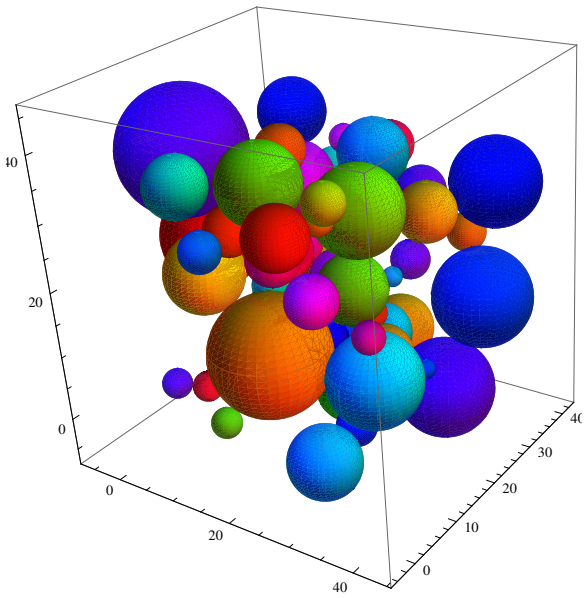

Figure 29: A constructed particle system particle system of a log normal size distribution and a packing density of 0.5 is depicted.

technique. Figure 29 depicts an example of a resulting particle system containing 64 spheres representing a log normal size distribution with a packing density of 0.5.

With the particle system initialized, atoms are filled into the crystallites. The orientation of the atomic lattice in each particle with respect to the reference frame of the box is specified by a set of Euler angles. For the case of a randomly oriented system, this set of angles was randomly chosen for each particle. The position of the atom i in the box is then described in terms of the position and orientation of particle M, to which it belongs, following

$$\mathbf{r}_i' = \mathbf{x}_M + \mathbf{R}_M \mathbf{r}_i, \tag{112}$$

where $\mathbf{x}_M$and $\mathbf{r}_i$are the positions of the particle, and atom position, in the reference frame of the practical respectively, and $\mathbf{R}_M$ is the orientation matrix defined in terms of the Bunge-Euler angles (ϕ_1, ψ, ϕ_2) as

$$\mathbf{R}_M = \begin{pmatrix} \cos\phi_1 \cos\phi_2 - \sin\phi_1 \sin\phi_2 \cos\psi & \sin\phi_1 \cos\phi_2 + \cos\phi_1 \sin\phi_2 \cos\psi & \sin\phi_2 \sin\psi \\ -\cos\phi_1 \sin\phi_2 - \sin\phi_1 \cos\phi_2 \cos\psi & \cos\phi_1 \cos\phi_2 \cos\psi - \sin\phi_1 \sin\phi_2 & \cos\phi_2 \sin\psi \\ \sin\phi_1 \sin\psi & -\cos\phi_1 \sin\psi & \cos\psi \end{pmatrix}. \tag{113}$$

With the atomic positions initialized the diffraction pattern can be calculated following either the CR, or HA methods previously described in Section 6.1.

For large simulation systems of defect free particles, the large amount of memory required to store all of the atomic coordinates can be avoided by expressing these distances in terms of the reference frame of a given particle. In the reference frame of the box, the distance between atom i and atom j is expressed as

$$\mathbf{d}_{ij} = \mathbf{r}_i' - \mathbf{r}_j' = \mathbf{x}_M + \mathbf{R}_M \mathbf{r}_i - (\mathbf{x}_N + \mathbf{R}_N \mathbf{r}_j) \tag{114}$$

Transforming this into the reference frame of particle M, the distance vector is found to be

$$\mathbf{R}_M^{-1} \mathbf{d}_{ij} = \mathbf{R}_M^{-1} \left[(\mathbf{x}_M - \mathbf{x}_M) - \mathbf{R}_N \mathbf{r}_j \right] + \mathbf{r}_i. \tag{115}$$

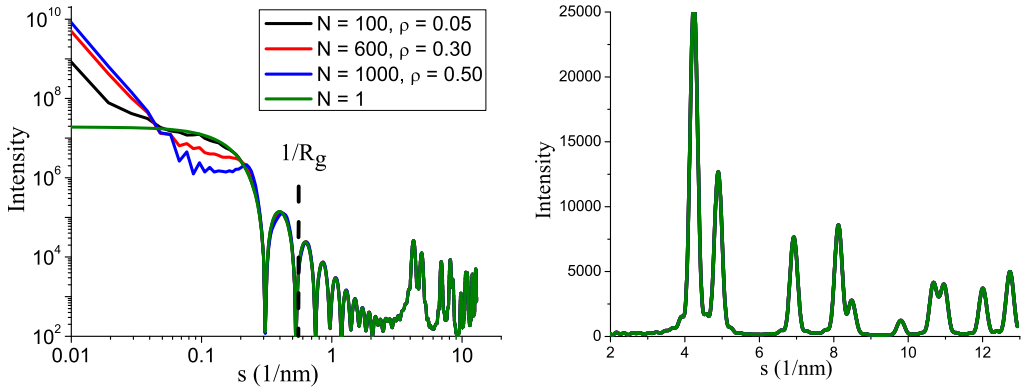

Figure 30: The patterns calculated by the crystallite reconstruction method for different systems of crystallites with a diameter of 4.6nm are compared.

Since in the powder pattern one is only concerned with the magnitude of this distance, the relation in Equation (115) will give an equivalent result. The memory necessary to describe the particle system is then only governed by the number of atomic positions within the largest particle.

6.2.2 Study of patterns from monodisperse systems

Systems of randomly packed particles, each having the same diameter, were generated following the routine described in Section 6.2.1 to study the diffraction patterns found from assuming the CR and HA methods. In this section, all particles were filled with a defect-free Au lattice ($a = 4.0809$Å), and random orientations were assigned to simulate a powder. Also, the patterns were simulated assuming polarized radiation with a wavelength of 1.54056 Å (Cu Kα_1).

The CR patterns from systems of particles having a diameter of 4.6nm

are depicted in Figure 30. They show that changing the characteristics of such a particle system only influences the small-angle regime of the calculated intensity. Changing the number of particles in the simulation has the effect of increasing the value of the intensity at $s = 0$, as expected considering that this value is found from Equation (24) to be $f^2(0)N^2$, where N is here the number of atoms in the system. From this point on the y-axis, the intensity decreases, following different trends which all eventually converge to the pattern from an isolated particle. The observed features in this region of the diffraction pattern are attributed to the effects of the auto-correlation of the system as a whole, as well as, the structure of the particles in the system. The autocorrelation largely determines the observed intensity near $s = 0$, while the features of the particle structure factor are seen in the region of the pattern where the intensity begins to resemble that from a single particle. For instance, by increasing the packing density of the simulated system, the intensity is found to dip below that from an isolated particle in the region around s of 0.1 nm^{-1}, even leading the slight formation of a peak at $s = 0.2$ nm^{-1} for the rather high packing density of 0.5. The existence of this peak is evidence that the generated particle system is beginning to become more ordered as it approaches the dense packing limit of 0.74 for a monodisperse system. The wide-angle pattern is found to be identical, and independent of the constructed system. This is further evidence that the assumption of independently scattering crystallites is completely

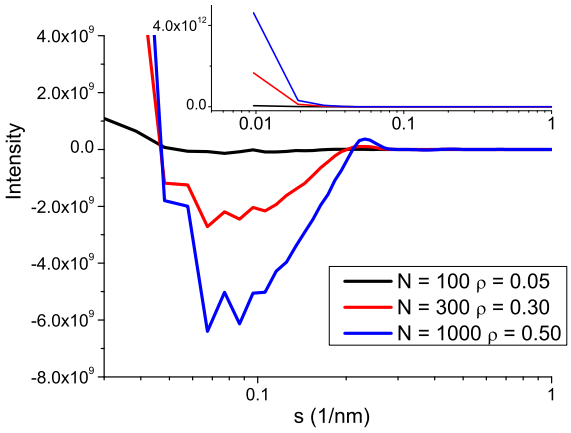

Figure 31: The inter-particle scattering contributions to the patterns calculated in Figure 30 are shown.

warranted when considering a powder.

Further credence for this claim is garnered by studying the contribution of inter-crystallite scattering to the patterns of Figure 30 This intensity is shown in Figure 31, and has been calculated from considering Equation (105). The inset of Figure 31 again shows how the size of the system is reflected in the intercept of the inter-crystallite intensity. The figure also demonstrates that the features attributed to the structure of the particle system are really coming from this inter-crystallite contribution to the intensity. Even the peak at 0.2 nm^{-1} is observed in the pattern found from the system with a packing density of 0.50. Finally, the inter-crystallite intensity is found to converge to zero for larger values of s. Therefore, the disorder in the simulated powder system was enough that the wide-angle intensity can be safely treated as if each crystallite scattered independently.

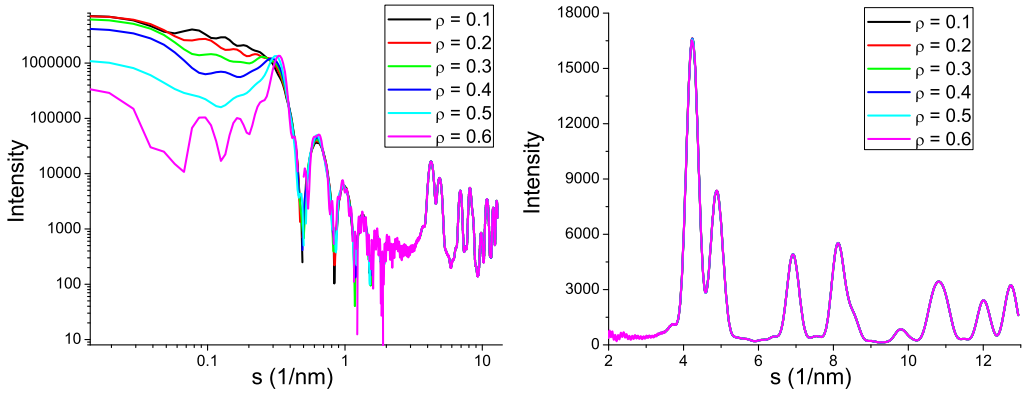

Figure 32: Patterns calculated by the homogeneous approximation from systems of 2000 particles with a diameter of 3nm are shown.

The same method creating a system of particles was also used to generate arrangements of particles for the calculation of the HA intensity described by Equation (109). In this case the particles were assumed to have a slightly smaller diameter of 3nm. The diffraction patterns resulting from this approach for a series of increasing packing densities are depicted in Figure 32. In the calculation, the maximum possible $r_c$was assumed — which is $L/2$, where L is the side length of the box. The intensities depicted in Figure 32 again find that the crystallite configuration only influences the small-angle regime. The striking feature of the calculated HA intensities is the clear emergence of a peak around 0.3 nm^{-1} as the packing density is increased. As in the case of the CR patterns, this peak is the result of the structuring into a more ordered system, however, it is much more evident in the HA calculated intensity. Further inspection finds that its position shifts to higher values of s with

increasing packing density. This trend is consistent with the consideration that a system of particles which is more densely packed, will have particles which are on average closer to one another. Also, the features observed in the HA patterns are in good agreement with those expected from a system of spheres having a hard-sphere interaction [59]. Furthermore, it is again found that the wide-angle patterns in Figure 32 are the same, and in agreement with that from an isolated sphere of the same size. The ability of the HA method to clearly depict features in both the wide-angle and small-angle, offers a lot of interesting possibilities to combine the refinement of patterns measured in the two regimes.

6.3 Critical system size of polydisperse systems

The reliability of the calculated diffraction pattern is related to how well the simulated system represents the real system. Since the size of a simulation is limited, it is important to understand the critical number of particles necessary for the simulated system to statistically resemble reality and produce a representative diffraction pattern. This critical size will be shown to be related to the degree of polydispersity in the system, where polydispersity can be defined in a general sense as the diversity of the objects in a collection. The cases of polydisperse systems describing different size distributions and defect densities will be considered in the following discussion.

6.3.1 Particle Size Distribution

It is already apparent from the patterns presented in Section 6.2.2, that one particle is sufficient to simulate the wide-angle pattern from a randomly oriented, monodisperse system. It is then desirable to determine what this critical system size, N_c, is for different log normal size distributions. The number of particles of each size in a simulated system was determined using Equation (110), with the log normal distribution defined as in Equation (69). A comparison of the distribution which is given by Equation (110) and the continuous log normal distribution is depicted in Figure 33. The volumetric moment and standard deviation of a log normal distribution, defined as

$$< D >_V = 3 \exp\left(M + 7S/2\right)/4, \tag{116}$$

and

$$\sigma = \left\{ \left[\exp(S^2) - 1 \right] \exp\left(2M + S^2\right) \right\}^{1/2} \tag{117}$$

respectively, were used to characterize a given distribution. The patterns from systems containing multiple particles (MP), were then compared to the wide-angle patterns simulated from the isolated particle (IP) approach described in Section 3.3.1, which arrives at the intensity by appropriately weighting the intensity from a particle of a given size.

Figure 34 depicts the how the patterns simulated from systems having $< D >_V$ of 4.6nm but different standard deviations converge to the IP pattern as N is increased. The qualitative trends describing the influence

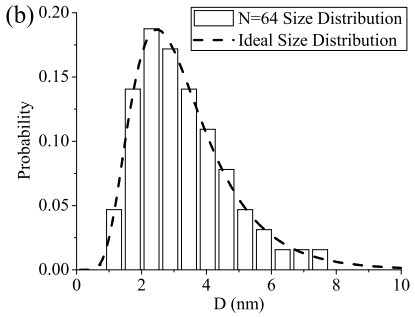

Figure 33: The size distribution which is generated in a constructed system is compared to the desired log normal distribution function.

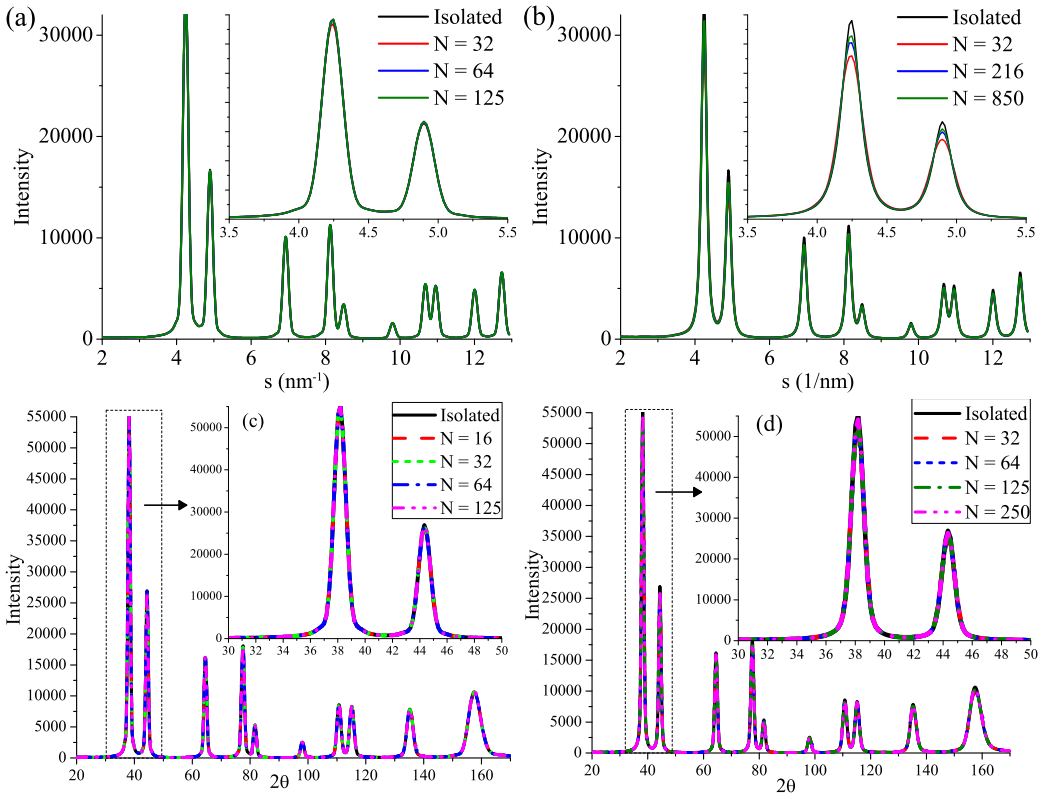

Figure 34: The simulated patterns from systems having a size distribution characterized by (a) $< D >_V$=4.6nm σ = 0.90nm, (b) $< D >_V$=4.6nm σ = 1.59nm, (c) $< D >_V$=7.5nm σ = 1.42nm, and (d) $< D >_V$=7.5nm σ = 2.10nm are shown.

of polydispersity on N_c is apparent from just considering these two cases. The MP patterns, shown in Figure 34(a) for systems with a narrower size distribution, find a match with the IP pattern for a much smaller simulation size of 125 particles, while the patterns from a broader size distribution in Figure 34(b) requires a much larger number of particles. If we consider the breadth of the size distribution as a measure of the polydispersity, it is apparent that N_c must increase with the amount of polydispersity in the system. This trend was also observed in the patterns from systems having a larger average particle size, as in Figure 34(c) and 34(d).

To obtain a more quantitative estimate of N_c, the value of χ^2 between the MP and IP wide-angle patterns was calculated according to

$$\chi^2 = \left\{ \sum_s \frac{1}{I_{IP}(s)} \left[I_{MP}(s) - I_{IP}(s) \right]^2 / n \right\}^{1/2}, \qquad (118)$$

where n is the number of intensity points considered. In this context the wide-angle pattern was defined as the scattering vector, s, range between 2 and 13 nm^{-1}, composed of about 900 points. The N_c was then defined as the minimum number of particles necessary for $\chi^2 \leq 1$. The variation of χ^2 with the particle population, N, is shown in Figure 35(a) for four different distributions — each having $< D >_V$ of 4.6nm, but different standard deviations. It is evident that the rate of convergence of the MP pattern to the IP pattern is somehow related to σ. However, the study of other systems with different mean sizes shows that N_c is not determined

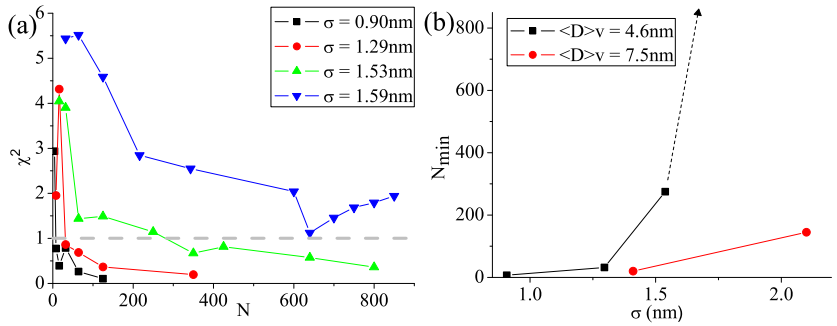

Figure 35: The trends of χ^2 versus the particle number of crystallites in the system is depicted for the for the size distributions considered. The dotted line shows an approximation of N_c for the distribution having $< D >_V = 4.6$nm and $\sigma = 1.59$nm, as the real value N_c was larger than the maximum particle population possible.

by σ alone. The N_c obtained for a series of size distributions having a mean size 4.6nm and 7.5nm are plotted in Figure 35(b). This figure shows that the N_c for a log normal distributions is also related to the average particle size. Further tests are required to develop a better model which might allow for the prediction of N_c. However, the aforementioned trend has been further demonstrated as N_c increases with the width of the size distribution, or polydispersity, in the system.

The cause for the discrepancy between the MP and IP patterns is the difference in the actual size distribution present in a system, and the ideal size distribution. As shown in Figure 33 this difference is primarily exhibited in the abundance of the larger particles in the tail of a broad distribution. Since $n(D)$ is restricted to integer values, then $g(D)_{MP} = n(D)/N\Delta_D$ will be a poor approximation to $g(D)$ from Equation (69) when N is small. Furthermore, diffraction is a volume weighted

measurement, therefore, small discrepancies in the large particle tail of the two distributions will be magnified in the diffraction pattern.

6.3.2 Particles Containing Defects

Polydispersity can also be realized in a system in the form of local differences in atomic density, or defect densities. To investigate the influence of such characteristics, systems of crystallites were created containing varying densities of stacking faults. In order to focus on the effect of polydispersity due to faulting, systems were simulated with particles of the same size. Either twin faults, or deformation faults, were created during the particle construction by disrupting the {111} planar ordering accordingly. The fault probability of a system was defined as the ratio between the number of fault planes, and the total number of (111) planes in the system patterns. This definition follows the conventional terminology describing the effect of faulting on close packed planes in LPA [103, 153]. A slight discrepancy is expected between the fault probability created in the simulated particle systems and the value obtained from LPA, since the LPA theory assumes that all faults have an equal surface area — which cannot be true for faults at different positions in a spherical particle. Each fault in the particle system was randomly assigned to a particle, a different {111} plane, and a different position in the particle. Some resulting patterns for systems with different densities of deformation faults, α, and twin faults, β, are depicted in Figure 36(a). The diffraction pattern range depicted in the inset of Figure 36(a) shows

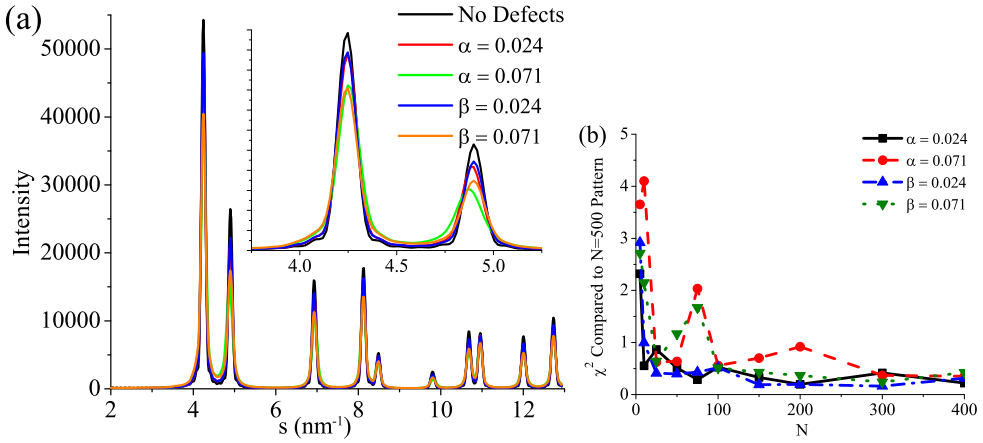

Figure 36: The patterns from systems containing faults and the trends of χ^2 are depicted.

that the pattern from a system containing deformation faults exhibits a pronounced shift of the 200 peak to smaller angle while the patterns from a system containing twin faults primarily shows broadening. These features are consistent with the expected effects on the powder pattern [155], and are evidence that the effects of faulting are still observable in powder patterns from small crystallites.

As in study of polydispersity due to different particle sizes presented in Section 6.3.1, the diffraction patterns from systems containing an increasing number of particles were compared with a reference pattern to determine N_c. However, a simple weighting scheme to simulate the diffraction pattern by IP methods does not exist. Therefore, in calculating χ^2, an MP reference pattern was used coming from a sufficiently large system, which was determined to be 500 particles. The trend of χ^2 as a function of the particle population depicted in Figure 36(b) shows

that systems with a higher probability of faults require a larger number of particles in order to reach the convergence threshold ($\chi^2 \leq 1$). Assuming that a slightly larger faulting density allows for more possibilities of faulting arrangements in a particle, this observation is consistent with the previously described trend that increased polydispersity requires a larger simulation size to generate a reliable diffraction pattern. Furthermore, it shows that N_c is not solely dependent on the particle size distribution, but also characteristics like the defect population.

6.4 Ordering and coherency

In recent literature it has been proposed that powder diffraction peak broadening is not only affected by crystallite size and strain, but also by the scattering from neighboring crystallites which are "coherently" ordered [111]. This phenomenon has been observed in the diffraction patterns from thin films [110], micro-dot arrays [109] and has even been used to explain uncharacteristic broadening observed in the pattern from ball milled nanocrystalline fluorides [114]. Two criteria exist for two crystallites to be said to be coherently ordered:

- the lattice orientations of the crystallites should differ by a small amount, and
- long range structure should exist in their crystallite positions.

Then, the presence of ordered crystallites in the case of thin films may be reasoned by evolutionary grain growth and interactions with the substrate during the thin film synthesis. However, it is unclear if this event can occur in ball-milled nanocrystalline materials as it is uncertain the degree which neighboring crystallites have similar lattice orientations, and more importantly, it is unlikely that regularity exists in their crystallite positions. Without delving into the physical mechanisms necessary to create such a microstructure, we will approach the question by assuming that such a microstructure can exist, and then study the wide-angle powder diffraction pattern from a many particle system as a function of each criterion for coherent ordering.

First, to study the influence of the lattice orientation, the particle positions from a loosely packed system were used. However, instead of assigning a random orientation to all particles, a certain number of particles were oriented such that the coordinate axes of the particle lattice were aligned with that of the simulation box. The term *coherency probability* is then defined as the percentage of particles in the system which were initialized with the same lattice orientation. In the cases of systems having a coherency probability less than one, the remaining particles in the system were initialized with a random lattice orientation.

The wide-angle patterns from 27 identical particles ($D = 4.6$nm) with a rather dense packing of 0.5 and containing different coherency probabilities are shown in Figure 37(a). The simulations with a lower

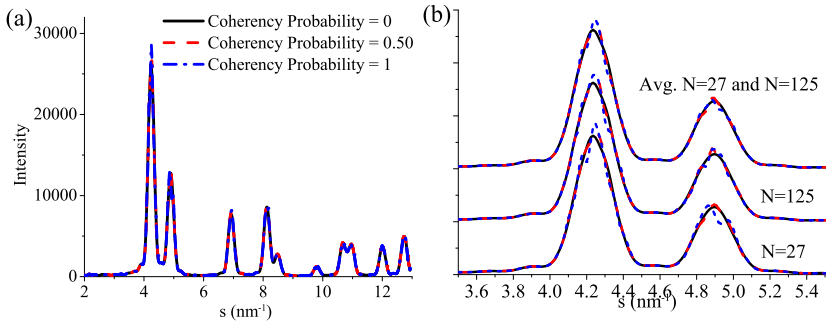

Figure 37: Patterns corresponding to randomly packed systems of differing (a) coherency probability and (b) coherency domain sizes are shown.

coherency probability of 0.5 model materials which have coherently oriented crystallites randomly interspersed in the microstructure. It is seen from Figures 37(a) and 37(b) that the diffraction pattern from this type of a system does not exhibit any noticeable signs of coherency as the pattern does not differ from that of a randomly oriented system. A distortion of the peak shape was only observed when the coherency probability approached unity, as seen in the slight narrowing and distortion of the 111 and 200 peaks from the 27 particle system in Figure 37(b). A peak narrowing at low angles is predicted by the theory of Rafaja [111], but the effect simulated here is much more subtle than what was observed by Ribarik, et al. in nanocrystalline fluorides [114].

Larger coherent systems consisting of more than 100 particles were also simulated to study how the coherently oriented volume, referred to as the *coherent domain size*, affects the diffraction peak shape. As the coherent domain size was increased to 125 particles, the effect of coherency on the pattern seen in Figure 37(b) is even further diminished. If regions

of coherently oriented crystallites are present in a real polycrystalline material, one would expect that the coherent domain size would not be identical throughout the material, and the diffraction measurement would be an average over a distribution of domain sizes. In an effort to study the effect of this averaging, the patterns from the 27 and 125 particle were averaged and the result is depicted in Figure 37(b). Even though only two coherent domain sizes were considered, the resultant average pattern already begins to mask any deviation of the 27 particle pattern from the randomly oriented particle pattern. As a larger set of coherent domain sizes was considered in the averaging, the resultant pattern continues to converge to the randomly oriented particle pattern, showing no effect of particle coherency. Therefore, both the cases of randomly interspersed coherently oriented crystallites, and the average diffraction pattern from different coherent domain sizes, result in the pattern from a randomly oriented particle system. It is therefore unlikely that crystallite coherency is an observable phenomenon in the diffraction pattern of nanocrystalline powders without long range ordering. In the study of Ribarik, et al., a bimodal size distribution was used to model the effect of the observed coherency. In this case the actual existence of such a size distribution in the sample could explain the observed peak broadening instead of the effects of coherency.

When the regular spacing condition for coherent scattering is implemented into a particle system by ordering the coherently oriented particles into a superlattice dramatic effects are observed in the wide-angle diffraction pattern. Figure 38 shows that when a simple cubic superlattice of particles is assumed the typical diffraction peaks from a gold lattice split into two or three clearly identifiable peaks which are modulated by the diffraction pattern of a single gold particle. The positions of these new peaks are dependent on the superlattice spacing, and can be indexed according to the new long range order which is present in the system. Since the superlattice spacing does not have to be a multiple of the atomic unit cell parameter, this ordering of coherent particles is then best described as a local incommensurate superlattice. While a coherent crystallite superlattice of this kind can exist in nature — shown to be due to interactions like nanoparticle surface ligand interactions, and magnetic ordering — it was demonstrated here to show the upper limit of the effect that coherency can have on the wide-angle pattern. Any system of coherently oriented crystallites can then be viewed as somewhere between the presented extremes of the randomly arranged system, and the ordered superlattice.

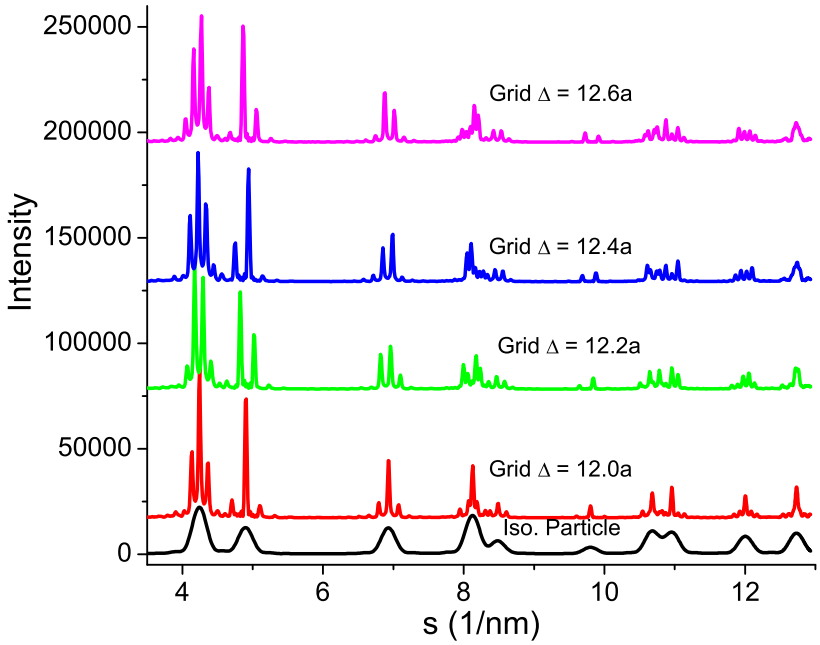

Figure 38: The patterns from orientationally ordered cubic superlattice of 125 patterns ($D = 4.6$nm) are shown for different cubic grid spacings (Grid Δ), which are expressed in terms of the lattice parameter of the FCC in the particles, a.

CHAPTER VII

EFFECTS OF THERMAL MOTION ON THE POWDER DIFFRACTION PATTERN

7.1 General TDS Theory

The theory describing the effects of thermal motion on the diffraction pattern was one of the first problems that was treated in x-ray diffraction, perhaps motivated by the popular belief at the time of the method's conception that the presence of this motion would destroy the diffraction signal from a lattice [46]. The theory can be expressed beginning with a static lattice, and including the consideration that each atom is vibrating around its average position. The position of an atom is then expressed as $\mathbf{r}_n = \mathbf{R}_n + \mathbf{u}_n$, with $\mathbf{R}_n$ and $\mathbf{u}_n$ signifying average atomic position, and its instantaneous displacement respectively. The intensity from Equation (16) then becomes

$$I = I_e \frac{Pol}{R^2} \left[\sum_n |f_n|^2 + \sum_m \sum_{n \neq m} f_m f_n^* \exp\left(-2\pi i \mathbf{d_{mn}} \cdot \mathbf{s}\right) \exp\left(-2\pi i \left(\mathbf{u}_m - \mathbf{u}_n\right) \cdot \mathbf{s}\right) \right], \quad (119)$$

where $\mathbf{d}_{mn} = \mathbf{R}_m - \mathbf{R}_n$. A common diffraction pattern is collected over a time scale much longer than that of atomic motion, so the observed pattern is really the time average of Equation (119). Assuming that the

thermal displacements are small relative to the spacing between atoms in the atomic lattice, we can use the relation

$$\langle \exp\left(-2\pi i\left(\mathbf{u}_m - \mathbf{u}_n\right)\cdot\mathbf{s}\right)\rangle = \exp\left(-\left\langle\left[2\pi\left(\mathbf{u}_m - \mathbf{u}_n\right)\cdot\mathbf{s}\right]^2\right\rangle/2\right). \quad (120)$$

The time average intensity then becomes

$$\langle I\rangle = k(s)\left[\sum_n |f_n|^2 + \right.$$
$$\left.\sum_m\sum_{n\neq m} f_m f_n^* \exp\left(-2\pi i\mathbf{d_{mn}}\cdot\mathbf{s}\right)\exp\left(-2\pi^2\left\langle\left[\left(\mathbf{u}_m - \mathbf{u}_n\right)\cdot\mathbf{s}\right]^2\right\rangle\right)\right], \quad (121)$$

where the terms in front of Equation (119) are now represented by $k(s)$. Expressing $\mathbf{u}\cdot\mathbf{s}$ as $u_m s\cos\theta_m$, and expanding the term $\left[\left(\mathbf{u}_m - \mathbf{u}_n\right)\cdot\mathbf{s}\right]^2$, we arrive at the expression

$$\langle I\rangle = k(s)\left[\sum_n |f_n|^2 + \sum_m\sum_{n\neq m} f_m f_n^* \exp\left(-2\pi i\mathbf{d_{mn}}\cdot\mathbf{s}\right)\right.$$
$$\left.\exp\left(-2\pi^2 s^2\left[\left\langle u_m^2\cos^2\theta_m\right\rangle + \left\langle u_n^2\cos^2\theta_n\right\rangle - 2\left\langle u_m u_n\cos\theta_m\cos\theta_n\right\rangle\right]\right)\right] \quad (122)$$

We can then define the Debye-Waller exponential factor

$$M_m = 2\pi^2 s^2\left\langle u_m^2\cos^2\theta_m\right\rangle = \frac{8\pi^2\sin^2\theta}{\lambda^2}\left\langle u_m^2\cos^2\theta_m\right\rangle, \quad (123)$$

resulting in the final general form of the intensity due to thermal motion

$$\langle I\rangle = k(s)\left[\sum_n |f_n|^2 + \sum_m\sum_{n\neq m} f_m f_n^* \exp\left(-2\pi i\mathbf{d_{mn}}\cdot\mathbf{s}\right)\right.$$
$$\left.\exp\left(-M_m - M_n\right)\exp\left(4\pi^2 s^2\left\langle u_m u_n\cos\theta_m\cos\theta_n\right\rangle\right)\right]. \quad (124)$$

The first exponential in Equation (124) is the unchanged Bragg scattering condition, the second is the well known Debye-Waller factor, while the final exponential is related to the average correlation of the atomic motion. The assumed form of this correlation term is then the point of contention between existing diffraction theories of thermal motion. The two extremes of random atomic motion, and coupled atomic motion will be treated in the following subsections.

It should be noted that the derivation which has been given follows the procedure of James [77] and Warren [155], as the time average is considered before the volume average. The reverse method, considering the spatial average and then the time average, has been described by Guinier [59] and Suortti [139] resulting in identical expressions for the scattered intensity, which is evidence of its ergodic nature.

7.1.1 Random Atomic Motion

The early work by Debye on the subject of thermal motion assumes that the atoms can be treated as *independent* harmonic oscillators [39]. This assumption carries with it the result that the correlation between any two atoms which is averaged over time is zero. Following this treatment, and assuming a monoatomic system, the intensity of Equation (124) reduces to

$$\langle I \rangle = k(s) \left| f_n \right|^2 \left[N + \exp\left(-2M\right) \sum_m \sum_{n \neq m} \exp\left(-2\pi i \mathbf{d_{mn}} \cdot \mathbf{s}\right) \right]. \quad (125)$$

Adding and subtracting the N terms which are necessary to complete the double sum, one finds the expression

$$\langle I \rangle = k(s) \left| f_n \right|^2 \Bigg[N \left[1 - \exp\left(-2M\right) \right] + \exp\left(-2M\right) \sum_m \sum_n \exp\left(-2\pi i \mathbf{d_{mn}} \cdot \mathbf{s}\right) \Bigg] . \quad (126)$$

This form of the thermal effect will be referred to as the Debye thermal diffuse scattering (TDS), since its general form was first described by Peter Debye in 1914 [39]. The first term in Equation (126) is a smooth increasing function with s that contributes isotropically to the background of the diffraction pattern. The second term is an exponential decay which diminishes the intensity of the diffraction spots with increasing s.

If the thermal motion is isotropic, then the exponential factor $2M$ can be expressed as $B_{iso}s^2/2$, resulting in the definition of the Debye-Waller factor as

$$B_{iso} = 8\pi^2 \left\langle u_m^2 \cos^2 \theta_m \right\rangle . \quad (127)$$

The quantity $u_m \cos\theta_m$ is the displacement of atom m in the direction of the scattering vector $\mathbf{s}$. For isotropic motion, the average value can be expressed in terms of the mean squared displacement (MSD) of an atom as $\langle \mathbf{u}_m^2 \rangle = 3 \langle u_m^2 \cos^2 \theta_m \rangle$ [59]. Therefore, B_{iso} is related to the MSD by

$$B_{iso} = \frac{8\pi^2}{3} \left\langle \mathbf{u}_m^2 \right\rangle . \quad (128)$$

7.1.2 Coupled Atomic Motion

The description of atomic motion as random is at odds with the knowledge that a network of bonds exist between atoms. Then, if one atom moves, a force will act upon its neighbors, ultimately resulting in their motion in a similar direction. The theory of lattice dynamics of such a coupled system was developed extensively by Max Born and coworkers [16] around the same time as when Debye was working on his theory of specific heat in solids. This theory was then employed in the early experiments by Laval [80] and Preston [107] to explain the temperature dependence of *diffuse* anisotropic streaking and satellite peaks observed in their measured diffraction pattern. The study of such features in the diffraction pattern is referred to as thermal diffuse scattering (TDS). Commonly the TDS is considered as only an observable feature in the background *between* peaks that does not contribute to a broadening of the diffraction peaks. However, it will be demonstrated that correlated atomic motion produces very broad peaks which are positioned under the Bragg peaks. Therefore, it becomes a concern for accurate line profile analysis, as the improper handling of such an effect can lead to wrong microstructure parameters.

Elasticity theory tells us that the displacement of an atom at any given moment can be decomposed into a sum over a set of normal elastic

plane waves as

$$\mathbf{u}_n(r_n, t) = \sum_g \sum_j A_{gj} \mathbf{e}_{gj} \cos\left(\omega_{gj} t - 2\pi \mathbf{g} \cdot \mathbf{r}_n - \delta_{gj}\right). \tag{129}$$

In this description $\mathbf{g}$ is the wave vector of the plane wave, $A_{gj}$is its amplitude, $\mathbf{e}_{gj}$ is a unit vector in the direction of the vibration polarization, ω_{gj} the angular frequency, and δ_{gj} an arbitrary phase. The index j then represents the different independent polarizations a wave can have in the solid. In a monoatomic three dimensional lattice $j = \{1, 2, 3\}$, representing the 2 longitudinal and 1 transverse acoustic waves possible for a given wave vector, $\mathbf{g}$. The total number of independent vibrations is then given as $3N$, where N is the number of atoms in the system.

This description of the atomic displacement can be used to obtain a suitable form of the correlation term in Equation (124). Expressing $su_m \cos\theta_m$ as $\mathbf{u}_m \cdot \mathbf{s}$, and using Equation (129), one finds that

$$s^2 \langle u_m u_n \cos\theta_m \cos\theta_n \rangle = \left\langle \left[\sum_g \sum_j A_{gj} \mathbf{e}_{gj} \cdot \mathbf{s} \cos\left(\omega_{gj} t - 2\pi \mathbf{g} \cdot \mathbf{r}_m - \delta_{gj}\right) \right] \left[\sum_{g'} \sum_{j'} A_{g'j'} \mathbf{e}_{g'j'} \cdot \mathbf{s} \cos\left(\omega_{g'j'} t - 2\pi \mathbf{g} \cdot \mathbf{r}_n - \delta_{g'j'}\right) \right] \right\rangle. \tag{130}$$

If the phase of each wave is arbitrary, the cross terms from the two summations will average to zero. Therefore, with the use of cosine identities, and considering that $\langle \cos(\omega t) \rangle = 0$ [155], it can be shown that the previous expression reduces to

$$s^2 \langle u_m u_n \cos\theta_m \cos\theta_n \rangle = \frac{1}{2} \sum_g \sum_j \left\langle A_{gj}^2 \right\rangle (\mathbf{e}_{gj} \cdot \mathbf{s})^2 \cos\left(2\pi \mathbf{g} \cdot \mathbf{d}_{mn}\right). \tag{131}$$

Using this result, and expanding the correlation exponential in Equation (124) in terms of a Taylor series, the intensity becomes

$$\langle I \rangle = k(s) \left| f_n \right|^2 \left[N + \sum_m \sum_{n \neq m} \exp\left(-2\pi i \mathbf{d_{mn}} \cdot \mathbf{s}\right) \right.$$
$$\left. \exp\left(-2M\right) \left(1 + \langle Y_{mn} \rangle + \langle Y_{mn} \rangle^2 / 2 + ...\right) \right], \quad (132)$$

where

$$\langle Y_{mn} \rangle = 2\pi^2 s^2 \sum_g \sum_j \left\langle A_{gj}^2 \right\rangle \cos^2 \theta_{gj} \cos\left(2\pi \mathbf{g} \cdot \mathbf{d}_{mn}\right). \quad (133)$$

Similar reasoning also leads to the relationship

$$2M = 2\pi^2 s^2 \sum_g \sum_j \left\langle A_{gj}^2 \right\rangle \cos^2 \theta_{gj}. \quad (134)$$

From Equation (132) it is clear that the form of the Debye TDS is the zeroth order approximation to the TDS found when assuming a coupled system. In addition there are higher order corrections, corresponding to the power of $\langle Y_{mn} \rangle$, which are added under the Bragg pattern.

7.1.3 Relating diffraction observables to vibrational density of states

For comparison of the developed description of the TDS with the observable features, the task at hand becomes relating the mean amplitude squared of a wave, $\left\langle A_{gj}^2 \right\rangle$, to other quantities like the density of states and temperature of a system. The mean kinetic energy of an elastic wave over time is given by $\langle K_{gj} \rangle = \frac{1}{4} N m \left\langle A_{gj}^2 \right\rangle \omega_{gj}^2$, where N is the number of atoms in the system, and m is the mass of each atom.

By the virial theorem, the average total energy is twice the mean kinetic energy, so $< E_{gj} >= \frac{1}{2} Nm \left\langle A_{gj}^2 \right\rangle \omega_{gj}^2$. Treating each elastic wave as a harmonic oscillator, this mean energy can also be expressed as $< E_{gj} >= \hbar\omega_{gj}(n(\omega_{gj}, T) + \frac{1}{2})$, where $\hbar$ is Plank's constant and $n(\omega_{gj}, T)$ is the partition function of the phonons. Since phonons follow Bose-Einstein statistics,

$$n(\omega_{gj}, T) = \frac{1}{\exp(\hbar\omega_{gj}/k_B T) - 1}, \tag{135}$$

which can be approximated as $n(\omega_{gj}, T) = k_B T$ at high enough temperatures. Therefore, the mean square amplitude is found to be

$$\left\langle A_{gj}^2 \right\rangle = \frac{2\hbar}{Nm\omega_{gj}}(n(\omega_{gj}, T) + \frac{1}{2}). \tag{136}$$

Often equipartition is assumed allowing the sum over g in the evaluation of quantities like $\langle Y_{mn} \rangle$ and $2M$ to be expressed in terms of an integral of the density of states, $\Gamma(\omega_{gj})$, over the first Brillouin zone. Equations (133) and (134) then become

$$\langle Y_{mn} \rangle = 4\pi^2 s^2 \frac{\hbar}{Nm} \int_g \sum_j \frac{\Gamma(\omega_{gj})}{\omega_{gj}} (n(\omega_{gj}, T) + \frac{1}{2}) \cos^2 \theta_{gj} \cos\left(2\pi \mathbf{g} \cdot \mathbf{d}_{mn}\right) \mathrm{d}g, \tag{137}$$

and

$$2M = 4\pi^2 s^2 \frac{\hbar}{Nm} \int_g \sum_j \frac{\Gamma(\omega_{gj})}{\omega_{gj}} (n(\omega_{gj}, T) + \frac{1}{2}) \cos^2 \theta_{gj} \mathrm{d}g, \tag{138}$$

respectively. Since the speed of sound in a lattice is frequency dependent, the relationship $\omega_{gj} = 2\pi c_{gj} g\varsigma(g)$ is necessary to convert between

ω and g, where $\varsigma(g)$ is the assumed dispersion relationship, and c_{gj} is the low frequency limit of the speed of sound for the wave vector g and polarization j.

7.1.4 Powder TDS for Cubic Materials

Until this point effort has been made to leave the relations in a general form, and avoid any approximations. However, general analytic solutions of Equations (137) and (138) are not possible. Also, when considering the powder intensity, the intensity described by Equation (132) needs to be further averaged over the powder sphere.

In order to find a solution which produces a reasonable representation of the TDS, multiple models have been proposed of varying complexity and realism. In the study of the TDS in a powder diffraction pattern from a cubic material, Warren proposed one of the first notable models [155]. However, it is somewhat limited to special cases as it: relies heavily on the Debye theory of lattice vibrations to approximate the density of states, assumes a constant average velocity of sound, neglects a frequency dispersion relationship, and was originally formulated for temperatures around the Debye temperature, Θ_D. Generalizations and improvements have been proposed in the past by a number of authors. The calculation of the first order TDS was extended to lower temperature by Herbstein and Averbach [67]. The allowance for a speed of sound which differs for the longitudinal and transverse modes, c_l and c_t respectively, was

considered by Paskin [102] following $c_l \backsimeq 2c_t$ as it is a common characteristic in cubic materials. Later, Suortti [139] considered the dispersion relationship of a linear chain, as well as pointed out the importance of convolving the TDS with the Bragg peak. Finally, Walker and Chipman [152] extended the treatment to allow for the description of a material with elastic anisotropy.

It is a common assumption that the first and second order terms dominate the TDS, therefore, most efforts are spent developing these relationships. Also, it is common to approximate the integral over the first Brillouin zone as an integral over a sphere of equal volume. While this approximation conserves the integrated intensity of the TDS, some doubt has been raised by Walker and Chipman regarding its ability to represent the true profile of the TDS peak [152].

Only a brief sketch of the derivation for the TDS in the powder pattern from an isotropic cubic material will be presented here as the full discussion is rather lengthy. The reader is directed to Sections 11.5, 11.10 and 11.11 of Warren [155] for more details. Following a series of simplifying assumptions — the use of the average speed of sound c_j, $\omega_j = 2\pi c_j g$, and the density of states assumed as a quadratic function in the first Brillouin zone — Equation (137) becomes

$$\langle Y_{mn} \rangle = 2M \frac{Si\left(z_{D_{mn}}\right)}{z_{D_{mn}}}, \tag{139}$$

where

$$Si(z) = \int_0^z \frac{\sin x}{x} \mathrm{d}x, \tag{140}$$

$$z_{D_{mn}} = 2\pi g_D d_{mn}, \tag{141}$$

and $2M$ is the Debye-Waller exponential factor, which at high enough temperatures can be approximated as

$$2M = \frac{3h^2 T}{m k_B \Theta_M^2} s^2. \tag{142}$$

The reciprocal space length g_D is the radius of a sphere whose volume equal to that of the first Brillouin zone, or $V_{BZ} = 4\pi g_D^3/3$. Also, the characteristic temperature Θ_M is similar to the Debye temperature, but is actually an average of the Debye temperatures for the longitudinal and transverse waves, Θ_l and Θ_t respectively, and is given by the relationship

$$\frac{3}{\Theta_M} = \frac{1}{\Theta_l} + \frac{2}{\Theta_t}. \tag{143}$$

Therefore, the intensity from Equation (132) for the l-th order TDS becomes

$$I_l(\mathbf{s}) = k(s) \left|f\right|^2 \exp\left(-2M\right) \frac{2M^l}{l!} \sum_m \sum_n \exp\left(-2\pi i \mathbf{d_{mn}} \cdot \mathbf{s}\right) \left[\frac{Si\left(z_{mn}\right)}{z_{mn}}\right]^l. \tag{144}$$

Equation (144) gives the intensity at a point in reciprocal space, as described in Section 2.2 the powder intensity is found by taking the average of this quantity over the powder sphere. In doing so the sum over the mn pairs can be replaced by the sum over nearest neighbor

shells at a distance d_i and with a multiplicity C_i. Then the l-th order powder TDS intensity is found to be

$$I_{P_l}(s) = k(s)N\left|f\right|^2 \exp\left(-2M\right)\frac{2M^l}{l!}Q_l, \tag{145}$$

where

$$Q_l = \frac{1}{2s}\sum_{hkl}\frac{m_{hkl}}{s_{hkl}}\Phi_l\left(\left|s - s_{hkl}\right|\right), \tag{146}$$

and

$$\Phi_l\left(\left|s - s_{hkl}\right|\right) = \frac{g_{max}^2 - \left|s - s_{hkl}\right|}{2} + \frac{1}{4\pi^2}\sum_{i=1}^{\infty}\frac{C_i}{d_i^2}\left[\frac{Si\left(z_i\right)}{z_i}\right]^l\left[\cos\left(2\pi\left|s - s_{hkl}\right|d_i\right) - \cos\left(2\pi g_{max}d_i\right)\right]. \tag{147}$$

After explicitly considering the first few nearest neighbor shells, the remainder of the infinite summation in Equation (147) can be approximated as an integral assuming a continuous atomic density. Warren finds that Φ_l for $l > 2$ can be approximated by Φ_2, resulting in the total TDS powder intensity simplifying to

$$I_{P_{TDS}} = k(s)Nf_n^2(s)\left[\exp\left(-2M\right)2M\left(Q_1 - Q_2\right) + \left(1 - \exp(-2M)\right)Q_2\right]. \tag{148}$$

It should be noted that the Lorentz factor is already included in the description of Q_l given in Equation (146). The intensity predicted by Equation (148) for an Al lattice at 300K is depicted in Figure 39. It is found that this form of the TDS results in very sharp peaks centered at the positions of the Bragg peaks with broad tails which extend between peaks. While the contribution of the TDS to the diffraction pattern is

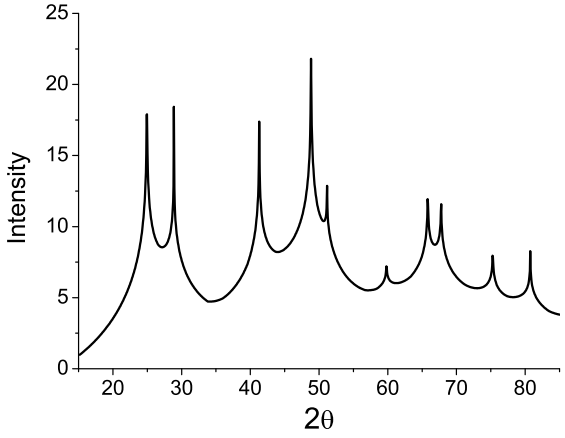

Figure 39: The Warren Powder TDS assuming an Al lattice is depicted.

small relative to the Bragg scattering, it can have an impact on changing the apparent shape of the diffraction peaks, especially in their tails. It will also be shown in the following section that the diffraction pattern from MD simulations at an elevated temperature also exhibit these features. The controllable nature of these simulations then allows for a precise study of the consequences of assuming different models for the TDS.

7.2 Simulating Bulk Lattice Vibrations and the Powder Diffraction Pattern

Molecular dynamics can be used to study the effects of thermal motion on the powder diffraction pattern by calculating the diffraction pattern from the atomic positions in the simulation. First, it was desirable to study the influence of bulk lattice vibrations, before attempting to understand the slightly more complicated case of the vibrations in smaller crystallites. The techniques used here to simulate the pattern are not standard, so a

description of the reasoning behind the employed procedure is necessary.

7.2.1 Molecular Dynamics Simulation Parameters

Molecular dynamics simulations were carried out assuming a periodic simulation box containing a perfect lattice, using the LAMMPS simulation software [106]. Starting from 0 K, the temperature of the system was gradually raised in steps of 100K and allowed to stabilize at temperatures from 100 K to 500 K. Once the system had stabilized at each temperature, the positions of the atoms were output for a series of time steps. The position information is an effective snapshot of the system at a given moment in time which can be used to simulate the diffraction pattern. The periodic structure of the system was avoided by only considering atoms in the center of the system. The powder diffraction patterns of the center atoms from each snapshot were directly calculated using the Debye function. The series of patterns at a given temperature were then averaged to obtain the time averaged pattern. This average pattern was treated as experimental data, and analyzed using modern line profile analysis techniques [124, 86].

It is necessary to carefully consider the setup and behavior of the MD simulations to ensure it exhibits realistic lattice dynamics. In the present study a simulation box containing 108,000 atoms and with an edge, L, consisting of 30 FCC unit cells ($L \sim 12$ nm) was created. The boundary conditions of the box were periodic, allowing for the study of the bulk thermal behavior and atomic vibrations. The number of atoms

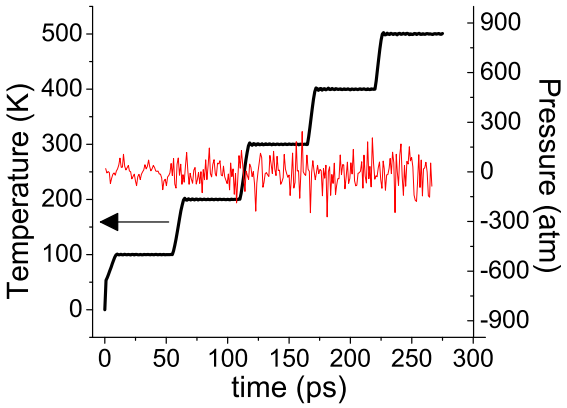

Figure 40: The temperature and pressure of an MD system is shown over the duration of a simulation which was used in this study.

(N), pressure (P) and temperature (T) were controlled throughout the simulation. The use of this ensemble allows the simulation box to account for thermal expansion and change its volume isotropically to maintain the desired pressure. The pressure of the system was kept at 0 atmospheres as only the effect of temperature was intended to be studied. As shown in the thermal and barometric history of the simulation depicted in Figure 40, the temperature was increased from 0K in steps of 100K, and allowed to stabilize for a time of 50 ps (50,000 time steps). After the stabilization period, the system was allowed to evolve for another 5 ps to obtain the series of atomic positions used in the diffraction pattern calculation.

The assumed interatomic potential describing the interaction between atoms determines the thermal response of a system. In the present work many-body interatomic potentials based on the theory of the embedded atom method were used. In the case of Cu the embedded atom method

(EAM) potential [52] was used, while for Al the effective medium theory (EMT) potential [72] was employed. These potentials have been developed using the elastic properties of the respective bulk metals measured at 300K, and are then appropriate for the setup and temperature range studied here.

As a test of the simulated lattice dynamics, the vibrational density of states (VDOS) was calculated from the atomic velocities. The atomic velocities were output at same time as the atomic positions. This velocity information was then used to calculate the velocity auto-correlation function, $c(t)$, defined in Equation (100). Following the methods described by Dove [163], the VDOS, $\Gamma(\nu)$, for a monoatomic material is obtained from the Fourier transform of the velocity auto-correlation function as in Equation (101). The VDOS obtained by analyzing the velocities of our MD simulations are depicted in Figure 41, and show a form consistent with that found from inelastic neutron scattering [136, 140]. Therefore, the atomic vibrations observed from this technique are indeed consistent with those of the real materials.

7.2.2 Simulation of the Powder Pattern

If the atomic positions of a time step are directly used to calculate the diffraction pattern, the periodic nature of the system will result in artifacts. Therefore, before the diffraction pattern was calculated, a sphere of diameter less than the simulation box size was carved out of the atomic

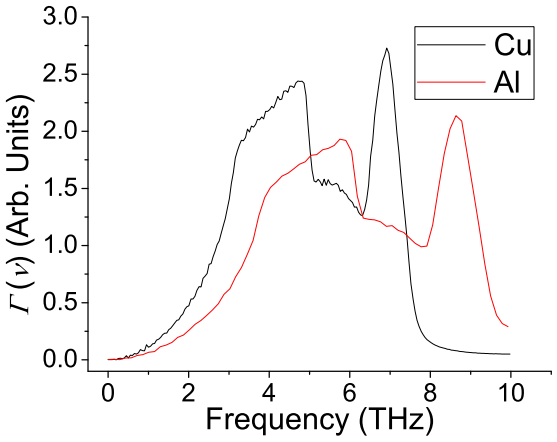

Figure 41: Comparison of the vibrational density of states calculated from the atomic velocities of the Cu and Al MD simulations at 300K.

positions. The choice of this shape is looking ahead to minimize the effects of the approximations made in the pattern analysis, as the sphere has an analytical shape function [104]. This method of carving the sphere from this perfect periodic system intentionally does not include the influences which defects, surfaces, or interfaces have on the lattice dynamics and powder pattern. Once the sphere was carved from the larger simulation system, the diffraction pattern is calculated using the Debye function as given by Equation (24). In this study the polarization factor describing the intensity from unpolarized incident x-rays, given by Equation (14), and a 1 Å wavelength of radiation were assumed. Since the pattern is already being calculated from a dynamic system, it is not necessary to include any temperature effect in the pattern calculation.

It is important to keep in mind that an experimental diffraction pattern is actually an average pattern collected over a time on the order of

seconds. The simulation of an MD system over a comparable time range is beyond the limit of existing computing power. Instead, a strategy of finding a representative time averaged pattern is necessary to effectively simulate the effects of thermal motion on the diffraction pattern. This can simply be accomplished by averaging the patterns from a series of snapshots until the average pattern converges, and the inclusion of the pattern from more time steps does not change the resulting pattern. The time range over which these patterns should be averaged should be on the order of the oscillation period of the longest wavelength vibration considered, while not so long to allow for atomic diffusion. In this study an average of 10 snapshots over a time range of 5 ps was found to be sufficient to calculate the time average pattern. It should be kept in mind that in calculating the pattern from each time step, a spatial average of the atomic oscillations is also being performed, so the number of time steps necessary to arrive to an average pattern is also dependent on the size of the system considered.

7.3 Comparing TDS Models

Some of different powder TDS models which are described in Section 7.1 have been used to study the patterns simulated by the methods described in Section 7.2. This allows for the evaluation of the ability of each model to represent the features in the diffraction pattern attributed to the TDS, as well as, the influence which each model has on the determined characteristics of the crystallite.

The described procedure of using MD to simulate the thermal effects on the diffraction pattern was carried out considering both a Cu and an Al lattice system. While both have an FCC lattice, these two metals exhibit very different thermal and elastic behaviors. Consideration of their experimental elastic constants shows that copper has an anisotropy factor of 3.2, while aluminum is nearly isotropic with a factor of 1.2 [6]. The thermal motion of atoms is then dependent on these elastic properties, and comparing the patterns from these two materials can show the effects of isotropic versus anisotropic thermal motion.

7.3.1 Debye vs Warren TDS

In an effort to convey the implications of the random and correlated atomic motion assumptions, the Debye TDS and Warren TDS models were used to model the patterns from the simulated Al and Cu particles. In this study spheres of diameter of 10nm were carved out of MD simulations stabilized at 300K. The Debye TDS described by Equation (126), as well as, the Warren TDS described by Equation (148), were implemented into the framework of the diffraction pattern modeling software PM2K [86]. The only other features which were assumed in the pattern modeling were the contributions of the crystallite size to the wide-angle peak broadening and small-angle signal. The small-angle scattering contribution was only included to correctly model the low angle tail of the 111 peak. The pattern refinement then consisted of finding the crystallite size, lattice parameter and thermal parameter which resulted in the best

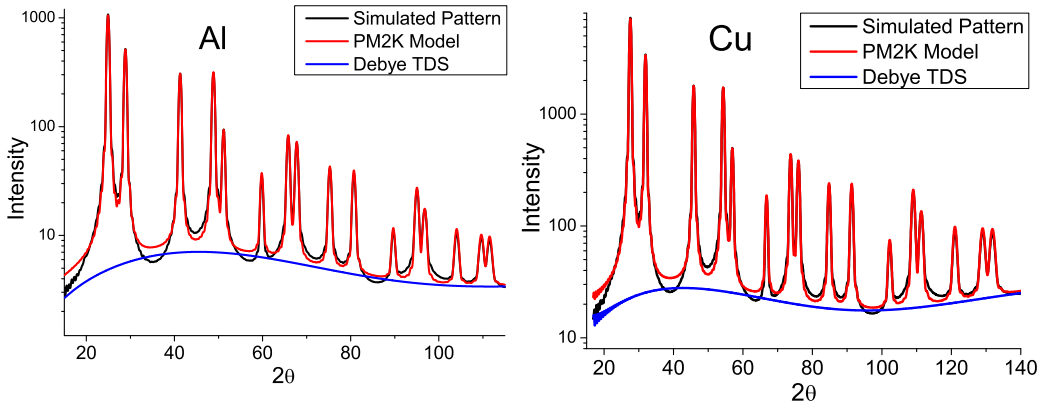

Figure 42: The fits assuming the Debye TDS to model MD simulated powder patterns are depicted.

fit of the simulated pattern for each assumed TDS model.

The fits from assuming the Debye TDS to model the patterns from Al and Cu are depicted in Figure 42. In both cases it is evident that the smooth TDS function which is the result of the Debye model does not appropriately represent the features in the tails of the simulated diffraction peaks. The parameters which resulted in the depicted best fits for each case is depicted in Table 2. The inability of this model to represent the diffraction pattern is also reflected in the deviation of the obtained diameter and B_{iso}. The use of the Debye TDS leads to an underestimation of the diameter. Also, somewhat surprisingly the obtained Debye-Waller parameters are less than expected. The inaccuracies resulting from the Debye model are evidence that the thermal motion of the simulated systems does not follow the random motion assumptions.

The same patterns were also modeled assuming the powder TDS

Table 2: Parameters found from the best fit *Experimentally measured values reported by Fox [53].

Al	GoF	a (nm)	D (nm)	B ($Å^2$)
Debye TDS	0.291	0.4011	9.77	0.740
Warren TDS	0.081	0.4011	9.95	0.914
Expected	-	0.4011	10.0	0.85*
Cu	GoF	a (nm)	D (nm)	B ($Å^2$)
Debye TDS	0.767	0.3632	9.77	0.465
Warren TDS	0.186	0.3632	9.97	0.587
Expected	-	0.3632	10.0	0.54*

model for cubic materials developed by Warren. The high level of agreement which this model allows is evident in the fits depicted in Figure 43. Comparing these fits with those obtained assuming the Debye TDS, it becomes evident that the specific features present in the Warren model are necessary to model correctly the features in the tails of the peaks. The parameters found from this model in Table 2 finds that the proper representation of the peak features also results in more accurate determination of the particle size and Debye-Waller parameter.

Studying the fits obtained from the Al and Cu systems does not find a dramatic difference in the ability of the Warren TDS model to represent the two cases. However, a slight improvement in the modeling of the Al patterns described by the GoF. This slight improvement is in agreement with the understanding that the Warren and Debye models have been developed assuming isotropic thermal motion. Still, this disagreement for Cu is very subtle, and does not effect the accuracy of the parameters

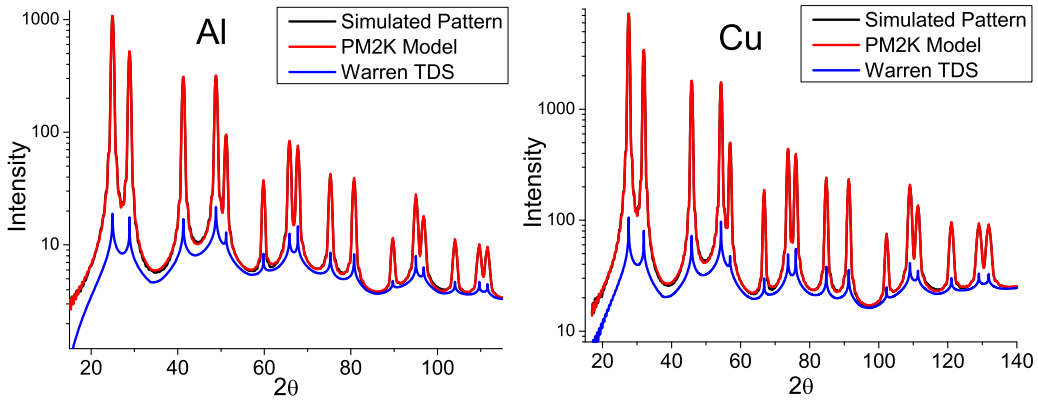

Figure 43: The fits assuming the Warren TDS to model MD simulated powder patterns are depicted

which were obtained from the modeling.

7.3.2 Assessment of Error from Neglecting the TDS

The methods described in Section 7.2 were again used to simulated the pattern from a 10nm sphere, but this time at a range of temperatures. The obtained patterns were modeled assuming the commonly employed technique of ignoring the TDS, and trying to fit the background with a smooth polynomial function. The obtained values of the particle size, lattice parameter and Debye-Waller factor were then compared the known values to understand what kind of errors are introduced into the modeling by improperly treating the TDS contribution. This analysis was again repeated for Al and Cu systems to demonstrate cases of differing degrees of elastic anisotropy.

Examples of the calculated average patterns from the Al and Cu simulations at different temperatures are shown in Figure 44. These calculated

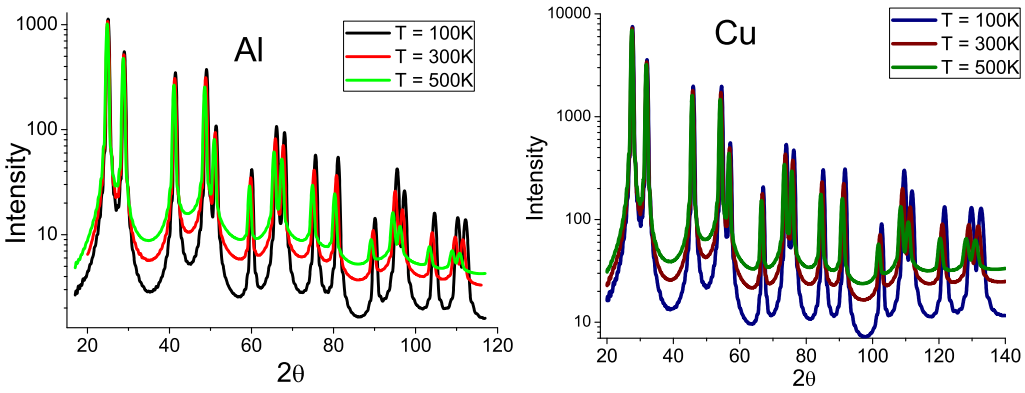

Figure 44: The patterns from a $D = 10$nm sphere carved from the Al and Cu systems at different temperatures are depicted. The patterns are shown in a log scale to highlight the features of the background.

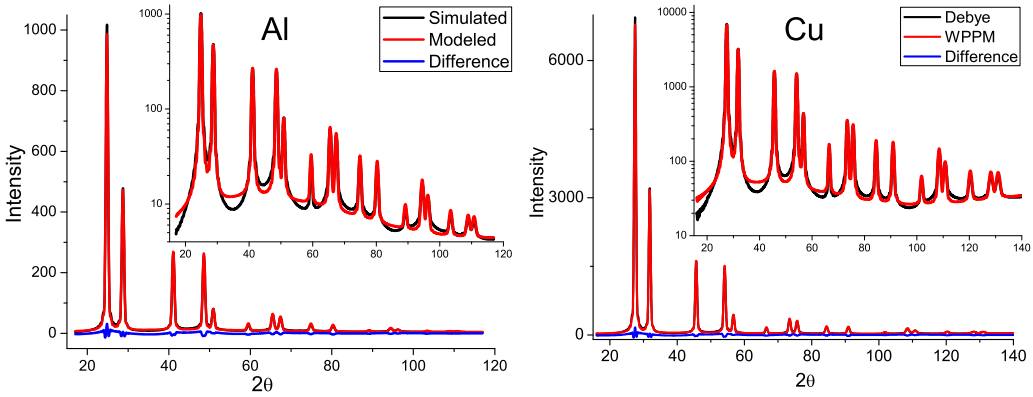

Figure 45: The fit of the pattern from the Al and Cu simulations at 500K shows the inability to completely represent the peak shape and background trend. The inset highlights the fit of the background.

patterns were then analyzed using the Whole Powder Pattern Modelling [124] software PM2K [86]. The patterns were input as experimental data and modeled assuming: a Delta size distribution of spheres containing an FCC lattice, Debye-Waller (D-W) temperature factor, and a fifth order Chebyshev polynomial to represent the background and TDS. An example of the level of agreement observed in the use of this model is depicted in Figure 45. The ability of this model to correctly fit the calculated patterns decreased as the temperature was increased, as shown in the increasing trends of the Goodness-of-Fit (GoF) of Figure 46. Therefore, the match shown in Figure 45 is an example of the poorest fits obtained for the Al and Cu particles in this study.

A comparison of the PM2K model parameters obtained from the Cu and Al patterns is shown in Figures 46 and 47. First it is interesting to note that the model is always able to fit the patterns from the Al system better than those of the Cu system. This is consistent with the understanding that the D-W factor is derived assuming isotropic atomic motion. The figure also shows how the trends of the determined lattice parameters as a function of temperature are nearly linear. The slope of this trend gives linear expansion coefficients of $20.8\text{x}10^{-6}\text{K}^{-1}$ and $16.6\text{x}10^{-6}\text{K}^{-1}$ for Al and Cu respectively. These values are in good agreement with the experimental values for these metals [6]. The determined B_{iso} coefficients are shown in Figure 47 to also increase nearly linearly with temperature. The higher slope of this trend for Al implies

a weaker bond than Cu, and correlates with the shallower potential well of Al.

Most importantly for the purpose of this study, the particle size determined from the line profile analysis is shown to decrease with temperature in Figure 47. This is caused by the correlated lattice dynamics of the system, which leads to a distribution of intensity into the peak tails. The peaks in the modeling are then broadened to obtain a better fit, resulting in a decrease in the obtained particle size. The error in the particle size due to this effect is not huge, and on the order of 2.5% at 300K for both Cu and Al. However, it should be kept in mind that not properly accounting for the thermal effect introduces this error, which can also propagate into the determination of other physical parameters such as the fault probability, and dislocation density.

It has been demonstrated how the coupling of molecular dynamics and Debye function calculation can be used to study the complex effect which lattice dynamics has on the powder diffraction pattern. The use of a Debye-Waller temperature factor and Chebyshev background has been shown to lead to an underestimation of the crystallites size which becomes worse as the temperature increases. This calls for the use of more sophisticated TDS models when accurate microstructural information is necessary. The discussion of extending of the developed models to be more appropriate for small crystallites is the topic of the next section.

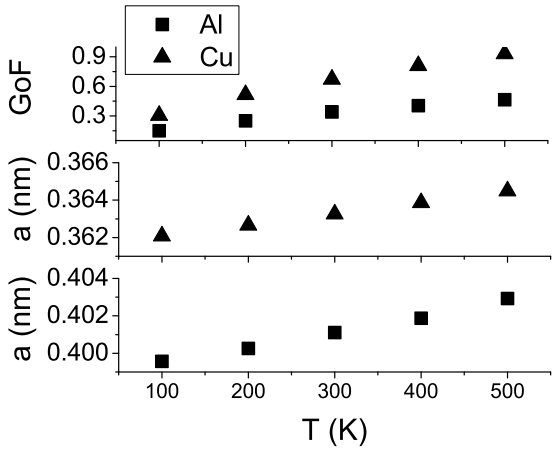

Figure 46: The comparison of the GoF obtained for the Al and Cu cases shows that the modeling is able to better represent the patterns from the Al system. Also the thermal expansion trends of the two systems are depicted.

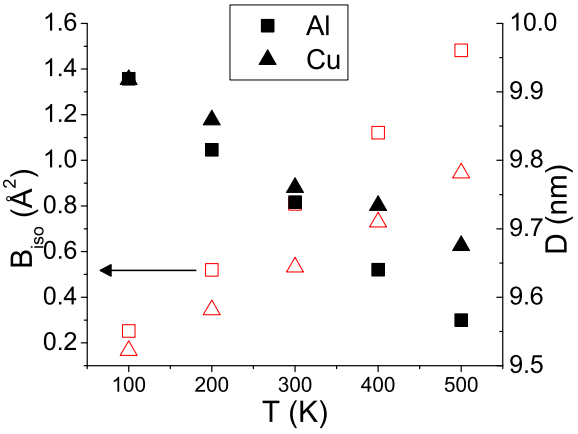

Figure 47: The determined Debye-Waller factors of the MD systems increase with temperature, while the determined particle size decreases.

7.4 Powder TDS for Small Crystallites

Like in much of the diffraction theory which has been discussed in this work, the TDS theory which has been presented in Section 7.1.4 has been derived assuming an infinite lattice. This is a fair assumption when the crystallite is large and dominated by scattering from the bulk. However, as the size becomes small the vibrational density of states (VDOS) changes, then so to must the TDS by virtue of relations like Equation (137).

7.4.1 Size Dependent Maximum Phonon Wavelength

Consideration of the maximum phonon wavelength observable in a crystallite yields the first expected influence of the particle size on the VDOS. Just as in acoustics, an approximation of the first harmonic in a crystallite can be thought of as a wave which travels through a particle having a node (or anti-node depending on the boundary conditions) positioned at either boundary of the particle. The wavelength of this mode is then related to the particle size by

$$\lambda_{max} \propto 2D, \tag{149}$$

where D is some size parameter of a crystallite. This first harmonic represents the maximum wavelength of a normal mode which can be present in an acoustically isolated crystallite. This maximum wavelength in turn can be related to a minimum vibrational wave vector, g_{min}, or frequency, ω_{min}, through the speed of sound and dispersion relationship

describing a given material. A small crystallite size then has the effect of forcing the density of states to zero for frequencies below ω_{min}. This influences the TDS by changing the limits of integration over the Brillouin zone as Equation (137) becomes

$$\langle Y_{mn} \rangle = 4\pi^2 s^2 \frac{\hbar}{Nm} \int_{g_{min}}^{g_{max}} \sum_j \frac{\Gamma(\omega_{gj})}{\omega_{gj}} (n(\omega_{gj}, T) + \frac{1}{2}) \cos^2 \theta_{gj} \cos\left(2\pi \mathbf{g} \cdot \mathbf{d}_{mn}\right) \mathrm{d}g, \tag{150}$$

and an analogous expression is also found for Equation (138). The total number of independent vibrational modes must be conserved as $3N$. Therefore, this was considered in the present study by defining the upper bound of the integral, g_{max}, as that which conserves the integrated density of states

$$\int_{g_{min}}^{g_{max}} \sum_j \Gamma(\omega_{gj}) \mathrm{d}g = 3N. \tag{151}$$

Assuming that the density of states continues to follow the quadratic form assumed in the Debye theory, this normalization condition results in the relationship $g_D^3 = g_{max}^3 - g_{min}^3$.

Considering this adjustment, the powder TDS of Warren is found to take a similar form, but now

$$\Phi_l\left(|s - s_{hkl}|\right) = \frac{1}{4\pi^2} \sum_{i=1}^{\infty} \frac{C_i}{d_i^2} \left[\frac{Si\left(z_{max_i}\right) - Si(z_{min_i})}{z_{D_i}}\right]^l \left[\cos\left(2\pi g_1 d_i\right) - \cos\left(2\pi g_{max} d_i\right)\right], \tag{152}$$

where $z_{max_i} = 2\pi g_{max} d_i$ and $z_{min_i} = 2\pi g_{min} d_i$. The reciprocal space length g_1 is conditionally dependent on the vicinity of the scattering

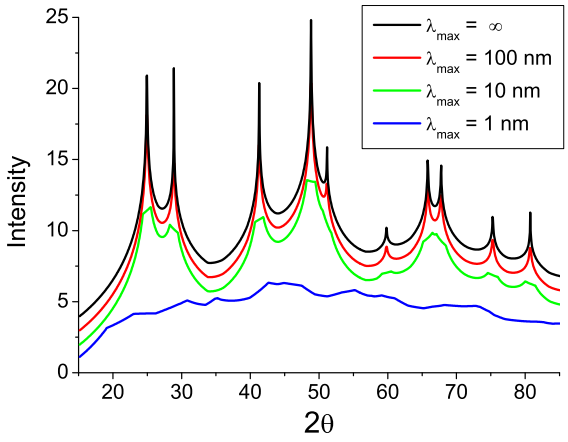

Figure 48: The TDS intensities predicted from the modified Warren TDS model is depicted for a series of values for λ_{max}. In this figure the TDS intensities have been offset for clarity.

vector, $\mathbf{s}$, to a reciprocal space point, $\mathbf{s}_{hkl}$, taking the values

$$g_1 = \begin{cases} |s - s_{hkl}| & |s - s_{hkl}| > g_{min} \\ g_{min} & |s - s_{hkl}| \leq g_{min} \end{cases} . \tag{153}$$

This relationship originates from the assumption that the density of states is zero below g_{min}, and has the effect of truncating the TDS peaks. This expression for Φ_l can then be used in Equation (146) to modify Warren's model for the powder TDS and account for this phonon confinement effect. The resulting effect on the TDS is shown in Figure 48 for a series of maximum phonon wavelengths. It is apparent that the truncation of the TDS only becomes apparent as the crystallite size approaches a few nanometers.

7.4.2 Surface and Edge Modes

The second influence of the small crystallite size is found from considering that the fraction of surface and edge vibration modes becomes sizable compared to the bulk modes for small crystallites. The influence of this effect on the Debye-Waller constant was first treated by Schoening [130], who's model was later extended to describe the first order TDS by Urban [146]. Schoening and Urban used the density of states derived from considering a cube whose boundaries are clamped or rigid, originally described by Bolt [15], Maa [90] and Roe [120]. The density of states which has not yet been averaged over the three polarizations, j, is then assumed to take the form

$$\Gamma(\nu_j) = \frac{4\pi V \nu_j^2}{c_3} + \frac{\pi S \nu_j}{2c_2} + \frac{L}{8c_1}, \tag{154}$$

where the volume, surface area and edge length of the crystallite are denoted by V, S, and L respectively. It is readily seen how the first term expresses the volumetric vibration modes, while the second and third terms describe the surface and edge modes respectively. The general density of states dependence on the frequency is then ν^{d-1}, where d is the dimensionality of the vibration mode. The c_i constants are related to the speed of sound of the longitudinal and transverse modes by

$$\begin{aligned} \frac{1}{c_1} &= \frac{\beta_2}{c_m}, \\ \frac{1}{c_2} &= \frac{\beta_1}{c_m^2}, \\ \frac{1}{c_3} &= \frac{1}{c_m^3}, \end{aligned} \tag{155}$$

where the average velocity, c_m, is found by the relation $\frac{3}{c_m^3} = \frac{1}{c_l^3} + \frac{2}{c_t^3}$, and the β constants are given by

$$\beta_1 = \frac{1 + \frac{2c_l^2}{c_t^2}}{\left(1 + \frac{2c_l^2}{c_t^2}\right)^{2/3}}, \tag{156}$$

and

$$\beta_2 = \frac{1 + \frac{2c_l^2}{c_t^2}}{\left(1 + \frac{2c_l^2}{c_t^2}\right)^{1/3}}. \tag{157}$$

An exact evaluation of the β parameters then requires knowledge of the speeds of the longitudinal and transverse waves in the material. Schoening sites a value of $\beta_1 = 1.35$ to be a reasonable approximation for a sphere, however, little explanation of this claim is found. While this model may not be exactly appropriate for stress free surfaces, the basic trend of more surface modes for small sizes is still embodied in this form of the density of states.

Following the arguments of Urban, and again considering the finite size of the crystallite as described Section 7.4.1, the first order TDS is found with Φ_1 taking the form

$$\Phi_1(|s - s_{hkl}|) = \frac{1}{3} \ln \left[\frac{g_{max}}{g_1}\right] + \frac{\beta_1 S}{12V} \left[g_{max}^{-1} - g_1^{-1}\right] + \frac{\beta_2 L}{96\pi V} \left[g_{max}^{-2} - g_1^{-2}\right], \tag{158}$$

where the reciprocal space length g_1 is defined in Equation (153). The first term in Equation (158) is found to be identical to the first order size-modified Warren TDS model, while the second and third terms represent the added contributions from the surface and edge vibrations respectively.

Studying the scale factors in front of each contribution to this TDS finds that the contribution from edge modes is more than two orders of magnitude less than the volumetric contribution. Therefore, even at small sizes the contribution from edge modes can be neglected in this model to a good approximation.

In some of the following studies involving the modeling of the TDS, a combination of the Urban and the modified Warren models has been used, where the first order TDS is taken to be that given by the Urban model but ignoring the edge mode contribution, and the higher order terms are given by the modified Warren model. The assumption of ignoring the contribution from surface and edge modes in the higher order TDS terms is believed to be reasonable given the very slight influence which these higher orders have on the diffraction pattern. A few examples of the TDS predicted by this model are depicted in Figure 49 for a series of different values of β_1. The first having $\beta_1 = 0$, is then equivalent to the modified Warren model for the TDS derived in the previous section. As β_1 is increased the features in the TDS become more prominent.

7.5 Simulating the TDS in the diffraction pattern from Small Crystallites

While the method of carving a sphere from a bulk sphere might be reasonable to study the effect of bulk phonons, it is not suitable to study the phonon confinement effects mentioned in Section 7.4. This is because the vibrational modes which exist throughout the carved sphere are actually

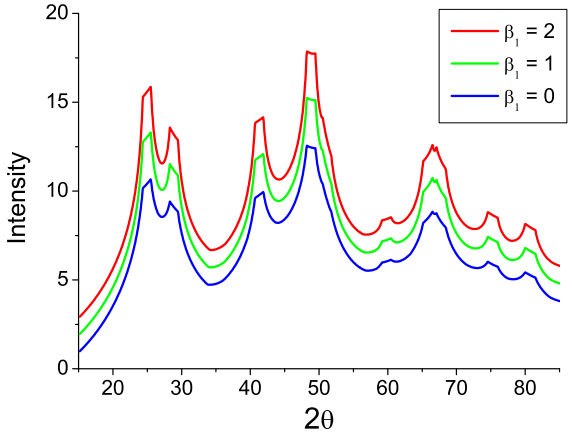

Figure 49: The TDS intensities predicted by the Urban model assuming a 10nm domain are depicted for different values of β_1. The TDS trends in this figure have been offset for clarity.

attributed to the larger periodic simulation box. Simulations were then carried out considering spherical nanoparticles of different sizes in order to study the size effects on the TDS. However, the minimization of the surface energy of a nanoparticle suspended in vacuum could have a few consequences, including strain of the atomic lattice near the surface, and even a restructuring of the entire crystallite. Therefore, a nanoparticle with a core-shell configuration was conceived to study the TDS effects.

The simulated core-shell particle consists of a core region, which was allowed to vibrate, and is surrounded by a shell region, where each atom was fixed in space and not allowed to vibrate. The volume of the core region was defined by the desired particle size, while the shell region then surrounded the core with a spherical shell having a thickness of 2nm. The entire particle was constructed having a uniform lattice, and the

interaction of the core atoms and shell atoms was governed by the same potential. The purpose of the shell is then to limit the restructuring of the core atoms, and also to define the volume of confinement for the possible phonon modes. In calculating the diffraction pattern, only the positions of the core atoms were considered, and the patterns from multiple time steps was averaged following the same considerations as in Section 7.2.

While this core-shell construction may not be consistent with a real nanoparticle, it serves as a good test of the models for the TDS size dependence described in Section 7.4. As already mentioned, it prevents the culmination of a lot of strain in the simulated nanoparticle, which can lead to the broadening and shifting of the peaks in the resulting diffraction pattern. Furthermore, the rigid shell serves to limit the atomic motion at the core particle boundaries. This is actually consistent with the VDOS adopted by the Urban model, which is based on a cube which has "clamped" surfaces and edges. However, what is not initially obvious is that encapsulating the free core by a rigid shell actually leads to a change in pressure in the core volume. This built up pressure in turn leads to an expansion, or contraction, of the lattice in the core. This is actually due to the energy coming from the interface which is now created at the boundary of the core and shell regions. To avoid this build up of pressure, the core-shell particle must be initialized with a shell which is already accounting for any change in the core volume.

The method of starting from the minimum energy state, and slowly

ramping the temperature, cannot be used stabilize the core atoms at a desired temperature as the corresponding thermal expansion will again build up pressure in core due to the rigid shell. Instead the velocities of the core atoms were initialized with a random distribution mimicking a system at 300K. The core atoms were then allowed to stabilize assuming an NVT ensemble, after which the atomic positions of the core atoms were used to calculate the diffraction pattern.

7.6 Modeling the Powder TDS from Small Crystallites

The simulated diffraction patterns were then treated as experimental data and modeled using the latest version of the WPPM software PM2K, which has been expanded to consider the different TDS models discussed in this work. In particular two models which have been developed for the special considerations of the TDS from small crystallites were employed to model the patterns from the core-shell simulations. The first model is the modification of the Warren TDS model to account for a maximum phonon wavelength which can exist in in the crystallite. The theory which governs this model has been described in Section 7.4.1. The second model was then the substitution of Warren's first order TDS with the TDS predicted by Urban's model. This theory has been laid out in Section 7.4.2, and includes a further extension of Warren's model which attempts to include the contributions of any surface modes to the TDS. The comparison of these two models then allows for the demonstration

of how each extension influences the results of the diffraction pattern modeling.

The procedure of simulating the atomic motion in the core, calculating the diffraction pattern and then modeling the pattern assuming these models for the TDS was repeated for particles having diameters from 5nm to 20nm. The high level of agreement between the simulated patterns and the best fit model is depicted in the different weighted sum of squares (wss) in Figure 50. It is observed that the Urban model actually resulted in a slightly better fit of the simulated pattern than the modified Warren TDS model. Also, the fit for patterns from smaller crystallites was found to be better than that for larger particles. It is possible that this is evidence that the TDS models are better suited to describe the diffuse scattering found in the diffraction pattern from these cases. However, it is also possible that the TDS is not as apparent in these cases as the broadening due to the small particle size dominates the simulated pattern. It was found that both models resulted in a systematic difference in the modeled pattern which was found for all sizes considered. The difference is most evident when studying the difference patterns of the fits obtained for the largest particles which have a diameter of 19nm, and are depicted in Figure 51. The same patterns in the difference was also found when using each model on the smaller sizes, however, the features became less defined as the particle size decreased.

Both models resulted a nearly perfect match of the obtained lattice

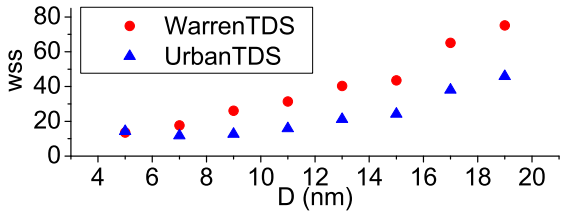

Figure 50: Weighted Sum of Squares (wss) which was obtained from modeling the patterns from the core-shell simulations.

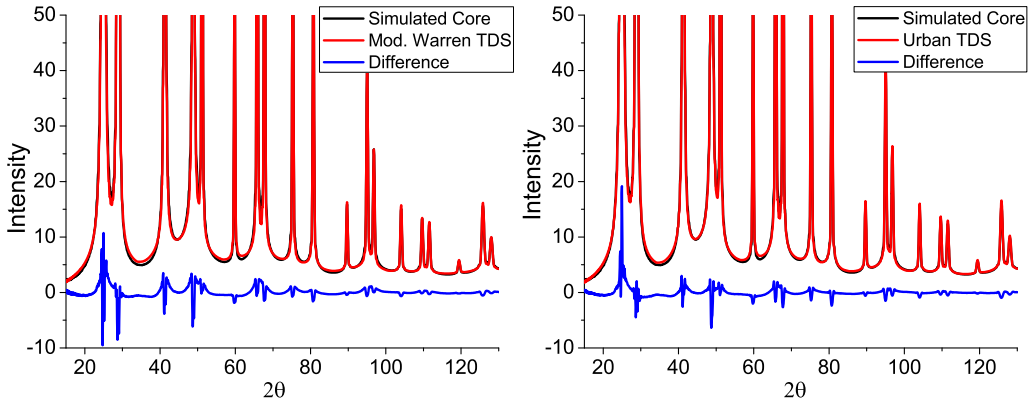

Figure 51: Best fits of core-shell patterns when assuming Warren TDS and Urban TDS

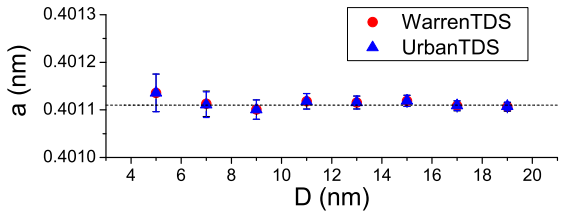

Figure 52: The lattice parameters (a) obtained from modeling the core-shell patterns.

parameter and particle size from the modeling. The trends of this agreement with particle size is shown in Figured 52 and 53 for the obtained lattice parameter and relative deviation of the crystallite size respectively. The Urban TDS model resulted in a slightly better agreement than the Warren model between the known core size and that obtained from the modeling. However, the difference is very slight, within the estimated standard deviation of each parameter. Also, the particle size is always correctly determined to within 1%. This high level of agreement should be compared to the errors introduced in the determined particle size when assuming a smooth Chebyshev polynomial to model the TDS, which is described in Section 7.3.2. Therefore, a proper handling of the TDS can be important when trying to quantitatively determine microstructural parameters like the particle size.

Finally, the values obtained for the Debye-Waller parameter, B_{iso}, can be compared. The atomic positions in the MD simulations have been analyzed to determine the mean squared displacement (MSD). The MSD, $\langle \mathbf{u}^2 \rangle$, is then related to B_{iso} by the relationship expressed in Equation

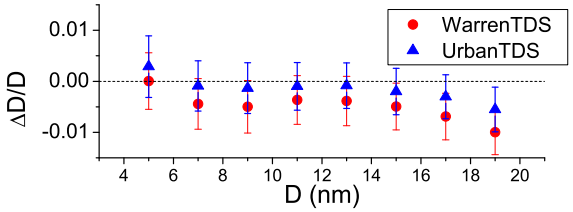

Figure 53: The relative error ($\Delta D/D$) in the diameter obtained in the modeling of the core-shell patterns.

(128). The results using both models are then compared to this expected value in Figure 54. Though all simulations were done at the same temperature, the trend of the B_{iso} of from the core atoms is increasing due to the pinning of the atoms near the interface by the rigid encapsulating shell. As the particle size decreases, the fraction of atoms which are pinned near this interface increases, leading to a decrease in the average MSD.

While for the smaller particle sizes both models tend to slightly overestimate the B_{iso}, on the whole, the modified Warren TDS model allows for a better match with the expected results. It is also evident that for the larger particle sizes, the Urban model tends to underestimate the B_{iso} of the system. This underestimation is believed to be due to the lack of normalization in the Urban model when considering the contribution from the surface modes. As mentioned in the derivation of the other models, the integrated density of states for the system must equal $3N$ (see Equation (151)). In the model which has been formulated by Urban

the contribution from the surface modes is just added on to the volumetric part, which already has been correctly normalized. Therefore, the total integrated density of states from the volumetric, surface and edge contributions will be greater than $3N$. This has the consequence of correspondingly scaling the TDS. To conserve the integrated intensity in the powder pattern, the only factor which should scale the TDS is the B_{iso} parameter. In the present modeling the β_1 in the Urban model was taken as the suggested (yet arbitrary) value of 1.35. Therefore, since the Urban TDS was slightly scaled by the surface contribution, a smaller B_{iso} parameter was necessary to model the TDS contribution. While this study points out this flaw in the Urban model, work is currently on going to correct for this and properly normalize the Urban model.

The initial purpose of the current study was to demonstrate that the small particle size actually limits the maximum wavelength which a phonon can have in the system, and this feature is also present in the observed TDS. The Warren and Urban TDS models have been implemented in such a way which allows for the refinement of this maximum wavelength parameter. A comparison of the values obtained from the two models is depicted in Figure 55, along with a line which depicts the trend of $\lambda_{max} = D$. The large uncertainty in the values obtained from the very small particle sizes unfortunately does not allow for a clear understanding of the observed trend for the smallest sizes studied. When

the particle size approaches 10 nm, it is found that the Warren model observed an trend of λ_{max} which is nearly equivalent to the diameter of the core region. The Urban model finds a similar increasing trend, however, the values of the obtained λ_{max} are slightly less than those found from the Warren model. While some disagreement in the value of the λ_{max} exists, it is important to note that both models find an increasing λ_{max} with particle size, which is evidence of the phonon confinement effect.

In the original formulation described in Section 7.4.1, it was predicted that λ_{max} was proportional to $2D$, while the results of the modified Warren model seem to suggest that for the considered system λ_{max} is proportional to D. This implies that in the simulated system the first harmonic mode is suppressed, and that the largest phonon mode is actually something like the second harmonic mode, which has a node also in the center of the core. This is reasonable since due to the fixed boundary conditions of the system, the existence of the first harmonic mode in the system would put an anti-node at the center of the particle, which would mean that those center atoms would undergo large displacement fluctuations. However, the spherical symmetry of the core region does not allow for this kind of motion, and displacement waves are expected to have a radial symmetry. Therefore, the finding that the second harmonic mode is the largest phonon is consistent with the constructed particle system.

In conclusion, this study of modeling the TDS from small core-shell

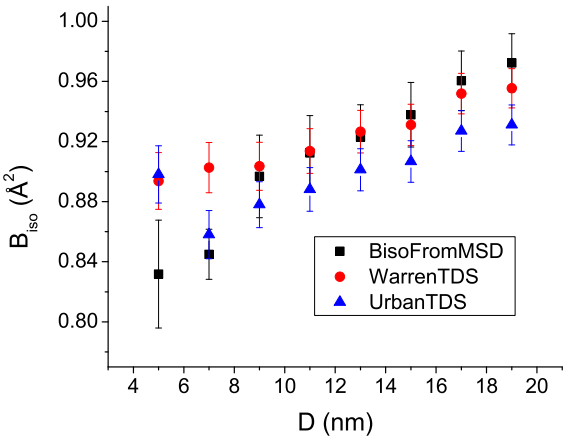

Figure 54: The Debye-Waller factor (B_{iso}) obtained from modeling the core-shell patterns.

crystallites shows the level of agreement which can be expected from applying the developed small crystallite TDS models in ideal circumstances. A number of reasons can be cited to explain the discrepancies found in the modeling. On the diffraction theory side the number of simplifying assumptions taken to arrive at the final form of the TDS, including the heavy reliance on the DOS predicted by the Debye model, can explain some of the differences found. Meanwhile, the simulation is also not without flaw, as the interaction potential is really the entity which is controlling the thermal behavior of the system, and artifacts cannot be ruled out from the constructed core-shell system. The current simulation then serves to showcase the current level of understanding on each side, and the many ways in which they can to be improved before a more exact modeling of the TDS can be obtained.

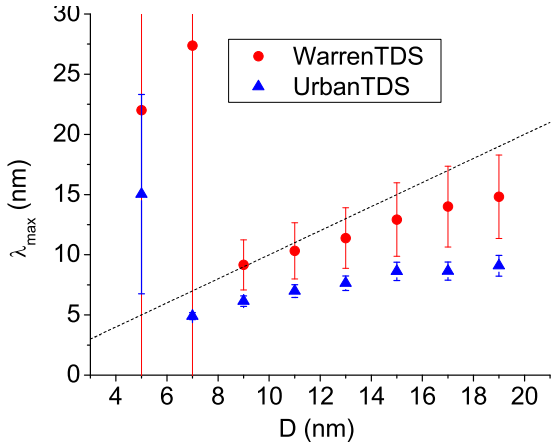

Figure 55: The maximum phonon wavelength (λ_{max}) obtained from modeling the core-shell patterns.

CHAPTER VIII

MODELING EFFECTS OF FAULTING IN A FINITE FCC CRYSTALLINE DOMAIN

The effect of both twin and deformation faults on the line profiles of FCC metals can be described using the method of difference equations developed for the FCC case by Paterson [103] and later adopted by Warren [153]. However, in this theory assumptions are made which are unjustified when the coherent domain size becomes small. First, an infinite stacking of planes is assumed when modeling the probability correlation function. This function commonly denoted $P_0(n)$ is the probability of finding two layers of the same type (i.e.: A, B, or C) n layers apart. Clearly this infinite stacking does not hold for the case of nanocrystalline materials, as the domain size shrinks to the limit where the number of planes becomes countable. Second, the crystallite is treated as having a constant cross-sectional area of each plane. This assumption is warranted as long as the crystallite is large enough such that the scattered intensity is dominated by a core region with a constant cross-section, and the intensity from the remaining crystallite volume is negligible. However, as the crystallite size diminishes the volume of this core region becomes

comparable to the remaining crystallite volume, and the constant cross-section assumption is no longer accurate. It is then the goal of this work to quantify how large is the error in the fault probabilities obtained from employing the latest theory of faulting in diffraction to analyze the diffraction pattern from crystallites which are small, and do not have a constant planar cross-section. Then, a new method of describing the effect of faulting in a finite planar stack will be developed and shown to be effective at representing the effect of faulting in small domains.

8.1 Powder Diffraction Theory of Faulting

Beginning with the description of Warren [155], the intensity in reciprocal space from a finite crystallite containing faults can be expressed as

$$I = \psi^2 \sum_{m=-\infty}^{\infty} N_m \left\langle e^{i\phi(m)} \right\rangle e^{2\pi i m h_3/3}. \tag{159}$$

In this expression (Warren, Equation 13.39) the FCC lattice is described in terms of a hexagonal lattice with continuous reciprocal space coefficients $h_1$and h_2 defined in the (111) plane and h_3 normal to the plane. The symbol ψ^2 represents the form factor of the planes and is factorized outside of the sum by approximating the crystallite as a columnar stack of (111) planes with equivalent cross sections. The term N_m represents the number of pairs of planes separated by a distance md_{111}, where m is an integer and d_{111} is the distance between planes in the stack, and $\left\langle e^{i\phi(m)} \right\rangle$ is the average phase factor due to the relative displacement of

each plane. This factor is determined considering how the phase changes when scattering occurs from two planes of different type. Since FCC can be represented as an ABC stacking there are only three distinct phase factors:

$$\begin{aligned}
&\phi_0(m) = 0 && \text{when pair is of the same type (i.e. AA),}\\
&\phi_1(m) = -2\pi(h_1 - h_2)/3 && \text{when pair is a positive sequence (i.e. AB),}\\
&\phi_2(m) = 2\pi(h_1 - h_2)/3 && \text{when pair is a negative sequence (i.e. AC).}
\end{aligned} \tag{160}$$

The average phase factor is then expressed as

$$\langle \exp(i\phi(m)) \rangle = P_0(m) \exp(i\phi_0(m)) + P_1(m) \exp(i\phi_1(m)) + P_2(m) \exp(i\phi_2(m)) \tag{161}$$

where $P_i(m)$ is the probability of finding a pair of planes of type i, separated by m planes. In a powder, symmetry exists between $P_1(m)$ and $P_2(m)$ because a positive stacking sequence will then become negative when observed from the opposite point of view. Therefore, these two probabilities are equal, and utilizing the normalization condition gives

$$\langle \exp(i\phi(m)) \rangle = P_0(m) + (1 - P_0(m)) \cos(2\pi(h_1 - h_2)/3). \tag{162}$$

Therefore, the effect of faulting on the powder pattern of FCC crystallites is completely determined by the probability correlation function, $P_0(m)$.

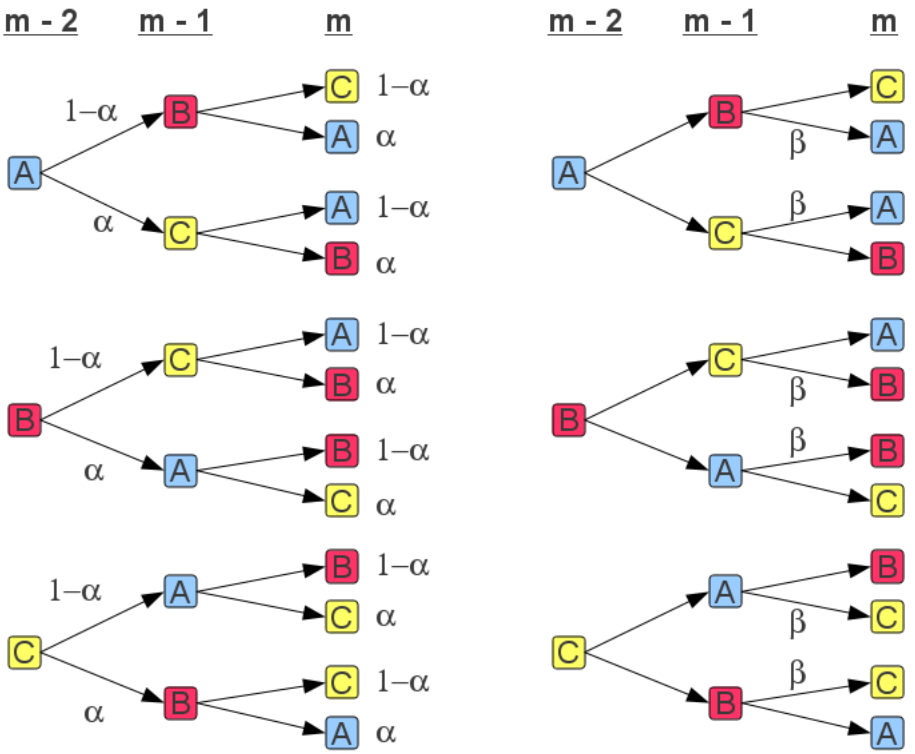

Figure 56: All possible sequences basal planes which make up an orthorhombic lattice are related to the probability of deformation faulting (left) and twin faulting (right).

8.1.1 Recursion solution to $P_0(m)$

Most existing methods to calculate the planar correlation function, $P_0(m)$, rely on a probabilistic treatment, similar to the initial works of Hendricks and Teller [65], as well as Wilson [162], which relates the probability of a fault existing on a given plane to the type of preceding plane. Figure 56 depicts all possible sequences of three FCC (111) planes, and relates them

to the probability of a fault existing in the sequence. From these kinds of sequences, recursion relations can be determined which describes the probability of finding a plane of the same type between different levels of the sequence. The resulting recursion relations take the form

$$P_0(m) + P_0(m-1) + P_0(m-2) - 1 = \alpha(1-\alpha)(3P_0(m-2) - 1) \quad (163)$$

and

$$P_0(m)+P_0(m-1)+P_0(m-2)-1 = \beta(P_0(m-1)+2P_0(m-2)-1), \quad (164)$$

for deformation and twin faults respectively. Assuming that the faulting configuration in the crystallite does not allow for the possibility of both a twin and deformation fault to exist near one another, the contribution of each to the correlation function (the right hand side of Equations (163) and (164)) are additive, and the general recursion relation becomes

$$P_0(m) + P_0(m-1) + P_0(m-2) - 1 = \alpha(1-\alpha)(3P_0(m-2) - 1)+ \beta(P_0(m-1) + 2P_0(m-2) - 1). \quad (165)$$

The final assumption, regarding of the nature of how the faults are distributed in a crystallite, has been explored by numerous authors to derive different recursion relations. Estevez-Rams *et al.* (E-R) [44] has shown that when both deformation and twin faults are allowed to exist within crystallite in a random arrangement without any assumption of their proximity, the expression of Equation (165) is missing factors of the form $\alpha\beta$ and $\alpha^2\beta$. Before this, the work of Jagodzinski and coworkers [74, 75]

studied how specific arrangements of twins and faults affected the correlation function by extending the recursion treatment to consider sequences of more than three layers.

Recursion relations like Equation (165) have a known solution of the general form

$$P_0(m) = a + bx^m. \tag{166}$$

The a, b, and x parameters are then solved for by plugging this solution into the recursion relation like Equation (165). In this case, the probability correlation function is found as [147]

$$P_0(m) = \frac{1}{3}\left[1 + \left(1 + \frac{i\beta}{\varphi}\right)\left(\frac{-(1-\beta) + i\varphi}{2}\right)^m + \left(1 - \frac{i\beta}{\varphi}\right)\left(\frac{-(1-\beta) - i\varphi}{2}\right)^m\right], \tag{167}$$

where

$$\varphi^2 = 3 - 12\alpha - 6\beta + 12\alpha^2 - \beta^2. \tag{168}$$

The solution corresponding to the recursion relations of E-R [44] follows the same form except the variable φ is found to be

$$\varphi_{ER}^2 = 3 - 12\alpha - 6\beta + 12\alpha^2 - \beta^2 + 24\alpha\beta(1-\alpha). \tag{169}$$

The reader is referred to the discussion presented by Estevez-Rams *et al.* [44], which describes how this solution changes for the cases when $\varphi^2 = 0$ and $\varphi^2 < 0$.

Often it is desirable to express the complex solution of the correlation function found in Equation (167) in polar form. It can be shown that

the correlation function is then found to be

$$P_0(m) = \frac{1}{3}\left[1 + 2(-1)^m Z^{|m|}\left(\cos m\gamma + \frac{\beta}{\varphi}\sin|m|\gamma\right)\right], \tag{170}$$

where

$$Z = \frac{1}{2}\left[(1-\beta)^2 + \varphi^2\right]^{1/2}, \tag{171}$$

and

$$\gamma = \arctan\left(\frac{\varphi}{1-\beta}\right). \tag{172}$$

8.1.2 Resulting Fourier transform of powder peak

As discussed by Warren [155], the average phase factor for a powder in Equation (162) can take on two forms

$$\langle \exp(i\phi(m))\rangle = \begin{cases} 1 & L_0 = 0 \pmod 3 \\ (3P_0(m)-1)/2 & L_0 = \pm 1 \pmod 3 \end{cases} \tag{173}$$

where L_0 is related to the FCC peak indices by $L_0 = h + k + l$. Since the average phase factor is not affected by a change in the probability correlation function when $L_0 = 0 \pmod 3$, we will refer to those members of the hkl family of reflections as the unbroadened subcomponents. Furthermore, those who satisfy $L_0 = \pm 1 \pmod 3$ will be referred to as the broadened subcomponents.

Considering Equation (170), the average phase factor of the broadened components is then given by

$$\langle \exp(i\phi(m))\rangle = (-1)^m Z^{|m|}\left(\cos m\gamma + \frac{\beta}{\varphi}\sin|m|\gamma\right). \tag{174}$$

This expression can then be used in Equation (159) to find the effect which faulting has on the distribution intensity in reciprocal space. Since all other factors are even in m, the imaginary part of the FT will cancel, leaving the intensity given as

$$I(h_1h_2h_3) = \psi^2 \sum_{m=-\infty}^{\infty} N_m Z^{|m|} \left(\cos m\gamma + \frac{\beta}{\varphi} \sin |m|\gamma \right) \cos\left(\frac{2\pi m h_3}{3} + \frac{1}{2} \right). \tag{175}$$

Using trigonometric identities to re-express the product of cosines and sines results in the intensity of the form

$$I(h_1h_2h_3) = \psi^2 \sum_{m=-\infty}^{\infty} N_m Z^{|m|} \left[\cos\left(2\pi|m| \left(\frac{h_3 - L_0}{3} + \delta_{B_3} \right) \right) + \sigma_{L_0} \frac{\beta}{\varphi} \sin\left(2\pi|m| \left(\frac{h_3 - L_0}{3} + \delta_{B_3} \right) \right) \right], \tag{176}$$

where δ_{B_3} the peak shift in the $\mathbf{B}_3$ direction defined as

$$\delta_{B_3} = \sigma_{L_0} \left(\frac{\gamma}{2\pi} - \frac{1}{6} \right), \tag{177}$$

and

$$\sigma_{L_0} = \begin{cases} +1 & L_0 = 1 \pmod 3 \\ 0 & L_0 = 0 \pmod 3 \\ -1 & L_0 = -1 \pmod 3 \end{cases}. \tag{178}$$

The intensity given by Equation (176) is actually the distribution of intensity around a Bragg spot. In order to obtain the powder intensity, the broadening due to the cross-section, ψ^2, is ignored, and the intensity in reciprocal space approximated as a thin rod extending from the Bragg

spot in the direction normal to the faulting plane. The powder intensity from that Bragg spot is then obtained by remapping this intensity in terms of the radial direction in reciprocal space, s. This transformation is given by

$$\begin{aligned} \Delta h_3 &= 3\frac{a^2 s_{hkl}}{L_0}\Delta s, \\ &= 3\frac{h_0^2}{L_0 s_{hkl}}\Delta s, \end{aligned} \tag{179}$$

where $h_0^2 = h^2 + k^2 + l^2$, and $\Delta s = s - s_{hkl}$. Therefore, neglecting the scale factor which will be given in Equation (214), the powder intensity becomes

$$I(s, s_{hkl}) \propto \sum_{m=-\infty}^{\infty} N_m Z^{|m|} \left[\cos\left(2\pi|m|\left(\frac{h_0^2}{L_0 s_{hkl}}\Delta s + \delta_s\right)\right) + \sigma_{L_0}\frac{\beta}{\varphi}\sin\left(2\pi|m|\left(\frac{h_0^2}{L_0 s_{hkl}}\Delta s + \delta_s\right)\right)\right], \tag{180}$$

where

$$\delta_s = \sigma_{L_0}\frac{L_0 s_{hkl}}{3h_0^2}\left(\frac{\gamma}{2\pi} - \frac{1}{6}\right). \tag{181}$$

In some cases it is preferable to express this relationship in the formalism of the Fourier integral. In which case, we introduce the real space variable

$$L = \frac{m h_0^2}{L_0 s_{hkl}}, \tag{182}$$

and express the powder intensity from the broadened components as

$$I(s, s_{hkl}) \propto \int_{-\infty}^{\infty} N_m Z^{|m|} \left[\cos\left(2\pi L\Delta s + \delta_s\right) + \sigma_{L_0}\frac{L_0}{|L_0|}\frac{L}{|L|}\frac{\beta}{\varphi}\sin\left(2\pi L\Delta s + \delta_s\right)\right] dL. \tag{183}$$

The factor N_m is really the size contribution, which can be expressed more generally as $A_S(L)$. Then the Fourier coefficients due to faulting are given by

$$A_F(L) = Z^{|\sigma_0 L_0 s_{hkl}/h_0^2|}, \tag{184}$$

$$B_F(L) = \sigma_{L_0} \frac{L_0}{|L_0|} \frac{L}{|L|} \frac{\beta}{\varphi}, \tag{185}$$

and the intensity is found to be

$$I(s, s_{hkl}) \propto \int_{-\infty}^{\infty} A_S(L) A_F(L) \left[\cos\left(2\pi L \Delta s + \delta_s\right) + B_F(L) \sin\left(2\pi L \Delta s + \delta_s\right)\right] dL. \tag{186}$$

This is the form of the intensity which is used in the WPPM method [124, 125] and is implemented in the program PM2K [86]. It should be kept in mind that the intensity given by relations like Equations (180) and (186) only give the intensity from a single component. The observable powder diffraction peak must be constructed by summing contributions from each component in the family of planes. The correct considerations for faulting has been presented by Velterop *et al.* [147], and a few examples will be presented in Section 8.4.1.

8.2 Study of Faulting in Nanoparticles

The following study will then test the validity of the expressions just described to predict the effect of faulting in small domains. The fault probability in a constructed model of a Au spherical nanoparticle will be

compared with that obtained from modeling the Debye simulated powder pattern using the WPPM methodology.

8.2.1 Atomistic Model and Pattern Simulation Procedure

Diffraction patterns were calculated by applying the Debye function (see Equation (24)) to a geometrical computer construction of a spherical Au particle containing either twin or stacking faults, such as those depicted in Figure 57. In this study the polarization effect describing the intensity from unpolarized incident x-rays, described by Equation (14), and a wavelength of Cu Kα_1 radiation (λ = 1.54056 Å) were assumed. A Debye-Waller temperature factor was not included in the calculation as it would only diminish the calculated intensity, and thereby make the effect of faulting less evident with the increase of scattering angle.

The simulated spherical particle used to calculate the interatomic distances was constructed beginning from a perfect Au FCC lattice (a = 4.0809 Å) of dimensions slightly larger than the desired sphere. A twin fault was created in the lattice by rotating all planes above the desired fault plane by 180° about the normal vector to the plane, while a deformation fault was created by removing the desired plane and shifting all atoms above by an interatomic spacing in the direction of the missing plane. The spherical particle of the desired size was then cut out of the faulted lattice.

Also considered in this study was an average pattern resulting from a

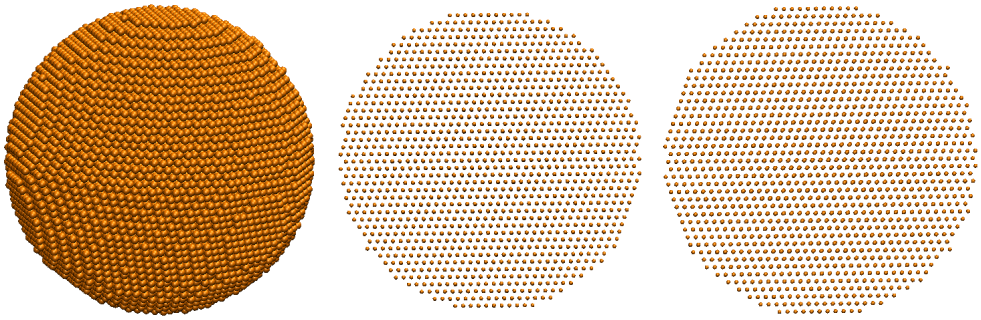

Figure 57: The left image is a 3D view of a constructed spherical particle ($D = 9.8$nm), the middle image is a cross-section view of a particle containing a deformation fault through its center, and on the right is a cross-section view of a particle containing a twin fault through its center.

system of many particles. The creation of this system follows the methods discussed in Chapter 6. All particles were created with the same diameter, however, the fault position was randomly chosen in each particle. A system of this type simulates a more realistic powder, and allows for an averaging over all possible fault positions. The contribution of inter-crystallite scattering was not considered to avoid the effect of particle packing density in the small-angle region. This approach allows for the modeling of the average pattern over the full range of the diffraction pattern without considering the particle structure factor.

8.2.2 Modeling the simulated pattern with modern theory

The calculated diffraction patterns were then treated as experimental data and modeled using PM2K [86], a modern line profile analysis software based on Whole Powder Pattern Modelling (WPPM) [126, 124, 128].

This is a line profile analysis method which combines the effects of crystallite characteristics on the diffraction peaks in reciprocal space, then uses their Fourier transform to model the observed pattern.

In the modeling it was only necessary to consider the effects of a delta size distribution of spherical crystallites and stacking faults on the wide-angle peak profiles. While the effects of a size distribution have been discussed elsewhere [124], the effect of faulting used in this study did not exactly follow that described in previous articles on the WPPM method. Instead, faulting Fourier coefficients were used which include previously neglected high order dependence on the fault probabilities. The low fault probability present in the crystallites of this study falls into the case of $s^2 > 0$ following the notation of Estevez-Rams *et al.* [44]. The Fourier coefficients of the diffraction peak shape due to faulting used in this work are then given by Equations (169), (184), and (185). These expressions were implemented in PM2K in place of Equation. 13a,b described in Reference [124]. This form of the faulting Fourier coefficients follows from considering a stacking which contains both deformation and twin faults simultaneously, and has been derived to be more accurate through the entire range of faulting probabilities [43, 44].

In this study both the small-angle and wide-angle regions were considered concurrently over the range of 2θ from 0 to 175 degrees. In order to account for the small-angle region in the modeling the known pattern from a monodisperse, isolated spherical particle was scaled and then

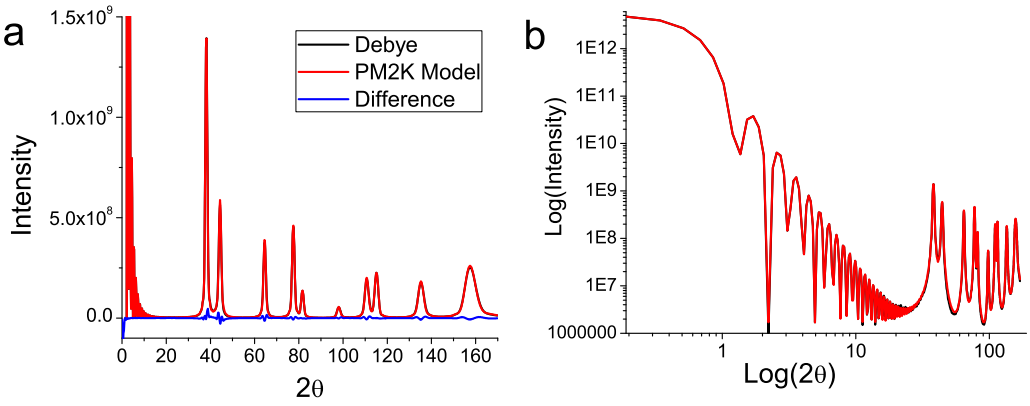

Figure 58: The depicted PM2K modeling from a sphere ($D = 9.8$nm) containing a twin fault at its center shows the level agreement in (a) the wide-angle, and (b) the small-angle regimes which was also achieved for the patterns from other studied crystallites.

added to the wide-angle pattern. By considering the value of the Debye function at zero degrees, it is evident that this scale parameter should be N^2, where N is the number of scatterers in the system. Also, the same atomic structure factor and polarization factor were applied to the small-angle pattern to be consistent with the Debye function calculation. The inclusion of the small-angle contribution was necessary, because as the simulated crystallites were very small, oscillations from this feature extended into the region near the 111 peak. Also, including the small-angle region allowed for an independent determination of the particle size, thereby, eliminating any correlation between the size and faulting found from solely studying the line profiles.

The modeled wide-angle diffraction pattern was scaled in electron units by an analytical factor to match the intensities given by the Debye

function. As already discussed in Section 3.2, Warren [154] and Patterson [104] have already shown that the crystallite size contribution to the powder peak is described by Equation (56). The use of this scale parameter, as well as the necessary polarization and atomic scattering factors, allows for a direct match of the PM2K modeled pattern and the Debye pattern without the use of a background function. In the modeling of the diffraction pattern only 4 free parameters where then necessary to refine: the lattice parameter, faulting probability, particle size, and a variable scale factor which was independent of 2θ. The variable scale factor was always found to be 1.0, which is a further verification of the normalization and analytical scale factor used. Figure 58 exhibits the quality of the fits obtained in both the small-angle and wide-angle regions of the pattern.

8.2.3 Discussion of Modeling Results

First, patterns simulated from individual spherical particles containing a single fault were modeled using the previously described method. A sequence of spheres containing a fault positioned increasingly distant from the center of the sphere was used to study the influence on the calculated intensity and the determined fault probability. The fault position was measured in terms of the distance from the particle center to the fault plane along the fault plane normal vector. Keeping with the implicit assumptions of the Paterson-Warren treatment, if each (111) plane has an equal area and equal probability of containing a fault plane, and given

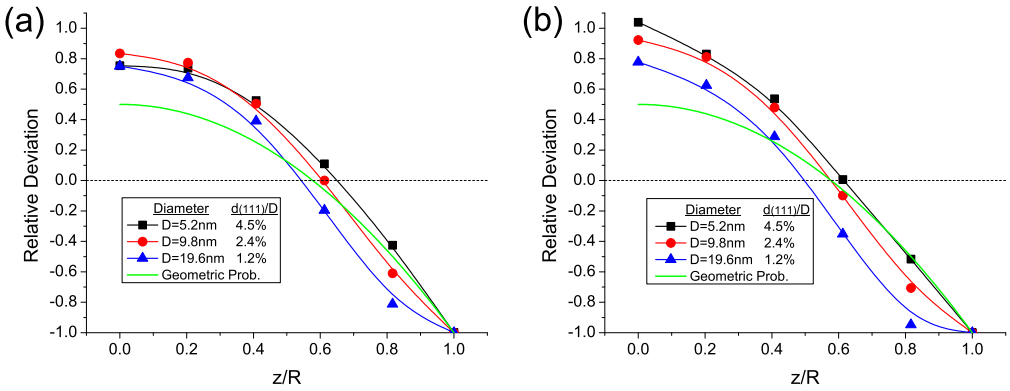

Figure 59: The relative deviation from the planar fault probability of the PM2K determined fault probability for (a) spheres containing a deformation fault, and (b) spheres containing a twin fault are shown as a function of fault position. The relative deviation is defined as $(\alpha_{PM2K} - \alpha_p)/\alpha_p$. The fault position ($z$) is also normalized by the sphere radius (R) to allow for direct comparison of the observed trends with increasing size.

that each particle contains one fault, the fault probability is simply given by the inverse of the number of (111) planes, N_{111}. In terms of the particle size, D, and interplanar distance, d_{111}, this planar probability, α_p, is given simply as

$$\begin{aligned} \alpha_p &= \frac{d_{111}}{D}, \\ &= \frac{a}{D\sqrt{3}}. \end{aligned} \tag{187}$$

The fault probability obtained from the modeling can then be compared to this value to measure a relative percent deviation from the equal planar area assumption. The trends of this deviation for different particle sizes are shown in Figure 59 for both twin and deformation faults, where the fault position has now been normalized by the sphere radius. As the fault moves away from the center, the effect on the pattern and

the determined fault probability decreases for both deformation and twin faults. A possible explanation of the decreasing trend of the determined fault probability is the corresponding decrease of the fault plane surface area. The area of a plane, A, intersecting a sphere at different distances from the sphere center, z, is geometrically found to be

$$A = \pi R^2 \sin^2 \left(\arccos \left(z/R \right) \right), \tag{188}$$

where R is the sphere radius. A volumetric fault probability, α_V, can then be defined from the fault plane area, the sphere volume, and assuming the fault thickness is equal to one interplanar distance

$$\begin{aligned} \alpha_V &= \frac{A d_{111}}{V}, \\ &= \frac{a\sqrt{3} \sin^2 \left(\arccos \left(z/R \right) \right)}{4R}. \end{aligned} \tag{189}$$

The relative deviation of this volumetric fault probability to the planar probability becomes independent of sphere size, and is compared with the determined fault probabilities in Figure 59. While the general trend of the determined fault probabilities is roughly represented by the volumetric probability, it is clear that it poorly represents the percent deviation when the fault is near the center of the particle and it does not account for the size dependence in the trends observed.

It is evident from Figure 59 that for a given fault position the relative deviation decreases as the particle size increases. This observation is related to finite stacking which is present in the particles. As a particle becomes larger it agrees more with the Paterson-Warren theory which

Table 3: Fault probabilities and relative deviations determined from the average patterns from systems containing 100 spheres with $D = 9.8$nm, and α_p of 0.0244.

	1 Fault / Particle		Constant System Fault Prob.	
	PM2K Prob.	Relative Dev.	PM2K Prob.	Relative Dev.
Def. Faults	0.0268	0.0996	0.0233	-0.0539
Twin Faults	0.0320	0.3140	0.0292	0.1975

assumes an infinite stacking, and the relative deviation decreases. This effect also accounts for the different shapes of the faulting probability trends and the changing intersection point of these trends with the planar and geometrically derived fault probabilities. Therefore, both the changing planar area, and the finite stacking present in nanocrystallites, are necessary to describe the trends observed in the determined fault probability, and the effects which faulting has on their diffraction peak shapes.

It is then of interest to study how this dependence on fault position is perceived on average. The use of a single particle to calculate the diffraction pattern using the Debye Function implies a powder of identical particles. A real system will contain crystallites with different minimum energy fault configurations and whose diffraction pattern is the average of the scattered intensity from each crystallite. As a first approximation the Paterson-Warren theory does not consider the energetics of a stacking sequence, but assumes that on average faulting will seem random with each plane having an equal probability to contain a fault. In this study, average patterns from systems of 100 particles were generated

following two different schemes to distribute faults among the particles which are consistent with this assumption. The first scheme assumed that each particle contained one fault and that the fault was randomly positioned. The second scheme assumed that only the total fault probability of the system was conserved, allowing for the number of faults in each particle and the respective fault positions to be randomly chosen. Therefore, in the second case some particles will contain multiple faults while others can contain no faults. In all systems only spheres with a diameter of 9.8nm were used, and the total planar fault probability was set to $1/N_{111}$, which is 0.0244 for this particle size. Also, the patterns from systems containing different numbers of particles were studied to ensure that 100 particles are enough to produce a statistically representative average pattern in each case following the methods discussed in Section 6.3. The values of the fault probabilities determined from modeling the resulting diffraction pattern, and their relative deviation from the planar fault probability, are compared in Table 3. The determined average fault probability is seen to fall within the bounds of the probabilities found in the fault position study. It is interesting to note that a lower deviation is observed for the particle systems containing deformation faults, and the deviation for those containing twins is found to be as much as 30%. The better agreement of the determined deformation fault probability with the planar fault probability is also observed in Figure 59. It is also interesting to note that the determined fault probability is different

depending on the assumptions used to distribute the faults throughout the system. This suggests a further correction to the Paterson-Warren theory, as faults which cannot be considered infinitely dilute and non-interacting can also affect the observed diffraction pattern and obtained fault density.

The recursion relation treatment of Paterson and Warren is a statistical method which describes the effect of faulting on the pattern from an average system, and thus must be compared with a pattern from an analogous system. When the pattern from a system containing different fault positions was considered the determined fault probability tended to overestimate the planar fault probability present in the system. This result is linked to the trend found for the fault position dependence in Figure 59 where the fault probability was generally over estimated until it was moved close to the surface. The obtained deformation fault probability seemed to agree better with the expected value than those obtained for systems containing twin faults as a maximum deviation of about 10% versus 30% was observed respectively for each. Furthermore, even at the low fault probability considered, differences were observed in patterns depending on how faults are distributed throughout the system. This seems to suggest that, for this small crystallite size, interaction between faults causing multiple disruptions of the crystalline stacking may have an enhanced influence on the resulting diffraction pattern.

This study has then shown that the effect which faulting has on the

powder diffraction pattern from a single crystallite is strongly dependent on the fault position. Both the finite stacking sequence present in a spherical nanocrystallite and a changing surface area of the planes must be considered to properly account for this position dependence. To this end, a further study on the consequence of having a finite stacking has been performed, and a modified theory accounting for this effect will be described in the remainder of the chapter.

8.3 Planar Correlation of Finite Domains Containing Faults

In order to study the effect of faulting in a small crystallite it is necessary to develop a different strategy to calculate the probability correlation function. In our approach, first a basic understanding of how a fault changes the correlation between a pair of planes will be discussed. Then, it will be shown how a termination in the sequence affects this correlation, and simple statistical reasoning will be used to derive analytical expressions for the probability correlation function of a finite stack containing a fault. Finally, an ensemble average of these expressions is carried out to obtain a form of the probability correlation function more consistent with that observed in a powder. A demonstration of the resulting diffraction profiles concludes this study along with a comparison with peak profiles obtained assuming the latest formulation of the recursion method solution for FCC materials. This type of model is especially suited for the case of small crystalline domains, thin films or metal nanoparticles,

whose energetics do not allow for large numbers of faults within a given domain. It is then not suited to study multiple twinned particles, which can contain three or five twin faults arranged in a non-crystallographic symmetry [91, 23].

8.3.1 Effect Of Deformation Faults

To understand how faulting changes the correlation between planes, it is enough to study an example stacking sequence before and after the creation of a fault. Here we will only consider the forward stacking direction and later account for the opposite stacking direction in the calculation of the powder diffraction pattern (see discussion leading to Equation (162)). The FCC lattice is represented as a stack of (111) planes and the ABC convention is used to denote the three different plane types. As shown in the following examples the fault position is denoted by a pipe "|" in the sequence.

$$\ldots ABCABCA\ldots \text{(perfect)} \tag{190a}$$

$$\ldots ABCA|CAB\ldots \text{(deformation fault)} \tag{190b}$$

$$\ldots ABCA|CBA\ldots \text{(twin fault)} \tag{190c}$$

Any pair of planes can be characterized by the number of planes which are spanned, m, and the number of steps between these planes in a forward permutation, which we will call the pair type, i (i.e. $i = 1$ for (AB), and $i = 2$ for (AC)). It is readily noticed that for a perfect

stacking sequence all pairs with a separation m are of type i, where $i \equiv m \pmod{n}$ and n is the number of different plane types in the sequence. A separation, m, then can be said to belong to the set m_i, making the calculation of $P_0(m)$ trivial for an infinite perfect stacking sequence. In this case all spacings in the set m_0 are between pairs of type 0, implying $P_0(m_0) = 1$, and these are the only spacings between pairs of type 0, so $P_0(m_{i\neq 0}) = 0$.

By studying the planar sequence of Equation (190b), we find that a deformation fault affects the planes after the fault by changing them to the next type in the forward permutation sequence. Also, only a pair of planes which has a fault between them will have their pair type affected by this change. Comparison of stacking sequences with and without a deformation fault, such as those depicted in Equations (190a) and (190b), finds that a pair, Δ_i, which spans a fault will change its type, i, following

$$\Delta_0 \xrightarrow{f} \Delta'_1, \qquad \Delta_1 \xrightarrow{f} \Delta'_2, \qquad \text{and} \qquad \Delta_2 \xrightarrow{f} \Delta'_0. \tag{191}$$

In these relations the pairs which do not span a fault are depicted on the left of the arrow, while on the right denoted with an apostrophe are the new pair types due to the pair spanning a fault. By this notation, the transformation of $(AA) \xrightarrow{f} (AB)'$ falls in the case of $\Delta_0 \xrightarrow{f} \Delta'_1$. A stacking fault then not only increments the plane type, but also has the effect of incrementing the pair type.

In an infinite stack, the number of pairs separated by m planes which can span a fault is always m. However, in a finite stack the number of

pairs which span a fault depends on the distance from the fault plane to a surface boundary. For example, consider the three finite stacks:

$ABCA|CABCABC$ (p=4),

$ABC|BCABCABC$ (p=3),

$AB|ABCABCABC$ (p=2).

It is evident that in the case of the first fault position depicted, $p = 4$, four distinct pairs having a spacing of four planes ($m = 4$) can span the fault plane. When the fault position is moved to $p = 3$, only three such pairs span the fault and similarly two pairs for $p = 2$. Considering the cases of other pair separations it is found that the number of pairs which span a fault, N_f, is dependent on both the spacing, m, and the fault position, p, and is conditionally expressible as

$$N_f(N, m, p') = \begin{cases} m & m \leq p' \\ p' & p' < m \leq N - p' \\ N - m & N - p' < m \end{cases} . \tag{192}$$

Here p' is the number of planes from the fault to the *nearest* surface, and for a deformation fault,

$$p' = \begin{cases} p & p \leq N/2 \\ N - p & N/2 < p \end{cases} . \tag{193}$$

The case of $N - p' < m$ in Equation (192) means both boundaries are limiting the number of pairs which span the fault, and all pairs in the stack of separation m span the fault.

Using this relationship and the relations of Equation (191), the probability correlation function for a finite stack containing a deformation fault can be derived. If $m \in m_0$ every pair which spans the fault will become a 1-type, so the fraction of pairs which are 0-type is the complement of the fraction which spans the fault. When $m \in m_1$, the number of pairs which become 0-type does not change, and when $m \in m_2$ the fraction of faults which become 0-type is the fraction which spans the fault. These observations, along with Equation (192), result in a probability correlation function of the form

$$P_0(m) = \begin{cases} \underline{m_0} & \underline{m_1} & \underline{m_2} & \\ 1 - \frac{m}{N-m}, & 0, & \frac{m}{N-m} & m \leq p' \\ 1 - \frac{p'}{N-m}, & 0, & \frac{p'}{N-m} & p' < m \leq N - p' \\ 0, & 0, & 1 & N - p' < m \end{cases} . \tag{194}$$

A series of correlation functions calculated using this relationship is shown in Figure 60 for a 50 layer stack containing a deformation fault at different positions. When the fault is near the boundary the planar correlation resembles that of a perfect FCC stack as only correlations for large m are altered. As the fault is moved toward the center of the stack the $P_0(m)$ for smaller separations become increasingly affected. After the fault crosses the middle of the stack a symmetry is observed for the cases of $p = 15$ and $p = 35$, as well as $p = 5$ and $p = 45$, due to their equivalent distance to the nearest surface, p'.

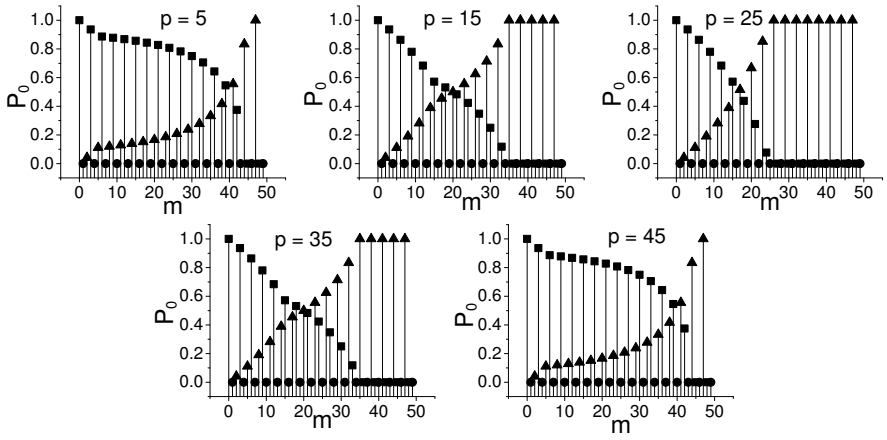

Figure 60: The probability correlation functions, $P_0(m)$, calculated by Equation (194) are depicted for a 50 layer stack containing a deformation fault at series of positions, p. In each case the values of the set m_0 are denoted by ■, those of the set m_1 by •, and those of the set m_2 by ▲ to allow for their clear distinction.

8.3.2 Effect of Twin Faults

The same general treatment described in the previous section can be adopted to study the case of a finite stacking sequence containing a twin fault. Considering a twin located on an A plane, as in the stack shown in Equation (190c), we find that the twin fault has the following effects on the pair type:

$$\begin{aligned}
&(AA) \xrightarrow{t} (AA)', \quad (BB) \xrightarrow{t} (BC)', \quad (CC) \xrightarrow{t} (CB)', \\
&(AB) \xrightarrow{t} (AC)', \quad (BC) \xrightarrow{t} (BB)', \quad (CA) \xrightarrow{t} (CA)', \\
&(AC) \xrightarrow{t} (AB)', \quad (BA) \xrightarrow{t} (BA)', \quad (CB) \xrightarrow{t} (CC)',
\end{aligned} \tag{195}$$

where now the t above the arrow signifies that transformations are due to the pair spanning a twin fault. Unlike the case of the deformation

fault, the expressions in Equation (195) are now specifically dependent on the pair and twin plane, so the Δ_i notation has not been used. Here we only describe the case of a twin on an A-type plane, but analogous expressions are found for a twin on a B or C plane. The transformations like those in Equation (195) define the important pairs to consider when calculating $P_0(m)$. For instance, for the case of an A-type twin it becomes apparent that $P_0(m_0)$ of an ideal stacking will be decreased by an amount proportional to the number of (BB) and (CC) pairs which span the twin fault. Also, $P_0(m_1)$ will be increased by an amount related to the number of (BC) pairs spanning the fault, and similarly $P_0(m_2)$ will be increased by the proportion of (CB) pairs. Assuming the fault is not near a boundary, we find that the number of the important pairs has a solution independent of the fault type

$$N_0(m, m \leq p) = \begin{cases} 2m/3 & m \in m_0 \\ (m-1)/3 & m \in m_1 \\ (m+1)/3 & m \in m_2 \end{cases}, \tag{196}$$

where N_0 stands for the number of pairs which span the twin fault and influence $P_0(m)$ — the second criterion being what differentiates this quantity from N_f, defined in Equation (192).

When the number of important pairs becomes influenced by the presence of a surface boundary, the relationship describing their abundance becomes dependent on the twin plane type. We will define the twin plane

type, t, relative to its distance from the *left* boundary by $t \equiv p \pmod{n}$. The number of important pairs for $p' < m \leq N - p'$ is found by considering a sequence without a boundary, and subtracting the number which are missing due to the nearest boundary. This can be expressed as

$$N_0(p') = N_0(m, m \leq p') - N_X^{m-p'}, \tag{197}$$

where $N_X^{m-p'}$ is the number of planes of type X in a perfect stack of length $(m-p')$. The plane type, X, is determined as the first plane of an important pair for a given twin type. For instance, considering again an A-type twin ($t = 1$), when $m \in m_1$, the important pair is (BC), so X is B in this case. Using expression (197), and considering the three possible twin types, the following expression for N_0 when $p' < m \leq N-p'$ is found

$$N_0(m, p' < m \leq N - p') = \begin{cases} (2p' + a_0)/3 & m \in m_0 \\ (p' + a_1)/3 & m \in m_1 \\ (p' + a_2)/3 & m \in m_2 \end{cases}, \tag{198}$$

where the constants, a_i, have a dependence on the twin type, t, and are given in Table 4

The final case to consider is when the planar spacing is large enough that the correlation function is influenced by both surfaces. Now all pairs in the system span the fault so it is necessary to determine the number

Table 4: Constants for $N_0(m)$ of Equation(198)

	a_0	a_1	a_2
$t=0$	0	0	0
$t=1$	-2	-1	-1
$t=2$	-1	-2	1

Table 5: Constants for $N_0(m)$ of Equation (199)

	b_0			b_1			b_2		
	$s=0$	$s=1$	$s=2$	$s=0$	$s=1$	$s=2$	$s=0$	$s=1$	$s=2$
$t=0$	0	1	2	1	0	2	-1	1	0
$t=1$	0	-2	-1	1	0	-1	-1	-2	0
$t=2$	0	1	-1	-2	0	-1	2	1	0

of important pairs which exist in a stack of length N. In doing so one finds $N_0(m)$ is not only a function of the fault type, which determines the important pairs, but also is dependent on the extent of the stacking. Therefore, we can define the stack type, s, as, $s \equiv N \pmod{n}$. Again, considering all possible combinations of s, t and m it is found that $N_0(N-m)$ takes the form

$$N_0(m, N-p' < m) = \begin{cases} (2(N-m)+b_0)/3 & m \in m_0 \\ ((N-m)+b_1)/3 & m \in m_1 \\ ((N-m)+b_2)/3 & m \in m_2 \end{cases}, \qquad (199)$$

where the constants, b_i, are given in Table 5 for the possible combinations of t and s.

Putting together the three discussed cases, the probability correlation function for a finite stack of N planes containing a twin fault at position p is given by

$$P_0(m) = \begin{cases} \underline{m_0} & \underline{m_1} & \underline{m_2} & \\ 1 - \frac{2m}{3(N-m)}, & \frac{m-1}{3(N-m)}, & \frac{m+1}{N-m} & m \leq p' \\ 1 - \frac{2p'+a_0}{3(N-m)}, & \frac{p'+a_1}{3(N-m)}, & \frac{p'+a_2}{3(N-m)} & p' < m \leq N - p' \\ 1 - \frac{2(N-m)+b_0}{3(N-m)}, & \frac{(N-m)+b_1}{3(N-m)}, & \frac{(N-m)+b_2}{3(N-m)} & N - p' < m \end{cases} . \tag{200}$$

It should be noted just like for deformation faults, *p'* is actually the distance of the twin plane to the nearest boundary. However, for twins the fault position changes depending on which boundary is considered. For example, a twin position defined from the left boundary is *ABCAB*|*ACBA*, as the disruption in the stacking is only evident *after* the fifth plane. However, the twin position for the same stack starting from the right boundary and moving to the left is *ABCA*|*BACBA*. Therefore, it follows for twins,

$$p' = \begin{cases} p & p \leq (N+1)/2 \\ N - p + 1 & (N+1)/2 < p \end{cases} . \tag{201}$$

This relationship also defines the symmetry of $P_0(m)$ with respect to the twin position (i.e. the case of $p = 5$ is equivalent to $p = N - 4$).

The probability correlation functions given by Equation (200) for a planar stack containing a twin at different positions are plotted in Figure

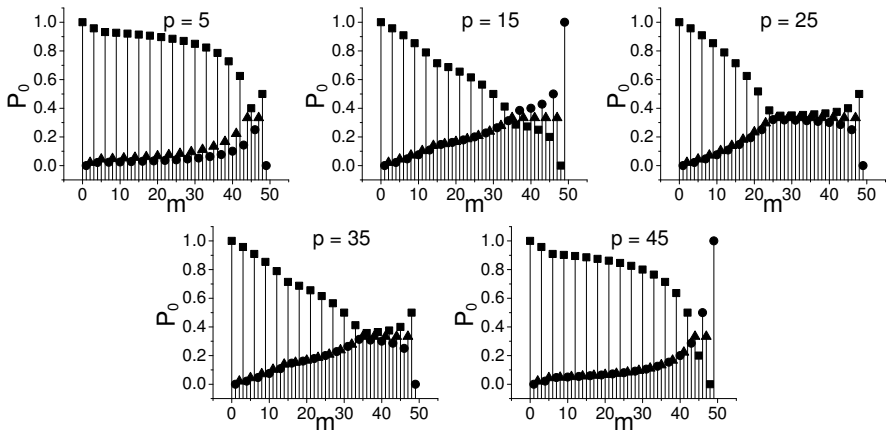

Figure 61: The series of $P_0(m)$ shown has been calculated using Equation (200) for a stack containing a twin fault at different positions, p. The sets m_i are denoted by the same shapes as in Figure 60.

61. The effect of a twin fault on the planar correlation is seen to be strikingly different than that of a deformation fault, depicted in Figure 60, as the function now tends to $1/3$ for large m, and the values for the set m_1 are no longer zero. It is apparent that as the twin moves beyond the center of the stack, positions like $p = 5$ and $p = 45$ result in similar correlation functions, but differ at larger m, as the rule for twin position symmetry is not exactly observed in this case.

8.3.3 Average Fault Position

The above expressions can be used to derive the average probability correlation function which results from a system of crystallites each containing one fault at different positions. This quantity is of more interest to powder diffraction since the observed pattern is the result of an averaging over the intensity from many crystallites in a sample. For the moment,

assuming that all crystallites in a system contain the same number of planes, the average correlation function is given simply as

$$\overline{P_0(m)} = \sum_p w_p P_0(m) \tag{202}$$

where w_p is the number fraction of the fault positions considered in the average and thus must follow $\sum_p w_p = 1$. Neglecting any consideration of fault energetics, the most straightforward assumption is one where all fault positions are equally probable. While possibly unjustified in some cases, this assumption puts the developed model on similar footing as previous models for the effect of faulting on the diffracted intensity, as it is commonly assumed that all planes have an equal probability of containing a fault. In this case, for crystallites containing a deformation fault the sum over p in Equation (202) is from the first plane to the $N-1$ plane, because a deformation fault on the N-th plane does not result in a fault in the stacking sequence. The number fraction for an equally probable fault position is then given by $w_p = 1/(N-1)$. The expression for the correlation function of this average fault position can be solved analytically by considering two cases, that of $0 \leq m < N/2$, and $N/2 \leq m \leq (N-1)$. For the first case the average probability correlation function when $m \in m_0$ is given by

$$\overline{P_0(m)} = \frac{2\sum_{p'=1}^{m}\left(1-\frac{p'}{N-m}\right)+2\sum_{p'=m+1}^{N/2}\left(1-\frac{m}{N-m}\right)}{N-1},$$
$$\overline{P_0(m)} = 1 - \tfrac{m}{N-1}.$$

While in the second case for, $N/2 < m \leq N-1$, the average probability correlation function is expressed as

$$\overline{P_0(m)} = \frac{2\sum_{p'=1}^{N-m-1}\left(1-\frac{p'}{N-m}\right)+2\sum_{p'=N-m}^{N/2}0}{N-1},$$
$$\overline{P_0(m)} = 1-\tfrac{m}{N-1}.$$

In the above derivation only the relations for the set of m_0 were shown, but following the same steps expressions for m_1 and m_2 can be derived. The final expression for the average correlation function for a system of crystallites each containing one deformation fault is then found to be

$$\begin{array}{cccc} & \underline{m_0} & \underline{m_1} & \underline{m_2} \\ \overline{P_0(m)} = & \left\{ 1-\frac{m}{N-1}, & 0, & \frac{m}{N-1} \right. . \end{array} \tag{203}$$

The average fault position correlation function for crystallites containing a twin fault is also calculated in this way. However, in this case only $N-2$ twin positions are considered, since the twin positions $p=1$ and $p=N$ result in a planar correlation which is the same as a perfect stack. Following steps as the deformation fault case, and properly accounting for the a_i and b_i constants, results in an average correlation function of the form

$$\begin{array}{cccc} & \underline{m_0} & \underline{m_1} & \underline{m_2} \\ \overline{P_0(m)} = & \left\{ 1-\frac{2m}{3(N-2)}, & \frac{m-1}{N-2}, & \frac{m+1}{N-2} \right. . \end{array} \tag{204}$$

It is then interesting to compare this form of the correlation function with that derived from the recursion equation method. The expression for the probability correlation function given by Estevez-Rams (E-R) [44] is the most recent form which has been derived for faulting in close packed FCC lattices. The average correlation function for a powder of crystallites of fifty layers containing one fault is compared to the E-R correlation function for a stacking sequence of the same fault probability ($a = 1/50$, or $\beta = 1/50$) in Figure 62. The difference between these expressions, shown below the correlation functions, clearly depicts how these models deviate with increasing correlation length. The E-R model decays slower than the derived model, and asymptotically tends to the value of 1/3 for both deformation and twin faults. Differences in the trends are expected because, as previously discussed, the recursion relation method is solved assuming an infinite stack and intrinsically allows for the possibility that a crystallite contains multiple faults in terms of increasing faulting probability. The developed models, instead, are more specific and only consider the effect of one fault in a finite stack of layers.

8.3.4 Limit of $P_0(m)$ as N becomes large

The fault position and plane spacing can be expressed in terms of the stack length N,

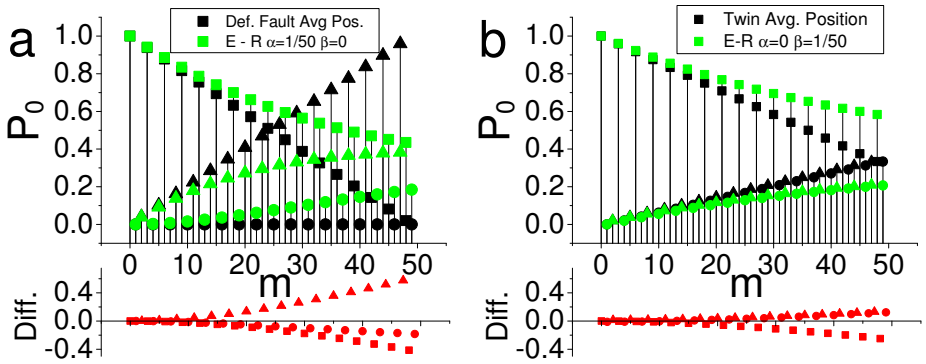

Figure 62: Comparison of $\overline{P_0(m)}$ with that given by the expression of Estevez-Rams *et al.* (E-R) for a stack of 50 planes containing (a) a deformation fault, or (b) a twin fault. Below each figure the difference is given, Diff. $= \left(\overline{P_0(m)} - P_0^{E-R}(m)\right)$. Again, the sets m_i are denoted by the same shapes as in Figure 60.

$$m = \mu N \qquad 0 \leq \mu < 1 \tag{205}$$

$$p = \rho N \qquad 0 < \rho < 1 \tag{206}$$

where μ and ρ are fractional coefficients. Substituting these expressions into Equation (194), the probability correlation function for a stack containing a deformation fault then becomes independent of N,

$$P_0(m) = \begin{array}{c} \underline{m_0} \quad \underline{m_1} \quad \underline{m_2} \\ \left\{ \begin{array}{lll} 1 - \frac{\mu}{1-\mu}, & 0, & \frac{\mu}{1-\mu} \quad \mu \leq \rho \\ 1 - \frac{\rho}{1-\mu}, & 0, & \frac{\rho}{1-\mu} \quad \rho < \mu \leq 1-\rho \\ 0, & 0, & 1 \quad 1-\rho < \mu \end{array} \right. \end{array} . \tag{207}$$

This independence of N means that the effect of a single deformation

fault on the correlation function is the same regardless of the domain size.

The case of a twin fault is different. Substituting the new expressions for m and p into Equation (200), a functional dependence on N remains from Equations (198) and (199), and the expression of $P_0(m)$ for a twin becomes

$$P_0(m) = \begin{cases} \underline{m_0} & \underline{m_1} & \underline{m_2} & \\ 1-\frac{2\mu}{3(1-\mu)}, & \frac{\mu}{3(1-\mu)}, & \frac{\mu}{3(1-\mu)} & \mu \le \rho \\ 1-\frac{2\rho+a_0/N}{3(1-\mu)}, & \frac{\rho+a_1/N}{3(1-\mu)}, & \frac{\rho+a_2/N}{3(1-\mu)} & \rho < \mu \le 1-\rho \\ 1-\frac{2(1-\mu)+b_0/N}{3(1-\mu)}, & \frac{(1-\mu)+b_1/N}{3(1-\mu)}, & \frac{(1-\mu)+b_2/N}{3(1-\mu)} & 1-\rho < \mu \end{cases} . \tag{208}$$

Therefore, some terms in the planar correlation function of a twinned stack have a $1/N$ dependence, which will be prevalent for *small* domain sizes. As N becomes large the constants a_i/N and b_i/N go to zero and this expression can be approximated as

$$P_0(m) = \begin{cases} \underline{m_0} & \underline{m_1} & \underline{m_2} & \\ 1-\frac{2\mu}{3(1-\mu)}, & \frac{\mu}{3(1-\mu)}, & \frac{\mu}{3(1-\mu)} & \mu \le \rho \\ 1-\frac{2\rho}{3(1-\mu)}, & \frac{\rho}{3(1-\mu)}, & \frac{\rho}{3(1-\mu)} & \rho < \mu \le 1-\rho \\ \frac{1}{3}, & \frac{1}{3}, & \frac{1}{3} & 1-\rho < \mu \end{cases} . \tag{209}$$

The error introduced when using the large N expression goes as $1/N$, so a stack of 100 layers containing a twin fault will be within roughly 1% of the exact expression when using Equation (209) instead of Equation

(200). This size dependence is not possible to describe in the correlation functions derived from recursion relations due to the previously discussed infinite stack assumption.

8.4 From Planar Correlation to the Powder Diffraction Peak

8.4.1 Calculating the Powder Peak from $P_0(m)$

The remainder of this study will be focused on the powder diffraction peak profile resulting from the described models for the planar correlation function. Recalling the discussion in Section 8.1.2 and considering the broadened case, it is shown that the expression for the intensity in reciprocal space given by Equation (159) becomes

$$I(h_1 h_2 h_3) = \psi^2 \sum_{m=-\infty}^{\infty} N_{|m|} \frac{3P_0(|m|) - 1}{2} \cos\left(2\pi \left|m\right| h_3/3\right), \qquad (210)$$

as both $P_0(m)$ and N_m are mirrored about $m = 0$. The continuous variable h_3 can then be expressed in terms of its vicinity to the reciprocal space point L_0 as

$$h_3 = L_0 + \Delta h_3.$$

After substituting this expression for h_3 into Equation (210), expanding the cosine and properly accounting for the dependence of the sine function on $|m|$ into the amplitude coefficient, the sum in Equation (210) becomes a Fourier series

$$I(h_1 h_2 \Delta h_3) \quad = \psi^2 \sum_{m=-\infty}^{\infty} A_m \cos\left(2\pi m \Delta h_3/3\right) + B_m \sin\left(2\pi m \Delta h_3/3\right) \tag{211a}$$

$$A_m = N_{|m|} \frac{3P_0(|m|) - 1}{2} \cos(2\pi m L_0/3) \qquad \text{when } L_0 = \pm 1 \pmod 3 \tag{211b}$$

$$B_m = -\frac{m}{|m|} N_{|m|} \frac{3P_0(|m|) - 1}{2} \sin(2\pi m L_0/3) \quad \text{when } L_0 = \pm 1 \pmod 3 \tag{211c}$$

This expression then gives the general relation between the probability correlation function, $P_0(m)$, and the Fourier coefficients A_m and B_m. For the unbroadened subcomponents a similar Fourier series is found with coefficients of the form

$$A_m \quad = N_{|m|} \quad \text{when } L_0 = 0 \pmod 3 \tag{212}$$

$$B_m \quad = 0 \quad \text{when } L_0 = 0 \pmod 3 \tag{213}$$

which are not surprisingly only influenced by the stack size.

The powder pattern intensity from a given *hkl* component can be approximated by remapping the intensity given in Equation (211a) to that observed along the $\mathbf{s}_{hkl}$ direction [147, 155], where $s_{hkl} = \sqrt{h^2+k^2+l^2}/a = 2\sin\theta_{hkl}/\lambda$ and a is the FCC unit cell parameter. Therefore, the contribution to the peak profile from a single component of a family of reflections becomes

$$I(s_{hkl},\Delta s)=\frac{I_e(\theta)N_aR\lambda^2f^2(\theta)L(\theta)3a^2s_{hkl}}{16\pi V_a\left|L_0\right|}\sum_{m=-\infty}^{\infty}\frac{A_m}{N}\cos\left(\frac{2\pi a^2s_{hkl}}{L_0}m\Delta s\right)+\frac{B_m}{N}\sin\left(\frac{2\pi a^2s_{hkl}}{L_0}m\Delta s\right), \quad (214)$$

which is analogous to Warren's Equation 13.59, and most of the variables have the same meaning. The only differences are that here N_a represents the number of atoms, V_a signifies the volume per atom, and $L(\theta)$ represents the Lorentz factor as the polarization factor is included in Warren's definition of $I_e(\theta)$ (see [155] p. 29). Also, the term $1/B_3|\sin\varphi|$ used in Warren's expressions has been expressed here in the form $3a^2s_{hkl}/L_0$.

The observed diffraction profile is then the sum of the peaks from all broadened and unbroadened subcomponents of an *hkl* reflection, and can be calculated following the considerations described by Velterop [147]. To highlight the effect of faulting on the peak profile we will consider the intensity without the contributions from the Lorentz-Polarization, or atomic scattering factors defined as

$$I'(s_{hkl},\Delta s)=\frac{3a^2s_{hkl}}{|L_0|}\sum_{m=-\infty}^{\infty}\frac{A_m}{N}\cos\left(\frac{2\pi a^2s_{hkl}}{L_0}m\Delta s\right)+\frac{B_m}{N}\sin\left(\frac{2\pi a^2s_{hkl}}{L_0}m\Delta s\right). \quad (215)$$

It should be noted that the peak broadening given by this formulation only considers the contributions from faulting and finite stack size normal to the fault plane. Peaks from small crystallites will also be broadened

due to their small planar cross section. It is then only used in the present study as a means of comparing the peak shapes resulting from the different models for faulting in an FCC lattice.

As an example of how the powder diffraction peak is affected by different fault positions, a series of profiles of broadened subcomponents were calculated employing the probability correlation functions given by Equations (194) and (200) for deformation and twin faults respectively. The subcomponents broadened by deformation faults are depicted in Figure 63 for a series of fault positions in a stack of 50 Au (111) planes. It is seen that the profile shows the most broadening and shifting when the fault is in the center of the stack ($p = 25$) for all peaks considered. For this fault position, a large amount of asymmetry is observed in the peak shape, even to the extent that a second peak is apparent opposite to the peak shift. Moving the deformation fault closer to the boundary (decreasing p) has the effect of diminishing the features due to the deformation fault, and the contribution for size broadening becomes the defining characteristic. This behavior is best understood by considering that a fault has the most influence on $P_0(m)$ when it is at the stack center, as shown in Figure 60. The more that the correlation function deviates from that of a perfect stack, the more the peak profile is influenced.

The same study of the broadened components due to a twin fault at different positions is shown in Figure 64. The effect of the twin on the peak shape is different from that due to the deformation fault as the

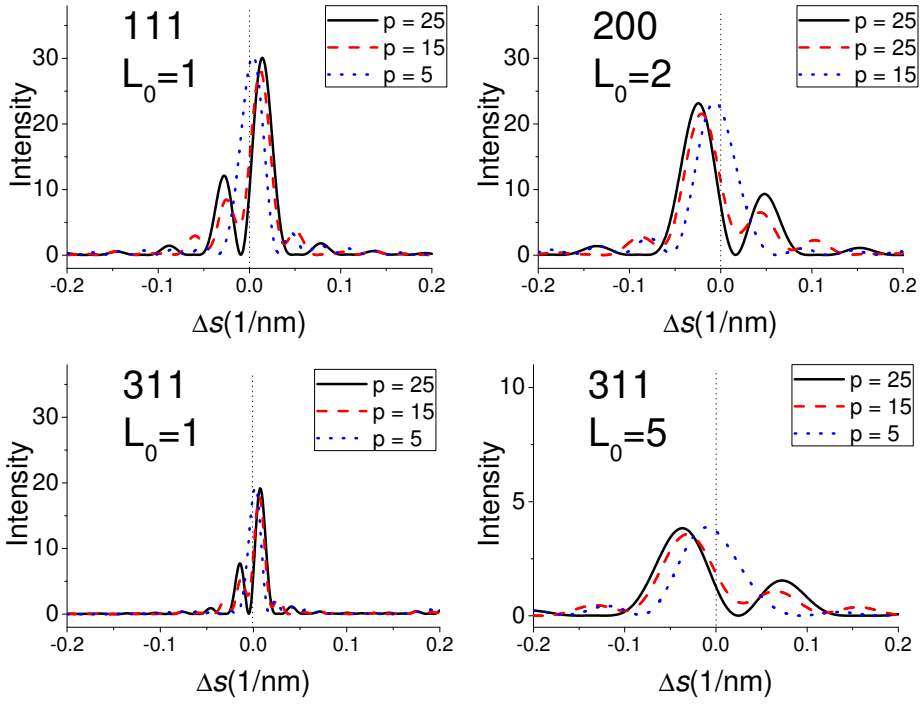

Figure 63: The extent of broadening and shifting caused by a deformation fault at different positions, p, is depicted for a few broadened sub-components of powder diffraction peak profiles. A stack of 50 Au (111) planes with a lattice parameter, a, of 0.40809nm was assumed in the calculation of the presented profiles. The case of $p = 25$ is then a fault at the center of the stack with the fault moving toward the left boundary as p is decreased.

predominant effect is observed to be profile broadening. It is again found that the most broadened profile is obtained when the twin is in the center of the stack, and the broadening decreases as the fault moves toward the boundary.

In terms of the powder pattern the positional dependence is not as important as the average quantity. The diffraction profile due to a collection of crystallites which contain one fault and equal probability all fault

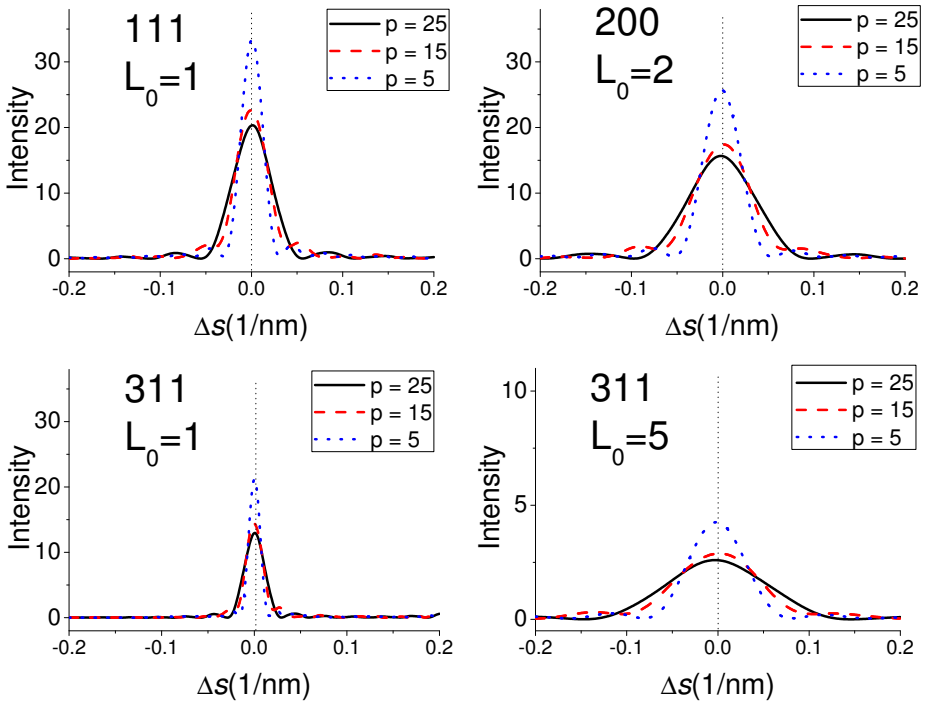

Figure 64: The extent of broadening caused by a twin fault at different positions, p, is depicted for a few broadened sub-components of powder diffraction peak profiles. The assumptions of the size and type of stack used to calculate the profiles are the same as those given in Figure 63.

positions can also be calculated using Equation (215), but now employing Equations (203) and (204) to describe $P_0(m)$. Some resulting powder peaks, as well as the contributions from all subcomponents of the peak (broadened and unbroadened), are depicted in Figure 65 for deformation faults, and Figure 66 for twin faults. Also depicted in these figures are the profiles resulting from the E-R correlation functions, as well as, the difference between the total profiles from the two models. In all cases the profiles are calculated assuming a stack of 50 Au (111) planes, with a faulting probability assumed to be 1/50.

The case of deformation faulting leads to the largest difference in the peak profiles predicted by the two models. As shown in Figure 65, the peaks from the developed average fault position model are more shifted and broadened than the those found using the E-R model. The calculated 111 and 200 peaks are prime examples, as the calculated differences between the peak shapes are shown to reach as much as +/- 20% of the calculated intensities. For the patterns due to twinning a better agreement is found between the developed model and the E-R model. The peaks from the average position model show only slightly more broadening than the E-R model peaks. Again the 311 peaks are found to have the best agreement, as the 111 and 200 peaks differ by at most +/- 10% of the calculated intensities. Referring back to Figure 62, it is apparent that the better agreement for the case of twinning stems from the fact that there is a better match between the two twin correlation functions

than those for deformation faults.

8.4.2 Influence of $P_0(m)$ on Peak Broadening and Asymmetry

To further study the influence of $P_0(m)$ on the broadened peak shape, the sum in Equation (211a) can be rewritten as

$$I(h_1 h_2 \Delta h_3) = \psi^2 \sum_{n=-\infty}^{\infty} \left\{ A_{3|n|-1} \cos\left(2\pi \left(3\,|n| - 1\right) \Delta h_3/3\right) + \right.$$
$$B_{3|n|-1} \sin\left(2\pi \left(3\,|n| - 1\right) \Delta h_3/3\right) + \; A_{3|n|} \cos\left(2\pi 3\,|n|\, \Delta h_3/3\right) +$$
$$B_{3|n|} \sin\left(2\pi 3\,|n|\, \Delta h_3/3\right) + A_{3|n|+1} \cos\left(2\pi \left(3\,|n| + 1\right) \Delta h_3/3\right) +$$
$$\left. B_{3|n|+1} \sin\left(2\pi \left(3\,|n| + 1\right) \Delta h_3/3\right) \right\}. \quad (216)$$

After expanding the cosine and sine functions this is found to be equivalent to

$$I(h_1 h_2 h_3') = \psi^2 \sum_{n=-\infty}^{\infty} A_n' \cos\left(2\pi n \Delta h_3\right) + B_n' \sin\left(2\pi n \Delta h_3\right) \quad (217a)$$

$$A_n' = A_{3|n|} + \cos\left(2\pi \Delta h_3/3\right) \left(A_{3|n|+1} + A_{3|n|-1}\right) +$$
$$\sin\left(2\pi \Delta h_3/3\right) \left(B_{3|n|+1} - B_{3|n|-1}\right) \quad (217b)$$

$$B_n' = \frac{n}{|n|} \left[B_{3|n|} + \cos\left(2\pi \Delta h_3/3\right) \left(B_{3|n|+1} + B_{3|n|-1}\right) + \right.$$
$$\left. \sin\left(2\pi \Delta h_3/3\right) \left(A_{3|n|-1} - A_{3|n|+1}\right)\right] \quad (217c)$$

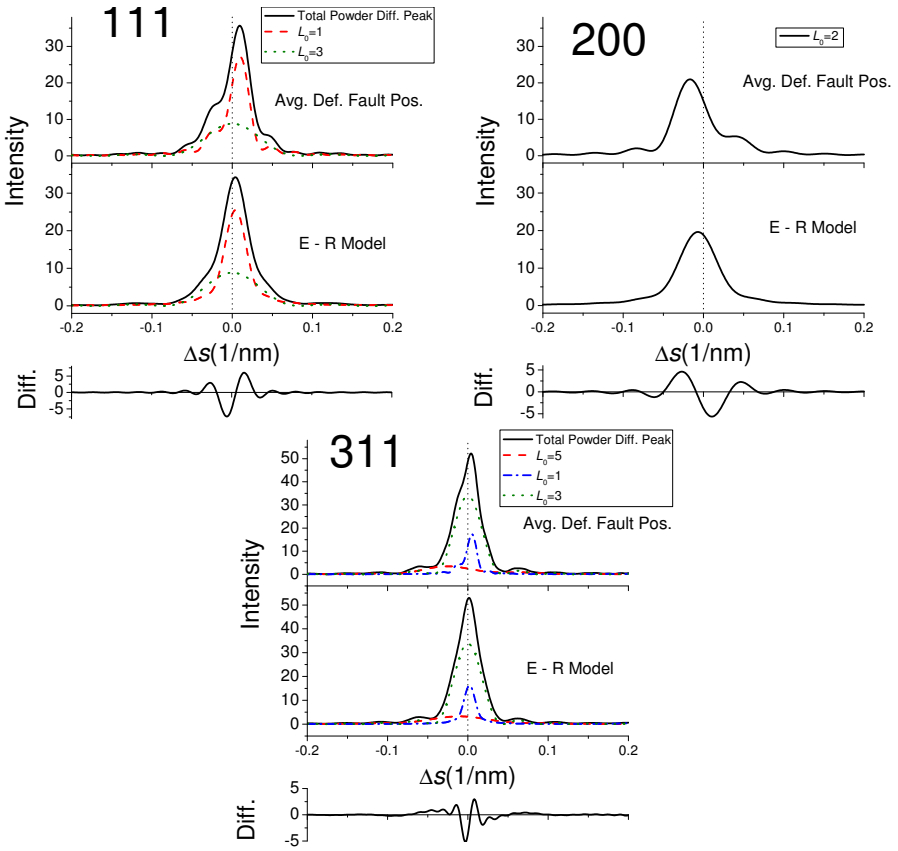

Figure 65: The sub-components and total diffraction profiles are given for the 111, 200, and 311 peaks assuming both the average deformation fault position model, and the model for FCC faulting developed by Estevez-Rams [44]. For consistency the fault probabilities assumed in the E-R model were: $\alpha = 1/50$ and $\beta = 0$. Below the calculated peaks is the difference between the total profiles given from the relation, Diff. $= I_{Avg.Pos.} - I_{E-R}$. In each peak the "broadened" components are depicted by dashed lines, while the "unbroadened" component is depicted by a dotted line.

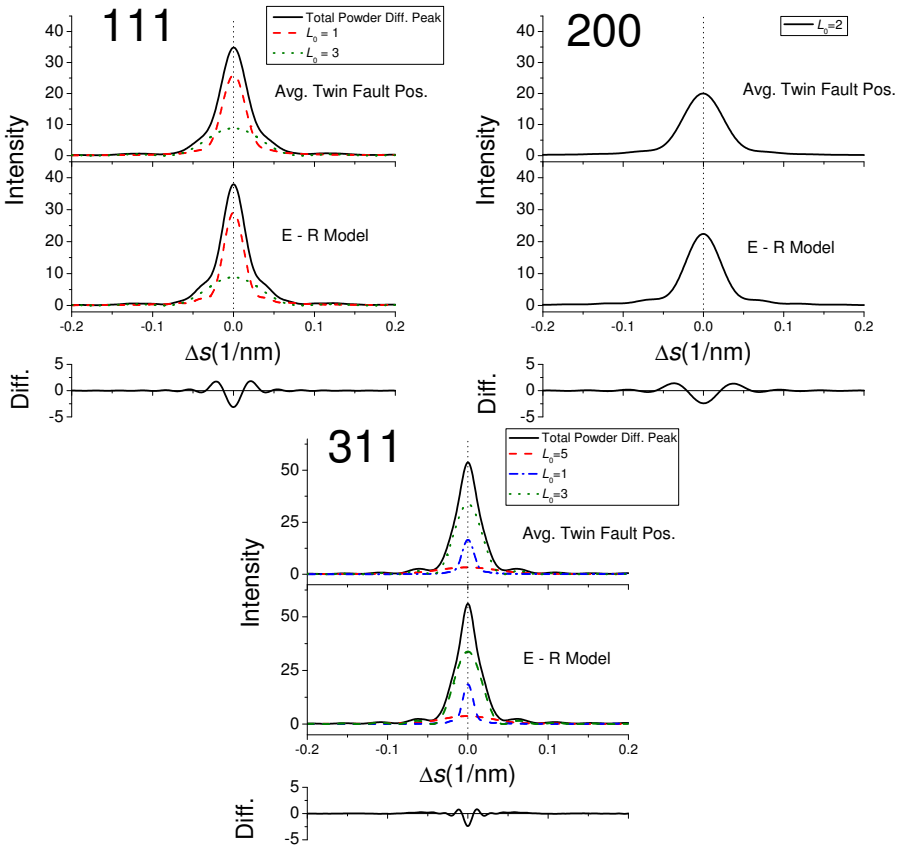

Figure 66: The subcomponents and total diffraction profiles are given for the 111, 200, and 311 peaks assuming the average twin fault position model, and the model for FCC faulting developed by Estevez-Rams [44]. In this case the fault probabilities assumed in the E-R model were: $\alpha = 0$ and $\beta = 1/50$. The difference between models and the components of each peak are depicted in the same way described in Figure 65.

Substituting in the expressions for A_m, and B_m in Equation (211) leads to the following relationships defining the coefficients of Equation (217):

$$A'_n = N_{3|n|}\left[\cos\left(2\pi L_0/3\right)\frac{3P_0(3\,|n|)-1}{2}+\right.$$
$$\left.\cos\left(2\pi(L_0+\Delta h_3)/3\right)\left(\frac{3\left(P_0(3\,|n|+1)+P_0(3\,|n|-1)\right)}{2}-1\right)\right]+$$
$$\frac{3\left(P_0(3\,|n|+1)-P_0(3\,|n|-1)\right)}{2} \quad (218a)$$

$$B'_n = -\frac{n}{|n|}\left\{N_{3|n|}\left[\sin\left(2\pi L_0/3\right)\frac{3P_0(3\,|n|)-1}{2}+\right.\right.$$
$$\left.\sin\left(2\pi(L_0+\Delta h_3)/3\right)\left(\frac{3\left(P_0(3\,|n|+1)-P_0(3\,|n|-1)\right)}{2}-1\right)\right]+$$
$$\left.\frac{3\left(P_0(3\,|n|-1)-P_0(3\,|n|+1)\right)}{2}\right\} \quad (218b)$$

When n is small these coefficients are dominated by the part multiplied by $N_{3|n|}$. It is then evident in Equation (218) that the cosine coefficients, A_n', which can be attributed to peak broadening, are largely dependent on the sum of the $P_0(m_1)$ and $P_0(m_2)$ terms. Furthermore, the sine coefficients, B_n', commonly attributed to the peak asymmetry, are determined by the difference between these $P_0(m_1)$ and $P_0(m_2)$ terms. These relationships are true in general for any probability correlation function of an FCC stacking. In terms of our study this is the key to

explain why the peak shape of a stack containing a deformation fault exhibits an asymmetry and shift, whereas that containing a twin is primarily broadened. The correlation function derived for a deformation fault in Equation (203) has a difference in the $P_0(m_1)$ and $P_0(m_2)$ terms given by, $-P_0(m_2)$. Whereas this difference for a twin fault, given from Equation (204), is nearly zero except when there are few planes in the stacking.

It can then be argued that some of the observed shift in peak position commonly attributed to deformation faults is actually a consequence of the *strong* peak asymmetry. This result maybe somewhat surprising since, following the treatment of Warren [155], it is commonly believed that any peak asymmetry is only due to twin faulting. As shown in Figure 66, it is not incorrect that peaks broadened by twins exhibit slight asymmetry, however, the fact that the profiles from deformation faults also result in peak asymmetry calls into question the validity of methods which rely solely on the peak asymmetry and peak shift to quantify the deformation and twin fault densities.

The true limit of information obtainable from studying a faulted FCC powder diffraction peak profile is found by considering that due to the nature of the Fourier series in Equation (218), a profile can only be uniquely linked to an average $P_0(m)$. Therefore, if multiple faulting scenarios result in the same average correlation function, then powder diffraction cannot distinguish between them. The separation of the faulting effect

from the broadening due to crystallite size and other strains is only possible by simultaneously considering the profiles of multiple reflections in the pattern. The modified Williamson-Hall analysis is one proposed method to consider the effect of faulting on the broadening of multiple reflections [145]. However, only information on the peak in terms of its full-width half-maximum (FWHM) or integral breadth (IB) is used to determine the faulting densities. In the process of simplifying the treatment, important information about the complicated shape of the peak from the many subcomponents, and faulting effects is neglected [147], making the fault densities found from this method quantitatively less reliable [127]. A slightly more sophisticated treatment has been recently proposed in the convolutional multiple whole profile (CMWP) modeling framework which has parametrized the influence of different fault probabilities on the FWHM, asymmetry and peak positions of profile subcomponents [9]. While accounting for some aspect of the peak shape by considering multiple subcomponents, the description of the profiles in terms of a few parameters again neglects a fair amount of information in the peak shape, and use of a Lorentzian function to describe the peak shape may bias the results. Just by inspecting the subcomponents of peak profiles simulated in the present paper it is quickly concluded that a profile due to faulting is not necessarily Lorentzian, or any other analytical peak function, but is instead determined from the probability correlation function. Given the complexity of the determining a reasonable faulting density from the

powder pattern it is best to utilize all of the information possible from the measured intensity, and properly treat the peak as the Fourier transform of a real physical model. These are the fundamental assumptions of the whole powder pattern modeling (WPPM) method, which has been developed to consider the most recent models of faulting in FCC materials [44, 124].

8.5 Summary and Conclusions

The fundamental differences between the disorder caused by a deformation fault versus a twin fault has been clearly traced, through the probability correlation function, to their effects on the diffraction peak profile. Furthermore, when considering a finite stack the planar correlations have been shown not only to depend on the fault position, but also on the extent of the stack when considering twin faults, implying the same must be true for the diffraction profile. In fact, recent simulation studies have found that the presence of a fault at different positions in a spherical nanocrystallite results in similar trends on the peak broadening and shifting, as well as, dramatic differences in the observed fault probability [13]. This is evidence that the description of broadening which has been presented is not completely masked by the broadening due to the small cross section of a nanocrystallite. Nonetheless, for a proper description of the peak profile from such a case, a convolution of the described features in the intensity with those due to the particle size and shape must be made. As the general form of the Fourier coefficients is

given in Equation (211), modern reciprocal space modeling techniques like Whole Powder Pattern Modelling (WPPM) [124] show promise in utilizing the developed model and performing this convolution in reciprocal space. The same can be said regarding the use of the developed model to describe the effect of faulting in powders of crystallites with a broad size distribution. The development of such a robust line profile analysis tool is ongoing, along with experimental validation of the proposed model to describe faulting in small crystallites.

When considering the average correlation function, the model allows for considerable flexibility as the possibilities for different average planar correlation functions extend far beyond the uniform fault position distribution demonstrated in Section 8.3.3. If a more complex fault position distribution is found to be suitable for a given system, then only the weights, w_p, in Equation (202) need to be adjusted and the resulting peak profile recalculated.

The current limiting assumption of the developed model is that only one fault is allowed to exist in a given crystallite. In this regard it might be true that the recursion equation model [44, 155] is more appropriate to represent faulting in many FCC materials, especially those with a large crystallite size. Accounting for multiple faults in the developed theoretical framework is not impossible, but becomes increasingly complex, as the number of cases to consider increases with the number of faults. For example, a finite stack containing just two faults requires the

consideration of each fault being either a deformation fault or twin fault, as well as all the different possible distances between faults, and their positions relative to the boundaries. With the computation power available in modern desktop computers, it might be better suited to directly compute the correlation functions and averages of the desired faulting scenarios. In which case, the general expression of Equation (211) is still applicable to model the peak profile from the calculated correlation functions.

CHAPTER IX

SUMMARY AND FUTURE WORK

9.1 Summary

This work was focused on investigating the influence which structural and dynamic characteristics of metal nanoparticles have on the resulting line profiles in the powder diffraction pattern. A systematic approach of singling out each feature which influences the shape of diffraction peaks was carried out through the use of atomistic models and the Debye function. In many cases this allowed for the existing theory governing line profile analysis to be tested, and extended, to the limit of the smallest possible crystalline domains. Furthermore, this work explored the possibility of combining atomistic simulations like molecular dynamics with the study of powder diffraction. This allowed for the consideration of energetics into the construction of the appropriate nanoparticle models, as well as, the simulation of the dynamic behavior of the atoms at an elevated temperature. Finally, on the experimental side, this work contributed to the development of an emerging line profile analysis technique called Debye function analysis (DFA). This technique tests the models used to represent nanoparticles in the powder pattern generation, and was shown to allow for the characterization of a sample of shape controlled platinum

nanoparticles.

Almost every structural aspect of a crystallite has some influence on the observed diffraction pattern. With this in mind it is important to consider some expected hierarchy of the features in a pattern which is being analyzed. As discussed in Chapter 3, the small size of a nanoparticle has the most dramatic influence on the observed peak profiles. This also carries with it the consequence that an appropriate assumption of the crystallite shape is important to explain all of the features in the profile. The discussion of Section 3.1 presented the theory of size and shape broadening in a very general way, which is more appropriate for the consideration of small crystalline domains. In the process, the limitations of assuming the tangent plane approximation to describe the powder intensity from these small domains were laid out. In Section 3.2 a new proposed method of carrying out the powder integral numerically was described, and the resulting diffraction patterns were compared with those found assuming the tangent plane approximation and the Debye function. The level of agreement found between the Debye function and this numerical powder integration technique is offers a lot of insight into the theory of size broadening, and offers an interesting avenue for future line profile analysis. Finally, in Section 3.3 the consequences of assuming a size distribution were demonstrated, and excellent agreement was found between the reciprocal space and Debye function approaches.

The development of the Debye function into a robust line profile analysis tool for the analysis of experimental patterns was presented in Chapter 4. This method was then employed in an attempt to characterize the crystallite shapes present in a sample of platinum nanoparticles which were synthesized to preferentially expose 111 surfaces. The experimental data collected in a laboratory setting were refined by the developed DFA routine in an attempt to determine the relative fraction of different crystallite shapes in the sample. The model which resulted in the best fit found a dominance of octahedral particles having a size of around 8.5 nm. This result was found to be in good agreement with TEM analysis, and the line profile analysis method of whole powder pattern modelling. The same abundant particle shape was also supported by the TEM analysis and cyclic voltammetry characterization which found a predominance of 111 surfaces in the sample.

Chapter 6 explored the starting assumption taken in much of diffraction theory, which is that each crystallite can be treated as if it scatters independently. A routine for simulating a densely packed system of spherical particles was described in Section 6.2, and the resulting diffraction patterns from the different approaches for simulating the pattern were described. The consideration of a polydisperse system of particles of different sizes and containing different defects was shown to result in an increase in system size necessary to result in an accurate powder diffraction pattern. Finally, the simulations discussed in Section 6.4 found that

the independent scattering assumption is not valid to describe the wide-angle peaks system of crystallites when ordering exists in the spatial arrangement, as well as, the orientation of the crystallites.

The implications of breaking away from the descriptions of atoms in a lattice as being static is discussed in Chapter 7 in terms of the study of the thermal diffuse scattering (TDS). Molecular dynamics simulations were used to generate the time averaged powder pattern influenced by the bulk lattice vibrations, and the results of assuming various models to describe the TDS were compared in Section 7.2. These simulations found that the assumption of an inappropriate model for the TDS led to an inaccurate determination of the Debye-Waller factor and an underestimation of the particle size. A few improvements to extend the TDS theory to consider the effect of a finite crystallite size were proposed in Section 7.4. The results of these considerations were tested on molecular dynamics simulations of Al core-shell nanoparticles, and the modeling of the patterns found that the consideration of the effects of phonon confinement on the modified Warren model were necessary for an accurate determination of the vibrational characteristics of the system.

Finally, Chapter 8 considered the effect of faulting in a small crystalline domain. The effect of faulting in the powder diffraction pattern is found to be dependent on the position of the fault plane in the crystallite, decreasing as the fault moved toward the surface. Section 8.2 exhibits how this can be incorrectly interpreted as a decreasing fault probability

when trying to model the pattern from spherical nanoparticle containing different faults. This study also found that the cross-section of the particle matters, and that it might not always be appropriate to treat the faults as dilute and non-interacting when an exact faulting probability is desired. A new approach to describing the effect of faulting in finite domains is presented in Sections 8.3 and 8.3.3. This theory shows that the decreased effect of faulting which is observed as the fault moves toward the surface of a crystallite is really due to changes in the planar correlation function. A method of calculating this function for a crystallite containing a single fault of either twin or deformation type is presented. Also, a general formulation to calculate the resulting diffraction peak profiles from the planar correlation function is given. This method is used to compare the peaks from the new approach to modern diffraction theory which does not consider the finite size of the crystallite.

9.2 Future Avenues of Research

The studies presented in this thesis, which constitute a broad investigation into the levels of information which is contained in the diffraction pattern from nanoparticles, is really only scratching the surface of each respective topic. A few interesting doors which have been opened during the course of this work will be outlined here as well as the possible impact which these directions can have on the treatment of diffraction measurements.

9.2.1 DFA and Global Modeling Routines

The analysis of Pt nanoparticles presented in Chapter 4 required the combined characterization using multiple, complementary techniques. Each technique provided different kind of information which was crucial to avoid biases of a single method and arrive at a coherent understanding of the studied system. Conceptually this can be thought of as a global modeling engine, which inputs the data from a series of experiments, and outputs the model which works best with all known results. While this paradigm has been circulating in the scientific literature for some time now, the approaches of how to correctly weight and stitch together the information from each technique are still in their infancy.

The Debye function can offer a lot opportunities to further the understanding of these global modeling approaches and bridge different methods of modeling diffraction pattern. For instance, the radial distribution function (RDF) is an automatic by product of calculating the diffraction pattern via the Debye function. There is nothing preventing the comparison of this RDF information with the local structural information obtainable by treatment of the diffraction pattern following the methods of Total Scattering. This can then allow for a simultaneous modeling of the diffraction data from the measured RDF, as well as, the measured wide-angle diffraction pattern to find the best structural model. Furthermore, as briefly discussed in Chapter 6, the Debye function also allows for the simulation of the small-angle diffraction pattern. This can lead to

a unification of the diffraction pattern, which allows for complementary information to be obtained over spanned length scales. As detector technology is also currently available which can withstand the intensity of the primary beam. This has resulted in 2D detectors which can measure beautifully and continuously the pattern through the small-angle and into the wide-angle. As these measurements become more popular techniques of modeling the data will be increasingly desired, and the Debye function then offers a possible solution.

However, before Debye function analysis can make a lasting impression of these new areas of diffraction analysis, appropriate methods of how to handle instrumental effects on the simulated diffraction peaks must be further developed. At present, the contribution of the instrument is either neglected, or attempted to be removed from the measured data by deconvolution. Both of which lead to uncertainties in the analysis and cloud the fine features which are trying to be modeled by the Debye function. Ideally the contributions should be convolved with the simulated intensity, however, the continuous nature of the intensity from the Debye function prevents such an approach. A solution to this problem might be to not use the Debye function explicitly, but instead use the Debye-like approach of numerically evaluating the powder integral, described in Section 3.2 which allows for the accurate calculation of the powder intensity peak by peak. This treatment of the simulated intensity is then much more amenable with a convolution operation with any

instrumental contribution.

9.2.2 Development of Structural Models

As already demonstrated in the discussed case studies, the combination of atomistic simulations and diffraction line profile analysis offers an new and rich approach which can deepen our understanding of the structure of materials. While it might be desirable to think that one day the atomistic descriptions of molecular dynamics will replace the empirical models used to model the diffraction pattern from nanomaterials, a lot of work still has to be done to improve both methods before that goal can be achieved. The use of atomistic simulation in diffraction allows for the better observation of what aspects of the structure result in observable features in the diffraction pattern. Furthermore, they serve to test the existing models, and hopefully lead to improvements which will lead to a better characterization of a material through the diffraction pattern. The cases of lattice dynamics which have been investigated in this study are just a few examples of the many kinds of phenomena which can be investigated by this approach. The structural models of polycrystalline materials opens another research door, not to mention the exploration of effects from seemingly amorphous and glassy structures.

The coupling of these techniques should really be considered a two way street, as diffraction offers a useful means to compare the predictions made by the simulation with the phenomenon which is actually observed experimentally. Then the information on the aspects which might be

lacking in the atomistic simulation can be refined and improved to develop the methods of the simulation. This might lead to the development of better interatomic potentials, as well as, the more accurate simulation a microstructure evolution, such as that for nucleation and growth. With the perspective of so much enlightening development of both simulation and experiment, it is my belief that the coupling of molecular dynamics and diffraction pattern analysis will offer a lot of insight into behavior of materials for a long time to come.

REFERENCES

[1] Ahmadi, T. S., Wang, Z. L., and Henglein, A., "Cubic colloidal platinum nanoparticles," vol. 8, no. 6, pp. 1995–1997, 1996.

[2] Ahmadi, T., Wang, Z., Green, T., Henglein, A., and El-Sayed, M., "Shape-controlled synthesis of colloidal platinum nanoparticles," *Science*, vol. 272, no. 5270, p. 1924, 1996.

[3] Alder, B. J. and Wainwright, T. E., "Phase Transition for a Hard Sphere System," *The Journal of Chemical Physics*, vol. 27, no. 5, p. 1208, 1957.

[4] Alder, B. J. and Wainwright, T. E., "Studies in molecular dynamics. I. General method," *The Journal of Chemical Physics*, vol. 31, no. 2, p. 459, 1959.

[5] Allen, M. P. and Tildesley, D. J., *Computer Simulation of Liquids*. New York: Oxford University Press, 1987.

[6] Ashcroft, N. and Mermin, D., *Solid State Physics*. Orlando, FL: Harcourt, 1976.

[7] Baletto, F., Ferrando, R., Fortunelli, a., Montalenti, F., and Mottet, C., "Crossover among structural motifs in transition and noble-metal clusters," *The Journal of Chemical Physics*, vol. 116, no. 9, p. 3856, 2002.

[8] Baletto, F. and Ferrando, R., "Structural properties of nanoclusters: Energetic, thermodynamic, and kinetic effects," *Reviews of Modern Physics*, vol. 77, pp. 371–423, May 2005.

[9] Balogh, L., Ribárik, G., and Ungár, T., "Stacking faults and twin boundaries in fcc crystals determined by x-ray diffraction profile analysis," *J. Appl. Phys.*, vol. 100, no. 2, p. 023512, 2006.

[10] Barnard, A. S., "Using theory and modelling to investigate shape at the nanoscale," *Journal of Materials Chemistry*, vol. 16, no. 9, p. 813, 2006.

[11] Baskes, M., "Modified embedded-atom potentials for cubic materials and impurities," *Physical Review B*, vol. 46, no. 5, p. 2727, 1992.

[12] Beyerlein, K., Cervellino, A., Leoni, M., Snyder, R., and Scardi, P., "Debye equation versus whole powder pattern modelling: Real versus reciprocal space modelling of nanomaterials," *Z. Kristallogr. Suppl.*, vol. 30, pp. 85–90, 2009.

[13] Beyerlein, K., Leoni, M., Snyder, R., and Scardi, P., "On faulting in nanocrystallites of fcc metals," *Mat. Sci. For.*, vol. 681, pp. 13–18, 2011.

[14] Beyerlein, K., Solla-Gullón, J., Herrero, E., Garnier, E., Pailloux, F., Leoni, M., Scardi, P., Snyder, R., Aldaz, A., and Feliu, J., "Characterization of (111) surface tailored pt nanoparticles by electrochemistry and x-ray powder diffraction," *Materials Science and Engineering: A*, vol. 528, no. 1, pp. 83 – 90, 2010.

[15] Bolt, R., "Frequency Distribution of Eigentones in a Three-Dimensional Continuum," *The Journal of the Acoustical Society of America*, vol. 10, no. 1932, p. 258, 1939.

[16] Born, M. and Huang, K., *Dynamical Theory of Crystal Lattices*. Oxford University Press, 1962.

[17] Brandstetter, S., Derlet, P. M., Van Petegem, S., and Van Swygenhoven, H., "Williamson-hall anisotropy in nanocrystalline metals: X-ray diffraction experiments and atomistic simulations," *Acta Materialia*, vol. 56, no. 2, pp. 165–176, 2008.

[18] Bratlie, K. M., Lee, H., Komvopoulos, K., Yang, P., and Somorjai, G. a., "Platinum nanoparticle shape effects on benzene

hydrogenation selectivity.," *Nano letters*, vol. 7, pp. 3097–101, Oct. 2007.

[19] Buehler, M. J., *Atomistic Modeling of Materials Failure*. Springer, 2008.

[20] Burda, C., Chen, X., Narayanan, R., and El-Sayed, M. a., "Chemistry and properties of nanocrystals of different shapes.," *Chemical reviews*, vol. 105, pp. 1025–102, Apr. 2005.

[21] Caglioti, G., Paoletti, A., and Ricci, F. *Nuclear Instruments & Methods in Physics Research*, vol. 3, p. 223, 1958.

[22] Cauchy, A., *Oevre's Completes d' Augustin Cauchy, Vol. II*, vol. II. Paris: Gauthier-Villars, 1908.

[23] Cervellino, A., Giannini, C., and Guagliardi, A., "Determination of nanoparticle structure type, size and strain distribution from x-ray data for monatomic f.c.c.-derived non-crystallographic nanoclusters," *J. Appl. Crystallogr.*, vol. 36, pp. 1148–1158, 2003.

[24] Cervellino, A., Giannini, C., and Guagliardi, A., "On the efficient evaluation of fourier patterns for nanoparticles and clusters," *Journal of Computational Chemistry*, vol. 27, no. 9, pp. 995–1008, 2006.

[25] Cervellino, A., Giannini, C., Guagliardi, A., and Ladisa, M., "Nanoparticle size distribution estimation by a full-pattern

powder diffraction analysis," *Phys. Rev. B*, vol. 72, no. 3, p. 035412, 2005.

[26] Chui, Y., Grochola, G., Snook, I., and Russo, S., "Molecular dynamics investigation of the structural and thermodynamic properties of gold nanoclusters of different morphologies," *Physical Review B*, vol. 75, pp. 1–4, Jan. 2007.

[27] Chui, Y. H., Opletal, G., Snook, I. K., and Russo, S. P., "Modeling the crystallization of gold nanoclusters - the effect of the potential energy function," *Journal of Physics: Condensed Matter*, vol. 21, p. 144207, Apr. 2009.

[28] Chushak, Y. and Bartell, L., "Molecular dynamics simulations of the freezing of gold nanoparticles," *The European Physical Journal D-Atomic, Molecular, Optical and Plasma Physics*, vol. 16, no. 1, pp. 43–46, 2001.

[29] Cleveland, C., Landman, U., Schaaff, T., Shafigullin, M., Stephens, P., and Whetten, R., "Structural Evolution of Smaller Gold Nanocrystals: The Truncated Decahedral Motif," *Physical Review Letters*, vol. 79, pp. 1873–1876, Sept. 1997.

[30] Cleveland, C. L. and Landman, U., "The energetics and structure of nickel clusters: Size dependence," *The Journal of Chemical Physics*, vol. 94, no. 11, p. 7376, 1991.

[31] Cleveland, C. L., Landman, U., Shafigullin, M. N., Stephens, P. W., and Whetten, R. L., "Structural evolution of larger gold clusters," *Zeitschrift für Physik D Atoms, Molecules and Clusters*, vol. 40, pp. 503–508, May 1997.

[32] Cullity, B. D., *Elements of X-ray Diffraction*. Addison-Wesley Publishing, 1956.

[33] Daw, M., "The embedded-atom method: a review of theory and applications," *Materials Science Reports*, vol. 9, pp. 251–310, Mar. 1993.

[34] Daw, M., "Model of metallic cohesion: The embedded-atom method," *Physical Review B*, vol. 39, no. 11, p. 7441, 1989.

[35] Daw, M. and Baskes, M., "Embedded-atom method: Derivation and application to impurities, surfaces, and other defects in metals," *Physical Review B*, vol. 29, no. 12, p. 6443, 1984.

[36] de Keijser, T., Mittemeijer, E. J., and Rozendaal, H. C. F., "The determination of crystallite-size and lattice-strain parameters in conjunction with the profile-refinement method for the determination of crystal structures," *Journal of Applied Crystallography*, vol. 16, pp. 309–316, Jun 1983.

[37] Debye, P., "X-ray dispersal," *Ann. Phys.*, vol. 46, no. 6, pp. 809–823, 1915.

[38] Debye, P. and Scherrer, P., "Interference on inordinate orientated particles in roentgen light," *PHYSIKALISCHE ZEITSCHRIFT*, vol. 17, pp. 277–283, 1916.

[39] Debye, P., "Interferens von Rontgenstrahlen und Warmebewegung," *Annalen der Physik*, p. 49, 1914.

[40] Derlet, P. M., Van Petegem, S., and Van Swygenhoven, H., "Calculation of x-ray spectra for nanocrystalline materials," *Physical Review B*, vol. 71, no. 2, p. 024114, 2005.

[41] Egami, T. and Billinge, S. J. L., *Underneath the Bragg peaks : structural analysis of complex materials*. Pergamon materials series v. 7, Amsterdam ; Boston: Pergamon, 1st ed., 2003.

[42] El-Sayed, M. a., "Some interesting properties of metals confined in time and nanometer space of different shapes.," *Accounts of chemical research*, vol. 34, pp. 257–64, Apr. 2001.

[43] Estevez-Rams, E., Leoni, M., Scardi, P., Aragon-Fernandez, B., and Fuess, H., "On the powder diffraction pattern of crystals with stacking faults," *Philosophical Magazine*, vol. 83, pp. 4045–4057, Dec. 2003.

[44] Estevez-Rams, E., Welzel, U., Pentón Madrigal, a., and Mittemeijer, E. J., "Stacking and twin faults in close-packed crystal structures: exact description of random faulting statistics

for the full range of faulting probabilities.," *Acta crystallographica. Section A, Foundations of crystallography*, vol. 64, pp. 537–48, Sept. 2008.

[45] Ewald, P. P., "X-ray diffraction by finite and imperfect crystal lattices," *Proc. Phys. Soc.*, vol. 52, no. 1, p. 167, 1940.

[46] Ewald, P. P., "Max von Laue. 1879-1960," *Biographical Memoirs of Fellows of the Royal Society*, vol. 6, pp. 134–156, Nov. 1960.

[47] Farges, J., Feraudy, M. F. d., Raoult, B., and Torchet, G., "Noncrystalline structure of argon clusters. i. polyicosahedral structure of ar[sub n] clusters, $20 < n < 50$," *The Journal of Chemical Physics*, vol. 78, no. 8, pp. 5067–5080, 1983.

[48] Farges, J., Feraudy, M. F. d., Raoult, B., and Torchet, G., "Noncrystalline structure of argon clusters. ii. multilayer icosahedral structure of ar[sub n] clusters $50 < n < 750$," *The Journal of Chemical Physics*, vol. 84, no. 6, pp. 3491–3501, 1986.

[49] Farges, J., Raoult, B., and Torchet, G., "Crystalline and noncrystalline effects in electron diffraction patterns from small clusters in an argon cluster beam," *The Journal of Chemical Physics*, vol. 59, no. 7, pp. 3454–3458, 1973.

[50] Feynman, R. P., *Six Easy Pieces*. Basic Books, 1995.

[51] Finnis, M. W. and Sinclair, J. E., "A simple empirical n-body potential for transition metals," *Philosophical Magazine A*, vol. 50, no. 1, pp. 45–55, 1984.

[52] Foiles, S., Baskes, M., and Daw, M., "Embedded-atom-method functions for the fcc metals Cu, Ag, Au, Ni, Pd, Pt, and their alloys," *Physical Review B*, vol. 33, no. 12, p. 7983, 1986.

[53] Fox, A. and Fisher, R., "A summary of low-angle X-ray atomic scattering factors measured by the critical voltage effect in high energy electron diffraction," *Australian Journal of Physics*, vol. 41, no. 3, pp. 461–468, 1988.

[54] Germer, L. H. and White, A. H., "Electron diffraction studies of thin films. ii. anomalous powder patterns produced by small crystals," *Physical Review*, vol. 60, no. 6, pp. 447–454, 1941.

[55] Gilbert, B., Huang, F., Lin, Z., Goodell, C., Zhang, H., and Banfield, J. F., "Surface chemistry controls crystallinity of ZnS nanoparticles.," *Nano letters*, vol. 6, pp. 605–10, Apr. 2006.

[56] Gilbert, B., Huang, F., Zhang, H., Waychunas, G. a., and Banfield, J. F., "Nanoparticles: strained and stiff.," *Science (New York, N.Y.)*, vol. 305, pp. 651–4, July 2004.

[57] Gilbert, B., Zhang, H., Huang, F., Finnegan, M. P., Waychunas, G. a., and Banfield, J. F., "Special phase transformation and crystal growth pathways observed in nanoparticles," *Geochemical Transactions*, vol. 4, no. 4, p. 20, 2003.

[58] Gnutzmann, V. and Vogel, W., "Structural sensitivity of the standard pt/sio2 catalyst europt-1 to h-2 and o-2 exposure by insitu x-ray-diffraction," *Journal of Physical Chemistry*, vol. 94, no. 12, pp. 4991–4997, 1990.

[59] Guinier, A., *X-ray Diffraction in Crystals, Imperfect Crystals, and Amorphous Bodies*. Series of books in physics, San Francisco: W.H. Freeman, 1963.

[60] Haftel, M., "Surface reconstruction of platinum and gold and the embedded-atom model," *Physical Review B*, vol. 48, no. 4, p. 2611, 1993.

[61] Haftel, M., Andreadis, T., Lill, J., and Eridon, J., "Surface relaxation of iron and the embedded-atom method," *Physical Review B*, vol. 42, no. 18, p. 11540, 1990.

[62] Hall, B. D., Flüeli, M., Monot, R., and Borel, J. P., "Electron diffraction on unsupported ultrafine silver particles," *Zeitschrift für Physik D Atoms, Molecules and Clusters*, vol. 12, pp. 97–101, 1989.

[63] Hall, B. D., Flueli, M., Monot, R., and Borel, J. P., "Multiply twinned structures in unsupported ultrafine silver particles observed by electron-diffraction," *Physical Review B*, vol. 43, no. 5, pp. 3906–3917, 1991.

[64] Hall, B. D. and Monot, R., "Calculating the debye-scherrer diffraction pattern for large clusters," *Computers in Physics*, vol. 5, no. 4, pp. 414–418, 1991.

[65] Hendricks, S. and Teller, E., "X-ray interference in partially ordered layer lattices," *J. Chem. Phys.*, vol. 10, no. 3, pp. 147–167, 1942.

[66] Hendy, S. and Hall, B., "Molecular-dynamics simulations of lead clusters," *Physical Review B*, vol. 64, pp. 1–11, Aug. 2001.

[67] Herbstein, F. H. and Averbach, B. L., "Temperature-diffuse scattering for powder patterns from cubic crystals," *Acta Crystallographica*, vol. 8, pp. 843–844, Dec. 1955.

[68] Hosemann, R. and Bagchi, S., *Direct Analysis of Diffraction by Matter*. North-Holland Pub. Co., 1962.

[69] Hubbell, J. H. and Seltzer, S. M., "Tables of x-ray mass attenuation coefficients and mass energy-absorption coefficients from 1 kev to 20 mev for elements z = 1 to 92 and 48 additional substances of dosimetric interest," July 2004.

[70] Ino, T. and Minami, N., "X-ray-diffraction by small crystals," *Acta Crystallogr. A*, vol. 35, pp. 163–170, 1979.

[71] Ino, T. and Minami, N., "Intensity profile of debye-scherrer line from small crystallites," *Acta Crystallographica A*, vol. 40, pp. 538–544, 1984.

[72] Jacobsen, K., Norskov, J., and Puska, M., "Interatomic interactions in the effective-medium theory," *Physical Review B*, vol. 35, no. 14, p. 7423, 1987.

[73] Jaeger, H. M. and Nagel, S. R., "Physics of the granular state," *Science*, vol. 255, no. 5051, pp. 1523–1531, 1992.

[74] Jagodzinski, H., "Eindimensionale Fehlordnung in Kristallen und ihr Einfluss auf die Röntgeninterferenzen. I. Berechnung des Fehlordnungsgrades aus den Röntgenintensitäten," *Acta Crystallogr.*, vol. 2, pp. 201–207, Aug 1949.

[75] Jagodzinski, H., "Eindimensionale fehlordnung in kristallen und ihr einfluss auf die rontgeninterferenzen. ii. berechnung der fehlgeordneten dichtesten kugelpackungen mit wechselwirkungen der reichweite 3," *Acta Crystallogr.*, vol. 2, no. 4, pp. 208–214, 1949.

[76] Jalali, P. and Li, M., "An estimate of random close packing density in monodisperse hard spheres," *Journal of Chemical Physics*, vol. 120, no. 2, pp. 1138–1139, 2004.

[77] James, R. W., *The Crystalline State Vol. II: The Optical Principles of the Diffraction of X-rays*. London: G. Bell and Sons, 1962.

[78] Langford, J. I. and Louër, D., "Diffraction line profiles and scherrer constants for materials with cylindrical crystallites," *J. Appl. Crystallogr.*, vol. 15, no. 1, pp. 20–26, 1982.

[79] Langford, J. I. and Wilson, A. J. C., "Scherrer after 60 years - survey and some new results in determination of crystallite size," *J. Appl. Crystallogr.*, vol. 11, pp. 102–113, 1978.

[80] Laval, J. *C. R. Acad. Sci. Paris*, vol. 208, p. 1512, 1939.

[81] Lee, B. and Cho, K., "Extended embedded-atom method for platinum nanoparticles," *Surface Science*, vol. 600, pp. 1982–1990, May 2006.

[82] Lee, B. and Baskes, M., "Second nearest-neighbor modified embedded-atom-method potential," *Physical Review B*, vol. 62, no. 13, p. 8564, 2000.

[83] Lee, B.-J., Baskes, M., Kim, H., and Koo Cho, Y., "Second nearest-neighbor modified embedded atom method potentials for bcc transition metals," *Physical Review B*, vol. 64, Oct. 2001.

[84] Lee, B.-J., Shim, J.-H., and Baskes, M., "Semiempirical atomic potentials for the fcc metals Cu, Ag, Au, Ni, Pd, Pt, Al, and

Pb based on first and second nearest-neighbor modified embedded atom method," *Physical Review B*, vol. 68, pp. 1–11, Oct. 2003.

[85] Lee, I., Morales, R., Albiter, M. a., and Zaera, F., "Synthesis of heterogeneous catalysts with well shaped platinum particles to control reaction selectivity.," *Proceedings of the National Academy of Sciences of the United States of America*, vol. 105, pp. 15241–6, Oct. 2008.

[86] Leoni, M., Confente, T., and Scardi, P., "Pm2k: a flexible program implementing whole powder pattern modelling," *Z. Kristallogr. Suppl.*, vol. 23, pp. 249–254, 2006.

[87] Lisiecki, I., "Size, shape, and structural control of metallic nanocrystals.," *The journal of physical chemistry. B*, vol. 109, pp. 12231–44, June 2005.

[88] Longo, A. and Martorana, A., "Distorted f.c.c. arrangement of gold nanoclusters: a model of spherical particles with microstrains and stacking faults," *Journal of Applied Crystallography*, vol. 41, pp. 446–455, 2008.

[89] Luedtke, W. D. and Landman, U., "Structure, Dynamics, and Thermodynamics of Passivated Gold Nanocrystallites and Their Assemblies," *The Journal of Physical Chemistry*, vol. 100, pp. 13323–13329, Jan. 1996.

[90] Maa, D., "Distribution of eigentones in a rectangular chamber at low frequency range," *The Journal of the Acoustical Society of America*, vol. 10, p. 235, 1939.

[91] Marks, L., "Experimental studies of small particle structures," *Reports on Progress in Physics*, vol. 57, no. September 1993, 1994.

[92] Marquardt, D. W., "An algorithm for least-squares estimation of nonlinear parameters," *SIAM Journal on Applied Mathematics*, vol. 11, no. 2, pp. 431–441, 1963.

[93] Martinez-Garcia, J., Leoni, M., and Scardi, P., "A general approach for determining the diffraction contrast factor of straight-line dislocations," *Acta Crystallographica Section A*, vol. 65, no. 2, pp. 109–119, 2009.

[94] Martyna, G., Tuckerman, M., Tobias, D., and Klein, M., "Explicit reversible integrators for extended systems dynamics," *Molecular Physics*, vol. 87, pp. 1117–1157, Apr. 1996.

[95] Martyna, G. J., Klein, M. L., and Tuckerman, M., "Nose-Hoover chains:The canonical ensemble via continuous dynamics," *Journal of Chemical Physics*, vol. 97, no. 4, pp. 2635–2643, 1992.

[96] Martyna, G. J., Tobias, D. J., and Klein, M. L., "Constant pressure molecular dynamics algorithms," *The Journal of Chemical Physics*, vol. 101, no. 5, p. 4177, 1994.

[97] Niederdraenk, F., Seufert, K., Luczak, P., Kulkarni, S. K., Chory, C., Neder, R. B., and Kumpf, C., "Structure of small ii-vi semiconductor nanoparticles: A new approach based on powder diffraction," *Phys. Status Solidi (c)*, vol. 4, no. 9, pp. 3234–3243, 2007.

[98] Nosé, S., "A molecular-dynamics method for simulations in the canonical ensemble," *Molecular Physics*, vol. 52, no. 2, pp. 255–268, 1984.

[99] Palosz, B., Grzanka, E., Gierlotka, S., Stel'makh, S., Pielaszek, R., Bismayer, U., Neuefeind, J., Weber, H.-P., Proffen, T., Von Dreele, R., and Palosz, W., "Analysis of short and long range atomic order in nanocrystalline diamonds with application of powder diffractometry," *Z. Kristallogr.*, vol. 217, pp. 497–509, 2002.

[100] Palosz, B., Grzanka, E., Gierlotka, S., and Stelmakh, S., "Nanocrystals: Breaking limitations of data analysis," *Z. Kristallogr.*, vol. 225, no. 12, pp. 588–598, 2010.

[101] Parrinello, M. and Rahman, A., "Polymorphic transitions in single crystals: A new molecular dynamics method," *Journal of Applied Physics*, vol. 52, no. December, pp. 7182–7190, 1981.

[102] Paskin, a., "Elastic wave velocity effect on temperature diffuse scattering in cubic powders," *Acta Crystallographica*, vol. 12, pp. 290–294, Apr. 1959.

[103] Paterson, M., "X-Ray Diffraction by Face-Centered Cubic Crystals with Deformation Faults," *Journal of Applied Physics*, vol. 23, no. 8, pp. 805–811, 1952.

[104] Patterson, A. L., "The diffraction of x-rays by small crystalline particles," *Phys. Rev.*, vol. 56, no. 10, p. 972, 1939.

[105] Petroski, J. M., Wang, Z. L., Green, T. C., and El-Sayed, M. a., "Kinetically Controlled Growth and Shape Formation Mechanism of Platinum Nanoparticles," *The Journal of Physical Chemistry B*, vol. 102, pp. 3316–3320, Apr. 1998.

[106] Plimpton, S., "Fast parallel algorithms for short-range molecular dynamics," *Journal of Computational Physics*, vol. 117, no. 1, pp. 1–19, 1995.

[107] Preston, G. D., "Diffraction of x-rays by crystals at elevated temperatures," *Proc. Roy. Soc. London A.*, vol. 172, pp. 116–126, 1939.

[108] Prince, E., ed., *International Tables for Crystallography Volume C: Mathematical, physical and chemical tables*. IUCr / Wiley Publications, 2006.

[109] Rafaja, D., Valvoda, V., Kub, J., Temst, K., Van Bael, M., and Bruynseraede, Y., "Long-range periodicity and disorder in two-dimensional arrays of metallic dots studied by x-ray diffraction," *Physical Review B*, vol. 61, pp. 16144–16153, June 2000.

[110] Rafaja, D., Dopita, M., Ruzicka, M., Klemm, V., Heger, D., Schreiber, G., and Sima, M., "Microstructure development in Cr - Al -Si - N nanocomposites deposited by cathodic arc evaporation," *Surface and Coatings Technology*, vol. 201, pp. 2835–2843, Dec. 2006.

[111] Rafaja, D., Klemm, V., Schreiber, G., Knapp, M., and Kužel, R., "Interference phenomena observed by X-ray diffraction in nanocrystalline thin films," *Journal of Applied Crystallography*, vol. 37, pp. 613–620, July 2004.

[112] Rao, C. N. R., Thomas, P. J., and Kulkarni, G. U., *Nanocrystals: synthesis, properties, and applications*. Springer series in materials science v. 95, New York: Springer, 2007.

[113] Reinhard, D., Hall, B. D., Berthoud, P., Valkealahti, S., and Monot, R., "Unsupported nanometer-sized copper clusters studied by electron diffraction and molecular dynamics," *Physical Review B*, vol. 58, no. 8, p. 4917, 1998.

[114] Ribárik, G., Audebrand, N., Palancher, H., Ungár, T., and Louër, D., "Dislocation densities and crystallite size distributions in nanocrystalline ball-milled fluorides, M F 2 (M = Ca, Sr, Ba and Cd), determined by X-ray diffraction line-profile analysis," *Journal of Applied Crystallography*, vol. 38, pp. 912–926, Nov. 2005.

[115] Ribárik, G., Gubicza, J., and Ungár, T., "Correlation between strength and microstructure of ball-milled al-mg alloys determined by x-ray diffraction," *Materials Science and Engineering A*, vol. 387-389, pp. 343–347, Dec. 2004.

[116] Ribárik, G., Ungár, T., and Gubicza, J., "Mwp-fit: a program for multiple whole-profile fitting of diffraction peak profiles by ab initio theoretical functions," *Journal of Applied Crystallography*, vol. 34, pp. 669–676, Oct 2001.

[117] Rietveld, H. M., "Line profiles of neutron powder-diffraction peaks for structure refinement," *Acta Crystallographica*, vol. 22, pp. 151–&, 1967.

[118] Rietveld, H. M., "A profile refinement method for nuclear and magnetic structures," *Journal of Applied Crystallography*, vol. 2, pp. 65–71, Jun 1969.

[119] Rioux, R. M., Song, H., Grass, M., Habas, S., Niesz, K., Hoefelmeyer, J. D., Yang, P., and Somorjai, G. a.,

"Monodisperse platinum nanoparticles of well-defined shape: synthesis, characterization, catalytic properties and future prospects," *Topics in Catalysis*, vol. 39, pp. 167–174, Oct. 2006.

[120] Roe, G., "Frequency distribution of normal modes," *The Journal of the Acoustical Society of America*, vol. 13, p. 1, 1941.

[121] Rose, J., Smith, J., and Guinea, F., "Universal features of the equation of state of metals," *Physical Review B*, vol. 29, p. 2963, 1984.

[122] Scardi, P. and Antonucci, P., "Xrd characterization of highly dispersed metal catalysts on carbon support," *Journal of Materials Research*, vol. 8, no. 8, pp. 1829–1835, 1993.

[123] Scardi, P. and Leoni, M., "Diffraction line profiles from polydisperse crystalline systems," *Acta Crystallographica Section A*, vol. 57, pp. 604–613, 2001.

[124] Scardi, P. and Leoni, M., "Whole powder pattern modelling," *Acta Crystallogr. A*, vol. 58, pp. 190–200, 2002.

[125] Scardi, P. and Leoni, M., *Diffraction analysis of the microstructure of materials*, ch. Whole Powder Pattern Modelling: Theory and Applications, pp. 51–91. Springer-Verlag, 2004.

[126] Scardi, P. and Leoni, M., "Line profile analysis: pattern modelling versus profile fitting," *Journal of Applied Crystallography*, vol. 39, pp. 24–31, 2006.

[127] Scardi, P., Leoni, M., and Delhez, R., "Line broadening analysis using integral breadth methods: a critical review," *Journal of Applied Crystallography*, vol. 37, pp. 381–390, 2004.

[128] Scardi, P., Leoni, M., and Dong, Y., "Whole diffraction pattern-fitting of polycrystalline fcc materials based on microstructure," *Eur. Phys. J. B*, vol. 18, no. 1, pp. 23–30, 2000.

[129] Scherrer, P., "Bestimmung der grösse und der inneren struktur von kolloidteilchen mittels röntgenstrahlen," *Nachr. Ges. Wiss. Göttingen*, vol. 26, pp. 98–100, 1918.

[130] Schoening, F., "The Debye-Waller factor for small cubes and thin films," *Acta Crystallographica Section A: Crystal Physics, Diffraction, Theoretical and General Crystallography*, vol. 24, no. 6, pp. 615–619, 1968.

[131] Shim, J., "Molecular dynamics simulation of the crystallization of a liquid gold nanoparticle," *Journal of Crystal Growth*, vol. 250, pp. 558–564, Apr. 2003.

[132] Shinoda, W., Shiga, M., and Mikami, M., "Rapid estimation of elastic constants by molecular dynamics simulation under constant stress," *Physical Review B*, vol. 69, pp. 16 –18, Apr. 2004.

[133] Simmons, G. and Wang, H., *Single Crystal Elastic Constants and Calculated Aggregate Properties: A Handbook*. Cambridge, MA: MIT Press, 1971.

[134] Snyder, R. L., Fiala, J., and Bunge, H. J., eds., *Defect and Microstructure Analysis by Diffraction*. IUCr Monographs on Crystallography, vol. 10, Oxford University Press, 1999.

[135] Solla-Gullón, J., Vidal-Iglesias, F., Herrero, E., Feliu, J., and Aldaz, A., "CO monolayer oxidation on semi-spherical and preferentially oriented (100) and (111) platinum nanoparticles," *Electrochemistry Communications*, vol. 8, pp. 189–194, Jan. 2006.

[136] Stedman, R., Almqvist, L., and Nilsson, G., "Phonon-frequency distributions and heat capacities of aluminum and lead," *Physical Review*, vol. 162, no. 3, p. 549, 1967.

[137] Stokes, A. R. and Wilson, A. J. C., "A method of calculating the integral breadths of debye-scherrer lines," *Proceedings of the Cambridge Philosophical Society*, vol. 38, pp. 313–322, 1942.

[138] Stokes, A. R. and Wilson, A. J. C., "The diffraction of x rays by distorted crystal aggregates - i," *Proceedings of the Physical Society*, vol. 56, no. 3, p. 174, 1944.

[139] Suortti, P., "Correction of integrated bragg reflections of cubic powders for thermal diffuse scattering," *Annales Academiae Scientiarum Fennicae Series A*, vol. 240, pp. 2–33, 1967.

[140] Svensson, E. C., Brockhouse, B. N., and Rowe, J. M., "Crystal dynamics of copper," *Physical Review*, vol. 155, no. 3, p. 619, 1967.

[141] Torchet, G., Bouchier, H., Farges, J., de Feraudy, M. F., and Raoult, B., "Size effects in the structure and dynamics of co[sub 2] clusters," *The Journal of Chemical Physics*, vol. 81, no. 4, pp. 2137–2143, 1984.

[142] Torchet, G., Schwartz, P., Farges, J., de Feraudy, M. F., and Raoult, B., "Structure of solid water clusters formed in a free jet expansion," *The Journal of Chemical Physics*, vol. 79, no. 12, pp. 6196–6202, 1983.

[143] Torquato, S., Truskett, T. M., and Debenedetti, P. G., "Is random close packing of spheres well defined?," *Phys. Rev. Lett.*, vol. 84, p. 2064, Mar. 2000.

[144] Ungár, T. and Borbély, A., "The effect of dislocation contrast on x-ray line broadening: A new approach to line profile analysis," *Applied Physics Letters*, vol. 69, no. 21, pp. 3173–3175, 1996.

[145] Ungár, T., Ott, S., Sanders, P., Borbély, A., and Weertman, J., "Dislocations, grain size and planar faults in nanostructured copper determined by high resolution x-ray diffraction and a new procedure of peak profile analysis," *Acta Materialia*, vol. 46, pp. 3693–3699, June 1998.

[146] Urban, J., "Thermal diffuse X-ray scattering for small samples and small coherent scattering domains," *Acta Crystallographica Section A: Crystal Physics, Diffraction, Theoretical and General Crystallography*, vol. 31, no. 1, pp. 95–100, 1975.

[147] Velterop, L., Delhez, R., de Keijser, T. H., Mittemeijer, E. J., and Reefman, D., "X-ray diffraction analysis of stacking and twin faults in f.c.c. metals: a revision and allowance for texture and non-uniform fault probabilities," *J. Appl. Crystallogr.*, vol. 33, pp. 296–306, 2000.

[148] Vidal-Iglesias, F., Solla-Gullón, J., Montiel, V., Feliu, J., and Aldaz, a., "Screening of electrocatalysts for direct ammonia fuel cell: Ammonia oxidation on PtMe (Me: Ir, Rh, Pd, Ru) and preferentially oriented Pt(100) nanoparticles," *Journal of Power Sources*, vol. 171, pp. 448–456, Sept. 2007.

[149] Vogel, W., Rosner, B., and Tesche, B., "Structural investigations of gold (Au55) organometallic complexes by x-ray powder diffraction and transmission electron microscopy," *The Journal of Physical Chemistry*, vol. 97, pp. 11611–11616, Nov. 1993.

[150] Vogel, W., Bradley, J., Vollmer, O., and Abraham, I., "Transition from Five-Fold Symmetric to Twinned FCC Gold Particles by Thermally Induced Growth," *The Journal of Physical Chemistry B*, vol. 102, pp. 10853–10859, Dec. 1998.

[151] von Laue, M. *Z. Kristallogr.*, vol. 64, p. 115, 1926.

[152] Walker, C. B. and Chipman, D. R., "Thermal diffuse scattering in cubic powder patterns," *Acta Crystallographica Section A*, vol. 28, pp. 572–580, Nov. 1972.

[153] Warren, B., "X-ray studies of deformed metals," *Progress in Metal Physics*, vol. 8, no. 3, pp. 147–202, 1959.

[154] Warren, B. E., "Calculation of powder-pattern intensity distributions," *Journal of Applied Crystallography*, vol. 11, no. 6, pp. 695–698, 1978.

[155] Warren, B. E., *X-ray Diffraction*. New York: Dover, 1990.

[156] Warren, B. E. and Averbach, B. L., "The effect of cold-work distortion on x-ray patterns," *Journal of Applied Physics*, vol. 21, no. 6, pp. 595–599, 1950.

[157] Warren, B. E. and Averbach, B. L., "The separation of cold-work distortion and particle size broadening in x-ray patterns," *Journal of Applied Physics*, vol. 23, no. 4, pp. 497–497, 1952.

[158] Waychunas, G. a., "Natural nanoparticle structure, properties and reactivity from X-ray studies," *Powder Diffraction*, vol. 24, no. 2, p. 89, 2009.

[159] Whetten, R., Khoury, J., Alvarez, M., Murthy, S., Vezmar, I., Wang, Z., Stephens, P., Cleveland, C., Luedtke, W., and Landman, U., "Nanocrystal gold molecules," *Advanced materials*, vol. 8, no. 5, pp. 428–433, 1996.

[160] Whetten, R., Shafigullin, M., Khoury, J., Schaaff, T., Vezmar, I., Alvarez, M., and Wilkinson, A., "Crystal structures of molecular gold nanocrystal arrays," *Accounts of chemical research*, vol. 32, no. 5, pp. 397–406, 1999.

[161] Williamson, G. K. and Hall, W. H., "X-ray line broadening from filed aluminium and wolfram," *Acta Metallurgica*, vol. 1, no. 1, pp. 22–31, 1953.

[162] Wilson, A., "Imperfections in the structure of cobalt. ii. mathematical treatment of proposed structure," *Proc. Roy. Soc. London A*, vol. 180, pp. 277–285, 1942.

[163] Winkler, B. and Dove, M., "Thermodynamic properties of MgSiO3 perovskite derived from large scale molecular dynamics simulations," *Physics and Chemistry of Minerals*, vol. 18, pp. 407–415, Mar. 1992.

[164] Wolf, M. D. and Landman, U., "Genetic Algorithms for Structural Cluster Optimization," *The Journal of Physical Chemistry A*, vol. 102, pp. 6129–6137, July 1998.

[165] Zanchet, D., Hall, B. D., and Ugarte, D., "Structure Population in Thiol-Passivated Gold Nanoparticles," *The Journal of Physical Chemistry B*, vol. 104, pp. 11013–11018, Nov. 2000.

[166] Zernicke, F. and Prins, J. A. *Zeit Physik*, vol. 41, p. 184, 1927.